SURFACE ACOUSTIC WAVE SINGLE-PHASE UNIDIRECTIONAL TRANSDUCERS AND PHASE WEIGHTING

by

Edward Martin Garber

S.B. Massachusetts Institute of Technology (1975)
S.M. Massachusetts Institute of Technology (1980)
E.E. Massachusetts Institute of Technology (1980)

Submitted in Partial Fulfillment
of the Requirements for the Degree of

DOCTOR OF PHILOSOPHY

at the
MASSACHUSETTS INSTITUTE OF TECHNOLOGY
February, 1985

Signature of Author . . . . . .
Department of Electrical Engineering and Computer Science
February 1985

Certified by . . . . . .
Hermann A. Haus
Thesis Supervisor

Accepted by . . . . . .
Arthur C. Smith
Chairman, Department Committee

SURFACE ACOUSTIC WAVE SINGLE-PHASE UNIDIRECTIONAL TRANSDUCERS AND PHASE WEIGHTING

by

EDWARD MARTIN GARBER

Submitted to the Department of Electrical Engineering
and Computer Science on February 28, 1985,
in Partial Fulfillment of the Requirement for the Degree of
DOCTOR OF PHILOSOPHY

ABSTRACT

The single phase unidirectional transducer (SPUDT) has recently been invented by C. S. Hartmann [44]. It is a low loss surface acoustic wave (SAW) filter and is based on a distributed reflector being placed in the same region as a distributed source with proper phasing so as to achieve constructive interference in the forward direction and destructive interference in the reverse. Its key advantage is that low insertion loss can be obtained without the triple transit distortion which plagues bidirectional interdigital transducers (BIDT'S).

Coupled mode equations are extended to include resistive finger loss and propagation loss. Experimental unweighted SPUDT responses are compared with theoretical calculations based on the above model. Parameters can be chosen to obtain good agreement confirming the applicability of the coupled mode equations to the analysis of these structures. The SPUDT was matched to achieve 0.1 dB of insertion loss with 44.6 dB of triple transit suppression. This is 16.1 dB better than could be achieved with a lossless BIDT matched for the same insertion loss.

An analytical/numerical technique is developed to solve the coupled mode equations with an arbitrary distribution of transduction and reflection sources. These solutions are used to evaluate the range of applicability of a simple design algorithm (similar to the one used by P. V. Wright [115]) for SPUDT's in which multiple reflections are ignored, A paper design is presented for a 2.3 shape factor filter with 4.9 dB insertion loss, 60 dB rejection, and 40 dB triple transit suppression, assuming that continuously adjustable transduction elements and reflectors are available.

In Part II of this thesis, the focus is on the design of high performance frequency responses with constant strength and zero strength sources. The weighting is achieved solely by varying the spacing between these sources. Another goal is constraining the impulse response length to minimize the substrate area required. Although this has direct application to the design of SPUDT's, both the analysis and examples are geared toward BIDT's. Designs of this type with constant aperture transducers are also useful for suppression of both diffraction and transverse electrostatic end effects.

A quasi-Newton optimization procedure is used to design a low dynamic range amplitude and phase modulated waveform. A parameterization of the filter's response is used, instead of directly optimizing with respect to the source locations. This enables long filters to be designed with many more sources than parameters. An improved withdrawal weighting algorithm is then used with multiple envelopes to eliminate all amplitude modulation.

New structures for withdrawal weighting are presented that significantly increase the bandwidth over which the rejection band performance is good, and which also enable the passband ripple to be reduced. A paper design is presented for a very sharp 1.15 shape factor filter with -51 dB sidelobes and .37 dB peak-to-peak passband ripple. This represents more than an order of magnitude improvement over the best previously reported result with phase-only weighting. The sidelobes remain well controlled over a 55% fractional bandwidth and the device is 6.7% shorter than a Parks-McClellan amplitude modulated design of similar performance with two identical transducers. The Parks-McClellan design has good rejection over the full 300% fractional bandwidth, but would suffer from far more severe diffraction problems due to the 239:1 dynamic range of its source weights if implemented by apodization.

Thesis Supervisor: Hermann A. Haus
Title: Elihu Thomson Professor of Electrical Engineering

ACKNOWLEDGMENTS

I would like to thank Prof. H. A. Haus for his insight, advice and teaching. The powerful yet simple techniques he taught me will be useful long after graduation. C. S. Hartmann proposed working on the single-phase unidirectional transducer (SPUDT). Thanks are due him for many stimulating discussions, for having SPUDT's fabricated, and for allowing me to work on this thesis while at RF Monolithics. I would also like to thank my readers, Prof. J. S. Lim and Dr. J. Melngailis. I am grateful to Dr. J. Melngailis for providing me with useful and practical experimental advice and for his suggestions which helped improve this thesis. Gratitude is also due my colleagues N. A. Whitaker Jr., D. P. Chen and M. N. Islam for their valuable suggestions and encouragement.

I would like to thank the Macsyma Consortium and the MIT Laboratory for Computer Science for the use of their computer facilities. The expeditious work of G. J. Carrette, B. C. Neuman, J. I. Schiller and J. T. Wroclawski, in curing sick computer systems at critical times, was greatly appreciated. Thanks are also due the Analog Devices Group at Lincoln Laboratory for the use of their computer controlled RF measurement equipment, and to Dr. D. Oates for his instruction in its use.

Thanks go to R. Sezer for help with the typing. The assistance of my family and friends in the final preparation of this document was sincerely appreciated. E. W. Garber, B. H. Singer and Y. Q. Jin deserve special mention in this regard.

The support of the National Science Foundation Grants ENG79-09980 and ECS82-11650 are gratefully acknowledged.

To my parents

Table of Contents

PART II

Phase-Only Weighting

CHAPTER 1

INTRODUCTION

The interdigital surface acoustic wave (SAW) transducer (IDT) was first demonstrated by White and Voltmer [110]. In the ensuing 20 years, filters based on this device have been successfully used in many RF (10 MHz - 1 GHz) applications which can make good use of their selectivity, stability and flexibility in creating almost arbitrary magnitude and phase responses. In addition to their superior filtering performance compared to lumped element LC filters, SAW devices, which are fabricated using the planar technology of the integrated circuit industry, offer a cost advantage in mass production applications.

A fundamental disadvantage of standard SAW filters is their high insertion loss. In addition, although very good filters have been produced, there is a need to increase attenuation in the rejection band and to cut the ripple in the passband, while simultaneously reducing substrate area to minimize cost. The single-phase unidirectional transducer (SPUDT), which was invented by Hartmann [44] addresses the first issue, while phase weighting addresses the second. The SPUDT is the focus of the first part of the thesis, and phase weighting is discussed in the second.

SAW filters consist of two transducers, an input transducer which converts the electrical signal into an acoustic one, and an output transducer which converts it back again. The filtering is done in the electro-acoustic conversion process. The standard transducer consists of two interdigitated metal combs deposited on a piezoelectric substrate (Fig. 1.1). The

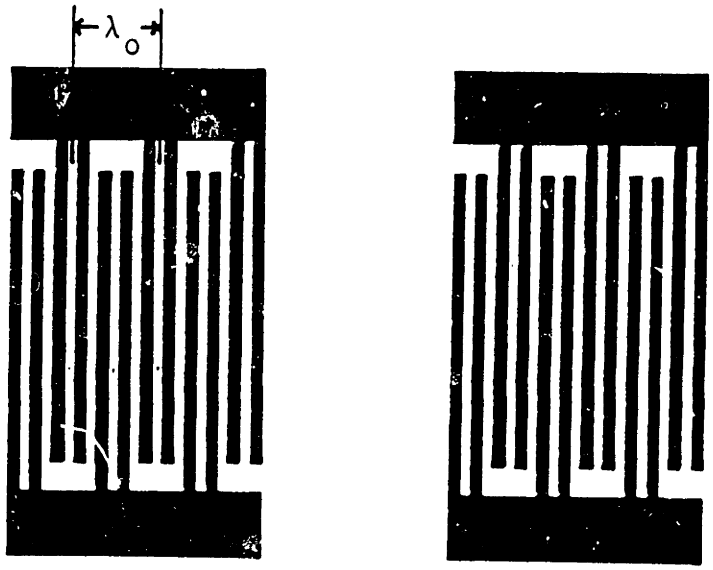

Figure 1.1 A Split Finger Interdigital SAW Filter
(After [32])

acoustic sources can be approximately localized to the gaps between fingers attached to opposite bus-bars. The space between sources can be simply treated as a time delay due to the dispersionless nature of SAW propagation. The impulse response of each transducer roughly consists of pulses at these gaps. Then the response of the entire filter is the convolution of these two responses in the time domain, or the product of their Fourier transforms in the frequency domain [41].

In order to obtain a large response in the vicinity of the center frequency, f_o, the period of the structure should be roughly the wavelength at center frequency, λ_o, so that the responses of each of these elemental sources will add in phase.

Due to the symmetry of the IDT's structure, it radiates equally well in the forward and backward directions. This immediately causes a 3 dB loss in the sending transducer if it is perfectly matched. Using reciprocity and power conservation, it can be shown that the receiving transducer will only pick up half the incident power, transmit 1/4 and reflect 1/4, if it is also perfectly matched to its electrical load (see Sec. 4.1).

This reflected signal is more properly called the regenerated signal, since it arises from reradiation by the voltage induced across the receiving transducer by the incident SAW wave. There is in addition a mechanical-electric (MEL) reflected signal caused by the acoustic impedance discontinuities introduced by the metal strips on the surface. This effect is not present in split finger structure of Fig. (1.1), since there are 4 electrodes/wavelength, and thus at the synchronous frequency for transduction, it is grossly detuned from the Bragg reflection condition. It is important to note that the energy reflected from the output transducer propagates back to the input transducer, reflects once again and travels to the output to be picked up. This signal, called the triple transit signal (TTS) due to its three transits of the region between the two transducers, is only 12 dB down from the main signal if both transducers are perfectly matched (see Sec. 4.1). The TTS is an undesirable distortion which would appear as ghosts on television broadcasts, cause intersymbol interference in digital data transmission over an analog medium, and would always distort the frequency response of filters by a ripple which would appear in the magnitude and phase responses.

The TTS signal of a standard bi-directional IDT can be greatly reduced by shorting out the regenerated field to a certain degree with a resistance which is less than the value required for a perfect match. It is generally accepted [C. S. Hartmann, personal communication] that at least 40 dB triple transit suppression is required in order for a filter to be useful. Attainment of this specification with a bi-directional IDT (BIDT) by mismatching, would require a 15 dB insertion loss. This is the magnitude of the insertion loss problem of BIDT's, not the 6 dB bi-directionality loss.

The obvious solution to the insertion loss and triple transit problems of the BIDT is the development of a unidirectional transducer (UDT). If a UDT were perfectly matched, all the energy would couple from the electrical port to the front acoustic port of the transmitting transducer, and by reciprocity would all be converted back to electrical energy at the receiving transducer. Thus there would be no loss and no triple transit. This was recognized almost immediately after the first demonstration of the BIDT in 1965 [110]. Between 1967 and the present, many papers were presented which proposed various types of UDT's.

1.1 Overview of Part I

There are two basic procedures for obtaining unidirectionality using structures similar to that of the interdigital transducer (IDT). The first is to use three or more electrical phases to drive the sources with phasing corresponding to that of a traveling wave. The result is constructive interference in the forward direction and destructive interference in the reverse direction. The second technique involves reflecting the backwards traveling wave into a forward directed one. Hartmann's [44] SPUDT is based on this second approach and benefits from not needing the complicated phase shift networks of the first type of unidirectional transducer, nor is a complicated fabrication procedure required. The SPUDT integrates the reflection and transduction functions in the same space for maximum bandwidth. In addition, these two functions can be weighted independently for flexibility as to spectral response. The SPUDT and other unidirectional transducers are reviewed in more detail in chapter 2.

The focus of Chapter 3 is on modeling IDT's, both the standard bidirectional variety (BIDT), and the new SPUDT. Hartmann's impulse transduction model [41] is extended to include both transduction and reflection. The coupling-of-modes (COM) [44,11] continuum approximation to IDT's, which includes both transduction and reflection is presented. It is shown that the COM model closely approximates the impulse transduction and reflection model in the limit of low reflection. The COM model is extended to include both propagation loss and resistive finger loss. Chapter 4 discusses a simple design algorithm [115] based on the low reflectivity limit of the COM equations. Several designs are performed, and the designed responses based on the low reflectivity approximation are compared with those predicted by the full COM equations. These examples show that if the reflectors and the transducers are continuously adjustable, quite good filters of moderate loss can be designed. Chapter 5 concludes Part I of the thesis with an experimental verification of the SPUDT. The triple transit signal is found to fall as the transducers are matched, unlike a standard BIDT. The experimental results are compared with theoretical calculations based on the COM equations.

1.2 Motivation for Phase-Weighting and Summary of Previous Work

In the second part of this thesis we investigate how these transduction and reflection functions can be implemented using easily fabricated constant strength elements. The focus of Part II is on the transduction function, but in the low reflectivity limit of the coupling-of-modes equations, it equally well applies to the synthesis of reflection responses.

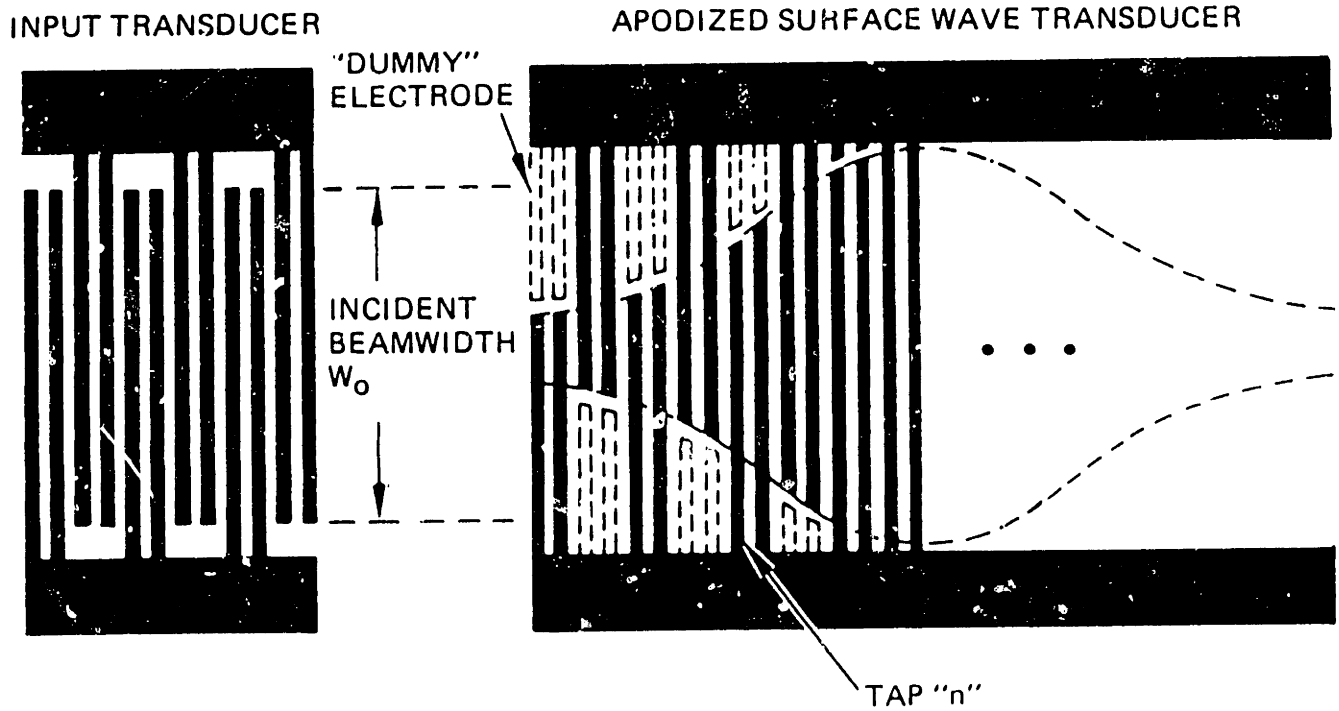

Figure 1.2 A Filter Employing One Apodized and One Uniform Transducer
Note: The "dummy" electrodes help to maintain a uniform velocity across the aperture. (After [32])

In order to achieve a desired transductio. or reflection frequency response, the corresponding spatial responses must be weighted. The standard weighting technique for transduction is apodization (Fig. 1.2). The receiving gaps do not extend over the full aperture of the transducer. They just contribute an increment of current to the bus bar proportional to the fraction of the full aperture intercepted by the gap.

Filters designed with this weighting technique, using standard design procedures such as the Parks-McClellan [85,80] algorithm, require large variation in weights in order to obtain high performance frequency responses (low passband ripple, high rejection outside the passband, sharp cut-off). Thus apodized filters with a reasonable maximum aperture have many small gaps, and their frequency responses are degraded by diffraction [82] and transverse electrostatic fringing fields [107].

Ideally we would like to be able to control both the amplitude and position of sources while maintaining a uniform aperture. Width weighting [74] is one such method. The

weighting is done by continuously varying the metalization ratio. The major problem with this technique is that the dynamic range is quite limited; for split finger transducers, only a 1.8:1 weighting range is available for metalization ratios ranging from .1 to .9 (see Eq. (3.69)). An additional problem with this procedure is that on strongly piezoelectric substrates, the velocity becomes a function of the weighting, since the larger the local metalization ratio the slower the wave. Since the piezoelectric slowing of a wave is an effect which extends over many wavelengths (see Sec. 3.9), it is not valid to simply assign one velocity to the metalized region and one to the gaps. Therefore, compensation is difficult.

Another technique for continuous control of transduction is capacitive tap weighting [90,65,5]. In this technique, a capacitive voltage divider is used to continuously adjust the voltage driving the fingers exciting the acoustic wave (see Fig. 1.3). These techniques suffer from some of the same practical difficulties as apodization since it is the variable overlap of fingers which control the variable capacitors in the practical implementation

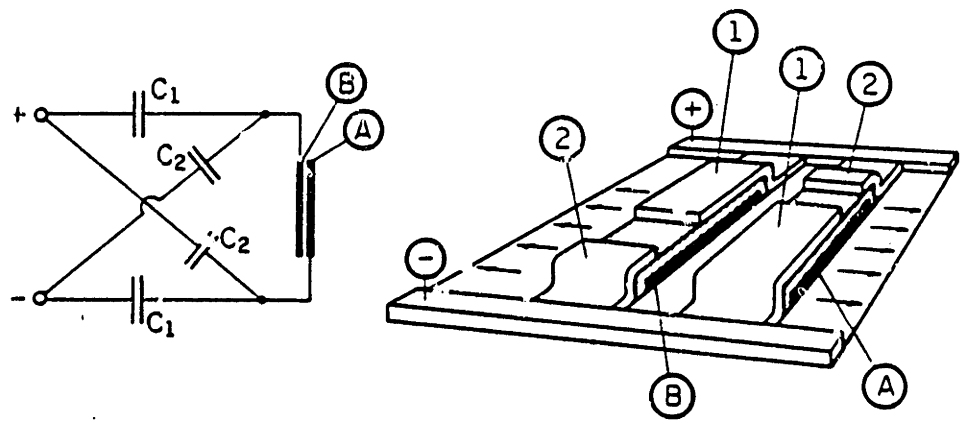

Figure 1.3 A Capacitively Weighted Electrode Pair
A,B: Metalization deposited directly on the substrate covered by a dielectric layer. The voltage difference between these electrodes is what drives the acoustic waves. 1,2: Electrodes connected to the bus bars which are capacitively coupled to the lower level of metalized electrodes A,B. (After [65])

of the technique. Thus, there is difficulty in controlling the small tap weights necessary for low sidelobe sharp cutoff filters due to fringing electrostatic fields. Another major problem is the increase of the input capacitance of these filters with a lot of low tap weights relative to the input conductance. This reduces the bandwidth over which a match can be achieved with a simple one element matching network [41] . Nevertheless, this device merits further study, especially the implementation due to Malocha and Hunsinger [65] which does not require any more substrate area than a standard IDT, but which does require a three-level fabrication process.

There are also problems with building structures with a continuously variable reflection coefficient as would be desirable for a SPUDT. The obvious technique would be to depth weight grooves [100] as has been done for reflective array compressors (RAC's), or to continuously control the thickness of a deposited overlay. The main problem with this is that the fabrication process is not amenable to mass production *. Each device on a wafer would have to be moved under an ion beam in the case of grooves or maybe a laser beam in the case of dielectric overlays at varying velocities to control the amount of material which is removed. Thus all devices on a wafer could not be fabricated simultaneously.

It is also possible to continuously adjust the width of reflectors to control the reflection weights. This would unfortunately cause the velocity of the wave to depend on the reflection function, necessitating detailed compensations to be done. Also, as with width weighted transduction, the dynamic range available is rather low. Furthermore, second order effects, $O((h/\lambda)^2)$, which depend on the shape [112,114] of the reflecting perturbation,

*Recall that one of the goals of this research is to develop a filtering block which can replace L-C lumped element filters in most applications. Thus the SPUDT must be easy to fabricate.

would necessitate the maintenance of very tight process controls in fabricating these devices if the compensations are to work well *.

Based on the above discussion, it is evident that there is a need for a weighting technique which leads to a uniform transverse beam profile, but which does not suffer from the dynamic range restrictions or fabrication complexities of the previous methods. A technique of this kind is one which uses elemental transducers or reflectors of uniform strength, and which obtains weighting only by varying the spacing between these elements.

One possible procedure for doing this is based on the stationary phase approximation for Fourier integrals and was studied by Fowle [30] . In this approximation, an acoustic wave is radiated only at frequencies which are synchronous with some part of the transduction array. Thus a sharp *brick wall* bandpass filter would be constructed by linearly chirping the array's instantaneous frequency across the passband. This approximation is best in the limit of large time-bandwidth product waveforms, which corresponds to a slow chirp rate. Unfortunately, high performance filters designed via this procedure are very long, orders of magnitude longer than those which are apodized via the Parks-McClellan [85,80] algorithm (See Table 6.8 of Sec. 6.6.4). Since one of our goals is to conserve substrate area in order to minimize cost, these designs are not suitable.

Another approach to this problem is to approximate an amplitude weighted design by varying the density of constant amplitude samples. This idea was first applied to the synthesis of radio telescope gain patterns [103] . Hartmann [42] independently developed a similar procedure for SAW devices which he calls withdrawal weighting. The fundamental difference is related to the fact that the antennas were broadside arrays, meaning that all the

*Knowing the velocity very precisely is critical to the successful construction of low sidelobe filters. Slobodnik [99] presents an example in which velocity perturbations as low as .5% , for which no compensation was performed, increased the sidelobe level from -35 dB to -20 dB, in addition to distorting the passband shape.

elements will add coherently to the gain peak if they have the same sign. Stronger sources can simply be produced by placing them close to one another*. A SAW device more closely approximates an endfire array in which sources separated by half a wavelength must be flipped in sign in order to add coherently. The added complication is that if the elements are more closely spaced, to obtain a stronger equivalent source, it will be synchronous at a higher frequency. In withdrawal weighting, a prototype sequence of amplitude modulated samples is approximated by a sequence of constant amplitude samples and some zero weight ones. The technique is based on the fact that in a narrow band sense, source weights can be moved by half a wavelength and flipped in sign, without affecting the frequency response very much.

Yamaguchi et. al. [116,117,118] investigated withdrawal weighting using integer optimization and dynamic programming. In all three of their approaches, they required the spatial distribution of the elements to be symmetric so that the array factor would be real. They also required that all possible points for the sources lie on a grid with half-wavelength spacing. Their starting point was a uniform array. This fixed the bandwidth and also the shape factor. They then symmetrically withdrew pairs of sources from this uniform section, and added them outside this region in such a way so as to minimize the sidelobes. Therefore they are not able to design sharp cut-off filters, or filters with arbitrary passband shape. Furthermore, the computation time for their optimal and suboptimal techniques, which are both based on integer programming, grows exponentially with the number of source samples, N. Thus they are limited to rather simple low-performance filters. Their simplest algorithm, which is based on dynamic programming, is much more efficient, the computation time required is only $O(N^3)$.

*This really can not be done since the element size restricts how closely they can be spaced

In the antenna field, the work of Hodjat and Hovanessian [49] and Redlich [87] is representative of what has been done. In both cases, optimized broadside arrays were designed by continuously varying the spacing between the elements and dynamically linearizing the equations about their most recent solution. Thus, quite good initial guesses are required to insure that the perturbation in source location on any one iteration is small. Their technique is best applied when the $sin(x)/x$ shape of a uniform array is just about correct, and all that is desired is to reduce the large inner sidelobes while maintaining roughly the same main lobe shape. In order to obtain linear equations, they were restricted to using conjugate symmetric source distributions, making the array factor real, and thereby avoiding having to take the magnitude of a complex function (see Sec. 6.1*). Since the parameters were the locations of the sources, and since linear equations had to be solved on each iteration of the algorithm, computation time is also $O(N^3)$, and only small arrays can be handled.

1.3 Overview of Part II

Recently, a technique involving quasi-Newton optimization, an improved withdrawal weighting algorithm with multiple envelopes, and a broader bandwidth structure when withdrawal weighted, was reported by Garber and Haus [31]. This algorithm is described in detail in Chapter 6. It allows the design of high performance filters with hundreds of sources. This is done by breaking the relationship between the number of parameters, M, and the number of sources, N, and reducing computation time to only $O(M^2)$. Furthermore, the source distribution is no longer restricted to be conjugate symmetric, and

*If the S_i of Eq. (6.5) are conjugate symmetric, the magnitude square is not necessary since the array factor is real except for a linear phase term.

frequency responses of arbitrary shape can be synthesized. Most of the design is based on a simple impulse model [41] , but extensions to handle second order effects are discussed. This extension is demonstrated by compensating for the element factor.

PART I

UNIDIRECTIONAL TRANSDUCERS

AND

MODELING

CHAPTER 2

SURVEY OF UNIDIRECTIONAL TRANSDUCERS

2.1 The Previous State of Art

There are two basic techniques which can be used to convert a bidirectional IDT into a unidirectional one:

1) The transduction elements can be spaced and phased relative to one another such that the waves emitted constructively interfere in the forward direction and destructively interfere in the reverse direction.

2) A reflector can be placed behind the transduction element so that the reflected wave adds coherently to the wave coming out the front port.

Engan [23] and Collins et. al. [13] both proposed designs based on the first method. In such a design an offset of $\lambda_o/4$ is placed between two N wavelength transducers, so that there is $(N+1/4)\lambda_o$ between the centers of the transducers. The transducers are driven $90°$ out of phase with respect to one another to obtain unidirectionality (Fig. 2.1).

Thus if $E(\beta)$ is the frequency response of each half of the structure of Fig. 2.1, the response in the forward and backward directions respectively, H_f and H_r, referenced to the midpoint of the transducer are:

$$H_f(\beta) = 2e^{-j[\beta x+\frac{\pi}{4}]}\cos\pi\left(\frac{\beta}{\beta_o}\left(N+\frac{1}{4}\right)-\frac{1}{4}\right)E(\beta) \qquad (2.1a)$$

$$H_r(\beta) = 2e^{j[\beta x-\frac{\pi}{4}]}\cos\pi\left(\frac{\beta}{\beta_o}\left(N+\frac{1}{4}\right)+\frac{1}{4}\right)E(\beta) \qquad (2.1b)$$

$$\text{Directionality Factor} = \cos\pi\left(\frac{\beta}{\beta_o}\left(N+\frac{1}{4}\right)-\frac{1}{4}\right) \qquad (2.1c)$$

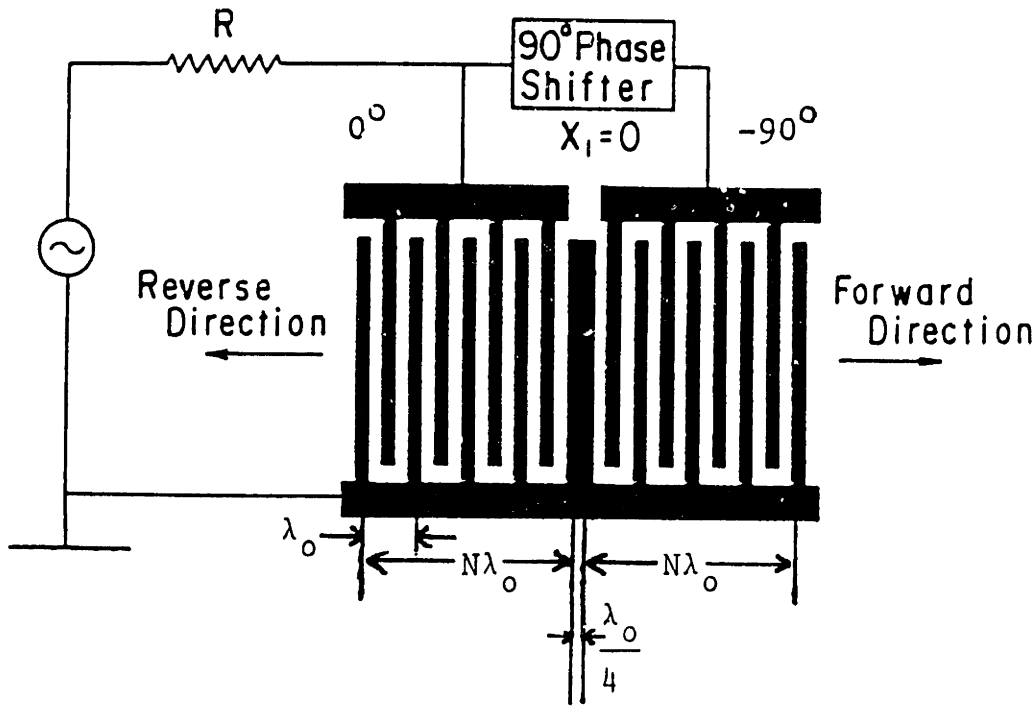

Figure 2.1 Engan's Proposed Design for a Unidirectional Transducer
The 90° phase shifter causes constructive interference to occur in the forward direction while destructive interference occurs in the backward direction. (Modified from [119])

where

$$\beta_o \triangleq \frac{2\pi}{\lambda_o}$$

We note that the 3 dB fractional bandwidth of the directionality factor is $1/(2N+1/2)$. The large spacing between the quadrature driven transducers restricts the bandwidth over which the unidirectionality and triple transit suppression are effective. Recognizing that the 3 dB fractional bandwidth of an unweighted IDT N wavelengths long is $1/N$, we note that the unidirectionality and triple transit suppression don't even cover the 3 dB points of the main lobe. Performance is even worse than it first seems, since triple transit suppression is necessary throughout both the full passband and the transition region of the frequency response. Furthermore, in a weighted IDT with sharp cutoff in the transition region, the total filter length is significantly greater than $1/\Delta f_{3dB}$, thus exacerbating an

already difficult problem. It is clear that the centers of transduction of the quadrature phased elements must be brought significantly closer to one another than the length of a full transducer.

Smith [101] proposed a unidirectional transducer based on placing a reflector an appropriate distance behind a transducer. Smith's reflector was another IDT tuned for maximum reflection. For a transducer of frequency response, $E(\beta)$, with a perfect reflector of reflection coefficient -1 placed $(N + 1/4)$ wavelengths behind it, the wave emitted from the front port is:

$$H_f(\beta) = 2je^{-j\beta(x+(N+\frac{1}{4})\lambda_o)} \sin\left(2\pi\frac{\beta}{\beta_o}\left(N+\frac{1}{4}\right)\right)E(\beta) \tag{2.2}$$

where

$$\beta_o = 2\pi/\lambda_o$$

The 3 dB bandwidth of the directionality factor, $1/(4N + 1)$, is about half what was obtained in the previous case. This is due to the longer path length of the backward traveling wave which is reflected. Thus, it is even more important in this case to ensure that the reflector is located very close to the transducer. Presently there is no known way of producing a strong lumped reflector, thus periodic reflective gratings are used in which the reflection per wavelength is very small. If κ is the reflection coefficient per unit length of such a grating, then $1/\kappa$ is roughly the center of reflection for a strongly reflecting grating. Thus, the center of reflection is of necessity many wavelengths behind the transducer, and the bandwidth over which such a transducer will be unidirectional and therefore suppress triple transit is limited.

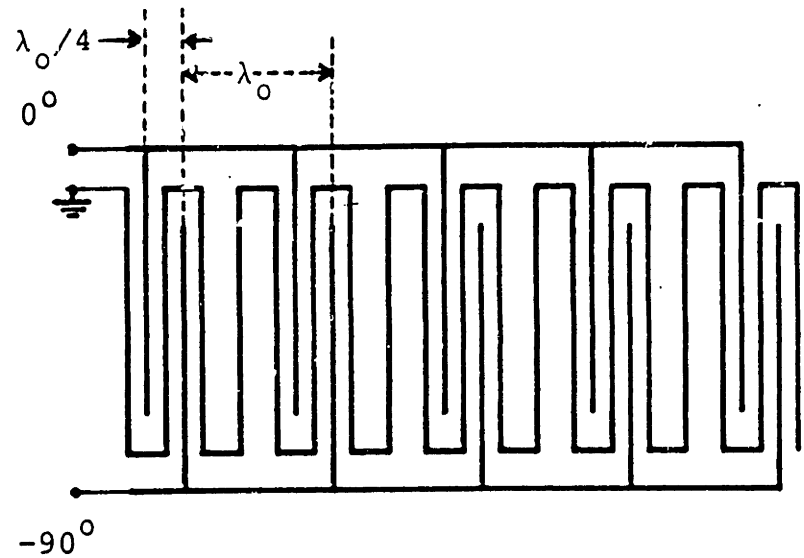

Figure 2.2 The Meandering Ground Unidirectional Transducer
(After [108])

Waldron [108] improved on Engan's [23] and Collins' [13] designs by interlacing the two quadrature phase shifted IDT's so that the distance between the two transducers is only $\lambda_o/4$ (see Fig. 2.2). This tremendously increases the bandwidth over which the unidirectionality and triple transit suppression are effective. The main problem with Waldron's structure is the high resistance of the long meandering ground line which threads through the quadrature phase shifted taps. This is a source of added insertion loss.

Yamanouchi's [119] group-type unidirectional transducer (see Fig. 2.3) solves this problem by increasing the number of fingers between each crisscross of the meandering ground, thereby reducing its length and thus its series resistance. This has the effect of reducing the bandwidth over which the unidirectionality is effective, since the distance between the centers of the quadrature phase shifted elemental transducers (called groups) has increased. A continuous tradeoff is available between insertion loss and the unidirectionality

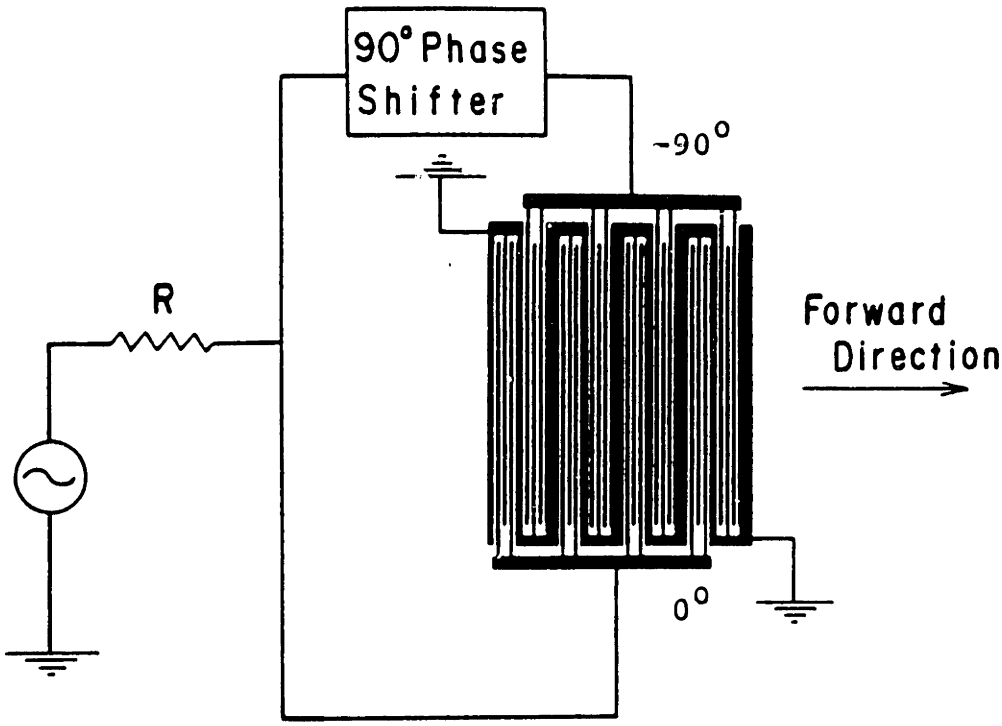

Figure 2.3 The Group-Type Unidirectional Transducer
Note that the interdigitated fingers are $\lambda_o/4$ wide, while the narrow vertical grounded lines are $\lambda_o/2$, and the widest ones are λ_o. (After [119])

bandwidth by controlling the number of fingers in each group. Another advantage of this design is that the minimum line width required is only $\lambda_o/4$, making it suitable for high frequency designs. A disadvantage of this type of transducer is the need to synthesize, build and adjust a broadband 90° phase shift network. Ideally, a SAW filter should be able to be plugged into a system just like an integrated circuit.

Hartmann [38] proposed a unidirectional structure with three sources per wavelength phased as in a traveling wave at 0°, 120° and 240° (Fig. 2.4). This structure has the wide bandwidth of Waldron's [108] design but eliminates the insertion loss caused by the meandering ground of Waldron's and Yamanouchi's [119] designs. In order that this device work well, the three phases must not be capacitively coupled; thus air insulated crossovers are required for one of the phases. These have proven to be very difficult to

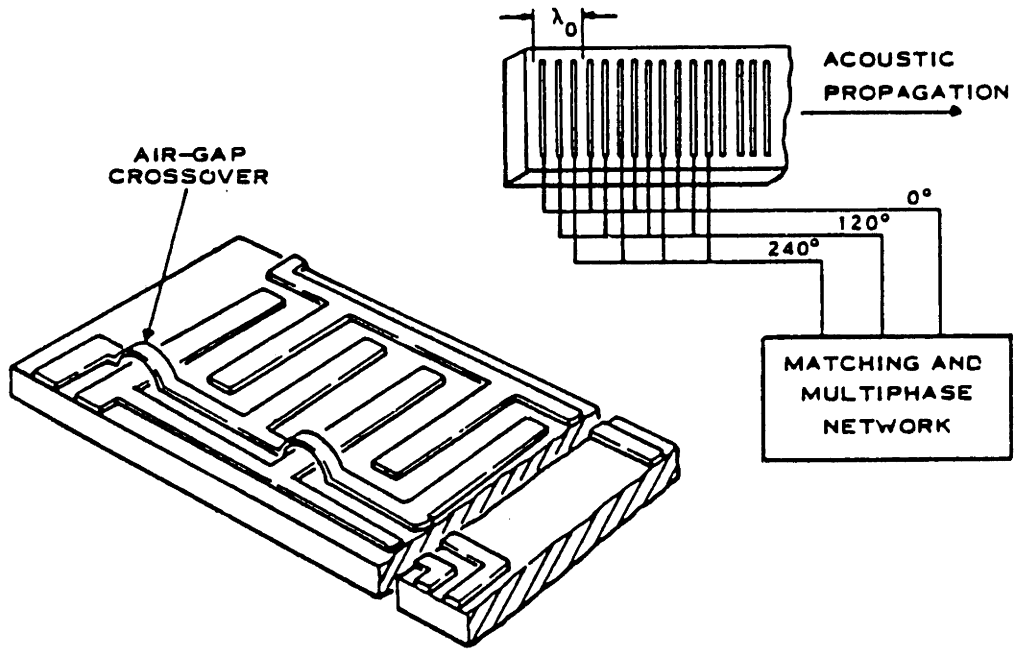

Figure 2.4 The Three Phase Unidirectional Transducer
(After [90])

fabricate economically. In addition, a complicated broadband phase shift network must be constructed and adjusted for proper operation of the transducer.

Additional representative work on this topic is a thin film ZnO (Fig. 2.5) implementation of Waldron's [108] design in which the lossy meandering ground is replaced by a solid ground plane either above or below the zinc oxide layer [92,96]. These thin film designs suffer from the necessity of building and adjusting broadband 90° phase shift networks as does the group-type design.

Marshall et. al. [68] invented a unidirectional transducer which is based on multistrip couplers (MSC) of half the length required for full transfer, $L_T/2$. If one track of a MSC of length $L_T/2$ is excited, signals of equal amplitude are present at the output, but are 90° out of phase. Using time reversal, it is clear that a MSC can also combine two signals in phase quadrature to produce an output in only one track. A unidirectional transducer

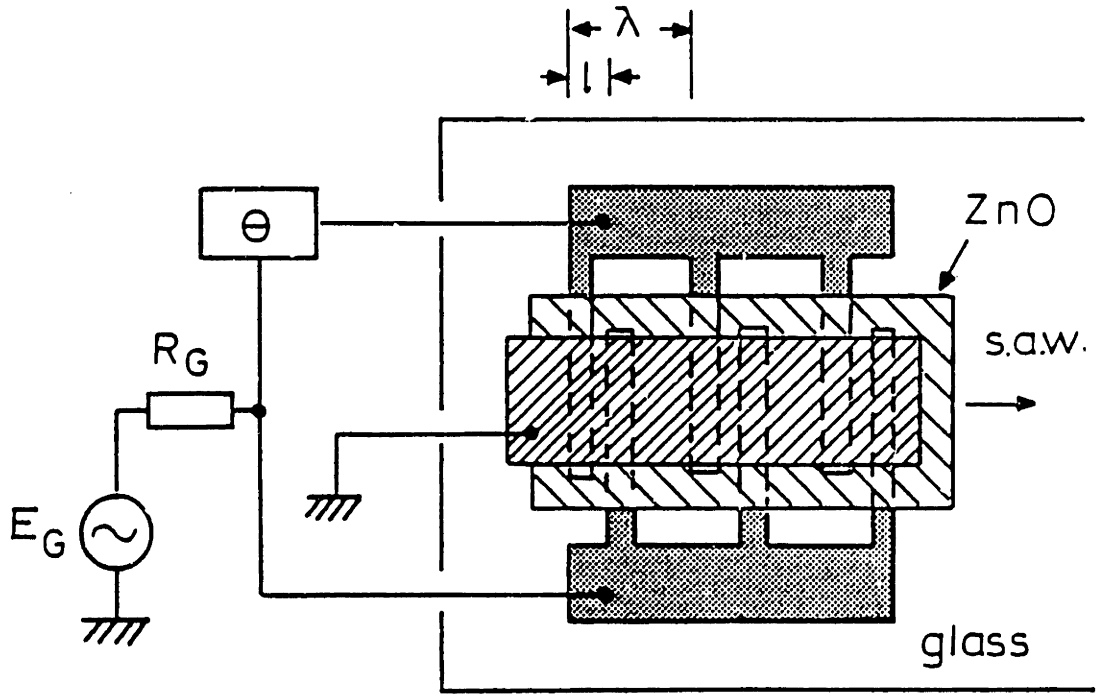

Figure 2.5 Thin-Film ZnO Unidirectional Transducer
Note $l = \lambda_o/4$ and $\theta = 90°$ for unidirectionality. (After [96])

is constructed by curving a MSC around a bidirectional transducer and displacing the transducer by $\lambda_o/8$ from the center of the curved MSC (Fig. 2.6).

This enables a single transducer to excite both tracks of a MSC with equal amplitude signals in phase quadrature. This UDT is the only one which can not be easily categorized as a type I or type II design. It contains elements of both. The main problem with this approach is the large substrate area (area costs money) required by the MSC, even on strongly piezoelectric materials such as lithium niobate. On weak piezoelectrics, such as quartz, this design would be totally impractical. The key advantage of Marshal's design is its wide unidirectional bandwidth.

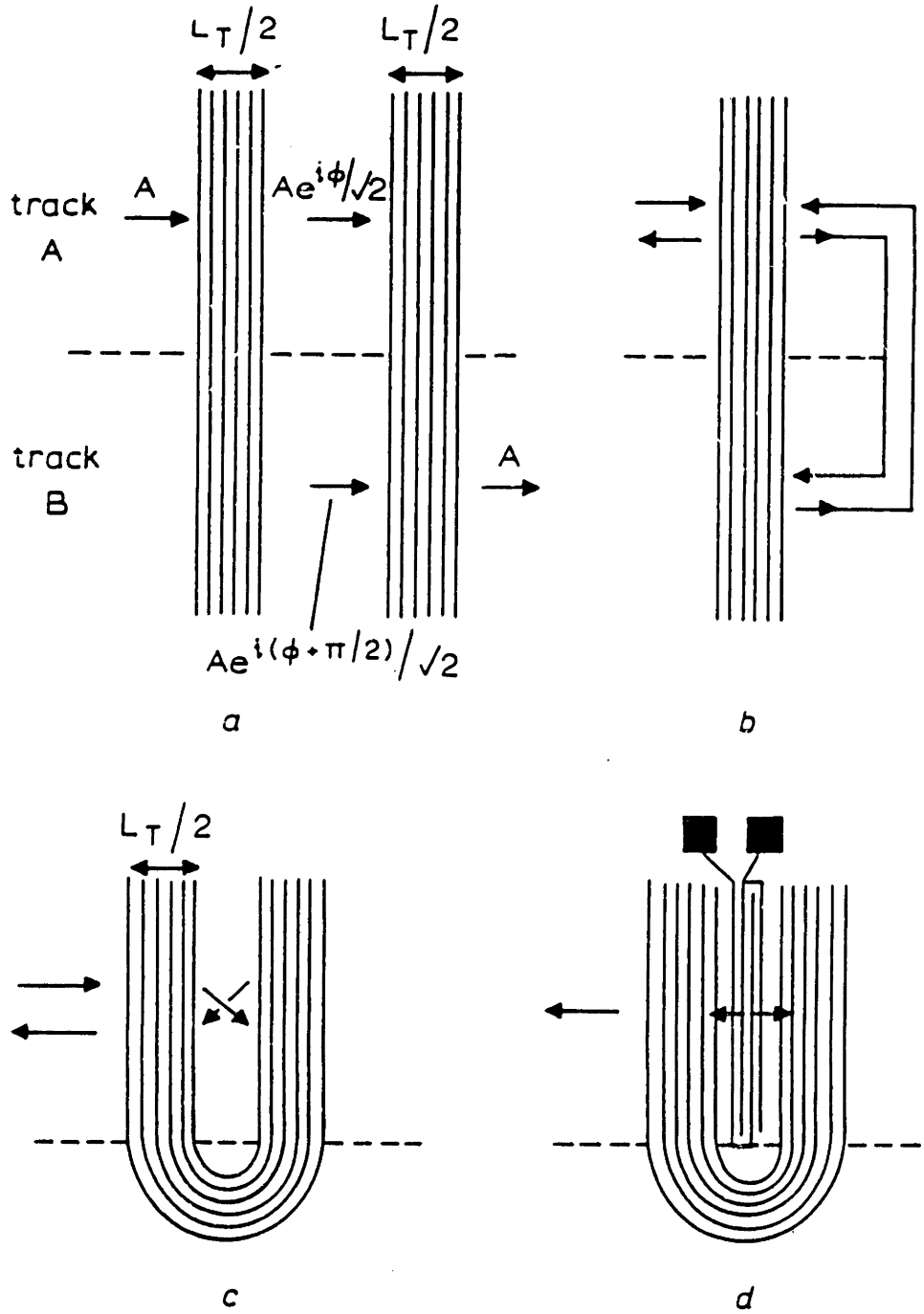

Figure 2.6 Multistrip Coupler based UDT

A diagrammatic representation of the evolution of a mirror and a unidirectional transducer from a multistrip coupler (MSC) of half the length required for full transfer. a) A MSC b) Tracks A and B are switched around to form a mirror if excited from the left, or a unidirectional transducer if excited from the right in phase quadrature. c) Physical implementation of the track switching to form a mirror. d) Physical implementation of the quadrature drive to form a unidirectional transducer. Note that the transducer is displaced by $\lambda_o/8$ toward the left to achieve the quadrature drive. (After [68])

2.2 The Single-Phase Unidirectional Transducer (SPUDT)

Hanma and Hunsinger [37] and Hartmann [44] proposed type II designs in which the reflector is constructed in the same region of space as the transducer. This will have the effect of increasing the bandwidth over which the unidirectionality and triple transit suppression are effective. In the Hartmann implementation (Fig. 2.7), extra metal or dielectric is deposited on every other finger of a split finger IDT, while in the Hanma approach every other finger is made wider (Fig. 2.8).

The unidirectionality is a distributed effect which can be understood only by looking at a large section of the device at once; any small segment is unidirectional only to a small degree. In order to understand this effect it is easiest to apply superposition to the transduction function and therefore to focus on only one source in an array of reflectors.

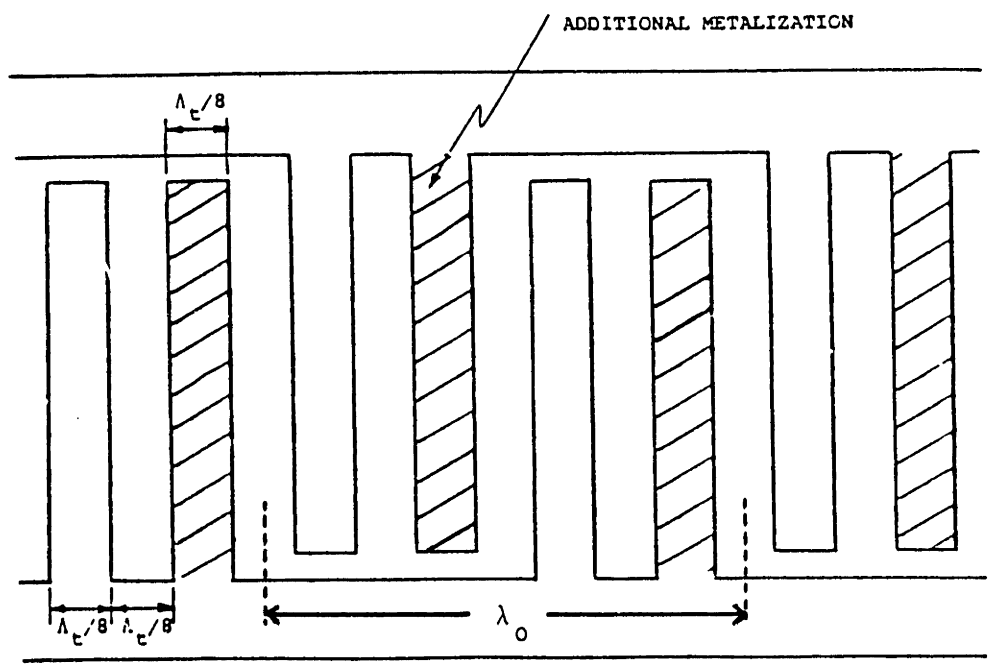

Figure 2.7 Hartmann Implementation of the SPUDT
$\Lambda_t = \lambda_o$ is the wavelength at center frequency. Note that every other finger is thicker for additional reflection. (After [44])

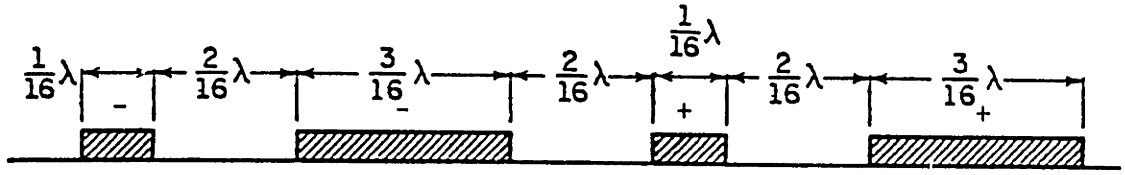

Figure 2.8 Hanma's Unidirectional Transducer
Note that every other finger is wider for additional reflection. (Side view) (After [37])

In the Hartmann implementation, called the SPUDT, the grating consists of ordinary fingers of thickness h and fingers with additional metalization deposited of total thickness H. Fingers can be decomposed into the superposition of a grating of periodicity $\lambda_o/4$ of fingers of thickness h, which also short the electric field, and a grating of periodicity $\lambda_o/2$ of fingers of thickness $H-h$. To first order in the height of the perturbation, the mechanical reflection coefficient at a multiple of the Bragg frequency is proportional to the corresponding Fourier expansion coefficient of the grating [114]. The component of periodicity $\lambda_o/4$ caused both by mechanical effects and piezoelectric shorting is so grossly detuned that it can be ignored near the center frequency.

The reflection coefficient from an arbitrary symmetrical lossless perturbation is shown to be pure imaginary in Sec. 3.4. The sign of the reflection from a strip depends on the relative mechanical properties of the overlay and the substrate [15,11]. For gold strips on ST-X quartz it was found experimentally (see chapter 5) to be +jt where t is positive, if referenced to the electric potential. The electric potential is anti-symmetric at a gap center between fingers attached to bus bars of opposite polarity. This implies that the forward traveling wave referenced to its potential will be opposite in sign to the backward traveling wave. Using this information, we can find the forward and backward propagating waves of the structure of Fig. 2.7 arising from only one source. Taking into account only first

order reflections and ignoring the non-unity transmission of the reflectors, we obtain:

$$\text{forward traveling wave} \quad \alpha \quad e^{-j\beta x}\Big[1 - jt\Big(e^{-2j\beta\frac{3}{8}\lambda_o} + e^{-2j\beta\left[\frac{\lambda_o}{2}+\frac{3}{8}\lambda_o\right]} + \cdots + e^{-2j\beta\left[n\frac{\lambda_o}{2}+\frac{3}{8}\lambda_o\right]} + \cdots\Big)\Big] \tag{2.3a}$$

$$\text{backward traveling wave} \quad \alpha \quad e^{j\beta x}\Big[-1 + jt\Big(e^{-2j\beta\frac{\lambda_o}{8}} + e^{-2j\beta\left[\frac{\lambda_o}{2}+\frac{\lambda_o}{8}\right]} + \cdots + e^{-2j\beta\left[n\frac{\lambda_o}{2}+\frac{\lambda_o}{8}\right]} + \cdots\Big)\Big] \tag{2.3b}$$

If N reflectors are assumed to be involved, then at synchronism Eqs. (2.3a, 2.3b) reduce to

$$\text{forward traveling wave} \quad \alpha \quad e^{-j\beta x}[+1 + Nt] \tag{2.4a}$$

$$\text{backward traveling wave} \quad \alpha \quad e^{+j\beta x}[-1 + Nt] \tag{2.4b}$$

This makes sense, of course, only if $Nt << 1$.

Thus at synchronism, all the reflections in the forward direction add coherently to the directly excited forward going wave, while the backward scattered waves destructively interfere with the direct backward going wave. In the above equations, it has been assumed that making every other electrode thicker, does not modify the electrical boundary conditions affecting transduction. The extra metal is assumed to only affect reflection. This should be an excellent assumption, since even the thick metal fingers are very thin compared to the electrode spacing.

The unidirectionality in the Hanma-Hunsinger [37] technique (Fig. 2.8) works in much the same way. The key difference is that the electrical boundary condition is affected by altering the width of the split fingers. If we ignore this effect, and assume that the center

of transduction still lies at the center of the gap between fingers of opposite polarity, then for one excited gap

$$\text{forward traveling wave} \quad \alpha \quad e^{-j\beta x}\left[\begin{array}{ll} 1 & -jt\left[\begin{array}{l} e^{-j2\beta\frac{2.5}{16}\lambda_o}+e^{-j2\beta(\frac{2.5}{16}\lambda_o+\frac{\lambda_o}{2})} \\ +\cdots+e^{-j2\beta(\frac{2.5}{16}\lambda_o+n\frac{\lambda_o}{2})}+\cdots \end{array}\right] \\ & -jat\left[\begin{array}{l} e^{-j2\beta\frac{8.5}{16}\lambda_o}+e^{-j2\beta(\frac{8.5}{16}\lambda_o+\frac{\lambda_o}{2})} \\ +\cdots+e^{-j2\beta(\frac{8.5}{16}\lambda_o+n\frac{\lambda_o}{2})}+\cdots \end{array}\right] \end{array}\right] \tag{2.5a}$$

$$\text{backward traveling wave} \quad \alpha \quad e^{j\beta x}\left[\begin{array}{ll} -1 & +jat\left[\begin{array}{l} e^{-j2\beta\frac{1.5}{16}\lambda_o}+e^{-j2\beta(\frac{1.5}{16}\lambda_o+\frac{\lambda_o}{2})} \\ +\cdots+e^{-j2\beta(\frac{1.5}{16}\lambda_o+n\frac{\lambda_o}{2})}+\cdots \end{array}\right] \\ & +jt\left[\begin{array}{l} e^{-j2\beta\frac{5.5}{16}\lambda_o}+e^{-j2\beta(\frac{5.5}{16}\lambda_o+\frac{\lambda_o}{2})} \\ +\cdots+e^{-j2\beta(\frac{5.5}{16}\lambda_o+n\frac{\lambda_o}{2})}+\cdots \end{array}\right] \end{array}\right] \tag{2.5b}$$

where jt is the reflection coefficient of a wide finger, and jat is the reflection coefficient of a narrow one. At synchronism, accounting for N wide and N narrow reflectors,

$$\text{forward traveling wave} \quad \alpha \quad e^{-j\beta x}[1-Nt(1-a)e^{-j\pi/8}] \tag{2.6a}$$

$$\text{backward traveling wave} \quad \alpha \quad e^{j\beta x}[-1-Nt(1-a)e^{j\pi/8}] \tag{2.6b}$$

Thus we see that the finger placement is not quite correct for best unidirectionality, the phase is off by $\pi/8$ from full constructive interference. Nevertheless, there is substantial constructive interference in the forward direction and destructive interference in the reverse. In order to obtain the correct finger positions and widths, the full electrostatic problem should be solved (See Sec. 3.9.1).

If the asymmetry of the electrical drive is properly accounted for, the Hanma-Hunsinger technique should work extremely well. It has the advantage over the Hartmann [44] technique of requiring only one level of metalization. However, the design of a weighted filter to meet a tight frequency specification using their structure would be much more difficult, since the transduction and reflection functions are not independently controllable.

2.3 Summary

In summarizing the present status of low-loss unidirectional SAW filters, it should be remembered that the techniques are based on two* different ways of modifying the bidirectional interdigital transducer. Method I involves spacing either transduction elements or whole transducers by an appropriate distance, and phasing them in such a way that the waves constructively interfere in the forward direction, and cancel in the backward one. In Method II, reflectors are placed behind these elemental sources, at such a distance so that constructive interference occurs in the forward direction. In both cases, in order that broadband unidirectionality and triple-transit suppression be exhibited, the spacial separation between the phased sources, or the sources and reflectors must be small. The techniques based on Method I suffer from the need to build and adjust a broadband phase shift network which is incompatible with the goal of building a simple RF filtering block which can simply be plugged into systems like integrated circuits.

The best candidates for such a low-loss RF filter, are the single-phase unidirectional transducer (SPUDT) invented by Hartmann [44] and the Hanma-Hunsinger [37] device. Neither requires a sophisticated fabrication technique, as does the 3-phase UDT [38], and neither requires any external elements other than a parallel inductor to resonate the

*Except for the multistrip coupler design [68] which is somewhat different.

capacitance, which is also required of standard bi-directional IDT's to reduce the mismatch loss. The SPUDT is easier to design since the transduction and reflection functions are performed by different parts of the structure. Therefore, the SPUDT will be the focus for our design and analysis techniques in this research.

CHAPTER 3

MODELING TRANSDUCERS WITH INTERNAL REFLECTION

3.1 Introduction

Before a single-phase unidirectional transducer (SPUDT) can be designed, it must be modeled. The accuracy to which it must be modeled is determined by error tolerances acceptable to people who use SAW devices. Typical specifications for standard high loss SAW devices would include peak-to-peak .6 dB passband ripple and peak-to-peak 3° phase deviation from linear, with -40 dB sidelobes [1] . This shows that the analysis of SAW devices must be quite good, especially since we are trying to improve upon the passband amplitude and phase ripple by eliminating the triple transit signal. Unfortunately, accurate models are ordinarily complicated, and therefore make design difficult. It is reasonable to use simple models in first cut designs, and then to use a more complicated analysis algorithm to check to see whether the response meets the specifications sufficiently well. If it doesn't, the more accurate analysis can be used to adjust parameters of the simplified analysis procedure, or the more exact analysis technique can be used in a more sophisticated design algorithm.

3.2 Impulse Model—Transduction

The simplest models [105,41], associate the source of the surface acoustic waves with the gaps between electrodes of opposite polarity and ignore internal reflection, diffraction, bulk wave excitation and loss. Ignoring diffraction is reasonable if the square of the acoustic aperture is large enough compared to the product of the wavelength and the propagation path length, to be in the Fresnel zone. The aperture size needed also depends on the degree of self focusing or defocusing of the anisotropic substrate [56,82,104]. Bulk wave excitation mainly degrades the sidelobe rejection level, and is not important to the basic operation of a SAW filter. Typically metal fingers would be made thick enough and path lengths short enough so that loss would not have a significant effect on the filter's characteristics. Reflection is the main effect being ignored in the impulse model. There are two sources of reflection. The first arises from the acoustic impedance discontinuities introduced by the metal fingers. It can be eliminated by using split finger transducers (Fig. 1.1); since at the fundamental frequency of the transducer response, the period of the grating produced by these split fingers is only half that required for constructive interference (the Bragg condition). Alternatively, the metal thickness and metalization ratio can be selected to cancel the reflection of mechanical origin with the one of piezoelectric origin [51,11]. The second source of reflection is acoustic regeneration. The acoustic wave is *received* by the gaps under which it propagates and induces a voltage across the bus bars. This voltage re-excites acoustic waves in both the forward and backward directions. This effect is minimized by matching the transducer with a conductance much higher than the input conductance, which tends to short out the induced voltage.

Under these conditions, it is reasonable to assign bi-directional acoustic plane wave sources to the gaps between fingers attached to opposite bus bars, and to assume that the

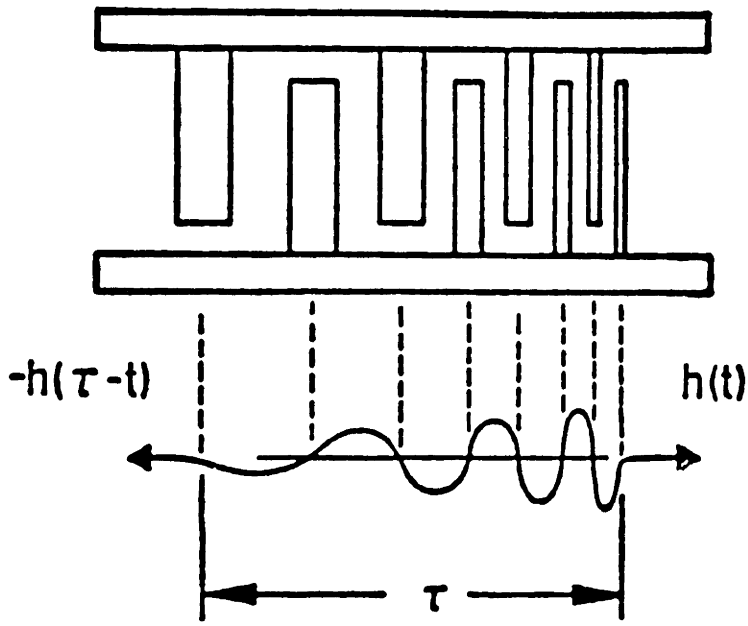

Figure 3.1 Relationship Between the Physical Structure and the Impulse Response
Note that the amplitude grows toward the high frequency end of the impulse response for a constant overlap, nonuniformly spaced transducer. (After [41])

waves propagate to the ends of the transducer, unaffected by the fingers under which they propagate. These source functions can be regarded to be impulses located at the electrode edges, impulses located at the gap centers, or half cycles of sine waves (Fig. 3.1). The size of the impulses is proportional to the electromechanical coupling constant, the square root of the aperture (since power is proportional to the aperture), and $f_o^{1/2}$, where f_o is the local synchronous frequency of the transducer (see Sec. 3.9.1 and Eq. 3.69). In the case of the sine-wave source function, the amplitude must be weighted by $f_o^{3/2}$, the extra factor of f_o being necessary to keep the area under a half cycle of a sine-wave equal to the area under an impulse. As long as the area under each representation of the source function is the same, the calculated response for a narrow band filter around its fundamental harmonic will be quite similar. Differences between the models are obvious only in very broad band devices, or at higher harmonics*

*If the correct field distribution is used instead of one of these simplifying approximations, broad band modeling of the devices is possible. This is discussed in Sec. 3.9.1

If both transducers are uniform in the direction transverse to that of wave propagation, the impulse response of each transducer is simply this source function, with the impulse response of the entire filter being the convolution of the impulse responses of the transmitting and receiving transducers. The frequency response is simply the Fourier transform of this combined impulse response, or equivalently the product of the Fourier transforms of the individual transducers' impulse responses. If the locations of the gaps and their amplitudes for the transmitting transducer are a_n and x_n, with the similarly defined quantities for the receiving transducer being c_n and y_n, this transfer function is proportional* to:

$$\begin{aligned} H(f) &= \sum_{n=1}^{N}\sum_{m=1}^{M} a_n c_m e^{j\beta(x_n - y_m)} \\ &= H_1(f)H_2(f) \\ &= \left[\sum_{n=1}^{N} a_n e^{j\beta x_n}\right]\left[\sum_{m=1}^{M} c_m e^{-j\beta y_m}\right] \end{aligned} \tag{3.1}$$

where

$$\beta = 2\pi\frac{f}{v}$$

The response from the reverse ports of these transducers is simply the Fourier transform of the time-reversed version of these individual transducers' impulse responses.

In order to calculate the response of a transducer with non-zero source and load impedances, the input admittance, Y, of the IDT must be computed. Hartmann [41] applied power conservation to each transducer individually obtaining

$$Re[Y] = G = |S_{21v}|^2 + |S_{31v}|^2 \tag{3.2}$$

*See Sec. (3.9.1) and Eqs. (3.76–3.85) for a complete discussion and the proportionality constant.

where S_{21v} and S_{31v} are the voltage to acoustic wave amplitude transfer functions in the forward and backward directions respectively. The imaginary part of Y consists of two parts, the static capacitance, $j\omega C$, and the radiation susceptance, jB. The capacitance is found by solving Laplace's equation for electrodes on a dielectric substrate, and jB is determined from causality considerations via the Hilbert transform [36,41] :

$$Y = G + j\omega C + jB \tag{3.3a}$$

$$B = \frac{1}{\pi}\int_{-\infty}^{\infty} \frac{G(\omega')}{\omega' - \omega}\, d\omega' \tag{3.3b}$$

3.3 Weighting and SPUDT's

Until now, it has been assumed that the transducers are uniform in the transverse direction. A very popular form of weighting used to control the frequency response involves adjusting the overlap of adjacent electrodes (Fig. 3.2). In order to analyze transducers of this type, they must be broken up into horizontal strips which are narrow enough so that the overlaps are uniform in each strip. If diffraction and the electrical coupling between the strips caused by the metal fingers connecting them can be ignored, the power radiated within a strip will not leave it. Since the strips are connected electrically in parallel, the input admittances can be computed by summing the radiated power from each strip. Similarly, the transfer function for the full device can be found by summing the transfer functions of the individual strips. $B(\omega)$ and the capacitance are calculated as before. An alternative expression can be based on the fractional overlap between the n^{th} and m^{th} gaps of the input and output transducers respectively, d_{nm}. The signal picked

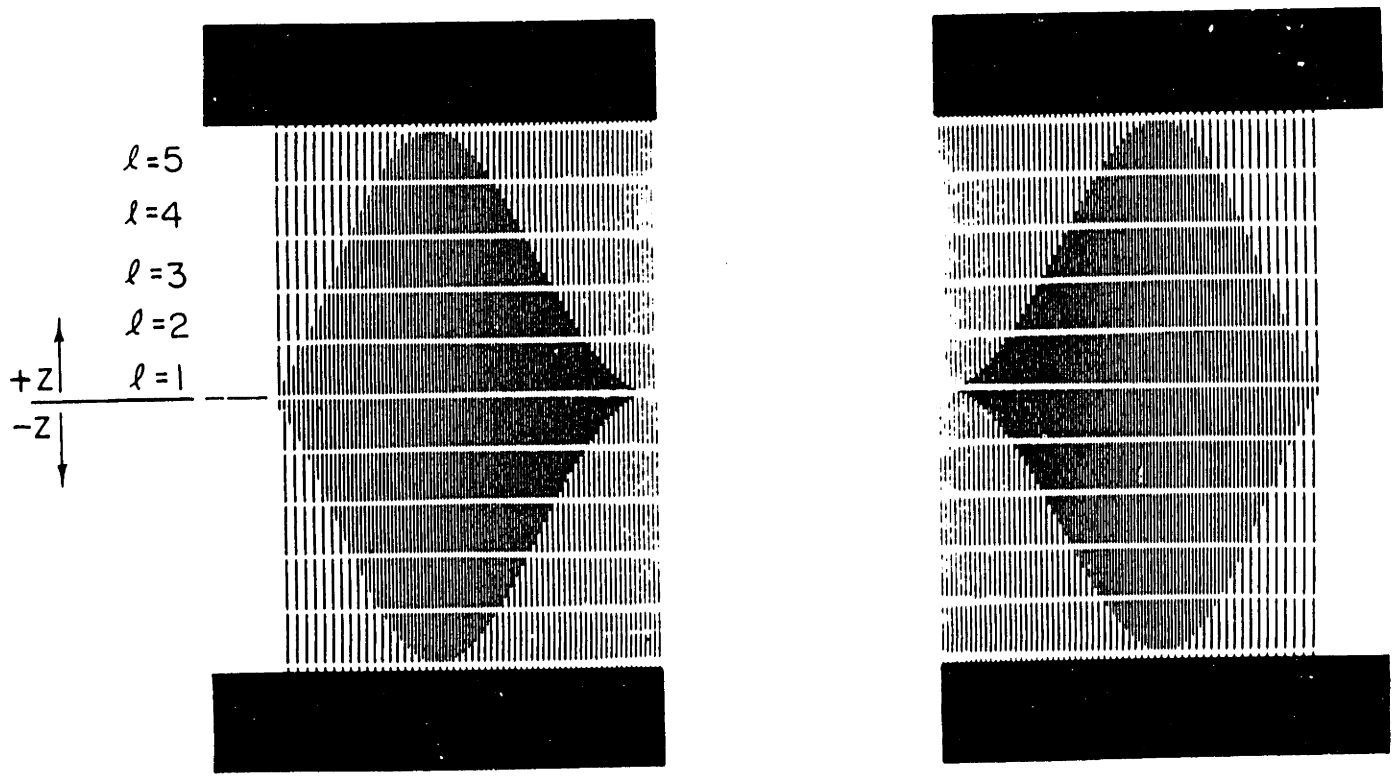

Figure 3.2 Two Apodized Transducers
The transducers shown are divided into horizontal strips in which the overlap is approximately constant. The transfer function is computed by summing the transfer functions for all the strips. Similarly the admittance is calculated by summing the admittance from each strip. (After [105])

up by the receiving gap due to a transmitting gap will be proportional to the product of this overlap and the strengths of the individual gaps:

$$\text{received-signal-strength} \quad \alpha \quad d_{nm} a_n c_m \tag{3.4}$$

since the acoustic field can only be integrated over the spatial overlap of the two gaps. Thus the transfer function is proportional to

$$H(f) \quad = \quad \sum_{n=1}^{N} \sum_{m=1}^{M} d_{nm} a_n c_m e^{j\beta(x_n - y_m)} \tag{3.5}$$

It is important to note that in this case, when both transducers are overlap weighted, the frequency response can not be factored due to the dependence of d_{nm} on both indices.

Therefore an impulse response can not be assigned to each transducer. This tremendously complicates the design of filters. If however only one transducer is apodized, $d_{n,n}$ equals the fractional overlap of the weighted transducer, and $H(f)$ once again is factorable. In this case, an effective impulse response can be defined for the overlap weighted transducer which yields the correct voltage to acoustic wave transfer function. The input admittance must still be calculated by splitting the transducer into strips.

The simple model presented above only describes the transduction process; it ignores all reflection effects which are crucial to the operation of a single phase unidirectional transducer (SPUDT). Before we include transversely nonuniform reflection in the model, it is worthwhile investigating the appropriateness of overlap weighting for a SPUDT.

The situation in which both transducers are overlap weighted would appear to be desirable since it gives greatest flexibility in the design. The more independent parameters that are available to control a response, the more accurately that response can approximate some desired response. Unfortunately, even in the absence of reflection, no good design algorithm has been found for this case due to the fact that the transfer function doesn't factor into responses of the individual transducers. Typically, only one transducer is overlap weighted, or a multistrip coupler [66,67,53] is used to convert a spatially nonuniform beam into a uniform beam at the average transverse wave amplitude. This makes the transfer function factorable. Both methods cause added insertion loss since the power radiated into the zero-average amplitude mode is not picked up by the receiving transducer. Since a major goal of this research is the development of low-loss filters, overlap weighting is not suitable.

If achieving the minimum insertion loss were not a problem, diffraction effects would make overlap weighting unattractive. In order to obtain sharp filter responses, the required

tap weights would include many lobes of a tapered $\sin(x/x)$. The combination of low overlaps and a long filter would result in a severe diffraction problem. This problem would be exacerbated in a SPUDT since the effective propagation path lengths would be increased by the internal reflections. For all these reasons, we will attempt to design a SPUDT without using overlap weighting. Thus in the remaining analysis procedures we will assume the transducers to be uniform in the transverse direction. An appropriate weighting technique satisfying this restriction, and an associated design algorithm is the focus of Chapter 6.

3.4 Scattering Parameter Analysis

In order to aid us in developing a consistent simple model which describes a SAW filter, let us first study 3-ports in general. Each IDT of a SAW filter has 3 ports, an electrical port, a front acoustic port and a rear acoustic port. A complete SAW filter can then be analyzed by connecting the front acoustic ports of each transducer with a transmission line.

In Fig. 3.3 two representations of a SAW IDT are presented. In both cases the acoustic waves are represented by complex amplitudes normalized so that their magnitudes' squared is power. In Fig. 3.3a the electrical port variables are complex wave amplitudes, while in Fig. 3.3b they are voltage and current. A voltage and current parameterization of the electrical port is more convenient for analysis and synthesis, since electromagnetically a SAW filter can be treated quasistatically.

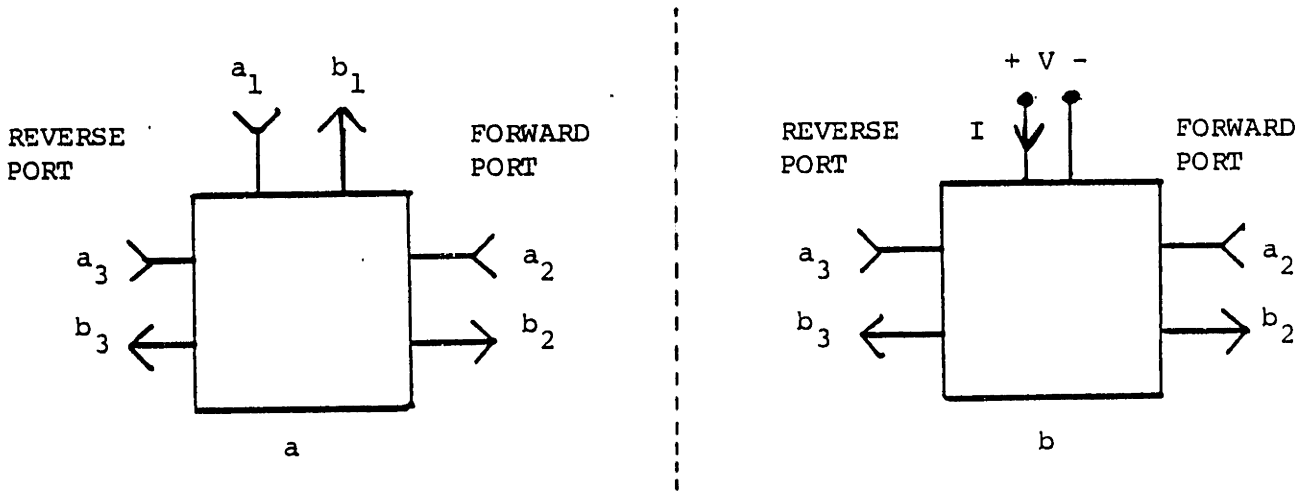

Figure 3.3 Three Port Representations of One SAW Transducer.
(a) Scattering matrix representation S (b) Mixed V-I Scattering matrix representation S_v

$$V = (a_1 + b_1)\sqrt{Z_o} \tag{3.6a}$$

$$I = \frac{a_1 - b_1}{\sqrt{Z_o}} \tag{3.6b}$$

where

Z_o = real source or load resistance

Reciprocity forces the scattering matrix, S representing Fig. 3.3a to be symmetric.

$$\begin{bmatrix} b_1 \\ b_2 \\ b_3 \end{bmatrix} = \begin{bmatrix} S_{11} & S_{21} & S_{31} \\ S_{21} & S_{22} & S_{23} \\ S_{31} & S_{23} & S_{33} \end{bmatrix} \begin{bmatrix} a_1 \\ a_2 \\ a_3 \end{bmatrix} \tag{3.7}$$

Using Eq. (3.6a, 3.6b) and reciprocity, the mixed scattering parameter matrix, S_v, representation of the three port is

$$\begin{bmatrix} I \\ b_2 \\ b_3 \end{bmatrix} = \begin{bmatrix} Y & -2S_{21v} & -2S_{31v} \\ S_{21v} & S_{22v} & S_{23v} \\ S_{31v} & S_{23v} & S_{33v} \end{bmatrix} \begin{bmatrix} V \\ a_2 \\ a_3 \end{bmatrix} \tag{3.8}$$

Relations between these two matrices are useful in synthesis, therefore they are tabulated below:

$$Y = \frac{1}{Z_0}\frac{1-S_{11}}{1+S_{11}} \tag{3.9a}$$

$$S_{21v} = \frac{S_{21}}{\sqrt{Z_0}(1+S_{11})} \tag{3.9b}$$

$$S_{31v} = \frac{S_{31}}{\sqrt{Z_0}(1+S_{11})} \tag{3.9c}$$

$$S_{22v} = S_{22} - \frac{[S_{21}]^2}{1+S_{11}} \tag{3.9d}$$

$$S_{23v} = S_{23} - \frac{S_{21}S_{31}}{1+S_{11}} \tag{3.9e}$$

$$S_{33v} = S_{33} - \frac{[S_{31}]^2}{1+S_{11}} \tag{3.9f}$$

Power conservation imposes six additional equations for each matrix. Using power conservation and reciprocity we obtain:

$$|S_{11}|^2 + |S_{21}|^2 + |S_{31}|^2 = 1 \tag{3.10a}$$

$$|S_{21}|^2 + |S_{22}|^2 + |S_{23}|^2 = 1 \tag{3.10b}$$

$$|S_{31}|^2 + |S_{23}|^2 + |S_{33}|^2 = 1 \tag{3.10c}$$

$$S_{21}^* S_{11} + S_{22}^* S_{21} + S_{23}^* S_{31} = 0 \tag{3.10d}$$

$$S_{31}^* S_{11} + S_{23}^* S_{21} + S_{33}^* S_{31} = 0 \tag{3.10e}$$

$$S_{31}^* S_{21} + S_{23}^* S_{22} + S_{33}^* S_{23} = 0 \tag{3.10f}$$

$$|S_{21v}|^2 + |S_{31v}|^2 = Re[Y] \triangleq G \tag{3.11a}$$

$$|S_{22v}|^2 + |S_{23v}|^2 = 1 \tag{3.11b}$$

$$|S_{23v}|^2 + |S_{33v}|^2 = 1 \tag{3.11c}$$

$$S^*_{23v}S_{22v} + S^*_{33v}S_{23v} = 0 \tag{3.11d}$$

$$S_{21v} + S^*_{21v}S_{22v} + S^*_{31v}S_{23v} = 0 \tag{3.11e}$$

$$S_{31v} + S^*_{21v}S_{23v} + S^*_{31v}S_{33v} = 0 \tag{3.11f}$$

Based on this scattering parameter analysis, we can now make two important conclusions about the phases of reflection and transduction in the small coupling and reflection limits. Let us apply the scattering formulation to a single reflector. We shall denote scattering parameters referencing a single reflector with a superscript $r1$. If the perturbation is a shallow etched groove, the transmission coefficient, S^{r1}_{23v}, is purely real since there is no velocity shift. This is the case for the mismatched transmission line model of a surface perturbation to first order in the impedance discontinuity. It is confirmed by the solutions obtained by Wright [114], Chen and Haus [11], and Hunsinger [51]. Requiring S^{r1}_{23v} to be real simplifies Eq. (3.11d).

$$S^{r1}_{22v} + S^{r1}{}^*_{33v} = 0 \tag{3.12}$$

Then using symmetry in addition, we obtain

$$S^{r1}_{22v} = S^{r1}_{33v} = j\Gamma \tag{3.13a}$$

where Γ is real. Using Eq. (3.11b) we find

$$S^{r1}_{23v} = \sqrt{1-\Gamma^2} \tag{3.13b}$$

If the perturbation is sufficiently thick, then energy storage in the evanescent fields around the perturbation causes a velocity shift which is second order in h, the depth of the groove [62,112,114,18]. Alternatively, a first order velocity shift, $O(h/\lambda)$, generally occurs if the material forming the grating, such as deposited films, has different mass density and/or elastic stiffness constants from those of the substrate [11,51]. Velocity shifts also occur in piezoelectric materials due to the shorting by metal films, of the tangential electric field at the surface. In these cases a similar procedure shows that if the transmission phase shift referenced to the midpoint of the perturbation is θ,

$$S^{r1}_{22_v} = S^{r1}_{33_v} = j\Gamma e^{j\theta} \tag{3.14}$$

In a 50% metalization ratio grating it is not obvious what to use for the unperturbed velocity in referencing phase shifts to particular planes. If the average velocity through the structure at some frequency* is used, then $S^{r1}_{23_v}$ becomes real at that frequency, and once again the reflection coefficients are pure imaginary.

Let us now model a single gap using the matrix formulation. These scattering parameters will be denoted with superscript $g1$. To the extent to which the electric fields exciting a wave can be localized to the gap between fingers of opposite polarity, we can treat the gap in one matrix, while the perturbation caused by the fingers exciting the gap can be handled in scattering matrices describing the adjacent sections (see Fig. 3.4). This is also reasonable if the perturbations caused by a finger are so small that a wave must pass under a lot of fingers for it to be significantly affected. Thus for a gap, $S^{g1}_{23_v}$ is exactly unity, while $S^{g1}_{22_v}$ and $S^{g1}_{33_v}$ are both zero. This makes perfect sense, since in the absence of mechanical perturbations the only source of a reflected signal will be a wave

* Deposited films give rise to wave guidance and thus dispersion. Another source of dispersion is the coupling of forward to backward waves by a grating near its Bragg frequency.

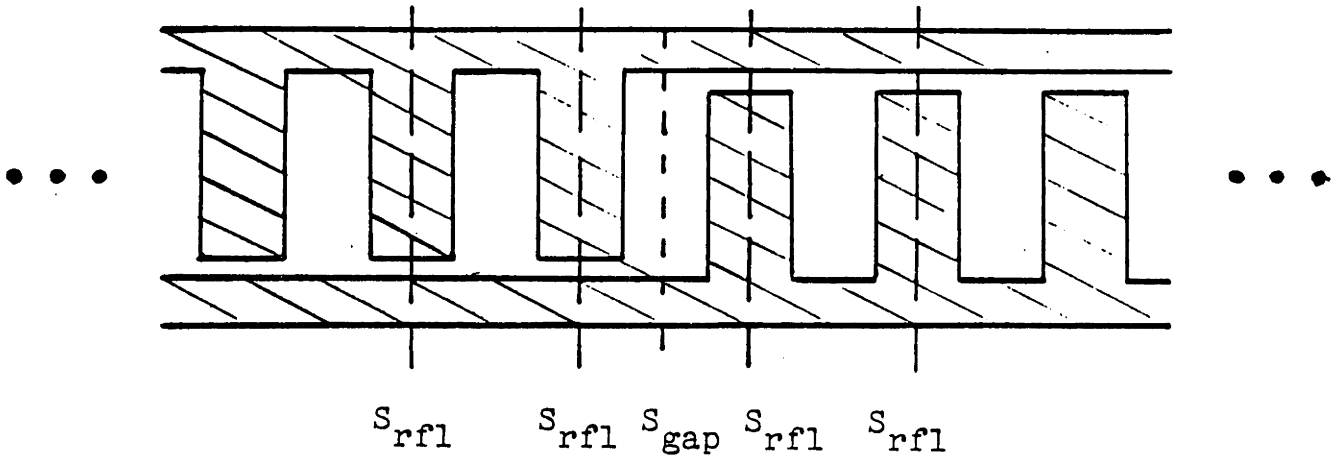

Figure 3.4 Modeling a Single Gap
The fingers exciting the gap are handled in separate scattering matrices. Only S_{gap} contains transduction terms. Only S_{rfl} contains reflection terms.

regenerated in the gap. Since S^{g1}_{22v} and S^{g1}_{33v} are defined with the gap voltage pinned at zero, there can be no reflected wave due to the gap. Thus Eqs. (3.11e, 3.11f) both simplify to

$$S^{g1}_{21v}{}^{*} + S^{g1}_{31v} = 0 \tag{3.15}$$

The electric potential is anti-symmetric about a gap center. This implies that S_{21v} and S_{31v} have opposite signs when referenced to the electric potential. Using this information together with Eq. (3.15) we find

$$S^{g1}_{21v} = -S^{g1}_{31v} = \alpha \tag{3.16}$$

where α is real.

3.5 Impulse Model—Transduction and Reflection

Let us assume that a transducer can be split into reflectionless transduction elements, and pure reflectors as in Fig. 3.4. Let the N plane wave radiating elements be localized at positions x_i, with elemental voltage to acoustic wave transfer functions in the forward and reverse directions α_{fi} and α_{ri}. Assume that the M reflectors are located at positions y_i (Fig. 3.5) with elemental forward and backward reflection coefficients r_{fi} and r_{ri}, and with transmission coefficients t_j. Note that we have allowed for an arbitrary relationship between the forward and backward excitation and reflection coefficients, although Eqs. (3.13a, 3.16) should be sufficient for low reflectivity perturbations, and to the extent that the electric field of the gap is unaffected by asymmetries in adjacent regions of the transducer. For notational convenience, we define

$$u(x_j) = \begin{array}{l}\text{index } k\text{, to the first reflector } y_k\text{,} \\ \text{to the right of the source at } x_k\end{array}$$

$$L(x_j) = \begin{array}{l}\text{index } k\text{, to the first reflector } y_k\text{,} \\ \text{to the left of the source at } x_j\end{array}$$

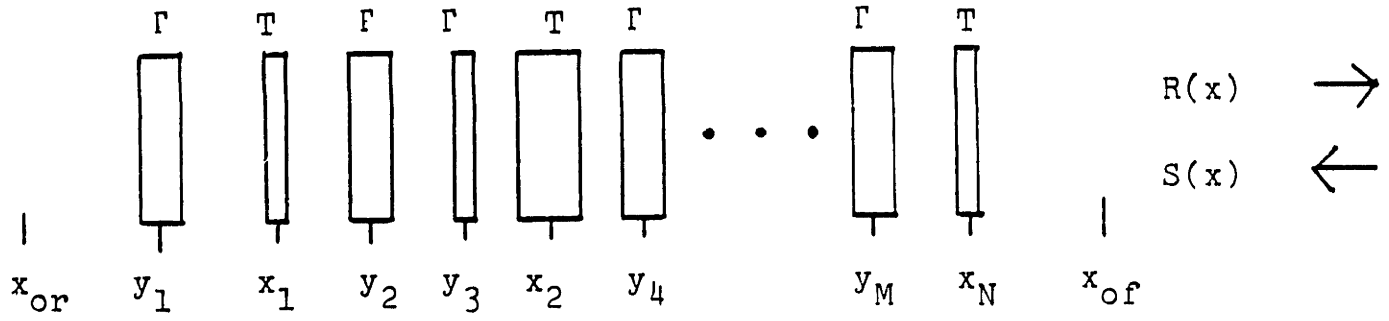

Figure 3.5 Generalized Transducer with Internal Reflections
Reflectionless transduction elements are located at positions x_i (T), and transductionless reflectors (Γ) are located at positions y_i. The observation points for the forward and backward ports are x_{of} and x_{or}.

Taking into account only single reflections, and ignoring the non-unity transmission coefficient through a reflector*, S_{21v} referenced to the origin is

$$\begin{aligned} S_{21v} &= e^{j\beta x_{of}} R(x_{of}) \\ &= \sum_{i=1}^{N} \alpha_{fi} e^{j\beta x_i} + \sum_{i=1}^{N} \alpha_{ri} e^{-j\beta x_i} \sum_{k=1}^{L(x_i)} \tau_{fk} e^{j2\beta y_k} \end{aligned} \tag{3.17a}$$

Similarly under the same set of approximations

$$\begin{aligned} S_{31v} &= e^{-j\beta x_{or}} S(x_{or}) \\ &= \sum_{i=1}^{N} \alpha_{ri} e^{-j\beta x_i} + \sum_{i=1}^{N} \alpha_{fi} e^{j\beta x_i} \sum_{k=u(x_i)}^{M} \tau_{rk} e^{-j2\beta y_k} \end{aligned} \tag{3.17b}$$

By following the path of all possible reflected rays through the structure with up to 3 reflections we obtain the following formulas:

$$\begin{aligned} S_{22v} = e^{j2\beta x_{of}} \frac{R(x_{of})}{S(x_{of})}\Big|_{v=0} &= \sum_{i=1}^{M} \tau_{fi} \Big(\prod_{i1=i+1}^{M} t_{i1}^2 \Big) e^{j2\beta y_i} \\ &+ \sum_{i=1}^{M} \tau_{fi} e^{j2\beta y_i} \sum_{k=i+1}^{M} \tau_{rk} e^{-j2\beta y_k} \sum_{l=1}^{k-1} \tau_{fl} e^{j2\beta y_l} \end{aligned} \tag{3.17c}$$

$$\begin{aligned} S_{33v} = e^{-j2\beta x_{or}} \frac{R(x_{or})}{S(x_{or})}\Big|_{v=0} &= \sum_{i=1}^{M} \tau_{ri} \Big(\prod_{i1=1}^{i-1} t_{i1}^2 \Big) e^{-j2\beta y_i} \\ &+ \sum_{i=1}^{M} \tau_{ri} e^{-j2\beta y_i} \sum_{k=1}^{i-1} \tau_{fk} e^{j2\beta y_k} \sum_{l=k+1}^{M} \tau_{rl} e^{-j2\beta y_l} \end{aligned} \tag{3.17d}$$

Double reflections do not appear in these sums since they contribute to the transmitted wave. Note that in the case of reflection, we must take into account the nonunity transmission through a reflector since terms $O(r^3)$ are contributed to the first sums in

* It is legitimate to ignore the nonunity transmission through a reflector, since it is $\sqrt{1-r^2} \approx 1 - \frac{1}{2}r^2$ for small reflectors. The r^2 term is of higher order than any term in Eqs. (3.17a, 3.17b).

Eqs. (3.17c, 3.17d). This effect is droppcd for the second sums in these equations since the effect is $O(r^5)$.

It is important to note that if we keep only the first terms of Eqs. (3.17a–3.17d), there is a Fourier transform relationship between the source excitations and the mixed scattering parameters. This will be used to advantage in the synthesis technique to be presented in Sec. (4.2).

Power conservation and causality can be used to advantage in finding the other elements of the mixed scattering matrix representation of the transducer. Equations (3.11b, 3.11c) require

$$|S_{23v}|^2 = 1 - |S_{22v}|^2 = 1 - |S_{33v}|^2 \tag{3.18}$$

while Eq. (3.11d) specifies the phase of S_{23v} within a multiple of π.

$$arg(S_{23v}) = \frac{(2n+1)\pi + arg(S_{22v}) + arg(S_{33v})}{2} \tag{3.19}$$

As with the impulse model, Eq. (3.11a) specifies the input conductance in terms of the forward and reverse voltage to acoustic wave transfer functions

$$G = R_e[Y] = |S_{21v}|^2 + |S_{31v}|^2 \tag{3.20}$$

Causality implies that the non-capacitive portion of the input susceptance is the Hilbert transform of G [36,41]

$$B(\omega) = \frac{1}{\pi}\int_{-\infty}^{\infty} \frac{G(\omega')}{\omega' - \omega}\, d\omega' \tag{3.21}$$

Finally the input capacitance can be evaluated by solving Laplace's equation for the particular geometry of the transducer ignoring the acoustic wave generation [39,25,81] .

It is important to note that although power conservation was used to find S_{23v} and G from the other mixed scattering parameters, not all 6 equations (3.11a–3.11f) defining power conservation are satisfied by the scattering parameters computed above. For example, $|S_{22v}| \neq |S_{33v}|$ although they are required to be equal by Eqs. (3.11b, 3.11c). If it is desired that power conservation be satisfied exactly, then the magnitude of the reflection coefficients can be adjusted to equal the geometric mean of the values computed via Eqs. (3.17c, 3.17d). The phases of the forward and backward reflection coefficients can then be obtained by solving Eqs. (3.11e, 3.11f) in terms of S_{21v} , S_{31v} , S_{23v} , and $|S_{22v}| = |S_{33v}|$. With these modifications, power conservation is satisfied exactly.

In obtaining Eqs. (3.17a–3.17d) only the first two terms of an infinite series have been used. Multiple bounces to any order and non-unity reflector transmission coefficients can be handled by this technique, although the expressions become quite complicated very quickly. As examples, S_{21v} considering reflections up to third order, and S_{22v} including up to five reflections and the effect of non-unity reflector transmission coefficients t_i are presented below:

$$S_{21v} = \sum_{i=1}^{N} \alpha_{fi}\left(\prod_{i_1=u(x_i)}^{M} t_{i_1}\right) e^{j\beta x_i} \bullet$$

$$\left[1 + \frac{\alpha_{ri}}{\alpha_{fi}} \sum_{k=1}^{L(x_i)} \tau_{fk}\left(\prod_{k_1=k+1}^{L(x_i)} t_{k_1}^2\right) e^{-j2\beta(x_i - y_k)} \left[1 + \sum_{l=k+1}^{M} \sum_{m=1}^{l-1} \tau_{rl}\tau_{fm}\left(\prod_{m_1=m+1}^{l-1} t_{m_1}^2\right) e^{-2j\beta(y_l - y_m)} \right] \right.$$
$$\left. + \sum_{k=u(x_i)}^{M} \sum_{l=1}^{k-1} \tau_{rk}\tau_{fl}\left(\prod_{l_1=l+1}^{k-1} t_{l_1}^2\right) e^{-2j\beta(y_k - y_l)} \right] \qquad (3.22a)$$

$$S_{22v} = \sum_{i=1}^{M} r_{fi}\left(\prod_{i_1=i+1}^{M} t_{i_1}^2\right) e^{j2\beta y_i} \cdot \left[1 + \sum_{k=i+1}^{M} \sum_{l=1}^{k-1} r_{rk} r_{fl} \left(\prod_{k_1=l+1}^{k-1} t_{k_1}^2\right) e^{-j2\beta(y_k - y_l)} \cdot \left[1 + \sum_{m=l+1}^{M} \sum_{n=1}^{m-1} r_{rm} r_{fn} \left(\prod_{m_1=n+1}^{m-1} t_{m_1}^2\right) e^{-j2\beta(y_m - y_n)} \right] \right] \quad (3.22b)$$

3.6 Transmission Matrix Method

It is clear from the complexity of the iterated sums of Eqs. (3.22a, 3.22b) that this is not the way to handle transducers with large internal reflection. A better approach would be to write mixed scattering matrices for each individual gap and reflector. These scattering matrices could then be used to match boundary conditions at the interface between the sections. An efficient way of doing this would be to convert the mixed scattering matrices into transmission matrices which can be cascaded simply by multiplication (see Fig. 3.6).

$$\begin{bmatrix} R_{n+1} \\ S_{n+1} \\ V_{n+1} \\ I_{n+1} \end{bmatrix} = \begin{bmatrix} T_{11} & T_{12} & T_{13} & 0 \\ T_{21} & T_{22} & T_{23} & 0 \\ 0 & 0 & 1 & 0 \\ T_{41} & T_{42} & T_{43} & 1 \end{bmatrix} \begin{bmatrix} R_n \\ S_n \\ V_n \\ I_n \end{bmatrix} \quad (3.23)$$

The zeros in the last column of the T matrix are due to the fact that only 3 complex amplitudes can be specified for a three port; here we have chosen R_n, S_n, and V_n. The physical current flowing into the n^{th} section, $J_n = I_n - I_{n+1}$, is computed in terms of these 3 quantities. The reason for defining the element in terms of I_n and I_{n+1} was only for computational and notational convenience in cascading sections.

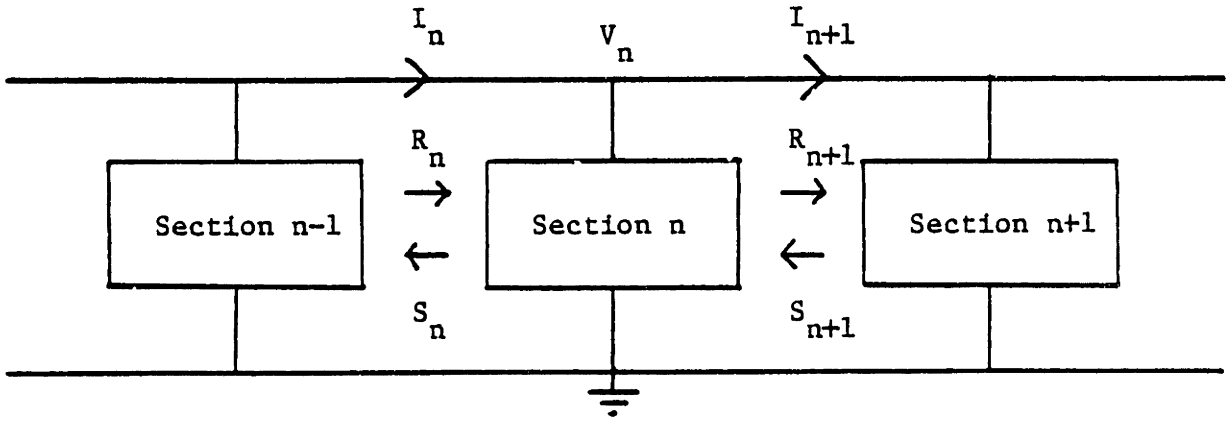

Figure 3.6 An IDT as a Cascade of Sections
The sections are connected acoustically in series, and electrically in parallel. Note that the current feeding section n is $I_n - I_{n+1}$.

3.7 Coupling-of-Modes Model (COM)

The coupling-of-modes (COM) formalism was first introduced by Pierce [83a] and since then has been widely used in microwaves and optics [47,63,120] . In the SAW field, COM has been successfully applied to the analysis and synthesis of grating devices like resonators and reflective array compressors (RAC's) [45,46,113] .

Recently, the COM equations have been extended to include transduction [11,44] . The equations basically represent a continuum approximation to the impulse transduction-reflection model previously discussed. Their advantage lies in the applicability of powerful approximate techniques for the solution of differential equations.

We begin the derivation of the coupled mode equations with a discretized version, then we will go to the continuum limit. We start by writing a difference equation for the forward traveling wave amplitude with reference to Fig. 3.7.

$$\begin{aligned} R(n) = R(n-1)e^{-j\beta\Lambda_{n-1}} &+ \kappa_{n-1}\Lambda_{n-1}S(n)e^{-2j\beta(\Lambda_{n-1}-a_{n-1})} \\ &+ a_{n-1}\Lambda_{n-1}Ve^{-j\beta(\Lambda_{n-1}-b_{n-1})} \end{aligned} \tag{3.24}$$

Equation (3.24) states that there are two possible ways for the forward traveling wave amplitude to be affected in going from position $n-1$ to n. The wave amplitude can

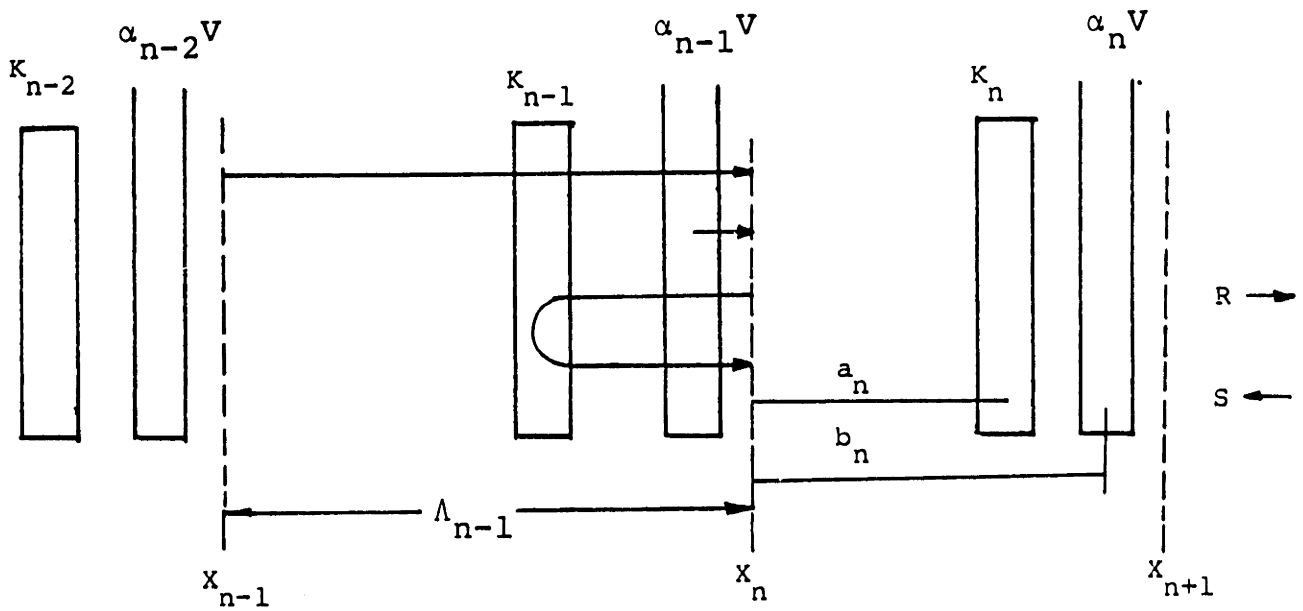

Figure 3.7 An IDT as a Cascade of Incremental Transducers and Reflectors
Transduction and reflection in each section are lumped in α_n and κ_n respectively.

be increased by transduction in the interval ($\alpha_{n-1}\Lambda_{n-1}V$), and in addition some of the backward traveling wave can be scattered into a forward traveling wave by a reflector ($\kappa_{n-1}\Lambda_{n-1}$).

In order to go to a continuum, we must use quantities which change very little between positions x_{n-1} and x_n. Thus we define slowly varying amplitudes $\hat{R}(n)$ and $\hat{S}(n)$, from which the propagation factors $e^{\mp j\beta x}$ have been removed.

$$R(n) = \hat{R}(n)e^{-j\beta x_n} \tag{3.25a}$$

$$S(n) = \hat{S}(n)e^{+j\beta x_n} \tag{3.25b}$$

The resulting equation is then

$$\frac{\hat{R}(n)-\hat{R}(n-1)}{\Lambda_{n-1}} = \kappa_{n-1}\hat{S}(n)e^{+j2\beta x_n}e^{-j2\beta(\Lambda_{n-1}-a_{n-1})} + \alpha_{n-1}V e^{j\beta x_n}e^{-j\beta(\Lambda_{n-1}-b_{n-1})} \tag{3.26}$$

We now have a quantity which is similar to a derivative on the left hand side of Eq. (3.26), but the quantities $e^{j2\beta x_n}$ and $e^{j\beta x_n}$ on the right hand side are not smoothly varying quantities. When we distribute a source or a reflector across an interval Λ_{n-1}, we must insure that it remains synchronous with the traveling wave across the full length of the region. Otherwise, when we go to the continuum limit, transduction and reflection will both approximately cancel in each section. The following is the required modification to maintain synchronism:

$$\kappa \rightarrow |\kappa| e^{-j2\int^{x} ds\, \beta_{o\kappa}(s)} \tag{3.27a}$$

$$\alpha \rightarrow |\alpha| e^{-j\int^{x} ds\, \beta_{o\alpha}(s)} \tag{3.27b}$$

where $\beta_{o\kappa}$ and $\beta_{o\alpha}$ are the local synchronous wave vectors of the reflection and transduction functions respectively*. In the case of periodic distributions, these reduce to the more familiar form:

$$\kappa \rightarrow |\kappa| e^{j\theta_\kappa} e^{-j2\beta_o x} \tag{3.28a}$$

$$\alpha \rightarrow |\alpha| e^{j\theta_\alpha} e^{-j\beta_o x} \tag{3.28b}$$

where

$$\beta_o = 2\pi/\lambda_o \tag{3.28c}$$

Let us now go straight to the continuum limit. We define V, I, R and S as in Fig. 3.6, but we make them functions of the continuous variable, x. We normalize the complex wave amplitudes R and S so that their magnitude squared is power. As in the difference equation case, we define slowly varying envelope quantities, $\hat{R}$ and $\hat{S}$:

*This formulation is general enough to handle the situation in which there is no relationship between the locations of the transduction and reflection elements.

$$R(x) = \hat{R}(x)e^{-j\beta x} \tag{3.29a}$$

$$S(x) = \hat{S}(x)e^{j\beta x} \tag{3.29b}$$

Then the one dimensional coupled mode equations in the absence of loss are:

$$\frac{d\hat{R}}{dx} = \kappa_1(x)e^{j2\beta x}\hat{S}(x) + \alpha_1(x)e^{j\beta x}V \tag{3.30a}$$

$$\frac{d\hat{S}}{dx} = \kappa_2(x)e^{-j2\beta x}\hat{R}(x) + \alpha_2(x)e^{-j\beta x}V \tag{3.30b}$$

$$\frac{dI}{dx} = -j\omega C(x)V + \xi_1(x)e^{-j\beta x}\hat{R}(x) + \xi_2(x)e^{j\beta x}\hat{S}(x) \tag{3.30c}$$

In the above equations, κ_1 and κ_2 represent the continuous distributed reflection per unit length, α_1, α_2, ξ_2 and ξ_2, are related to the transduction per unit length, and $C(x)$ is the electrostatic capacitance per unit length. κ and α both contain the phase terms of (3.27) or (3.28).

Power conservation and reciprocity impose conditions on the parameters of the COM equations which reduce the number of parameters which must be determined. Applying power conservation:

$$Re\left[\frac{d}{dx}V^*I\right] + \frac{d}{dx}|\hat{R}|^2 - \frac{d}{dx}|\hat{S}|^2 = 0 \tag{3.31}$$

we obtain

$$\kappa_1 = \kappa_2^* \tag{3.32a}$$

$$\xi_1 = -2\alpha_1^* \tag{3.32b}$$

$$\xi_2 = 2\alpha_2^* \tag{3.32c}$$

We assume that $R+S$ is analogous to the voltage on an electromagnetic transmission line and that $R-S$ corresponds to the current. Then if ($\hat{R}^a$, $\hat{S}^a$, V^a , I^a), and ($\hat{R}^b$, $\hat{S}^b$, V^b , I^b) are two different solutions to the problem, reciprocity imposes the following differential equation:

$$-2\frac{d}{dx}\left[\hat{R}^b\hat{S}^a\right]+2\frac{d}{dx}\left[\hat{R}^a\hat{S}^b\right]-V^a\frac{dI^b}{dx}+V^b\frac{dI^a}{dx} \quad = \quad 0 \tag{3.33}$$

Applying reciprocity we obtain:

$$\xi_1 \quad = \quad -2\alpha_2 \tag{3.34a}$$
$$\xi_2 \quad = \quad 2\alpha_1 \tag{3.34b}$$

Using reciprocity and power conservation simultaneously requires

$$\kappa_1 \quad = \quad \kappa_2^* \tag{3.35a}$$
$$\alpha_1 \quad = \quad \alpha_2^* \tag{3.35b}$$

yielding the final form for the lossless reciprocal COM equations:

$$\frac{d\hat{R}}{dx} \quad = \quad \kappa(x)e^{j2\beta x}\hat{S}(x)+\alpha(x)e^{j\beta x}V \tag{3.36a}$$

$$\frac{d\hat{S}}{dx} \quad = \quad \kappa^*(x)e^{-j2\beta x}\hat{R}(x)+\alpha^*(x)e^{-j\beta x}V \tag{3.36b}$$

$$\frac{dI}{dx} \quad = \quad -j\omega C(x)V-2\alpha^*(x)e^{-j\beta x}\hat{R}(x)+2\alpha(x)e^{j\beta x}\hat{S}(x) \tag{3.36c}$$

3.8 Comparison of COM with Other Models

It is important to point out some of the similarities and differences between COM and the other methods. It should be noted that Eq. (3.35b) resulting from the COM technique is identical to Eq. (3.15) of the scattering matrix characterization method*. This is reasonable since in both cases power conservation and reciprocity have been applied to general 3 ports assuming the transduction elements to be reflectionless when short circuited.

Similarly, Eqs. (3.35a) and (3.12) are identical. This though, represents a difference between the two methods. In order to derive Eq. (3.12), we had to assume that the perturbation produced by the reflector yields no velocity shift, making the elemental transmission scattering parameter S^{r1}_{23v} is purely real, or at worst that it causes a frequency independent velocity shift. On the other hand, Eq. (3.35a) must be satisfied exactly in the COM formulation if power conservation is to be satisfied.

Let us compute the voltage to acoustic wave transfer function, S_{21v}, using both the impulse model, and coupling of modes in the absence of reflection effects. If a transducer is N wavelengths long with gaps located every half wavelength (see Fig. 3.8), then using Eq. (3.17a) with $\tau_{fk} = 0$

$$S_{21v} = \alpha_g \frac{\lambda_o}{2} \sum_{n=-N}^{N-1} (-1)^n e^{j\beta(2n+1)\frac{\lambda_o}{4}} \tag{3.37a}$$

$$= \alpha_g \frac{\lambda_o}{2} e^{j\beta\frac{\lambda_o}{4}} \sum_{n=-N}^{N-1} \left(e^{-j\beta_o\lambda_o/2}\right)^n e^{j\beta n\lambda_o/2} \tag{3.37b}$$

$$= j\alpha_g \frac{\lambda_o}{2} \frac{\sin\left[N(\beta-\beta_o)\lambda_o/2\right]}{\sin\left[(\beta-\beta_o)\lambda_o/4\right]} \quad \text{Impulse Model} \tag{3.37c}$$

where β_o is the synchronous wave vector, $2\pi/\lambda_o$, and $\alpha_g\lambda_o/2$ is the transduction coefficient of one gap.

* There at first appears to be a sign difference between these two equations. The sign difference is easily resolved by recognizing that for the COM equations $-\kappa_2$ and $-\alpha_2$ are the reflection and transduction coefficients in the backward direction.

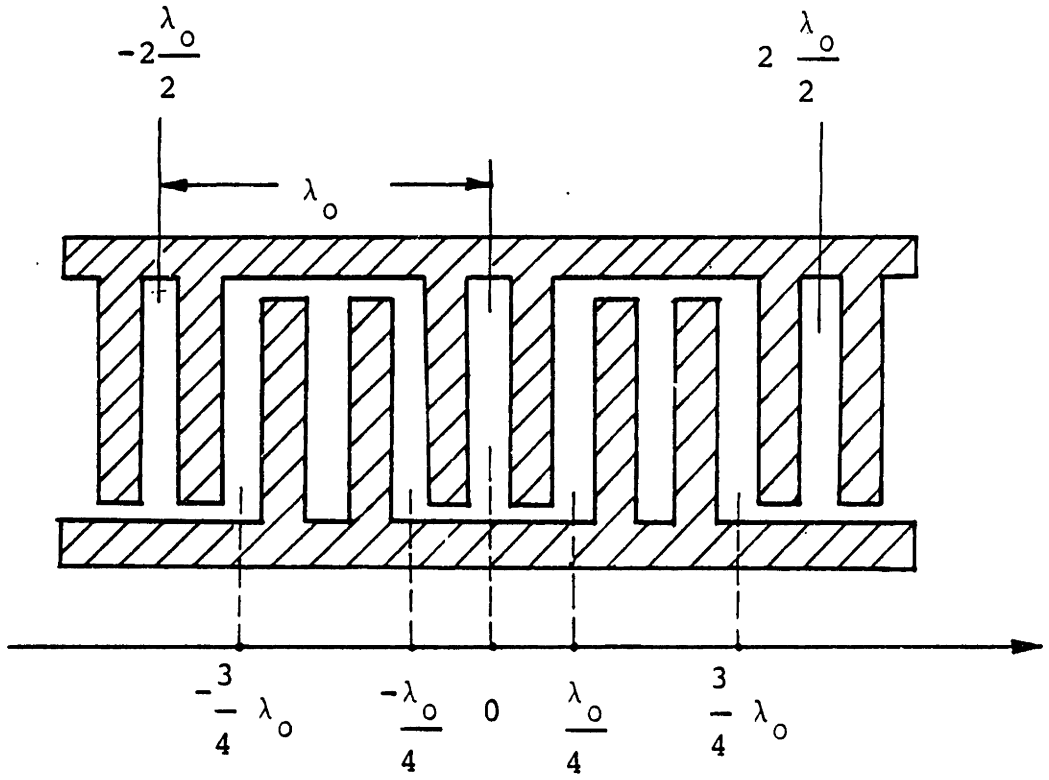

Figure 3.8 The Uniform Transducer to be Characterized by the Impulse and COM Models
In the COM approximation, the transducer is assumed to extend to the midpoint of the split fingers beyond the first and last gaps.

Using the COM model without reflections as the starting point

$$\frac{d\hat{R}}{dx} = j\alpha_g e^{j(\beta-\beta_o)x}V \tag{3.38}$$

Note that the COM transduction coefficient is $j\alpha_g e^{-j\beta_o x}$, so that at the first positive gap location (see Fig. 3.8) $x = \lambda_o/4$, we obtain the gap transduction coefficient

$$j\alpha_g e^{-j\beta_o\lambda_o/4} = \alpha_g \tag{3.39}$$

Regarding the transducer to extend from $-\frac{N}{2}\lambda_o$ to $\frac{N}{2}\lambda_o$, which includes the midpoints of the split fingers beyond the first and last gaps, Eq. (3.38) can be integrated directly to obtain

$$S_{21v} = j\alpha_g\frac{\lambda_o}{2}2N\,\mathrm{sinc}\left[N(\beta-\beta_o)\frac{\lambda_o}{2}\right] \quad \text{COM Model} \tag{3.40}$$

We note that the impulse model solution, Eq. (3.37c) and the COM solution, Eq. (3.40) are quite similar indeed. The ratio of the two is a slowly varying function, which is unity at synchronism.

$$\frac{S_{21v},\text{COM}}{S_{21v},\text{Impulse}} = \text{sinc}\left[(\beta-\beta_o)\frac{\lambda_o}{4}\right] \tag{3.41}$$

The transduction coefficient in the COM model could be divided by this factor so that exactly the same answer would result from the two models. However over a 50% fractional bandwidth, this factor varies by only .2dB, so that correction would only be necessary if a filter's passband were extremely broad.

An important similarity between COM and the impulse methods including reflections, is evident from an approximate solution of Eqs. (3.36a, 3.36b). In order to obtain S_{21v} for the entire transducer, we must find $R(x)$ at a point to the right of the transducer. This can be done approximately by setting κ to zero in Eq. (3.36b) and solving for $\hat{S}_o(x)$. This solution can then be plugged into Eq. (3.36a), integrated to find $\hat{R}_1(x)$ [43]. Performing this calculation and a similar one for $\hat{S}_1(x)$ yields approximate solutions for S_{21v} and S_{31v}:

$$S_{21v} = \int_{-\frac{L}{2}}^{\frac{L}{2}} ds\,\alpha(s)e^{j\beta s} - \int_{-\frac{L}{2}}^{\frac{L}{2}} ds\,\alpha^*(s)e^{-j\beta s}\int_{-\frac{L}{2}}^{s} du\,\kappa(u)e^{j2\beta u} \tag{3.42a}$$

$$S_{31v} = -\int_{-\frac{L}{2}}^{\frac{L}{2}} ds\,\alpha^*(s)e^{-j\beta s} - \int_{-\frac{L}{2}}^{\frac{L}{2}} ds\,\alpha(s)e^{j\beta s}\int_{s}^{\frac{L}{2}} du\,\kappa^*(u)e^{-j2\beta u} \tag{3.42b}$$

A similar procedure can be used to find S_{22v} and S_{33v}. In order to find

$$S_{22v} = \frac{\hat{R}(\frac{L}{2})}{\hat{S}(\frac{L}{2})}\Big|_{v=0} \tag{3.43}$$

we would first assume the incident wave to be undepleted, i.e. $\hat{S}_o(x) = \hat{S}_o(L/2)$. Equation (3.36a) is then integrated to obtain $R_1(x)$. This solution is plugged back into Eq. (3.36b)

and integrated to obtain $\hat{S}_1(x)$. Finally, $\hat{S}_1(x)$ is plugged into equation (3.36a) and integrated to obtain $\hat{R}_2(x)$ and thereby S_{22v}. Using this procedure we obtain

$$S_{22v} = \int_{-\frac{L}{2}}^{\frac{L}{2}} dv\, \kappa(v) e^{j2\beta v} \left[1 - \int_{v}^{\frac{L}{2}} ds\, \kappa^*(s) e^{-j2\beta s} \int_{-\frac{L}{2}}^{u} du\, \kappa(u) e^{j2\beta u} \right] \tag{3.44a}$$

$$S_{33v} = -\int_{-\frac{L}{2}}^{\frac{L}{2}} dv\, \kappa^*(v) e^{-j2\beta v} \left[1 - \int_{-\frac{L}{2}}^{v} du\, \kappa(u) e^{j2\beta u} \int_{u}^{\frac{L}{2}} ds\, \kappa^*(s) e^{-j2\beta s} \right] \tag{3.44b}$$

It should be noted that Eqs. (3.17a, 3.17b) for S_{21v} and S_{31v}, obtained from the impulse transduction and reflection model are exactly the same as Eqs. (3.42a, 3.42b) obtained by an approximate solution to the COM equations if two conditions are met:

1. The integrals must be approximated by a trapezoidal rule in which the sample points are chosen so that the phase samples are those of Eqs. (3.17a, 3.17b).

2. The transmission coefficient through an elemental reflector, S_{23v}, must be assumed to be pure real so that $r_{ri} = -r_{fi}^*$ (see Sec. 3.4). Similarly the transduction elements must be assumed to be reflectionless, so that $\alpha_{ri} = -\alpha_{fi}^*$.

In addition Eqs. (3.17c, 3.17d) for S_{22v} and S_{33v} using the impulse transduction and reflection model are the same as the approximate COM solutions of Eqs. (3.44a, 3.44b) if the nonunity transmission coefficient through a reflector is ignored. Thus the iterated integral solution based on the COM equations does not keep all terms $O(\kappa^3)$.

One further connection between these two models is evident from the expression for S_{22v} at Bragg for a constant period grating. In this case

$$\kappa(x) = \Gamma(x) e^{j\theta_\kappa} e^{-2j\beta_0 x} \tag{3.45}$$

where $\Gamma(x)$ is real, and [57]

$$S_{22v} = e^{j\theta_\kappa} \tanh\left(\int_{-\frac{L}{2}}^{\frac{L}{2}} dx\, \Gamma(x) \right) \tag{3.46}$$

If $\Gamma(x)\Lambda_{\kappa_o}$ is constant at Γ_o, then it can be shown that Eq. (3.22b) for S_{22v} reduces to the Taylor series expansion of $\tanh(\Gamma_o M)$ plus terms of the form $\Gamma_o^k M^{k-j}$, where j is positive, whether or not unity transmission is assumed for S_{23v}. Terms of the form $\Gamma_o^k M^{k-j}$ are negligible compared to $(\Gamma_o M)^k$ only in the limit of a large number of reflectors. This is a demonstration of the fact that COM and the iterated integral approximate solutions are best applied to problems with a large number of reflectors. In order to design devices based on these kinds of approximations, it will be necessary to investigate their range of applicability. An experimental confirmation of the coupled mode approach in one particular case is the subject of Chapter 5.

3.9 Detailed Analysis and Determination of Model Parameters

In order to use any of these models, the transduction, reflection and transmission coefficients must be determined. Our approach will be to analyze transduction and reflection separately, and then to use the impulse model, matrix multiplication method or COM to phenomenologically piece these two analyses together. The reason for doing this, is that a complete analysis of SAW transducers on anisotropic substrates, taking both piezoelectric and mechanical effects into account simultaneously, is so difficult that it has not been done*. Also, since the reflection coefficient per perturbation is so small, there really is no need to analyze transduction and reflection at the same time.

* Recently Chen and Haus [11] have developed a comprehensive model of transducers accounting for both piezoelectric and mechanical reflection effects. It achieves impressive agreement with experiment even though an isotropic model is used.

3.9.1 Transduction

The most complete analysis of transduction, ignoring the mechanically perturbative effects of the electrodes, and ignoring diffraction was performed by Milsom [69] . It is a Green's function approach based on the response of the surface potential $\phi(x,\omega)$, to a line source surface charge. Using linearity, the response due to an arbitrary surface charge distribution can be found using a convolution.

$$\phi(x,\omega) = \int_{-\infty}^{\infty} G(x-x',\omega)\sigma(x',\omega)\,dx' \tag{3.47}$$

If $\sigma(x,\omega)$ were known, the problem would be solved, but $\sigma(x,\omega)$ must be determined in such a way that $\phi(x,\omega)$ matches the potential of alternating polarity impressed on the fingers of the IDT. Milsom solves this boundary value problem taking full account of anisotropy, bulk waves and regeneration. His results are impressive; theory and experiment agree almost exactly over a very broad frequency range (see Fig. 3.9). The main discrepancy is an underestimate of the insertion loss, probably arising from Milsom's ignoring of propagation loss and resistive finger loss.

Milsom's analysis is complicated by the fact that the Green's function must be solved numerically for every material, and that it depends on frequency. This restricts Milsom's method to the analysis of relatively short transducers consisting of 30 electrode pairs or fewer [70] . Morgan [73] recognized that many of these complications would vanish if the bulk wave contribution to the Green's function could be ignored. This is a reasonable assumption since the bulk waves do not contribute much to the radiated power unless the transducers are very short. Milsom computes that for transducers on Y-Z lithium niobate with as few as 5 finger pairs, 88% of radiated power is radiated into the surface acoustic wave mode at the center frequency. For transducers with 10 or more finger pairs

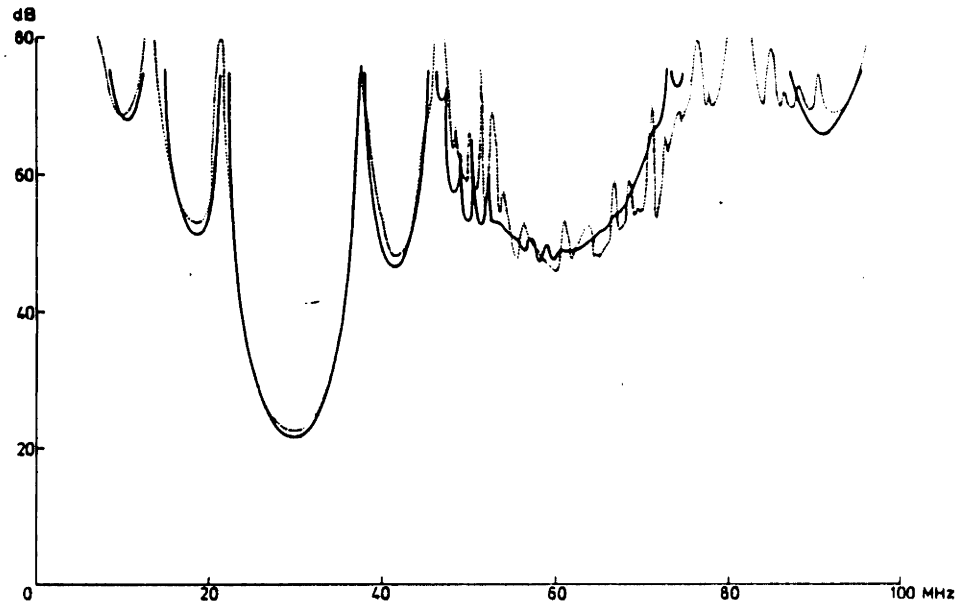

Figure 3.9 Milsom's Green's Function Theory
Insertion loss of two 4 electrode pair 50% metalization ratio transducers on Y-Z lithium niobate terminated in 50 ohm resistances. solid line = theory dotted line = experiment (After [69])

this percentage rises to 97%. Thus there is no problem with this approximation in the passband. The problem lies in the stopband, where surface skimming bulk mode radiation and reflection or mode conversion from the back surface contributes to the received signal, and can severely degrade the ultimate rejection level achieved. Shibayama [95] made a major contribution to the solution of this problem with the discovery of a cut of lithium niobate for which the coupling to the surface skimming bulk mode is very low, at least 60 dB weaker than the coupling to the surface wave mode. Roughening the back surface reduces the signal received by reflection from this surface.

Following Morgan [73], we ignore the bulk wave terms and find that the Green's function becomes independent of frequency and can be determined analytically

$$G(x) = G_e(x) + G_{SAW}(x) \tag{3.48}$$

where

$$G_e(x) = \frac{-\ln|x|}{\pi\epsilon_{s\infty}} \tag{3.49}$$

is an electrostatic term and

$$G_{SAW}(x) = -jG_s e^{-j\beta|x|} \tag{3.50}$$

is a surface wave term* where

$$G_s = \frac{1}{\epsilon_{s\infty}} \frac{v_m - v_o}{v_m} \tag{3.51a}$$

$$\beta = \omega/v_o \tag{3.51b}$$

$$\epsilon_{s\infty} \approx \epsilon_o + \left(\epsilon_{xx}^T \epsilon_{zz}^T - \epsilon_{xz}^{T\,2}\right)^{\frac{1}{2}} = \epsilon_o + \epsilon_p^T \tag{3.51c}$$

with v_o the free surface velocity and v_m the metalized surface velocity. The z axis is assumed to be normal to the surface and the superscript T indicates that the dielectric constants are to be evaluated at constant stress.

For a point outside the transducer region, the electrostatic fields can typically be ignored compared to the SAW term since the SAW term oscillates sinusoidally at constant amplitude if there is no loss, while the electrostatic term decays. In this case, the forward and backward propagating surface potentials are related to the charge distribution as follows:

$$\phi_+(x,\omega) = -jG_s e^{-j\beta x} \int_{-\infty}^{\infty} \sigma(x',\omega) e^{j\beta x'} dx' \tag{3.52a}$$

$$\phi_-(x,\omega) = -jG_s e^{j\beta x} \int_{-\infty}^{\infty} \sigma(x',\omega) e^{-j\beta x'} dx' \tag{3.52b}$$

Morgan now makes the further assumption that the electrostatic component of the Green's function, $G_e(x,\omega)$, is dominant within the transducer, which is reasonable on low-coupling substrates, and in general when split fingers are used to eliminate reflections. With

* This same result can be obtained by contour integration using the approximate dielectric response function for a piezoelectric, which was derived by Greebe [35]

this further assumption, $\sigma(x,\omega)$ becomes the purely real frequency independent solution to an electroquasistatic problem consisting of metal fingers on a dielectric half-space.

Let us define $\sigma_e(x)$ to be the charge distribution resulting when a potential difference of one volt is applied across the fingers of an IDT, with $\bar{\sigma}_e(\beta)$ being its Fourier transform.

$$\bar{\sigma}_e(\beta) = \int_{-\infty}^{\infty} \sigma_e(x) e^{j\beta x}\, dx \tag{3.53}$$

then Eqs. (3.52a, 3.52b) reduce to

$$\phi_+(x,\omega) = -jG_s V e^{-j\beta x}\bar{\sigma}_e(\beta) \tag{3.54a}$$

$$\phi_-(x,\omega) = -jG_s V e^{j\beta x}\bar{\sigma}_e^*(\beta) \tag{3.54b}$$

where x is assumed to be to the right and left respectively of the IDT in Eqs. (3.54a, 3.54b). It should be noted that Eqs. (3.54a, 3.54b) imply that a wave generated in one part of the transducer propagates out the front or back ports of the IDT unaffected by all the fingers under which it has passed. Thus under these assumptions, not only are mechanical reflections being ignored, but so are piezoelectrically generated ones*.

Recognizing that Eqs. (3.54a, 3.54b) are linear, we split the charge distribution into a sum of elemental distributions

$$\sigma_e(x) = \sum_j \sigma_j(x - x_j) \tag{3.55}$$

centered at x_j, the source locations. Then

* Our final model includes both mechanical and piezoelectric reflection effects via κ of the COM equations.

$$\phi_+(x,w) = -jG_sV\sum_i e^{-j\beta(x-x_i)}\int_{-\infty}^{\infty} dx'\,\sigma_i(x')e^{j\beta x'} \tag{3.56a}$$

$$\phi_-(x,w) = -jG_sV\sum_i e^{j\beta(x-x_i)}\int_{-\infty}^{\infty} dx'\,\sigma_i(x')e^{-j\beta x'} \tag{3.56b}$$

Since the time average power in a beam of width W with surface potential ϕ_s is [69]

$$\text{power} = -\frac{\omega W}{4G_s}|\phi_s|^2 \tag{3.57}$$

$$R(x) = -\frac{jV}{2}\sqrt{\omega W|G_s|}\sum_i \bar{\sigma}_i(\beta)e^{-j\beta(x-x_i)} \tag{3.58a}$$

$$S(x) = -\frac{jV}{2}\sqrt{\omega W|G_s|}\sum_i \bar{\sigma}_i^*(\beta)e^{j\beta(x-x_i)} \tag{3.58b}$$

We note that Eqs. (3.58a, 3.58b) are the same as Eqs. (3.17a, 3.17b) of the impulse-transduction-reflection model if reflection is ignored, and the following identifications are made:

$$\alpha_{fi}(\omega) = -\frac{j}{2}\sqrt{\omega W|G_s|}\,\bar{\sigma}_i(\beta) \tag{3.59a}$$

$$\alpha_{ri}(\omega) = -\frac{j}{2}\sqrt{\omega W|G_s|}\,\bar{\sigma}_i^*(\beta) \tag{3.59b}$$

where

$$\beta = \frac{\omega}{v} \tag{3.60}$$

It should be pointed out that

$$\alpha_{fi} = -\alpha_{ri}^* \tag{3.61}$$

as was determined in Eq. (3.15) based on power conservation arguments if the single gap transmission scattering parameter, S_{23v}^{g1} is exactly unity. Equations (3.59a, 3.59b) also determine $\alpha(x)$ of the COM equations.

Both the analysis and synthesis of SAW devices would be greatly simplified if $\bar{\sigma}_j(\beta)$ were not a function of j ; i.e. if each source weight did not have its own distinctive frequency response. This can easily be done in a periodic array [61,16] of fingers of arbitrary polarity sequence and phasing if $\sigma_j(x)$ is identified with the charge distribution induced in a grounded array by one excited finger, or the charge distribution of one excited gap (see Fig. 3.10). In both cases the frequency response separates into an element factor and an array factor. The array factor is simply the frequency response calculated by the impulse model, with source locations either at the finger centers or gap centers depending on which element factor is being used.

We will denote the unit tap charge distribution $\sigma_t(x)$ and its Fourier transform $\bar{\sigma}_t(\beta)$. Similarly $\sigma_g(x)$ and $\bar{\sigma}_g(\beta)$ will be used for the unit gap element factor. These distributions are related in a simple manner [72]. The linear superposition of the potential distributions of two gaps displaced by one period, p, yields the potential distribution of a tap (see Fig. 3.11). Thus by linearity the same must be true for the charge distributions.

$$\sigma_g(x+\frac{p}{2}) - \sigma_g(x-\frac{p}{2}) \quad = \quad \sigma_t(x) \tag{3.62}$$

On Fourier transforming this equation

$$\bar{\sigma}_g(\beta)e^{-j\beta p/2} - \bar{\sigma}_g(\beta)e^{j\beta p/2} \quad = \quad \bar{\sigma}_t(\beta) \tag{3.63}$$

we obtain the desired relationship

$$\bar{\sigma}_g(\beta) = \frac{\bar{\sigma}_t(\beta)}{-2j\sin(\beta p/2)} \tag{3.64}$$

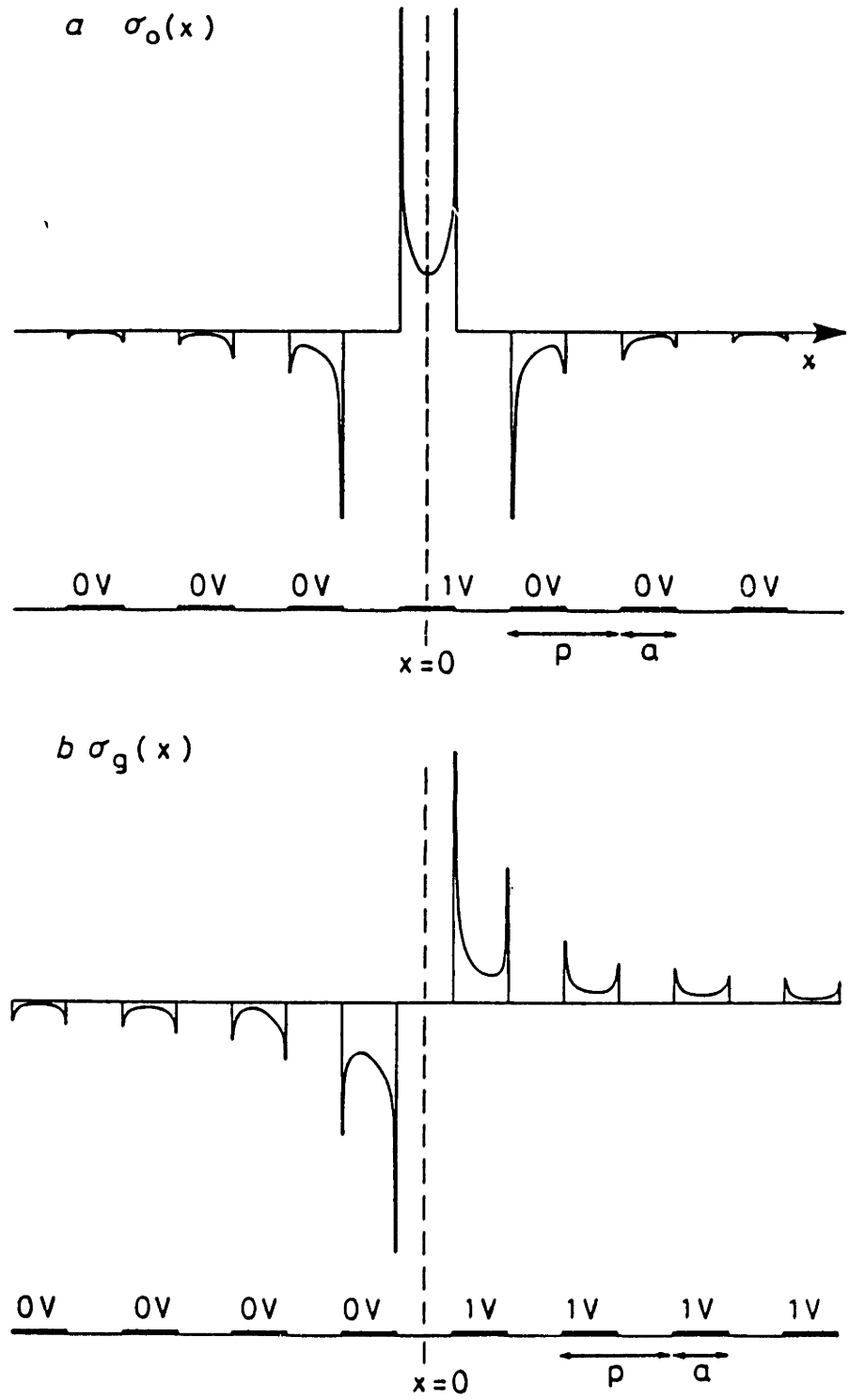

Figure 3.10 Fundamental Charge Density Functions for an Infinite Periodic Array
metalization ratio= a/p =.5 (a) Excitation of one electrode (b) Excitation of one gap
(After [72])

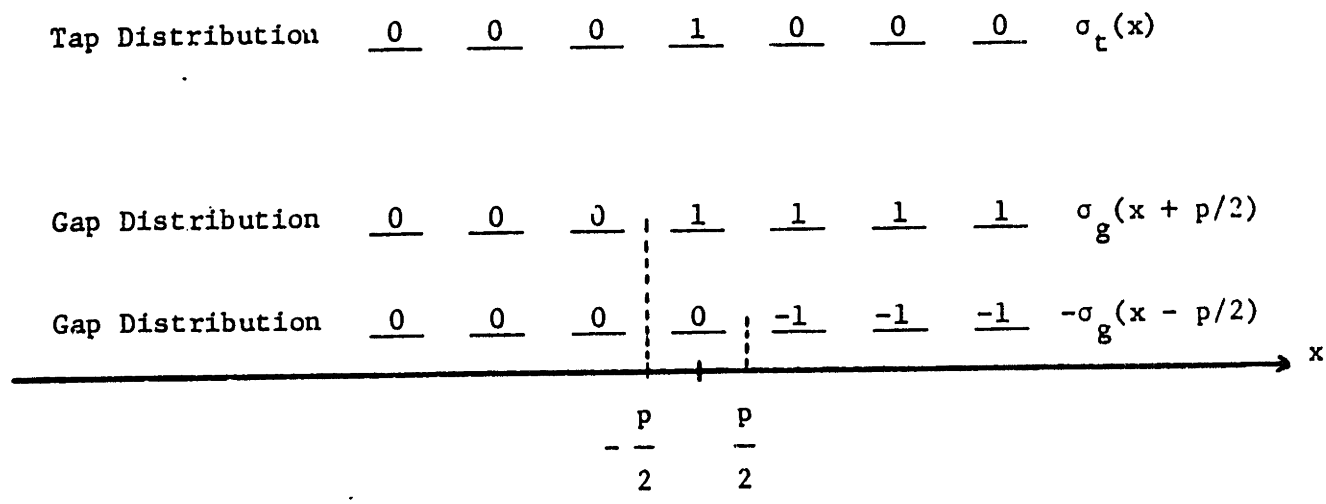

Figure 3.11 Superposition of Two Gaps to Form a Tap
The number above each electrode is its potential.

Using the unit tap charge distribution of Datta [19] , and the fact that $P_{\nu-1} = P_{-\nu}(x)$,

$$\bar{\sigma}_g(\beta) = j(-1)^n(\epsilon_o + \epsilon_p^T)\frac{P_n(\cos\Delta)}{P_{-s_o}(-\cos\Delta)} \tag{3.65}$$

where Δ is proportional to the metalization ration, η ,

$$\eta = a/p \tag{3.66a}$$
$$\Delta = \pi\eta \tag{3.66b}$$

The parameter s_o is the normalized wave number component wrapped back into the first Brillouin zone

$$s = \beta p/2\pi = s_o + n \tag{3.67}$$

$$0 < s_o < 1 \tag{3.68}$$

Thus for standard transducers with $\lambda_o = 2p$, $s = .5f/f_o$ for operation near the fundamental center frequency f_o. In the case of split finger transducers for which $\lambda_o = 4p$, $s = .25f/f_o$ for first harmonic operation. Using Eqs. (3.65, 3.59a, 3.51a, 3.51c), the full frequency dependent transduction coefficient, α_g, to be used in the coupling of modes equations* if the center of transduction is regarded to be a gap is

$$\alpha_g \frac{\lambda_o}{2} = \frac{1}{\sqrt{2}} \sqrt{\omega W((v_m - v_o)/v_m)(\epsilon_o + \epsilon_p^T)}(-1)^n \frac{P_n(\cos\Delta)}{P_{-s_o}(-\cos\delta)} \tag{3.69}$$

In this expression we assume that there is one excited gap every half wavelength at the center frequency. Note that the transduction coefficient is proportional to the electromechanical coupling constant, $\sqrt{2\Delta v/v}$, the square root of the aperture (since the power in the beam is proportional to its width), and $\omega^{1/2}$. Closed form expressions for the capacitance are also available for infinite periodic arrays. The capacitance per longitudinal wavelength for regular and split finger transducers, C_r and C_s are [25]

$$C_r\lambda_o = C_r 2p = W(\epsilon_o + \epsilon_p^T)\frac{P_{-.5}(\cos\delta)}{P_{-.5}(-\cos\delta)} \tag{3.70}$$

$$C_s\lambda_o = C_s 4p = \sqrt{2}W(\epsilon_o + \epsilon_p^T)\frac{P_{-.25}(\cos\delta)}{P_{-.25}(-\cos\delta)} \tag{3.71}$$

Normalized plots of these capacitances are presented in Fig. 3.12.

Presented in Fig. (3.13) are the Fourier transforms of the basic charge distributions for electrode and gap excitations for different metalization ratios. It is important to note that the element factor for gap weighting is much flatter than for electrode weighting, especially near $kp/\pi = .5$, the center frequency of split finger transducers. It is perfectly flat in the limit of an infinitesimal gap, but is reasonably flat for metalization ratios as low as .75.

* For exact agreement with the frequency responses based on the electrostatic field distributions in the low κ limit [73], α_g should be divided by Eq. 3.41 when used in the COM equations.

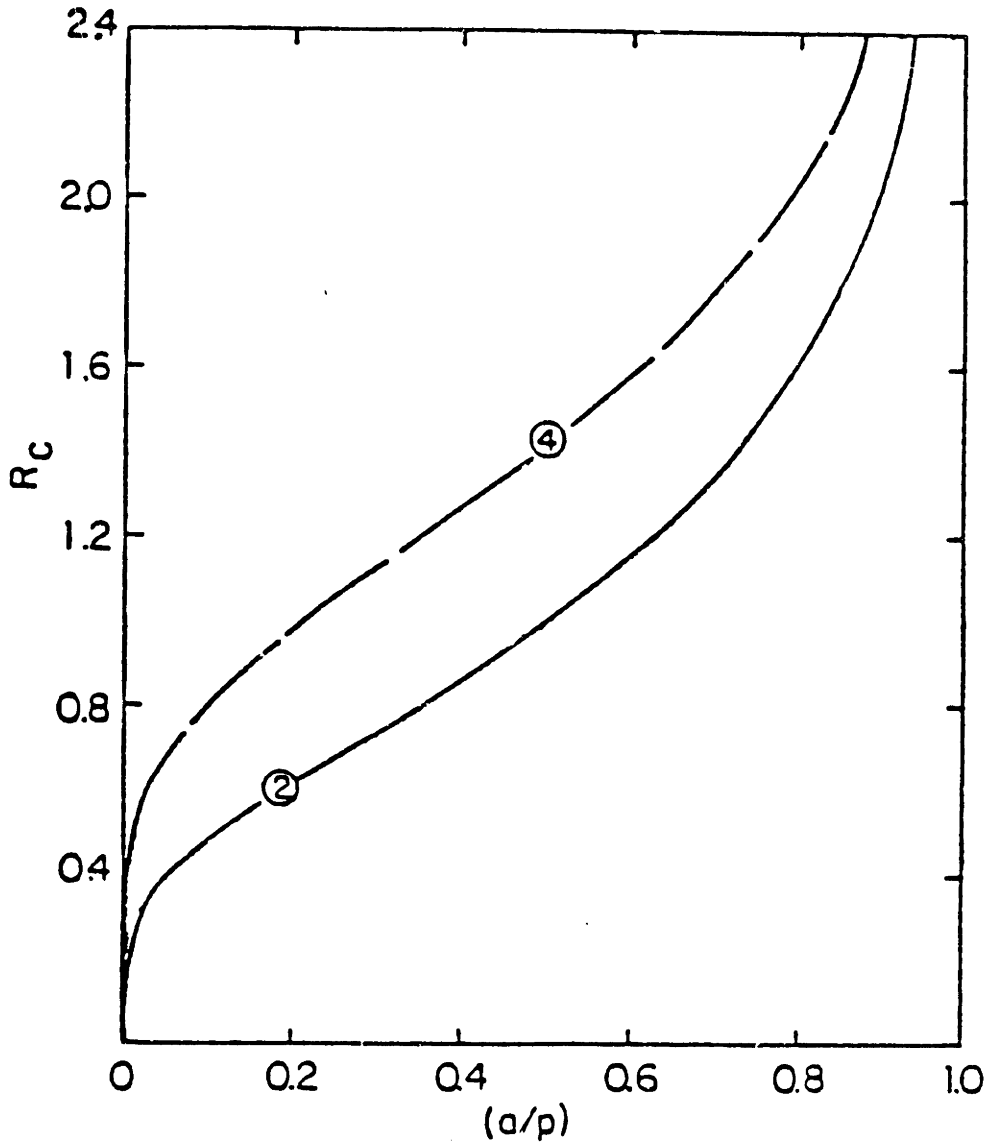

Figure 3.12 Normalized Capacitance
The Curve labeled 2 applies to standard transducers with 2 fingers/wavelength, while the curve labeled 4 applies to split finger transducers with 4 fingers/wavelength. (After [25])

This makes sense since the gap electric field is more localized, and thus more impulse like, thereby making its frequency response flatter. It seems that a high metalization ratio could be helpful in reducing the sensitivity of a SAW filter's source weights to variations local metalization ratio and periodicity. The only penalty incurred in doing this is an increase of the capacitance (see Fig. 3.12) of the IDT relative to its conductance, which reduces the bandwidth over which a match can be achieved.

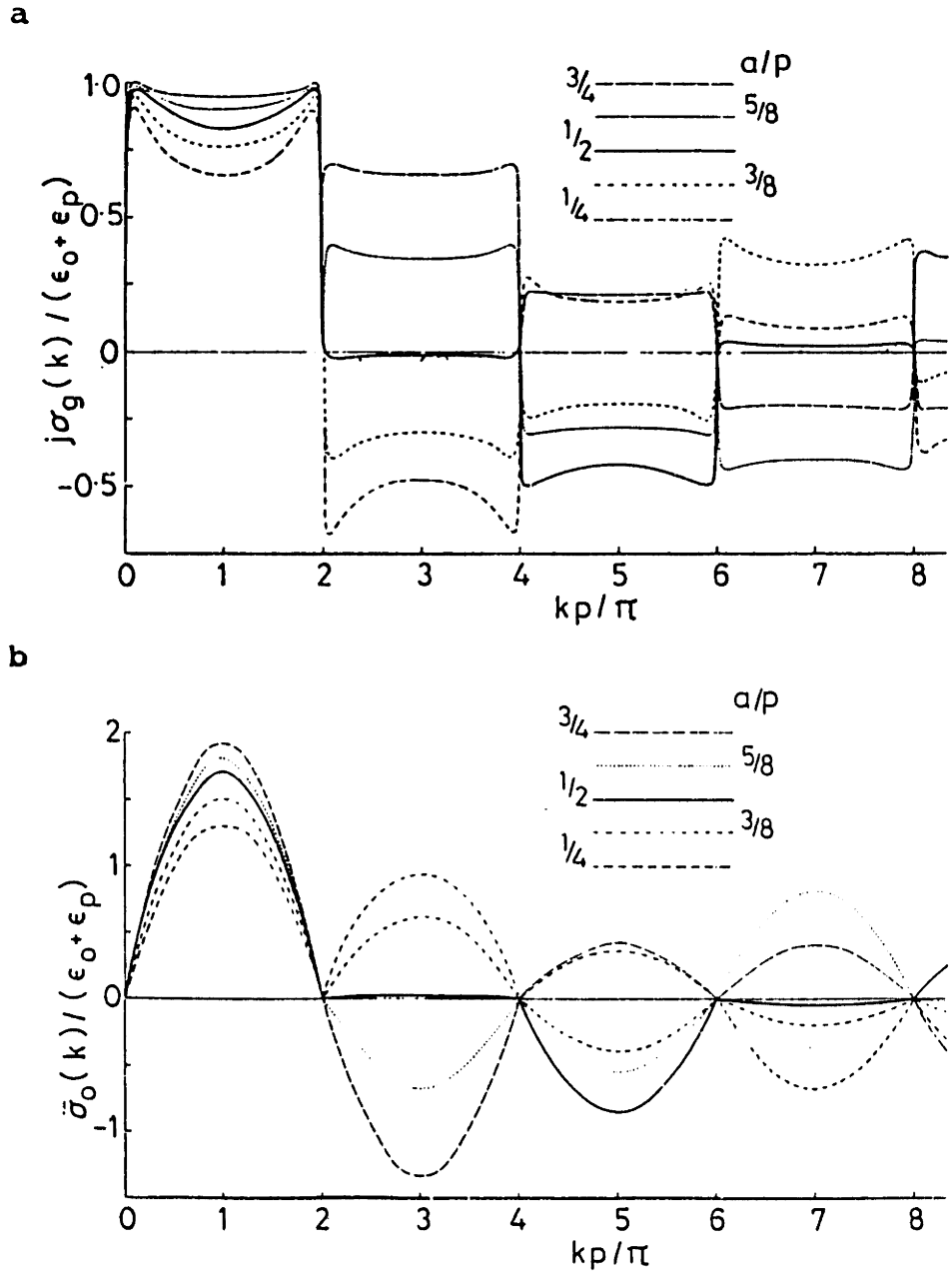

Figure 3.13 Element Factors for One Source in an Infinite Periodic Array
a) Gaps b) Electrodes p = period of the metalization a = width of the metal strips
(After [72])

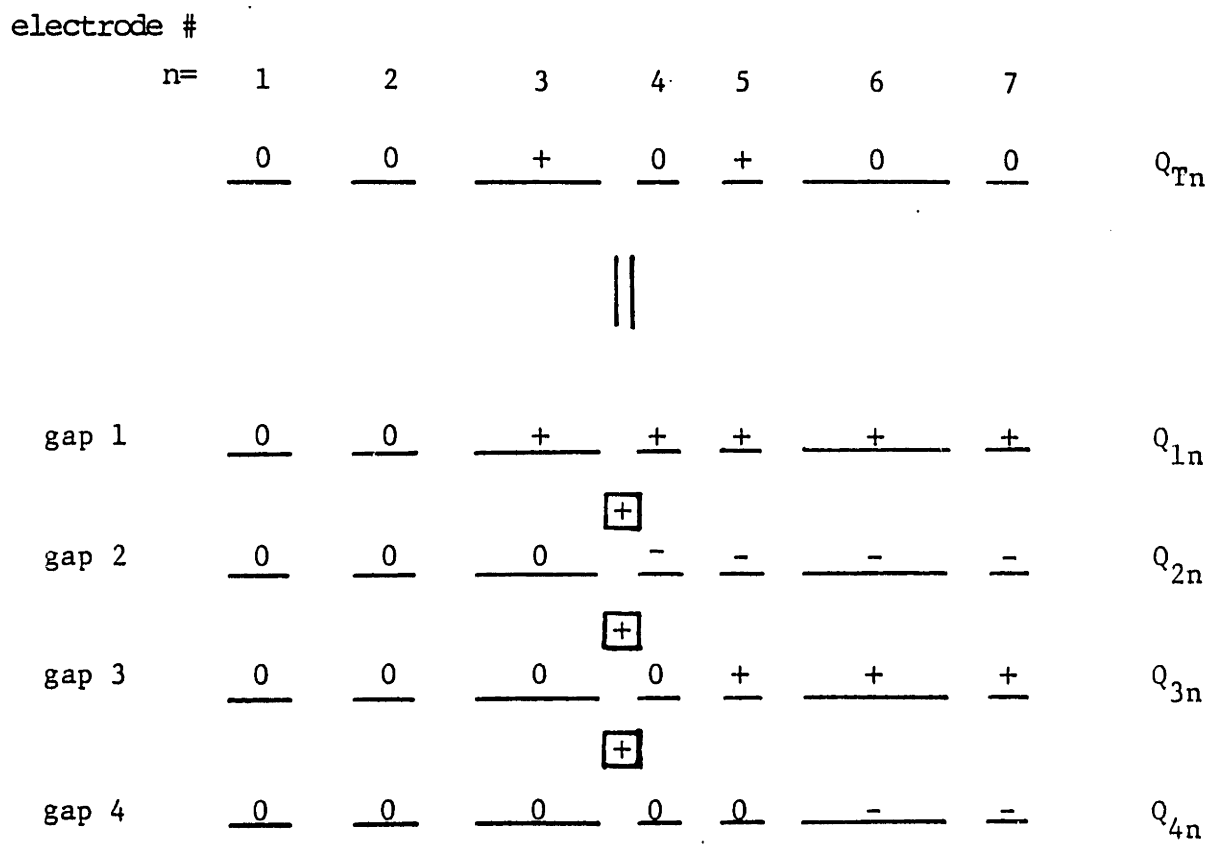

Figure 3.14 Decomposition of a Transducer into Gaps
Q_{Tn} =total charge on the n^{th} electrode under 1-volt excitation Q_{jn} =charge on n^{th} electrode with only the j^{th} gap under 1-volt excitation

Based on this discussion, it seems reasonable to decompose the electrostatic charge distribution of an aperiodic transducer into a superposition of excited gaps (see Fig. 3.14). It is important to note though, that if this decomposition is being done in order to split an IDT into a cascade of sections to be analyzed by the matrix multiplication method or by COM, the capacitance of each section cannot be the capacitance of each gap. This is demonstrated below with reference to Fig. 3.14.

$$C_T = \text{total capacitance} = Q_{T3} + Q_{T5}$$
$$= Q_{13} + Q_{15} + Q_{23} + Q_{25} + Q_{33} + Q_{35} + Q_{43} + Q_{45} \quad (3.72)$$

Defining

$$C_{gi} \triangleq \text{capacitance of the } i^{th} \text{ gap}$$

we find

$$C_{g1} = Q_{13} + Q_{14} + Q_{15} + Q_{16} + Q_{17} \quad (3.73a)$$
$$C_{g2} = -Q_{24} - Q_{25} - Q_{26} - Q_{27} \quad (3.73b)$$
$$C_{g3} = Q_{35} + Q_{36} + Q_{37} \quad (3.73c)$$
$$C_{g4} = -Q_{46} - Q_{47} \quad (3.73d)$$

and note that

$$C_{g1} + C_{g2} + C_{g3} + C_{g4} \neq Q_{T3} + Q_{T5} \quad (3.74)$$

Thus the sum of the gap capacitances is not the capacitance of the transducer. A reasonable and simple way of assigning capacitances based on the gap charges would be:

$$\hat{C}_{g1} = Q_{13} + Q_{15} \quad (3.75a)$$
$$\hat{C}_{g2} = Q_{23} + Q_{25} \quad (3.75b)$$
$$\hat{C}_{g3} = Q_{33} + Q_{35} \quad (3.75c)$$
$$\hat{C}_{g4} = Q_{43} + Q_{45} \quad (3.75d)$$

Now let us acoustically couple two transducers to form a filter. We will reference both 2-port and 3-port scattering matrices (Fig. 3.15). We use the superscript F as in S_v^F and S^F to represent the mixed and standard scattering matrices of a lossy 2-port, which is regarded to be connected to the outside world only through its electrical ports. The corresponding scattering matrix for the two transducers comprising the filter will be denoted with superscript P as in S^{1P} and S^{2P}. Using Eqs. (3.7, 3.8, 3.9) we can find the transfer ratios for the full filter in terms of the single transducer scattering parameters:

$$S_{21}^F = \frac{b_1^2}{a_1^1} = \frac{S_{31}^{2P} S_{21}^{1P}}{1 - S_{22}^{1P} S_{33}^{2P}}$$
$$= \sqrt{Z_{o1} Z_{o2}} \frac{(1 + S_{11}^{1P})(1 + S_{11}^{2P})}{1 - S_{22}^{1P} S_{33}^{2P}} S_{21v}^{1P} S_{31v}^{2P} \quad (3.76)$$

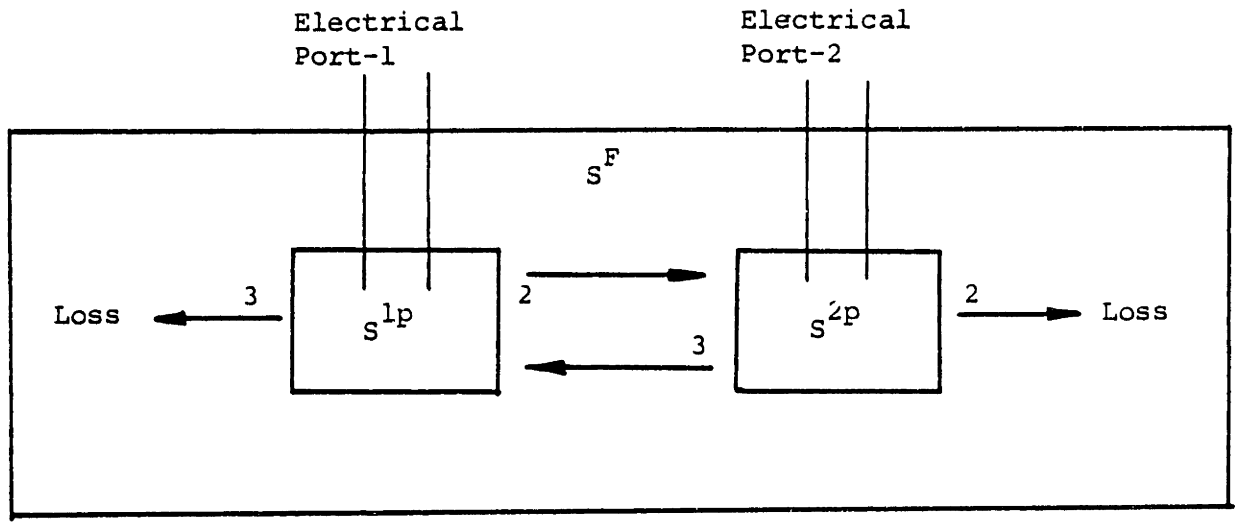

Figure 3.15 A SAW Filter Composed of Two Transducers
S^{1p} and S^{2p} are the 3-port scattering matrices of the two transducers, while S^F is the lossy 2-port scattering matrix of the electrical ports of the full filter

Since a bi-directional IDT must be matched such that the load approximates a short circuit in order to avoid triple transit problems, the acoustic port reflection coefficients, S_{22}^{1P} and S_{33}^{2P} will be quite small. In the case of a SPUDT these reflection coefficients are small even if the device is matched. Thus for both a standard BIDT and a SPUDT under their usual operating conditions,

$$S_{21}^F \approx \sqrt{Z_{o1}Z_{o2}}(1+S_{11}^{1P})(1+S_{22}^{2P})S_{21v}^{1P}S_{31v}^{2P} \tag{3.77}$$

The electrical return losses, S_{11}^{1P} and S_{22}^{2P} can be computed once the transducer's input admittance is found. The conductance is found from Eq. (3.11a) and its Hilbert transform (Eq. (3.21)) determines the radiation susceptance, jB. The capacitance must be determined separately.

$$Y = G + jB + j\omega C \tag{3.78a}$$

$$Y_n = YZ_o \tag{3.78b}$$

$$S_{11}^P = \frac{1-Y_n}{1+Y_n} \tag{3.78c}$$

It should be noted that $1 + S_{11}$ is a relatively slowly varying function of frequency. The dominant factors of Eq. (3.77) controlling the frequency response are S^{1P}_{21v} and S^{2P}_{31v}. If the sources of the input transducer are at x_j, while those of the output transducer are at y_j, then using Eqs. (3.58a, 3.58b)

$$S^{1P}_{21v}S^{2P}_{31v} = -\frac{\omega W G_s}{4}\left[\sum_i \bar{\sigma}^1_i(\beta)\, e^{j\beta x_i}\right]\left[\sum_k \left[\bar{\sigma}^2_k(\beta)\right]^* e^{-j\beta y_k}\right] \tag{3.79}$$

If the transducers are exactly periodic, and a few zero weight sources are added to the ends of each IDT so that the environment of each source is the same, then as we saw earlier in the section, $\bar{\sigma}_i(\beta)$ is no longer a function of i. The expression then simplifies to

$$S^{1P}_{21v}S^{2P}_{31v} = -\frac{\omega W G_s}{4}|\bar{\sigma}_o(\beta)|^2\left[\sum_i S^1_i e^{j\beta x_i}\right]\left[\sum_k S^2_k e^{-j\beta y_k}\right] \tag{3.80}$$

where S^1_j and S^2_k are the strengths of the sources in the two transducers. The frequency response has factored into the product of 2 array factors with the element factor

$$E(\omega) = -\frac{\omega W G_s}{4}|\bar{\sigma}_o(\beta)|^2 \tag{3.81}$$

If the two transducers are only slightly aperiodic, then it is unreasonable to expect that the full complexity of Eq. (3.79) will be required. More likely, the basic charge distribution, $\sigma_o(x)$, which is valid if the finger period is p_o, will simply scale to

$$\sigma_i(x) = \frac{p_o}{p_i}\sigma_o\left(\frac{p_o}{p_i}x\right) \tag{3.82}$$

in a region where the local periodicity is p_i. The scale factor out front, p_o/p_i, serves to keep the total charge on each electrode constant. This is necessary for consistency with

the known solution to Laplace's equation in which the capacitance between strips in a periodic metal grating is independent of the period [24,2] . The Fourier transform of this element factor is then

$$\bar{\sigma}_i(x) \quad = \quad \bar{\sigma}_o\left(\beta\frac{\beta_o}{\beta_i}\right) \tag{3.83}$$

where β_i is the local synchronous propagation, $2\pi/\lambda_i$.

The Fourier transform of the gap charge distribution (see Fig. 3.10), $\bar{\sigma}_g(\beta)$, is plotted in Fig. 3.16 using the formula derived by Datta and Hunsinger [19] . Note that for split finger transducers, over a very broad 300% fractional bandwidth about the center frequency, the plot is very nearly linear. Since log-log coordinates were used, this implies that

$$\bar{\sigma}_o(\beta) \quad = \quad c\beta^q \tag{3.84}$$

In the particular example shown which is for gaps with a 50% metalization ratio, q is $-.081$.

Therefore Eq. (3.79) can also be simplified if the spacing is almost periodic:

$$S_{21v}^{1P}S_{31v}^{2P} \quad \approx \quad -\frac{\omega W G_s}{4}\ |\bar{\sigma}_o(\beta)|^2\left[\sum_i S_i^1\left(\frac{\beta_0}{\beta_i}\right)^q e^{j\beta x_i}\right]\cdot \left[\sum_k S_k^2\left(\frac{\beta_0}{\beta_k}\right)^q e^{-j\beta y_k}\right] \tag{3.85}$$

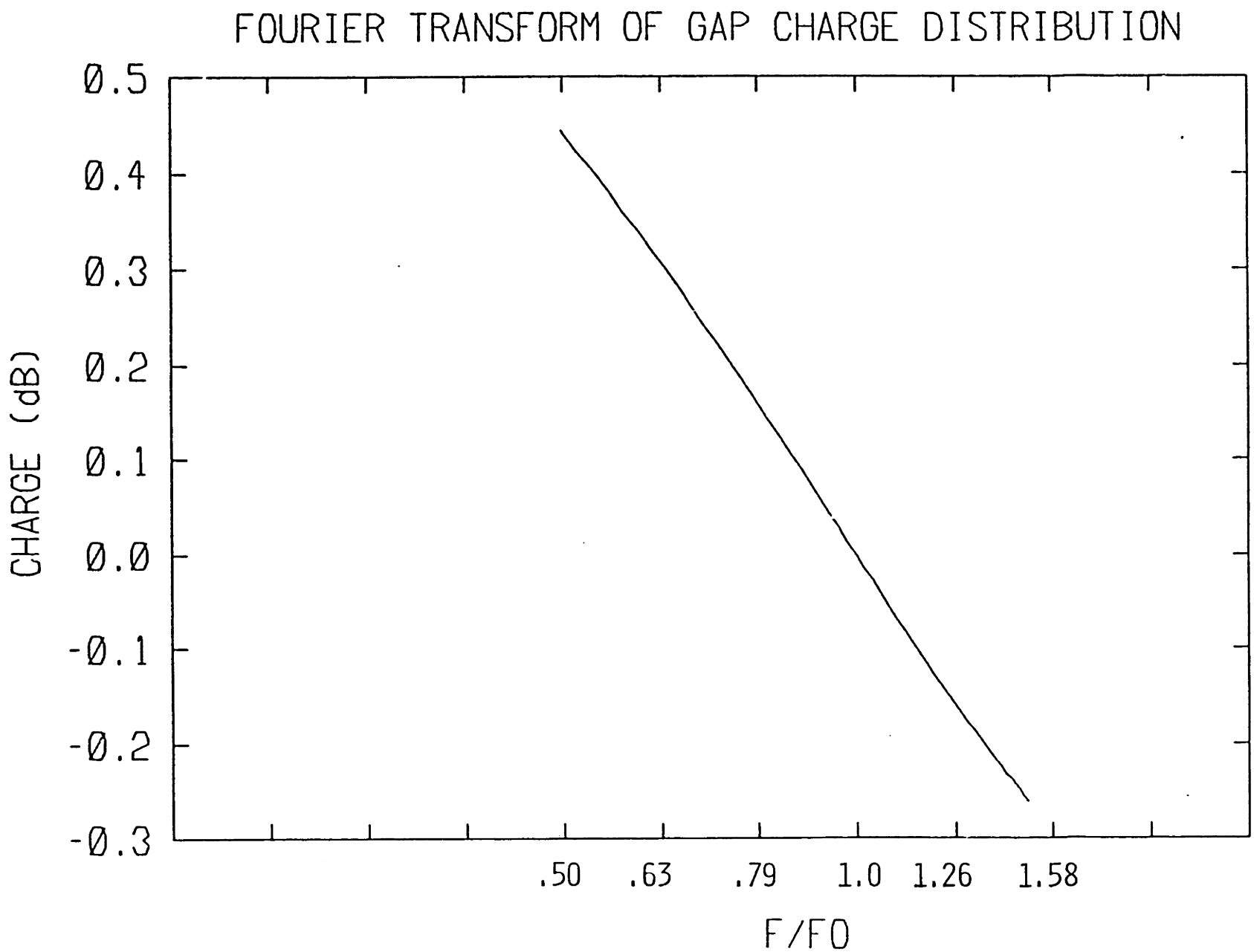

Figure 3.16 Fourier Transform of Gap Charge Distribution
(Normalized to the value at f_o.) Metalization ratio=50% f_o =center frequency for a split finger transducer Note that the curve is almost linear over a 300% fractional bandwidth.

3.9.2 Survey of Reflector Analyses

Since all SAW devices consist of combinations of metallic, dielectric and groove gratings, a tremendous amount of work has been done on their scattering properties. The reflection and transmission coefficients have two components, 1) a piezoelectric one, due to radiation by the charges induced by the incident wave on the metallic grating; and 2) a mechanical one due to radiation by the induced stresses. The former is proportional to the piezoelectric coupling constant, $2\Delta v/v$, and the later is proportional to the height of the surface perturbation. Most of this radiation is into forward and backward SAW waves but some is also radiated into the bulk at frequencies above Bragg [54].

Joshi and White [55], Aoki and Ingebrigtsen [2] and Datta and Hunsinger [17] all studied the electrical component of the reflection, ignoring the mechanical contribution due to the physical electrodes. The first two papers based their analyses on determining the dispersion diagrams for wave propagation along a grating, with the reflection coefficients near Bragg and its multiples being related to the size of the gap. Datta and Hunsinger used a perturbational approach to directly calculate the reflection and transmission coefficients. All the papers focused on periodic gratings. If information about aperiodic gratings is desired, it could be done by combining the electric field computational technique of Hartmann [39] with Morgan's [73] Green's function approach in a self-consistent manner.

None of these authors present any experimental results, but Panasik and Hunsinger [77] use the results of Datta and Hunsinger [17] to compute the acoustic reflection coefficients from 20 finger-pair aluminum IDT's on Y-Z lithium niobate. Their calculation actually includes mechanical effects, but due to the very high piezoelectric coupling constant of lithium niobate, the overwhelming reflection effect should be electrical in origin. Their phase calculations agree very well with experiment, but the magnitude of the calculated

short circuit reflection coefficient is 35% higher than the experimental one. In the open circuited case, theory exceeds experiment by 75%.

Skeie [97] takes into account both piezoelectric effects and mechanical loading effects to lowest order. He relates velocity shifts and reflection coefficients to changes in energy caused by the surface wave perturbations. Skeie checks his theoretical calculations by focusing on the input conductance and susceptance which are affected both by transduction and a transducer's internal reflections. One IDT consists of twenty 1500 Å aluminum electrodes on Y-Z lithium niobate (which is very thick since $h/\lambda = 2.5\%$ at $f_o = 575$ MHz). The calculated and measured conductances agree perfectly, while the calculated susceptance is smaller than the measured values by about 5–15%. The author attributes the discrepancy in the susceptance to parasitic capacitance caused by the interdigital fingers and bonding pads in the measuring circuit.

Skeie then introduced additional mass loading with a 750 Å ($h/\lambda = 1.2\%$) gold layer deposited on top of the aluminum electrodes. This slowed the wave by about 4.0% relative to the IDT with aluminum fingers alone. The theoretically predicted slowing was only 2.7–3.0%, depending on whether the metal films are assumed to retain their bulk mechanical properties or act like fluids with no shear moduli. The conductance was overestimated by about 40% while the susceptance was underestimated by 30%.

Datta and Hunsinger [15,17,18] analyze periodic gratings in three papers, the first covering scattering caused by mechanical effects of order (h/λ), the second covering electrical effects, and finally the third studies second order mechanical effects $O((h/\lambda)^2)$. All the analyses apply to gratings made from arbitrary anisotropic media deposited on arbitrary anisotropic crystals. The first order mechanical analysis is done for all frequencies via Auld's coupled mode equations [4], with an added impulse source term at the grating

edges. The second order analysis is done by a normal mode perturbation theory [4] and applies only at integer multiples of the Bragg frequency. There is a contradiction between this analysis and Wright's [114] analysis of second order effects in grooved gratings on isotropic substrates. Wright shows that the second order reflection and velocity shift coefficients are logarithmically divergent if the grating sidewalls are perfectly vertical, whereas Datta claims to find the same coefficients for this grating with no problem. The piezoelectrically generated reflection and transmission coefficients are computed in the standard way by first finding the charge induced in the array by the incident acoustic wave, and then computing the forward and backward wave radiated by this charge distribution.

Panasik and Hunsinger [77] combined the results of all three of the above papers with Datta's papers on transduction [16,19] (similar to Morgan [73,72]) to obtain a complete model of arbitrarily connected metal strips of uniform overlap on a piezoelectric substrate. They use their theory to compute the input conductance of the same 20-electrode IDT on lithium niobate that Skeie [97] analyzed. In the first case, the fingers consisted of 1500 Å of aluminum (h/λ = 2.5%). Their calculated conductance exceeded the experiment by 35% whereas Skeie's analysis was in perfect agreement with theory. On the same transducer, with an additional 750 Å of gold to increase the mechanical component of the transducer's internal reflections, Panasik overestimated the conductance by about 80% while Skeie was high by only 35%.

The final transducer that Panasik analyzed was a 20 wavelength transducer on Y-Z lithium niobate with 4 fingers per wavelength, of which every other one was floating. The computed short-circuit reflection coefficient overestimated the reflection by about 55% while the open-circuited reflection was overestimated by about 115%.

Recently Chen and Haus [11] developed a model of an IDT that includes transduction in addition to reflection due to both piezoelectric and purely mechanical effects. It is based on a single variational expression from which the coupled mode equations are derived along with the reflection and transduction parameters. Elastically everything is treated isotropically, but the full piezoelectric tensor is used. Its agreement with previously published experimental results is truly impressive for aluminum films on both ST-X quartz and Y-Z lithium niobate.

In the case of gold films on ST-X quartz, the calculation is higher than the experimental result by about 55%. Unfortunately, we would like to use gold overlays for SPUDT's due to the high reflection coefficients which can be obtained with relatively thin films.

3.9.3 Summary—Transduction and Reflection

In summarizing the theoretical state of the analysis of SAW devices, we note that piezoelectric transduction effects are very well modeled [69,70], and that good simplified analysis techniques exist [11,73,81,16,19,25].

In the case of reflectors the situation is different. If the reflection is mainly piezoelectric in origin, then models exist which agree well with experiment. In the case of deposited films however, discrepancies between theory and experiment still exist. Thus it is probably best to experimentally measure reflection coefficients.

It is possible that part of the discrepancy is due to an inaccurate characterization of the mechanical properties of thin films. The mechanical properties of thin films may be different from those of the bulk material and may depend on the way in which the films are deposited.

3.9.4 Loss

Until now loss has been ignored for simplicity. If the loss is very small then it can be introduced rather simply. Resistive loss can be added by placing resistors in series with the leads to each element of a lossless model and in series with the bus bars connecting the elements (see Fig. 3.17). The bus bar resistors would simply be twice the resistance of the portion of a bus bar connecting two sections to one another in order to account for the upper and lower bus bars.

If the dominant component of the input admittance of a finger is capacitive, the current flowing along a finger will be linear with position along a finger. Even in the case of strongly piezoelectric materials such as lithium niobate, the capacitive admittance of one finger pair dominates its acoustic radiation conductance. A more general analysis of a distributed RC transmission line by Lakin [58] confirms that the current distribution is linear unless the loss is extremely large. Thus using the definitions of Fig. 3.18, the total

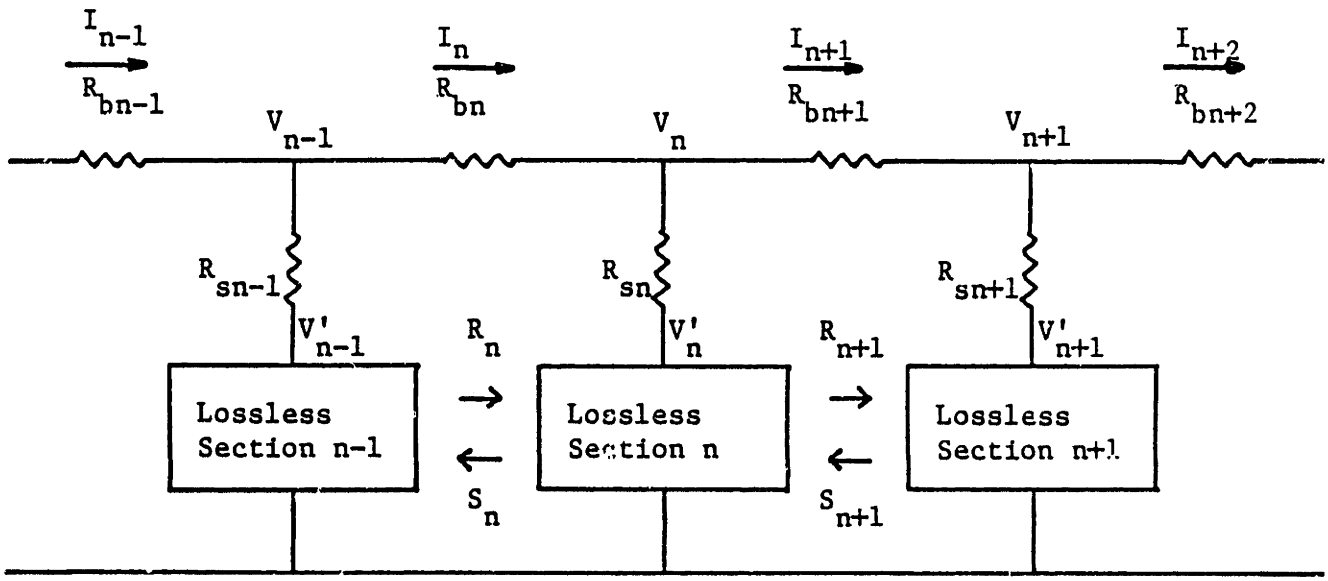

Figure 3.17 Addition of Resistive Loss to a Lossless Model
R_{sn} = equivalent series finger resistance R_{bn} = bus bar resistance

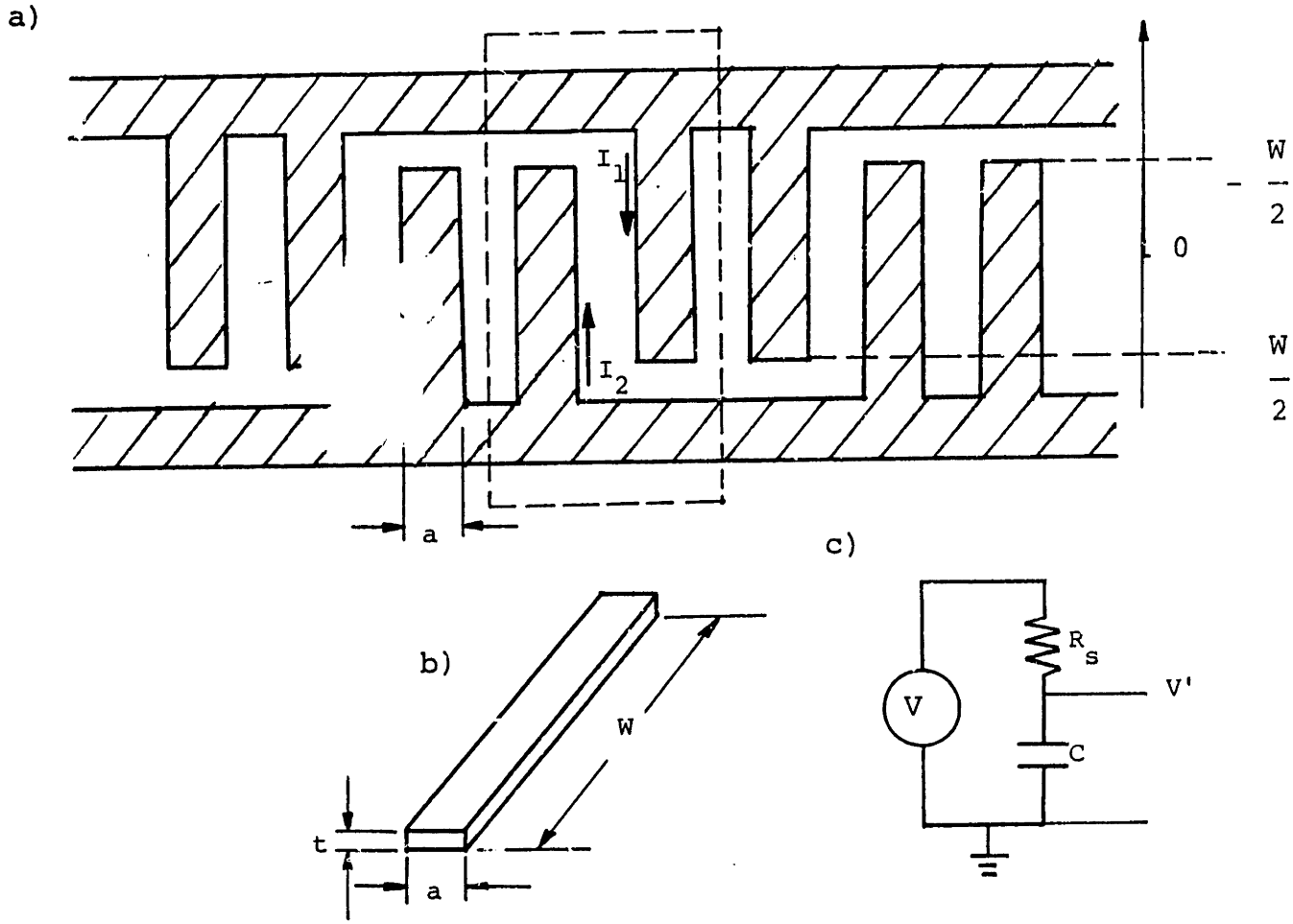

Figure 3.18 Loss Analysis of a Transducer
a) One finger pair for which loss is being calculated b) One finger of the transducer c) Equivalent circuit of one section for the loss analysis

electrode currents transverse to the direction of SAW propagation are:

$$I_1(z) = I_o(.5 - z/W) \tag{3.86a}$$

$$I_2(z) = I_o(.5 + z/W) \tag{3.86b}$$

We assume that the current is uniformly distributed along the width of a finger and equate the power dissipated in the equivalent series resistance, R_s of Fig. 3.18c, with the power dissipated in the distributed resistance.

$$I_o^2 R_s = R_l \int_{-W/2}^{W/2} [I_1^2(z) + I_2^2(z)]\, dz \tag{3.87}$$

and we obtain

$$R_s = \frac{2}{3} W R_l \tag{3.88}$$

where R_l is the resistance per unit length along a finger

$$R_l = \rho/(at) = \rho_s/a \tag{3.89a}$$
$$\rho = \text{bulk resistivity} \tag{3.89b}$$
$$\rho_s = \rho/t = \text{sheet resistance} \tag{3.89c}$$

The final result is the same as Lakin's [58] in the low sheet resistivity limit.

When finite sheet resistance fingers are used, the gap voltage depends on the transverse position, z. Using Eqs. (3.86a, 3.86b) and the input admittance of the equivalent circuit of Fig. 3.18c, this gap voltage

$$\Delta V(z) = \frac{V}{1 + j\omega R_s C}[1 + j\omega R_s C(-\frac{1}{8} + \frac{3}{2}\frac{z^2}{w^2})] \tag{3.90}$$

The total short circuit signal current received by an ideal gap is proportional to

$$\int_{-W/2}^{W/2} \Delta V(z)\, dz = \frac{VW}{1 + j\omega R_s C} \tag{3.91}$$

Note that V' of Fig. 3.18c

$$V' = \frac{V}{1 + j\omega R_s C} \tag{3.92}$$

If V' is assumed to be the uniform voltage across the transmitting gap, the received signal will be identical to that of Eq. (3.91). Thus if we choose the equivalent series resistance

of the circuit model to equalize the received signal, we obtain exactly the same answer as by equalizing the power dissipated.

Propagation loss can be handled by changing the propagation constant $\mp j\beta$ to $\mp j\beta \mp \gamma$. It should be noted that if both bus bar and finger resistive losses are included in addition to propagation loss, all 16 elements of the transmission matrix (Eq. (3.23)) become non-zero, whereas if bus bar loss is ignored, the same 5 terms which are zero in the absence of loss remain zero. Thus significant computation time can be saved if bus bar loss is ignored. There really is no reason to include bus bar loss in a synthesis algorithm since the bus bars can simply be made both wide and thick enough for this form of loss to be totally negligible.

We now illustrate this procedure for the COM equations (3.36a–3.36c). We also make use of Eqs. (3.35a, 3.35b) which were derived based on power conservation, since we shall assume the transducers and perturbations themselves to be lossless. All the loss is being lumped in the propagation path between the elements and in resistors in series with the fingers. We include propagation loss via the γ term and finger loss by redefining the voltage exciting the waves to be V', the voltage across the lossless equivalent fingers of Figs. (3.17, 3.18). The result is:

$$\frac{d\hat{R}}{dx} = -\gamma\hat{R} + \kappa(x)e^{j2\beta x}\hat{S}(x) + \alpha(x)e^{j\beta x}V' \qquad (3.93a)$$

$$\frac{d\hat{S}}{dx} = \gamma\hat{S} + \kappa^*(x)e^{-j2\beta x}\hat{R}(x) + \alpha^*(x)e^{-j\beta x}V' \qquad (3.93b)$$

$$\frac{dI}{dx} = -j\omega C(x)V' - 2\alpha^*(x)e^{-j\beta x}\hat{R} + 2\alpha(x)e^{j\beta x}\hat{S} \qquad (3.93c)$$

$$V'(x) = V + \frac{1}{G}\frac{dI}{dx} \qquad (3.93d)$$

Equation (3.93d) is simply Kirchoff's voltage law expressed in differential form. The conductance is defined so that

$$R_s = \frac{1}{G(\lambda_o/2)} \tag{3.94}$$

where R_s is the equivalent series resistance of a finger pair (Eq. 3.88). It should be noted that with this definition G is a function of x, just like κ, α and C. $V'(x)$ can be eliminated from Eqs. (3.93a–3.93d), to obtain the final form for the coupled mode equations in the presence of both propagation loss and finger resistance loss:

$$\frac{d\hat{R}}{dx} = -\left(\gamma + \frac{2|\alpha|^2}{G+j\omega C}\right)\hat{R} + \left(\kappa + \frac{2\alpha^2}{G+j\omega C}\right)e^{j2\beta x}\hat{S} + \frac{\alpha}{1+\frac{j\omega C}{G}}e^{j\beta x}V \tag{3.95a}$$

$$\frac{d\hat{S}}{dx} = \left(\gamma + \frac{2|\alpha|^2}{G+j\omega C}\right)\hat{S} + \left(\kappa^* - \frac{2(\alpha^*)^2}{G+j\omega C}\right)e^{-j2\beta x}\hat{R} + \frac{\alpha^*}{1+\frac{j\omega C}{G}}e^{-j\beta x}V \tag{3.95b}$$

$$\frac{dI}{dx} = -\frac{j\omega C}{1+\frac{j\omega C}{G}}V - \frac{2\alpha^*}{1+\frac{j\omega C}{G}}e^{-j\beta x}\hat{R} + \frac{2\alpha}{1+\frac{j\omega C}{G}}e^{j\beta x}\hat{S} \tag{3.95c}$$

Note that these equations are of the same form as the lossless COM Eqs. (3.36a–3.36c). A major difference is that the effective forward and reverse reflection coefficients, κ_{eff1} and κ_{eff2}

$$\kappa_{eff1} = \kappa + \frac{2\alpha^2}{G+j\omega C} \tag{3.96a}$$

$$\kappa_{eff2} = \kappa^* - \frac{2(\alpha^*)^2}{G+j\omega C} \tag{3.96b}$$

are no longer complex conjugates of one another as required by power conservation (see Eq. 3.35a). This, of course, is to be expected since we have introduced loss into the model. Similarly the effective forward and reverse transduction coefficients, α_{eff1} and α_{eff2} are

not complex conjugates when loss is added (see Eq. 3.35b).

$$\alpha_{eff1} = \frac{\alpha}{1 + j\omega C/G} \tag{3.97a}$$

$$\alpha_{eff2} = \frac{\alpha^*}{1 + j\omega C/G} \tag{3.97b}$$

Waves now attenuate as they propagate due to both acoustic loss and electrical resistive loss. The effective attenuation constant is

$$\gamma_{eff} = \gamma + \frac{2|\alpha|^2}{G + j\omega C} \tag{3.98}$$

Finally, the admittance term of Eq. (3.95c) is no longer purely capacitive*:

$$Y_{eff} = \frac{j\omega C}{1 + j\omega C/G} \tag{3.99}$$

* Clearly the input admittance of a lossless transducer is not purely capacitive, however any real component of Y_{eff} can be shown to be a source of loss in the COM approximation. The full input admittance of an IDT can only be obtained by solving Eqs. (3.95a-3.95c) for $I(0)/V$, and is not only Y_{eff}.

CHAPTER 4

SYNTHESIS OF SINGLE-PHASE UNIDIRECTIONAL TRANSDUCERS

4.1 Introduction

It may be possible to design a single-phase unidirectional transducer (SPUDT) directly from a matrix multiplication model, or based on the full coupling-of-modes (COM) equations. It would certainly be much easier if the synthesis could be based on the impulse transduction and reflection model, or equivalently on the iterated integral approximate solution to the COM equations. This is possible only if the reflectivity of the grating is low.

Therefore, in this chapter we first investigate the reflectivity required to build a SPUDT. We find that reasonably low reflectivity can yield interesting SPUDT's. Then we use the zeroth order Fourier transform relations between α and the transduction response, and between κ and the reflection response to synthesize a few SPUDT's as does Wright [115]. Finally we compare the responses based on this simple approximation with the exact solution based on the COM equations.

Ideally we would like our SPUDT to be matched at the electrical port in addition to the front acoustic port. Unfortunately, as pointed out by Wright [115], this generally is not possible for a lossless reciprocal 3-port. The scattering matrix would be restricted to be of

the following form:

$$S^P = \begin{bmatrix} 0 & e^{j\theta} & 0 \\ e^{j\theta} & 0 & 0 \\ 0 & 0 & 1 \end{bmatrix} \tag{4.1}$$

where superscript P is used to denote the scattering matrix one transducer of a filter.

This is exactly what is desired in the passband. In the transition and rejection bands, however, we must either give up perfect triple transit suppression or the electrical match. If we choose to give up only the electrical match, then reciprocity and power conservation (Eqs. 3.10a–3.10f) impose the following conditions:

$$|S_{21}^P| = \sqrt{1 - |S_{11}^P|} \tag{4.2a}$$

$$|S_{31}^P| = \sqrt{|S_{11}^P|(1 - |S_{11}^P|)} \tag{4.2b}$$

Using Eq. (3.9d) the required value for the short circuit front acoustic port reflection coefficient, S_{22v}^P, in order to obtain infinite triple transit suppression is

$$S_{22v}^P = \frac{-[S_{21}^P]^2}{1 + S_{11}^P} \tag{4.3}$$

This is the condition under which the shorted grating reflection, S_{22v}^P, exactly cancels the regenerated signal. At synchronism, the coupled-mode equations can be solved in closed form for the reflection coefficient if there is no chirping [57] :

$$|S_{22v}^P| = tanh\left(\int_{-\infty}^{\infty} |\kappa(x)|\, dx\right) \tag{4.4}$$

We can now show how the performance of an unchirped SPUDT depends on the grating reflection coefficient. For comparison purposes, we also present the triple transit

suppression of a standard bi-directional IDT with the same insertion loss as a SPUDT which we obtain below.

First we assume that $|S_{31}^P| = |S_{21}^P|$, as is the case for any transducer with no short circuit reflection coefficient, such as a split finger transducer. This can clearly be seen from Eqs. (3.36a, 3.36b, 3.42a, 3.42b). As long as κ is zero, the R and S waves can be obtained in closed form as the integral of functions which are complex conjugates of one another. Now that $|S_{31}^P| = |S_{21}^P|$, Eq. (3.10a) implies that

$$|S_{11}^P|^2 = 1 - 2|S_{21}^P|^2 \tag{4.5}$$

Using the fact that κ is zero, Eq. (3.9d) implies that

$$S_{22}^P = \frac{[S_{21}^P]^2}{1 + S_{11}^P} \tag{4.6}$$

Using Eqs. (4.5, 4.6) we obtain

$$|S_{22}^P| = \frac{1 - |S_{11}^P|^2}{2|1 + S_{11}^P|} \tag{4.7}$$

which is clearly minimized when S_{11}^P is real and positive as occurs when the transducer is matched on the short circuit side. Thus

$$|S_{22}^P|_{\min} = \frac{1 - |S_{11}^P|^2}{2(1 + |S_{11}^P|)} = \frac{|S_{21}^P|^2}{1 + \sqrt{1 - 2|S_{21}^P|^2}} \tag{4.8}$$

This is a general derivation of a formula which was first obtained by Smith et. al. [101] for symmetric transducers using a particular equivalent circuit model.

The above results are summarized in graphical and tabular form in Fig. 4.1. We note that in the limit of perfect unidirectionality, the required short circuit reflection coefficient goes to unity, and thus integrated κ approached infinity. If we allow for a moderate insertion loss of 6 dB, we only need a reflection coefficient .33, and the required integrated κ is .35. These two numbers are approximately the same in this case, indicating that we are in the regime in which Eq. (4.4) can be approximated as

$$|S^P_{22v}| \approx \int_{-\infty}^{\infty} |\kappa(x)|\, dx \tag{4.9}$$

This corresponds to the situation in which multiple reflections can be ignored and only the first terms of Eqs. (3.44a, 3.44b) are necessary. Although we are getting as much as 6 dB insertion loss in this situation, which is also obtainable with a standard bi-directional IDT, it should be noted that the BIDT would only have 12 dB of triple transit. The SPUDT ideally would have infinite triple transit suppression.

4.2 A Simple Design Algorithm

A simple synthesis technique can be based on the lowest order of Fourier transform relations between S^P_{21v} and $\alpha(x)$, and between S^P_{22v} and $\kappa(x)$ [115]. Keeping only the lowest order terms, Eqs. (3.42a, 3.44a) reduce to

$$S^P_{21v} = \int_{-\frac{L}{2}}^{\frac{L}{2}} du\, \alpha(u) e^{j\beta u} \tag{4.10a}$$

$$S^P_{22v} = \int_{-\frac{L}{2}}^{\frac{L}{2}} du\, \kappa(u) e^{j2\beta u} \tag{4.10b}$$

$\lvert S_{11}^P \rvert$	$\lvert S_{21}^F \rvert^2$ Forward IL (dB)	$\lvert S_{31}^F \rvert^2$ Reverse IL (dB)	Required S_{22V}^P	Required $\int K$	$\lvert S_{22}^P\text{-BIDT} \rvert^2$ Triple Transit Level of Standard IDT of Same IL (dB)
.2	- 1.93	-15.9	.67	.80	--
.5	- 6	-12	.33	.35	-12
.82	-14.9	-16.6	.099	.099	-40

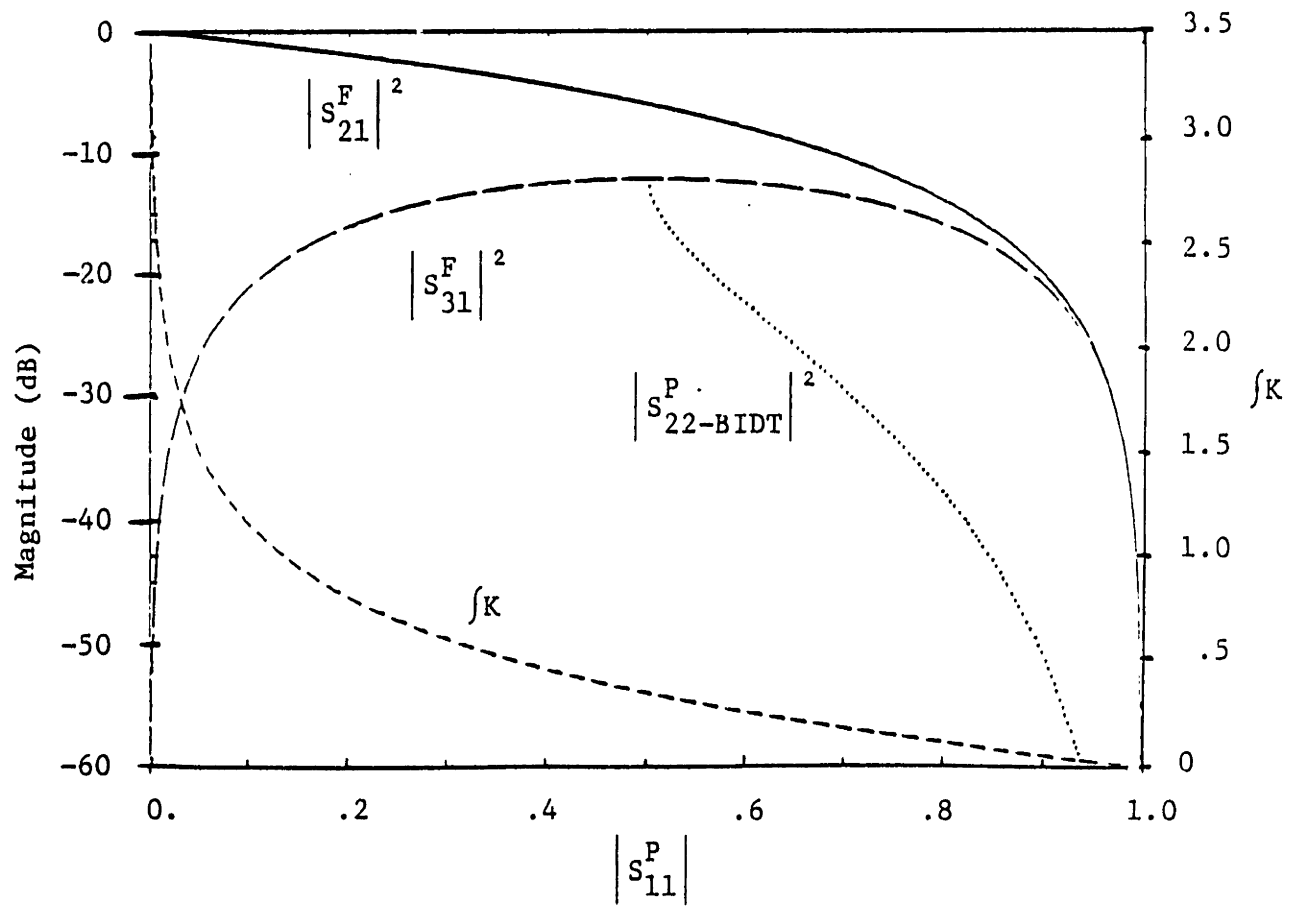

Figure 4.1 Three Port Scattering Parameter Relationships for SPUDT'S with Infinite Triple Transit Suppression

Under this approximation, which would be valid only in the limit of small κ, the voltage to acoustic transfer function, S^P_{21v}, is solely determined by $\alpha(x)$, and similarly only $\kappa(x)$ enters into the calculation of the short-circuit reflection coefficients. We really are only interested in the transfer function and acoustic reflection coefficients when the effects of the matching circuit are included. However, since Eqs. (4.10a, 4.10b) provide simple solutions only when there is no matching circuit, we use Eqs. (3.9b, 3.9d), which are repeated below to make the connection.

$$S^P_{21v} = \frac{S^P_{21}}{\sqrt{Z_o}(1+S^P_{11})} \tag{4.11a}$$

$$S^P_{22v} = S^P_{22} - \frac{[S^P_{21}]^2}{1+S^P_{11}} \tag{4.11b}$$

The synthesis task involves choosing $\alpha(x)$ and $\kappa(x)$ such that a specified frequency response S^P_{21} is realized with S^P_{22} always less than a certain value. It is desirable to make this selection with $\kappa(x)$ as small as possible since Eqs. (4.10a, 4.10b) are only reasonable for small κ. From Eq. (4.11b) and the Fourier transform relation between S^P_{22v} and κ, it is clear that the IDT should be matched so that S^P_{11} is purely real and positive near the center frequency.

If we further specify that S^P_{22} be exactly zero, so that infinite triple transit suppression is desired, then using reciprocity and power conservation (Eqs. 3.10) it can be shown that

$$|S^P_{11}| = 1 - |S^P_{21}|^2 \tag{4.12}$$

Thus, if we want a filter response which is flat in the passband, S^P_{11} will be very nearly constant in the passband where triple transit suppression is important. Therefore $1+S^P_{11}$

in the denominator of Eq. (4.11a) will not affect the frequency response much. If S_{22}^P is zero, then using Eqs. (4.11b, 3.9b) we obtain:

$$S_{22v}^P = -\frac{[S_{21}^P]^2}{1+S_{11}^P} = -Z_o(1+S_{11}^P)[S_{21v}^P]^2 \tag{4.13}$$

Assuming $1+S_{11}^P$ to be constant, which is always reasonable at least in comparison with S_{21v}^P and S_{22v}^P, Eqs. (4.10a, 4.10b, 4.13) imply that $\kappa(x/2)$ is proportional to the convolution of $\alpha(x)$ with itself. This is clear since S_{22v}^P is proportional to the square of S_{21v}^P which implies a convolution in the space domain. The scaling of the x-axis is due to the factor of two difference in the multiples of β in the Fourier transform of Eqs. (4.10a, 4.10b).

The prescription for this synthesis algorithm is now clear:

(1) Specify the desired single transducer minimum insertion loss and use Eq. (4.12) to find the corresponding value for $|S_{11}^P|$. Assume $S_{11}^P = |S_{11}^P(\beta_o)|$ for all frequencies.

(2) Use Eq. (4.11a) to specify $S_{21v}^P(\beta)$ in terms of the desired single transducer frequency response $S_{21}^P(\beta)$.

(3) Solve Eq. (4.10a) to obtain the $\alpha(x)$ which best approximates the desired $S_{21v}^P(\beta)$ obtained in (2). It is important to note that it would be unwise to simply inverse Fourier transform Eq. (4.10a) to solve for $\alpha(x)$ via Eq. (4.14) below:

$$\alpha(x) = \frac{1}{2\pi}\int_{-\infty}^{\infty} d\beta\, S_{21v}^P(\beta)e^{-j\beta x} \tag{4.14}$$

If designed in this manner, a typical filter, with its sharp transition from the passband to the stopband, would yield large ripples in the passband, and sidelobes down only about 13 dB. This is a result of the Gibbs phenomenon of Fourier transform theory [78,76]. It is necessary to use either a windowing technique or the Parks-McClellan algorithm [76,86,85].

(4) Use the assumption that $S_{11}^P(\beta)$ remains constant at its value at the center frequency in conjunction with Eqs. (4.10a, 4.10b, 4.13, 4.14) to obtain

$$\kappa(x) = \begin{cases} -\frac{Z_o}{\pi}(1+S_{11}^P)\int_{\max(-\frac{1}{2},2x-\frac{1}{2})}^{\min(\frac{1}{2},2x+\frac{1}{2})} du\,\alpha(u)\alpha(2x-u) & -\frac{L}{2} \le x \le \frac{L}{2} \\ 0 & x < -\frac{L}{2} \quad or \quad x > \frac{L}{2} \end{cases} \tag{4.15}$$

(5) Calculate the input admittance at center frequency and select a parallel matching inductor to make S_{11}^P pure real.

A convenient result of this method is that $\kappa(x)$ never has to be truncated. It is non-zero over exactly the same range as $\alpha(x)$.

This procedure was applied to the design of several single phase unidirectional transducers. In all cases, a $\cos^2$ + pedestal window function, with a 3:1 taper ratio, was used to window a sinc function. Only the first sidelobe on each side of the main lobe was kept.

$$W(x) = \frac{1}{3} + \frac{2}{3}\cos\left(\frac{2\pi x}{L}\right) \tag{4.16}$$

$$\alpha(x) = cW(x)sinc\left(\frac{4\pi x}{L}\right) \tag{4.17}$$

Each transducer was 200 half-wavelengths long. This window function has -26 dB frequency sidelobes which is 13 dB better than a rectangular window at a cost of 23% broadening of the main lobe. The Fourier transformed single transducer weighting function has -43.7 dB sidelobes, a 2.9% 1.5 dB bandwidth and a shape factor of 2.3 (ratio of bandwidth at peak sidelobe level to bandwidth at 1.5 dB level). The envelopes of the transduction and reflection functions, $\alpha(x)$ and $\kappa(x)$ are displayed in Figs. (4.2a) and (4.2b), respectively.

The coupled mode equations (3.36) were solved with these spatially varying transduction and reflection functions to obtain the transducer responses. The solutions were obtained by splitting the transducer into many sections, each of which being small enough to regard α and κ as being constant. The COM equations can be easily solved in closed form with constant α and κ (see Chap. 8 of Ref. [47] or Sec. 1.5 of Ref. [48]). These solutions were used to obtain transmission matrices of the sections which were then

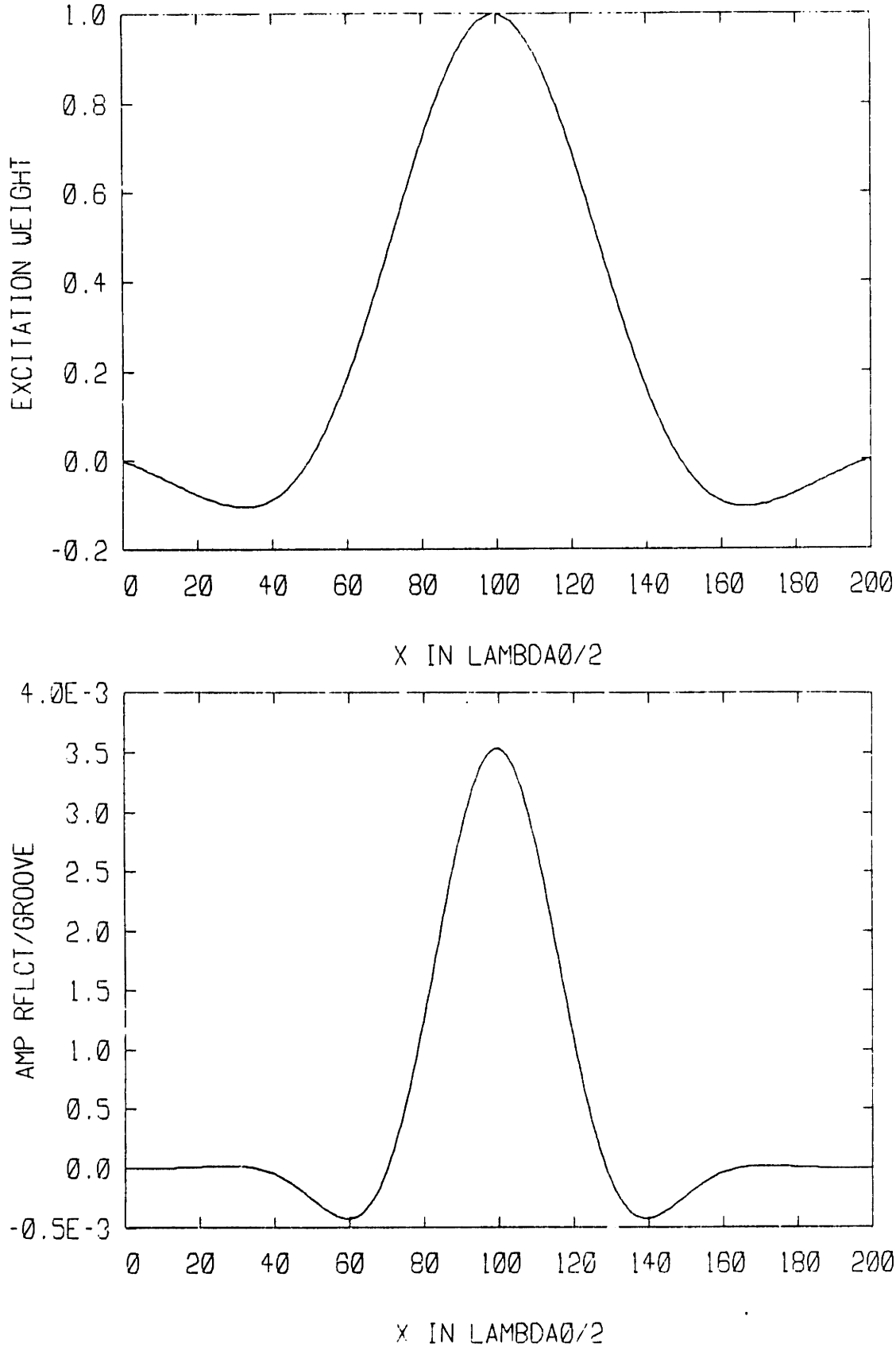

Figure 4.2 Transduction and Reflection Spatial Distributions
(a) $\alpha(x)$ = Windowed sinc(x) including one sidelobe on each side **(b)** $\kappa(x/2) = c\alpha(x) * \alpha(x)$
$*$ = convolution

multiplied together to obtain one transmission matrix for the entire transducer as in Sec. 3.6. Any desired scattering parameter can be computed from this composite transmission matrix.

In this set of calculations, loss was ignored and matching was done with a parallel inductor selected to make the input admittance purely real at the center frequency. The impedance level was set with an ideal transformer to make the acoustic reflection coefficient exactly zero at the center frequency. The piezoelectric coupling constant of ST-X quartz, $2\Delta v/v = .00134$ (Ref. [93] and Eq. (3.69)), was used along with an effective relative dielectric constant, ϵ_p^T/ϵ_o, of 4.55 (Ref. [98] and Eq. (3.51c)). Since the device is being matched to zero the acoustic reflection coefficient at f_o, essentially the same results would be obtained with any material, albeit at a different impedance level. The main difference between materials in this context is the bandwidth over which a match can be achieved. In strongly piezoelectric materials, the conductance is larger relative to the capacitive admittance which reduces the Q of the parallel tuned circuit representing a matched transducer.

In Figs. (4.3–4.5), we present plots of the single transducer insertion loss, S_{21}^P, the matched front port acoustic reflection coefficient, S_{22}^P, the voltage to acoustic wave transfer function S_{21v}^P and its approximation by the Fourier transform of $\alpha(x)$, $F\alpha$. Plots of the short circuit acoustic reflection coefficient S_{22v}^P and its approximation by the Fourier transform of $\kappa(x)$, $F\kappa$, are also presented. The insertion loss ranges from 10 dB to 1 dB, and the corresponding integrated κ's range from .05 to .8.

In Fig. 4.3b we see that the agreement between S_{21v}^P and $F\alpha$ is excellent as we would expect since integrated κ is only .05. Due to the low value for integrated κ, the insertion loss must be reasonably large in order for the regenerated signal to be as small

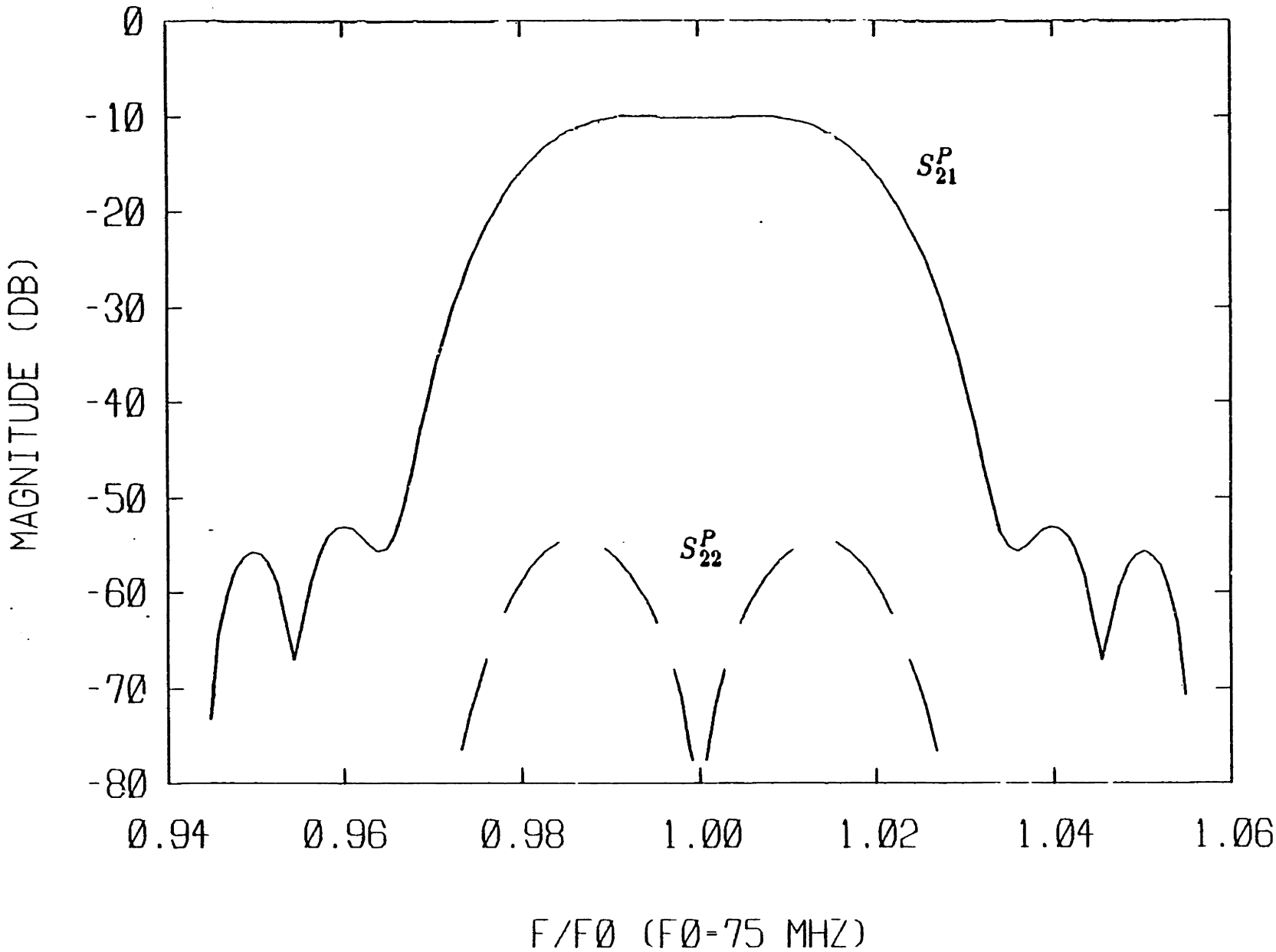

Figure 4.3a Simple Design Algorithm Results—Integrated $\kappa(x) = .05$

S_{21}^P and S_{22}^P, single transducer insertion loss, and front acoustic port reflection coefficient with the electrical port partially matched.

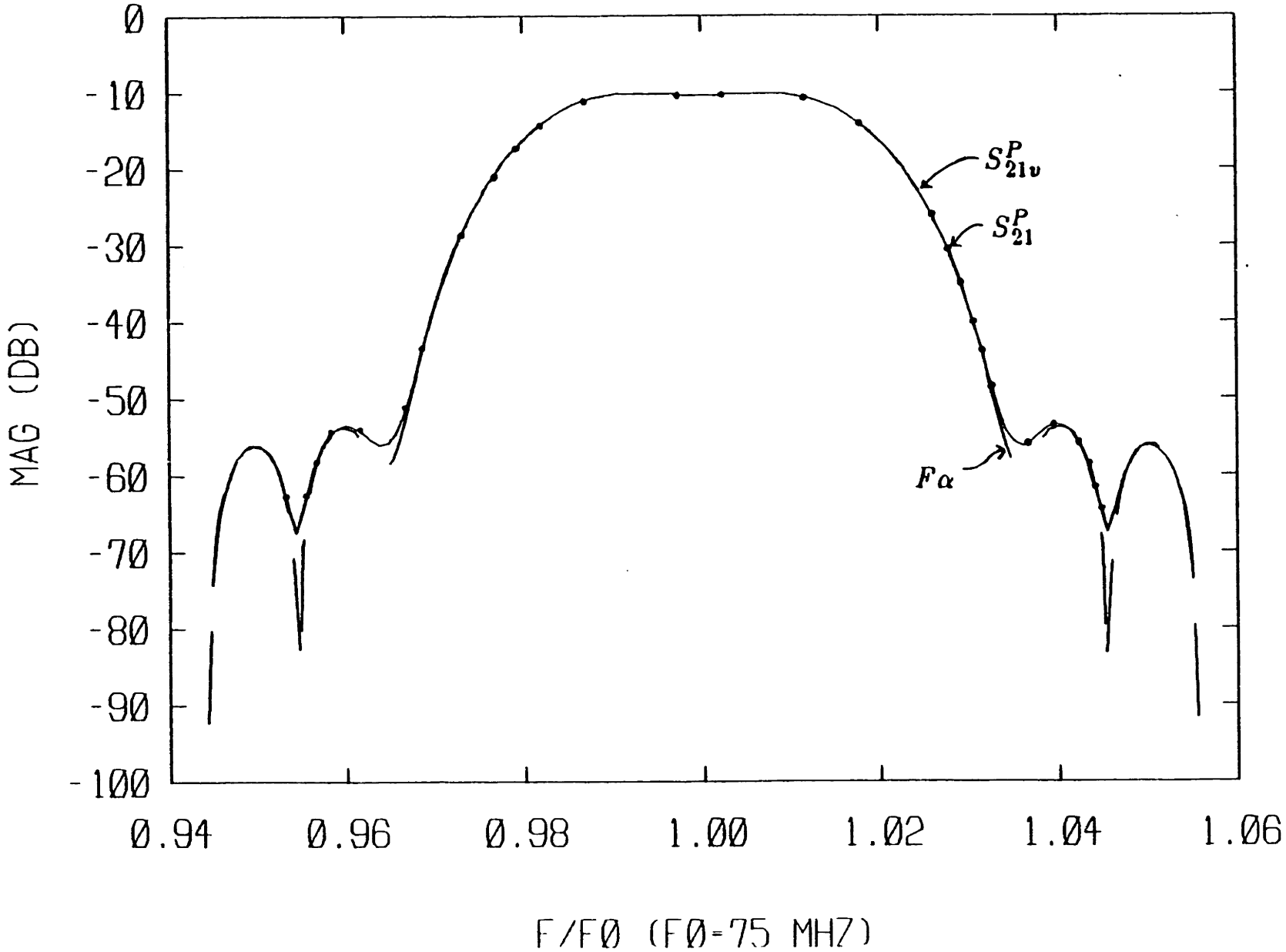

Figure 4.3b Simple Design Algorithm Results—Integrated $\kappa(x) = .05$

S_{21v}^P, $F\alpha$ and S_{21}^P, single transducer voltage to acoustic wave transfer function, its approx. by the Fourier transform of $\alpha(x)$, and insertion loss. (Note: S_{21}^P is scaled to agree with S_{21v}^P at f_o.)

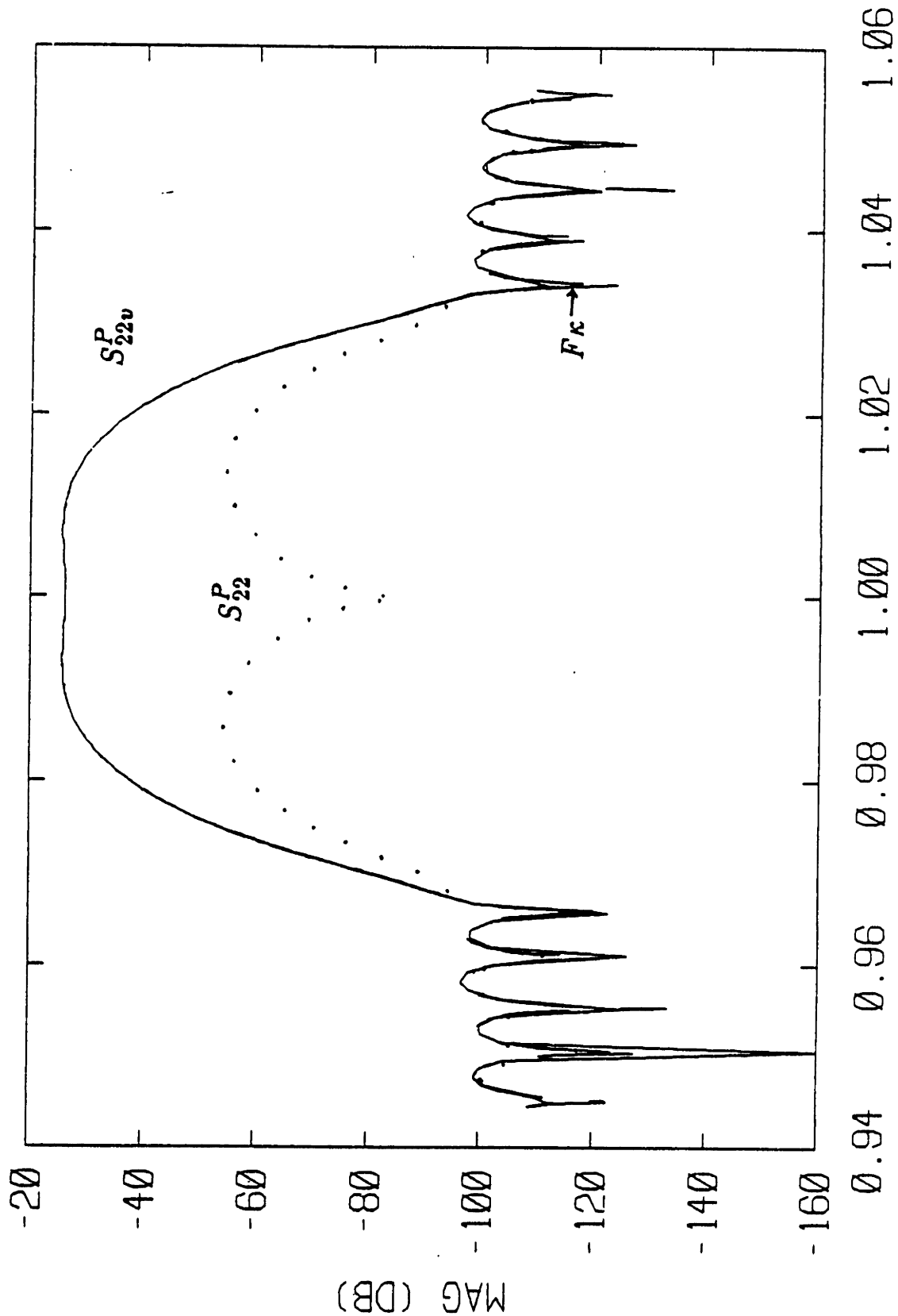

Figure 4.3c Simple Design Algorithm Results—Integrated $\kappa(x) = .05$
S^P_{22v}, $F\kappa$ and S^P_{22}, acoustic reflection coefficient when the electrical port is short-circuited, its approx. by the Fourier transform of $\kappa(x)$, and the front acoustic port reflection coefficient with the electrical port partially matched.

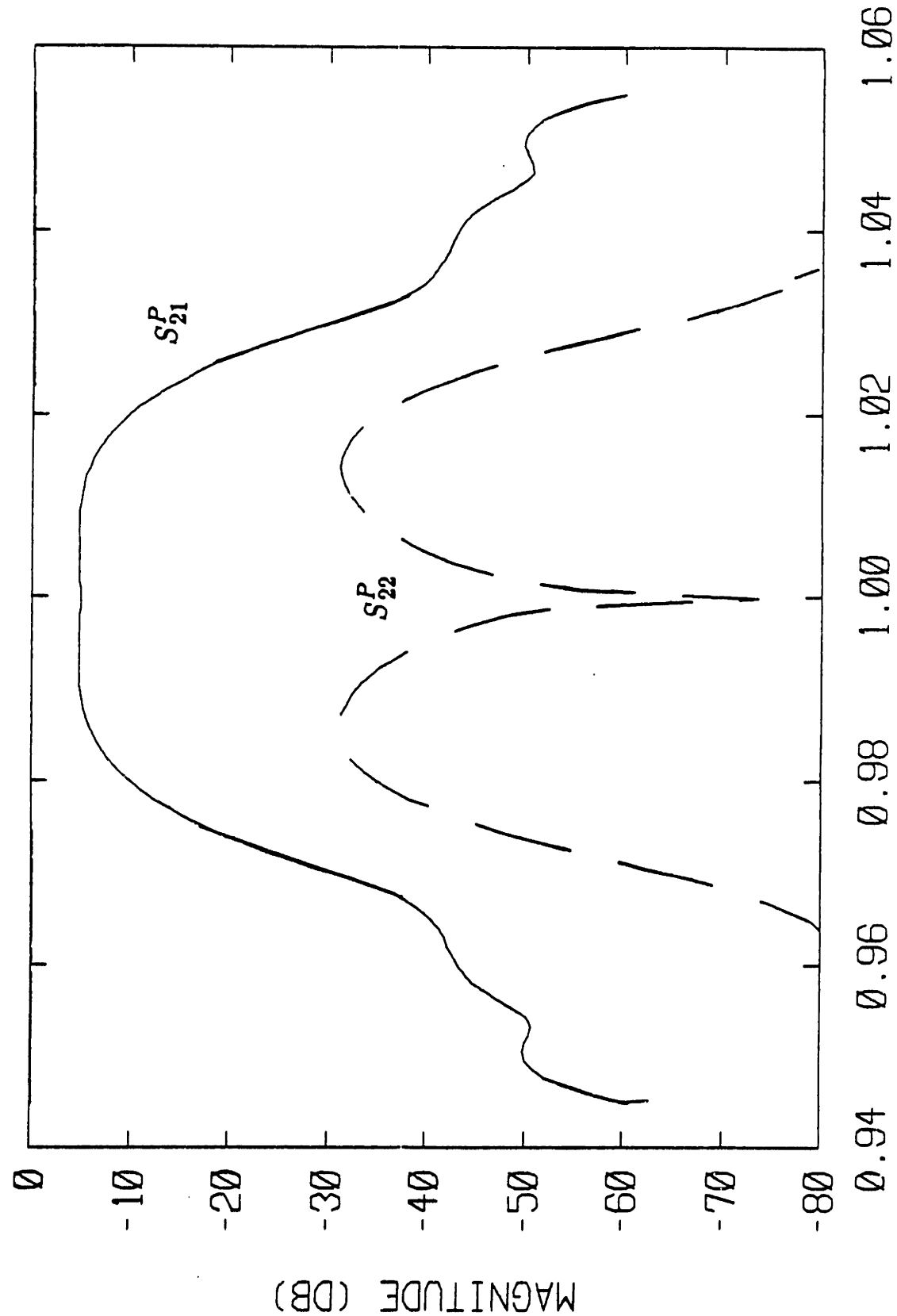

Figure 4.4a Simple Design Algorithm Results—Integrated $\kappa(x)$ = .20
S_{21}^P and S_{22}^P, single transducer insertion loss, and front acoustic port reflection coefficient with the electrical port partially matched.

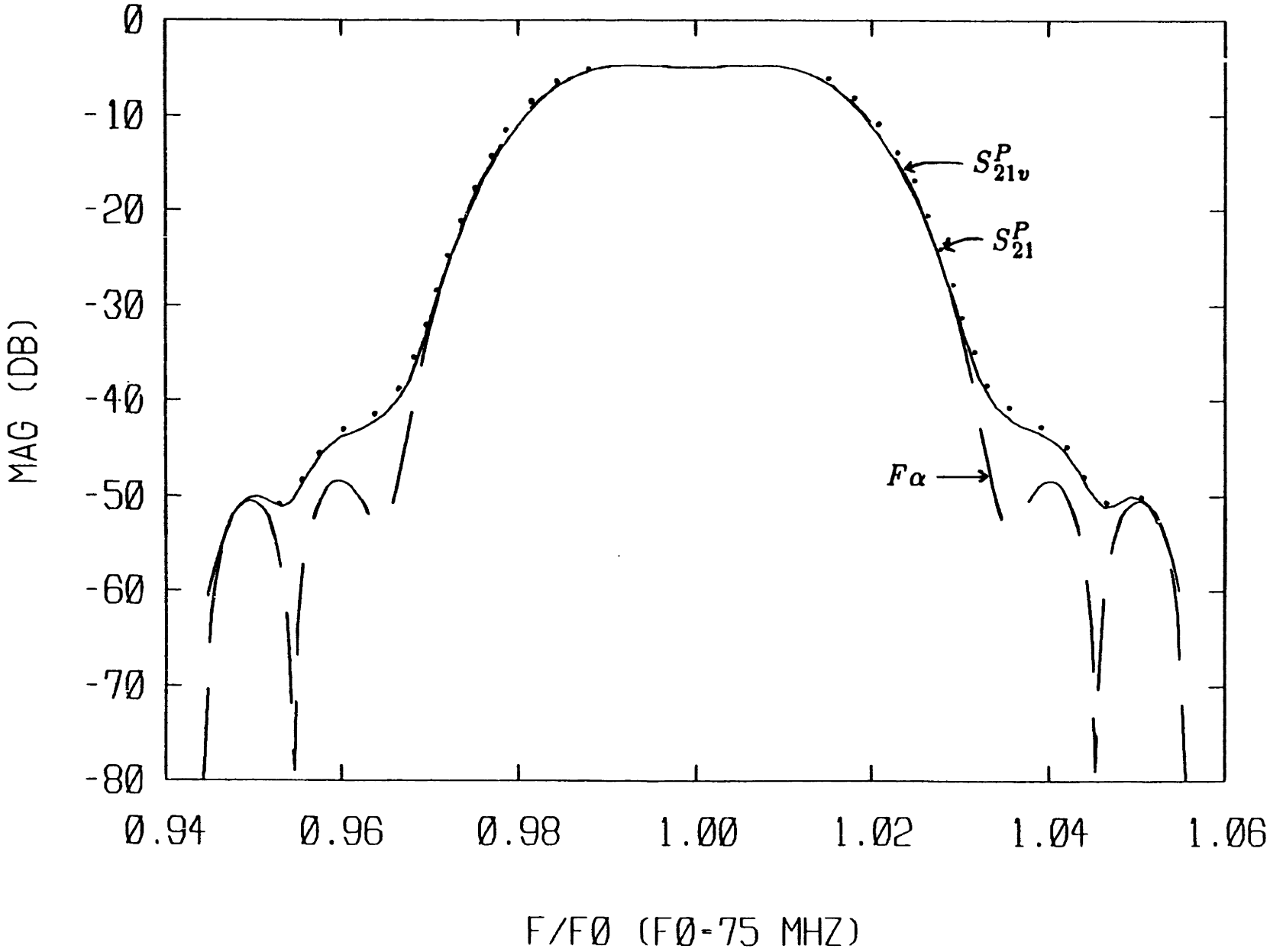

Figure 4.4b Simple Design Algorithm Results—Integrated $\kappa(x) = .20$
S_{21v}^P, $F\alpha$ and S_{21}^P, single transducer voltage to acoustic wave transfer function, its approx. by the Fourier transform of $\alpha(x)$, and insertion loss. (Note: S_{21}^P is scaled to agree with S_{21v}^P at f_o.)

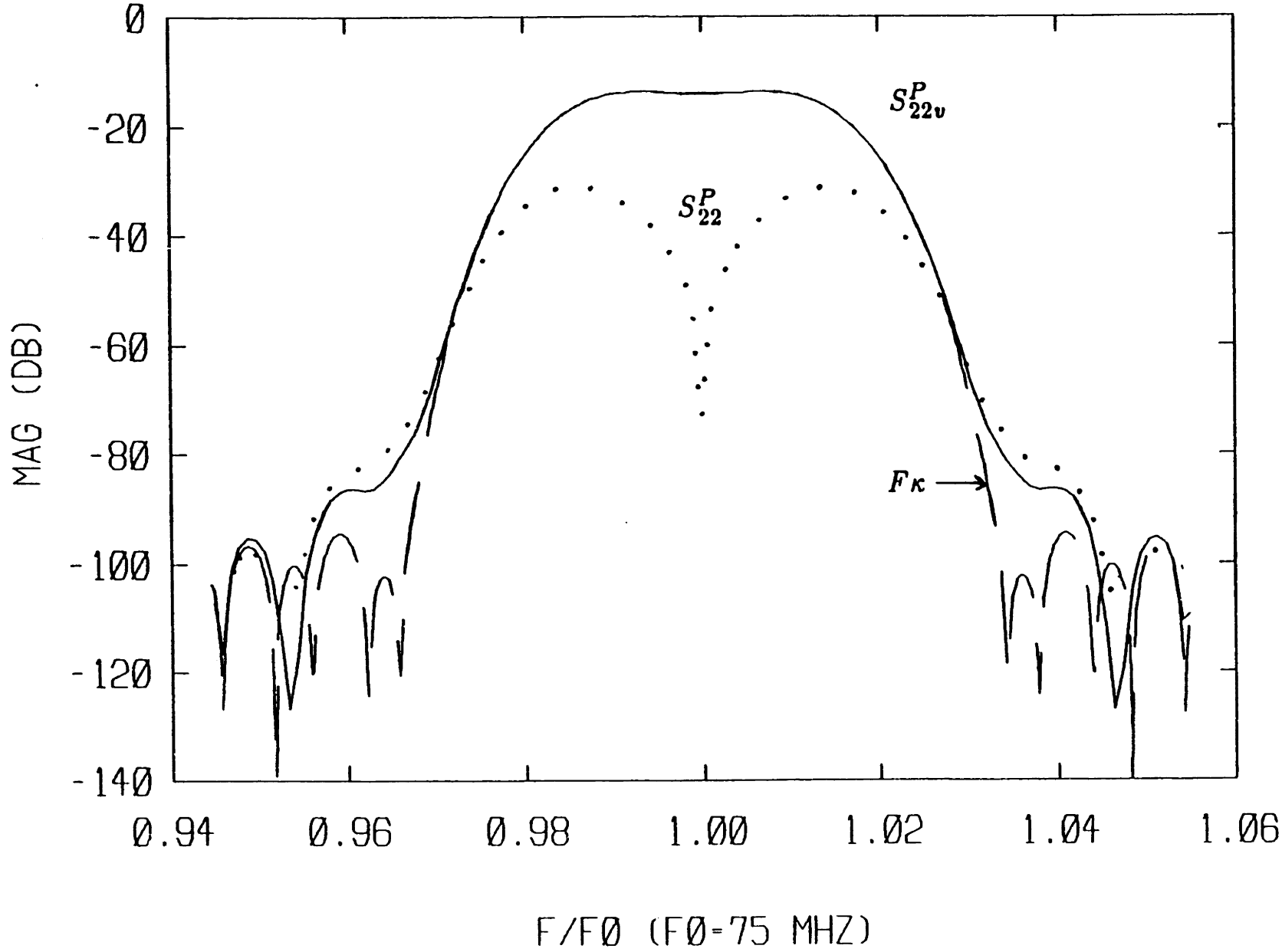

Figure 4.4c Simple Design Algorithm Results—Integrated $\kappa(x) = .20$

S_{22v}^P, $F\kappa$ and S_{22}^P, acoustic reflection coefficient when the electrical port is short-circuited, its approx. by the Fourier transform of $\kappa(x)$, and the front acoustic port reflection coefficient with the electrical port partially matched.

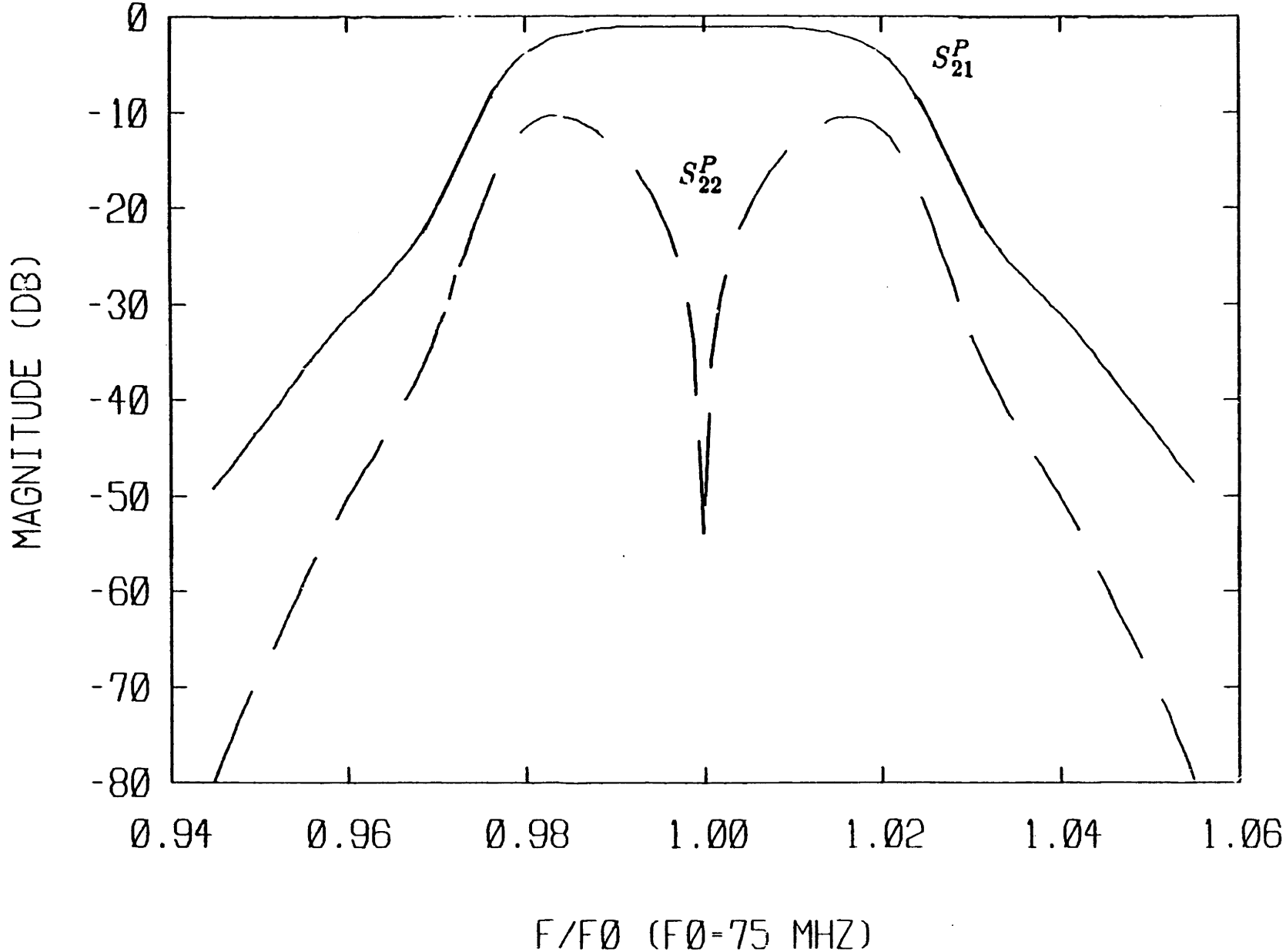

Figure 4.5a Simple Design Algorithm Results—Integrated $\kappa(x) = .80$

S_{21}^P and S_{22}^P, single transducer insertion loss, and front acoustic port reflection coefficient with the electrical port partially matched.

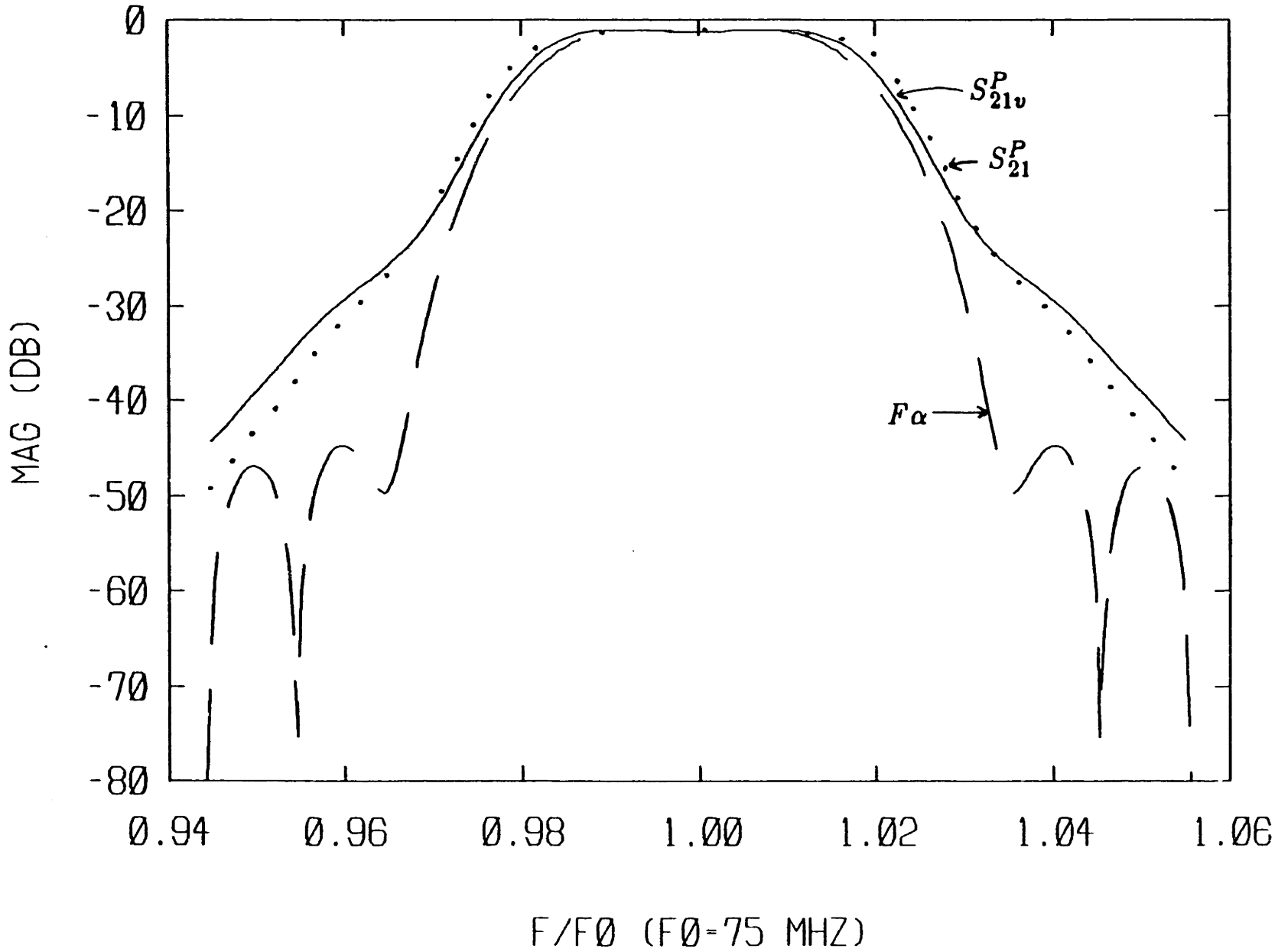

Figure 4.5b Simple Design Algorithm Results—Integrated $\kappa(x) = .80$

S_{21v}^P, $F\alpha$ and S_{21}^P, single transducer voltage to acoustic wave transfer function, its approx. by the Fourier transform of $\alpha(x)$, and insertion loss. (Note: S_{21}^P is scaled to agree with S_{21v}^P at f_o.)

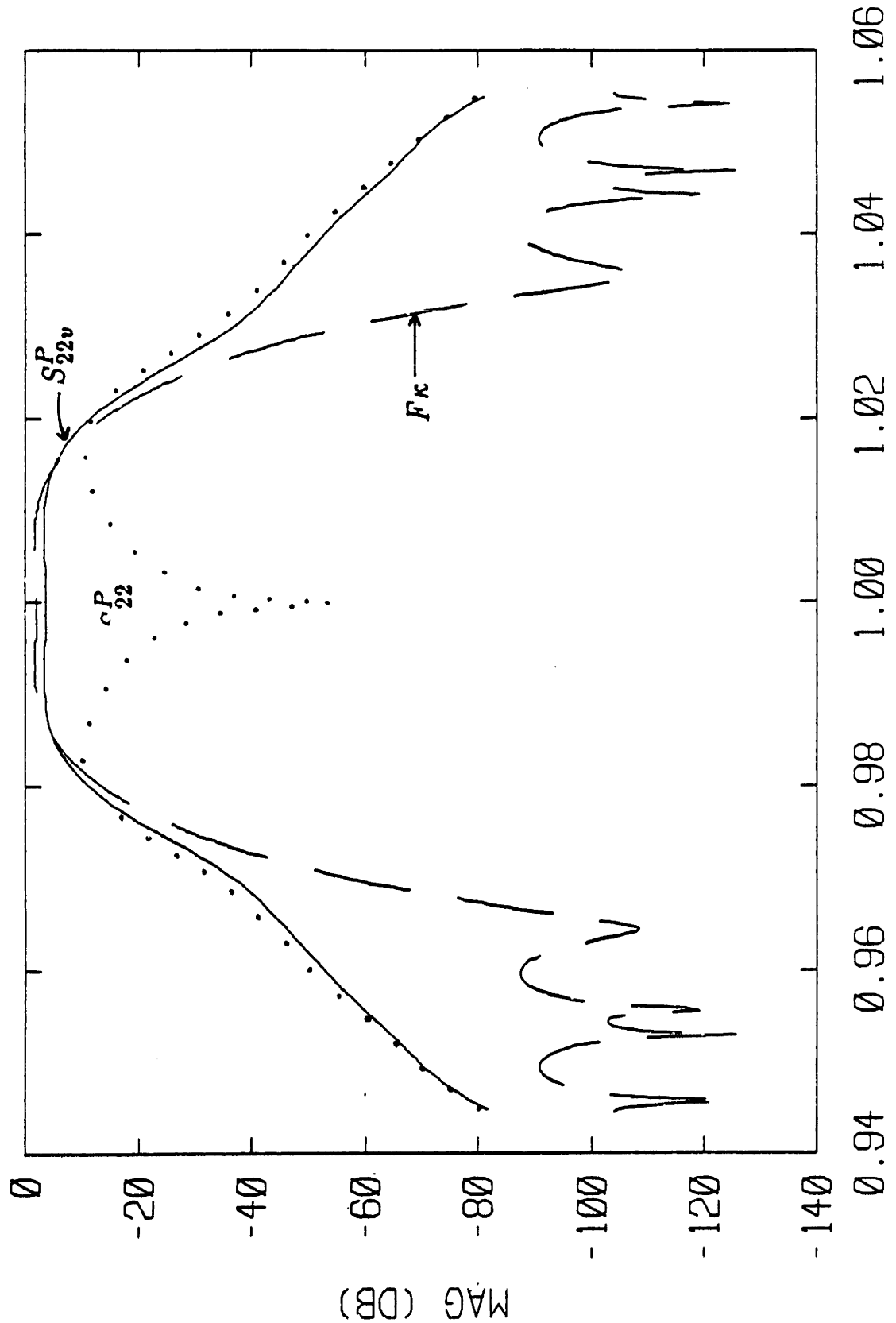

Figure 4.5c Simple Design Algorithm Results—Integrated $\kappa(x) = .80$
S^P_{22v}, $F\kappa$ and S^P_{22}, acoustic reflection coefficient when the electrical port is short-circuited, its approx. by the Fourier transform of $\kappa(x)$, and the front acoustic port reflection coefficient with the electrical port partially matched

as the grating reflection so as to be able to cancel it (Eq. (4.13)). Thus by Eq. (4.12) S_{11}^P will be close to 1*. From Eq. (4.11a) we note that $S_{21_v}^P$ will have the same shape as S_{21}^P as long as $1 + S_{11}^P$ is roughly constant. In this case $1 + S_{11}^P$ is almost constant at 2, and Fig. 4.3b confirms that $S_{21_v}^P$ agrees well with S_{21}^P †. $S_{22_v}^P$ and $F\kappa$ also agree very well since integrated κ is small and multiple reflections can be ignored. S_{22}^P and $S_{22_v}^P$ do not agree of course in the passband; they differ by the regenerated signal which cancels the grating reflection to reduce triple transit as expected from Eq. (4.11b). Outside the passband S_{22}^P and $S_{22_v}^P$ agree, since the regenerated signal, which goes as the square of the electroacoustic transfer function, is so small.

As integrated κ increases to .2 the insertion loss falls substantially from 10 dB to 4.6 dB for each transducer, but the maximum acoustic reflection coefficient increases from -54 dB to -31 dB. We note from Figs. (4.4b, 4.4c) that the Fourier transform relation between α and $S_{21_v}^P$ and κ and $S_{22_v}^P$ both start to break down, especially in the sidelobes. This is somewhat surprising since one would expect the effect of the reflections to first appear near the Bragg frequency where all the reflections are coherent. It isn't really all that surprising though on second thought, since when signals are down by 40 to 100 dB, as they are in the sidelobes, small absolute errors are much more significant. When integrated κ is increased to .8, the approximations involving transduction breaks down in the transition region while it is still accurate in the passband. In the case of the reflection responses, there is a discrepancy, even in the passband.

The above results are summarized in Fig. 4.6. Although the sidelobe level and triple transit level both degrade as integrated κ increases in order to reduce insertion loss,

---

* Recall that the matching was done to make the input admittance real at f_o which makes S_{11}^P real at f_o and approximately real over a reasonable bandwidth about the center frequency.

† Note: S_{21}^P is scaled to agree with $S_{21_v}^P$ at f_o in Figs. (4.3b, 4.4b, 4.5b). A direct comparison is not reasonable since the units are different.

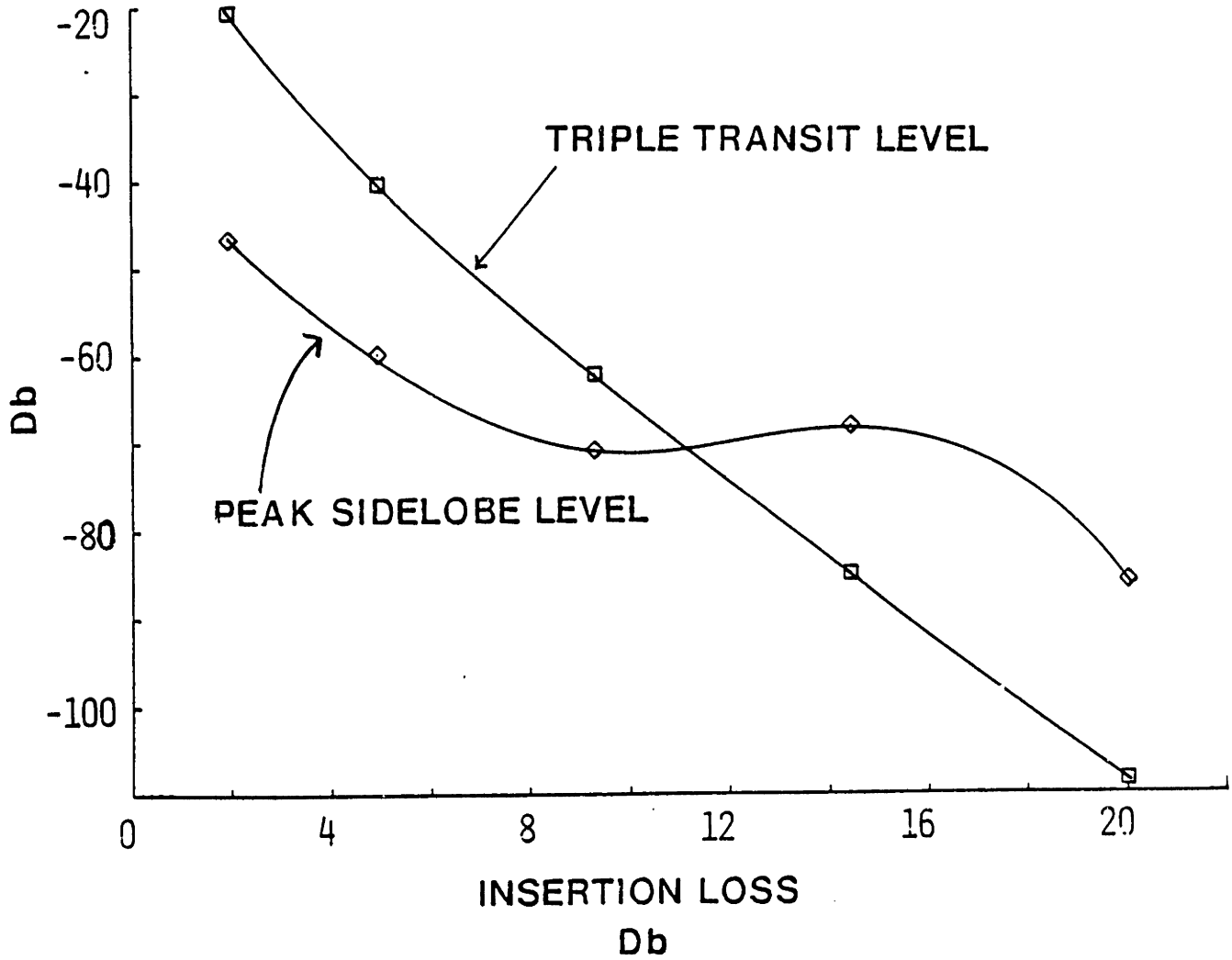

Figure 4.6 Summary of Results—Low-κ Design Algorithm
Note: In this plot the rejection band definition remains constant, so that the shape factor of all these filters is 2.3.

reasonable filters can be designed. For example, among the designs represented in Fig. 4.6 is one with 4.9 dB insertion loss, a shape factor of 2.3, 60 dB rejection, and 40 dB triple transit suppression. At an integrated κ level of .2 or less, which corresponds to at least 9.2 dB of insertion loss, acceptable agreement is obtained between the desired and achieved frequency responses. If better performance is desired, then more terms of the iterated integrals of Eqs. (3.42a, 3.44a) can be used in the design.

We should not forget that these results were obtained assuming that there is continuous control over κ and α. As explained in the introduction, continuous control over these parameters is not compatible with our desire to come up with an easily manufacturable design. One possible solution to this problem is presented in Chapter 6, where the focus is on the synthesis of high performance frequency responses with nonuniformly spaced sources of constant magnitude.

CHAPTER 5

EXPERIMENTAL AND THEORETICAL VERIFICATION OF THE SINGLE-PHASE UNIDIRECTIONAL TRANSDUCER

5.1 Introduction

We recall that one of the main goals of the single-phase unidirectional transducer (SPUDT) was to reduce insertion loss without incurring the penalty of increased triple transit. As discussed in the introduction, this triple transit signal results from a portion of the main acoustic signal being reflected from the output transducer, and then once again from the transmitting transducer, thereby making three transits of the region between the two transducers before being received. In a standard bi-directional split-finger transducer, the only source of reflection is really regeneration. The acoustic wave incident on a transducer induces a voltage between the fingers, which then reradiates yielding a reflected signal. As discussed in Sec. 4.1, when a standard transducer is matched on the short circuit side, this regenerated signal is weakened thereby reducing the triple transit signal. This unfortunately also increases insertion loss.

In Hartmann's [44] implementation of the SPUDT (Fig. 5.1), a second level metalization is deposited forming a reflective grating in such a position relative to the acoustic sources that the reflection from this grating tends to cancel the regenerated signal (see Sec. 4.1). The regenerated signal depends strongly on the load attached to a transducer. Near a

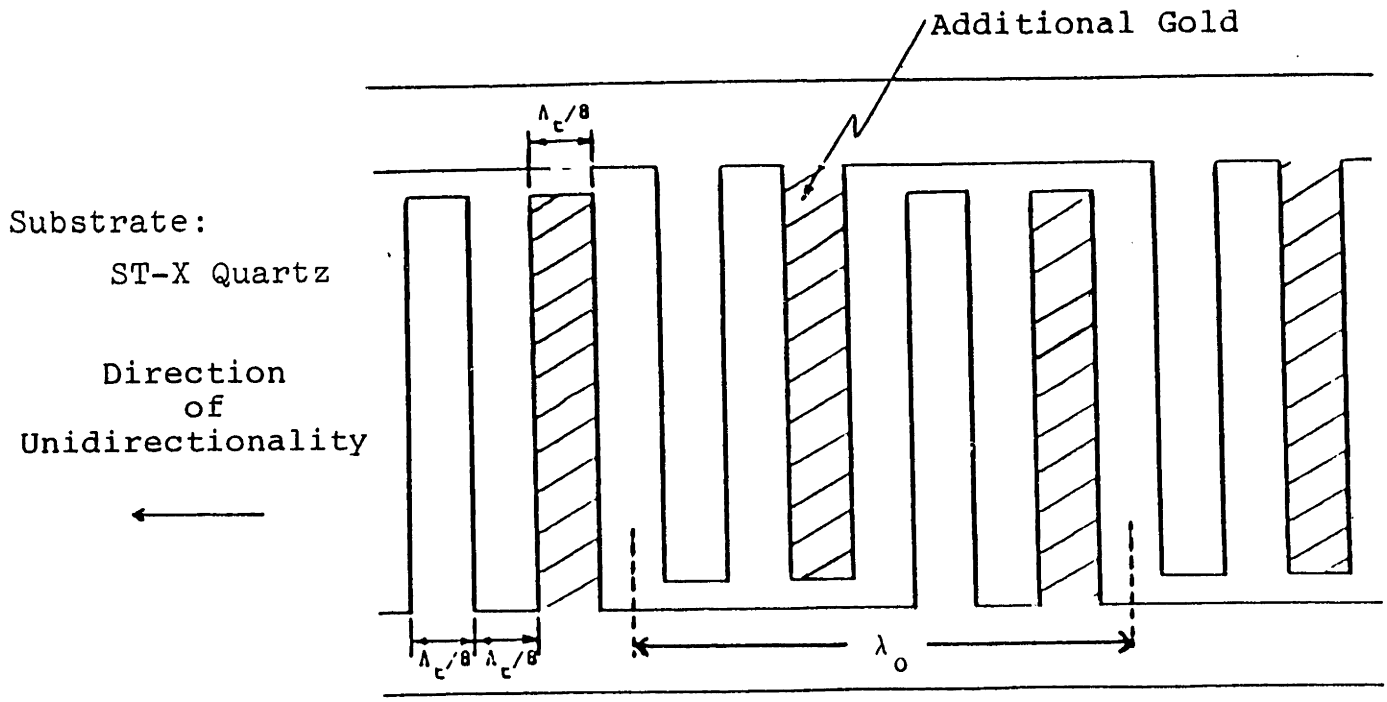

Figure 5.1 Hartmann's Implementation of the SPUDT
The above is one portion of a transducer. $\Lambda_t = \lambda_o$ is the wavelength at the center frequency.

short circuit condition, there is little regeneration and the triple transit signal will be large due to the grating reflection. Moving closer to a match (how close depends on the size of the grating reflection coefficient), the regenerated signal becomes larger until it equals the grating reflection in magnitude, at which point the triple transit signal falls to zero.

These intuitive notions are examined experimentally and theoretically using an unweighted SPUDT. The coupling-of-modes equations (3.95a–3.95c) are solved exactly, and these theoretical results are compared to what was experimentally observed, both in the frequency and time domains.

5.2 Experimental Results—COM

An unweighted single phase unidirectional filter [44] of the type discussed in Sec. 2.2 and sketched in Fig. 5.1 was constructed on ST-X quartz. Both transducers were 50.5 wavelengths long and of the split finger type. The aperture was 150 wavelengths and the separation between the end of the first transducer and the start of the next was only 25.25 wavelengths in an attempt to eliminate diffraction effects. The periodicity of the transducer was 42.09 μ yielding a center frequency of 74.61 MHz. All the fingers had a first level metalization consisting of 2000 Å aluminum, while the thicker fingers had an additional 500 Å of 90%-titanium-10%-tungsten, with a 1000 Å layer of gold on top. The titanium-tungsten layer's purpose was to help the gold adhere to the aluminum.

The devices were fabricated by first depositing all three metal layers and then chemically etching through all three using patterned AZ photoresist as a mask to form the transducer patterns. A second level mask was used to leave AZ resist on top of those fingers which were to retain the gold. Then ion beam milling [100] was used to remove both the gold and the titanium-tungsten from the exposed fingers. This process slightly narrowed the fingers from which the top two metal layers were removed. The end result was that the metalization ratio (fraction of the period which is metalized) for the gold covered strips was .38, while that of the aluminum strips was only .33.

In order to compare the experimental results with the theoretical results, we need the parameters which characterize a SPUDT which then fully specify the coupled mode equations. As discussed in Sec. 3.9.2, theoretically calculated reflection coefficients are not all that accurate. Therefore, a test structure was also built to measure the acoustic reflection coefficient. The structure was identical to a shorted SPUDT and consisted of 101 reflective strips with an aperture of 150 wavelengths. The peak reflection from the

full grating was – 4.26 dB, with a standard deviation of .06 dB based on 4 measurements. The reflection coefficient from a grating of N reflectors with an amplitude reflectivity of Γ /reflector is

$$\text{Magnitude Grating Reflection} = \tanh(N\Gamma) \tag{5.1}$$

This is the exact solution to the coupled mode equations at Bragg and was obtained by specializing Eq. (3.46) to the case of constant reflectivity reflectors. Inverting this expression, we obtain a reflection coefficient of $7.06x10^{-3}$ for each thick gold strip. The phase was chosen to be pure imaginary when referenced to the midpoint of a reflective strip, as discussed in Sec. 3.4. The sign was selected to be positive, which causes the transducer to be unidirectional in the experimentally observed direction which is indicated in Fig. 5.1. This sign also agrees with the theoretical calculation of Chen and Haus [11] and disagrees with the result in Datta and Hunsinger [15] . The center of transduction, the point at which the transduction coefficient $\alpha(x)$ is real, was assumed* to be the midpoint of the gap between fingers of opposite polarity, as discussed in Sec. 3.4. The slight asymmetry caused by the difference in metalization ratio between the aluminum and gold fingers was ignored. The bulk resistivity of aluminum was reduced 15% for the 2000 Å film to account for the finiteness of the mean free path of the electrons [40] . The acoustic propagation loss includes both intrinsic material loss and radiation into compressional waves in the air above the device [98] . All the parameters used and their sources are summarized in Table 5.1.

The coupled mode equations (3.95a–3.95c) were solved exactly to obtain the scattering parameters of a filter consisting of two SPUDT's. Equation (3.69) was used to determine the transduction coefficient and Eq. (3.71) was used for the capacitance. In both cases

* This is exactly true only if the metal strips are perfectly periodic. In this case, the periodicity is broken by difference in metalization ratio between the aluminum and gold fingers. (See Sec. 5.1).

Electromechanical Coupling Constant	Eq. 3.69	$\frac{2\Delta V}{V}$	$.00134^{[93]}$
Effective Relative Dielectric Constant	Eq. 3.51c	$\varepsilon_{pr}^{T} = \frac{\varepsilon_{p}^{T}}{\varepsilon_{o}}$	$4.55^{[98]}$
Reflection Coefficient per Gold Strip		r	$j7.06\times10^{-3}$ [Me]
Acoustic Attenuation Coefficient		γ	$.158$ db/cm [98]
Sheet Resistivity	Eq. 3.89c	ρ_s	$.16\Omega$/square [40]
Average Velocity		V	3.141×10^{5} cm/sec [Me]
Metalization Ratio		η	$.355^{[Me]}$
Transducer Period		λ_o	$42.09\mu M^{[Ma]}$
Acoustic Aperture		W	$150\ \lambda_o$ [Ma]
Transducer Length			$50.5\ \lambda_o$ [Ma]
Gap between Transducers			$25.25\ \lambda_o$ [Ma]

Table 5.1 Parameters used in the Theoretical Plots of Fig. 5.2
The above parameters which are neither measured nor specified by the mask are the generally accepted physical parameters of either ST-X quartz or aluminum. Beside many of the parameters is an equation number in which the parameter is defined and the reference from which the value was obtained. [Me] indicates that the parameter was measured and [Ma] indicates that the parameter value was determined by the mask.

all the strips were assumed to be identical in width, and the average of the metalization ratios of the aluminum and gold strips were used. The expression for α includes the full frequency dependence of the transduction element factor. On the other hand, any frequency dependence of κ was ignored.

Now that we are dealing with a full filter, consisting of two acoustically coupled transducers, we must distinguish between two different scattering matrices. The scattering matrix for a full 2-transducer filter will be denoted by S^F, while the scattering matrix

for a partial filter consisting of only one transducer will be denoted by S^P. The experimentally and theoretically determined insertion loss curves, S^F_{21}, for the device with no electrical matching in a 50 Ω system are presented Fig. (5.2a). The electrical port reflection coefficient, S^P_{11}, is presented in Fig. (5.2b).

Qualitatively, the experimental and theoretical curves in Figs. (5.2a, 5.2b) agree, but there are problems with the absolute levels. Outside the passband, it is very easy to apply power conservation to an individual three port since the transducers lose their unidirectionality, and acoustic reflections from the transducers are reduced. Therefore to a very high degree of approximation, the forward port single transducer scattering parameter, S^P_{21}, equals the corresponding scattering parameter for the reverse port, S^P_{31}, and $S^F_{11} = S^P_{11}$. Furthermore, since we are greatly detuned from Bragg, the reflected signals can be ignored and the full filter insertion loss S^F_{21}, is simply equal to $(S^P_{21})^2$ (See Eq. (3.76)). At the first sidelobe peak on the high frequency side, the

$$\text{loss} \quad = \quad 1 - |S^P_{21}|^2 - |S^P_{31}|^2 - |S^P_{11}|^2 \quad \approx \quad 1 - 2|S^F_{21}| - |S^F_{11}|^2 \tag{5.2}$$

in the experimental data is .089 while it is .023 in the theoretical calculation.

A second discrepancy between theory and experiment is the difference in heights of the passband ripples. The theoretical ripples are much higher than the ripples in the experimental curve. This is probably due to using too high a value for the strip reflectivity. Another difference is the asymmetry in the height of the passband ripples. The passband ripple is caused by interference between the direct acoustic response and the triple transit signal. The precise detail of the ripples depends on the phasing between these two signals. Only if there are an integral number of half wavelengths between the transducers are the ripples symmetrical. Although there are exactly 76 wavelengths between the center gold

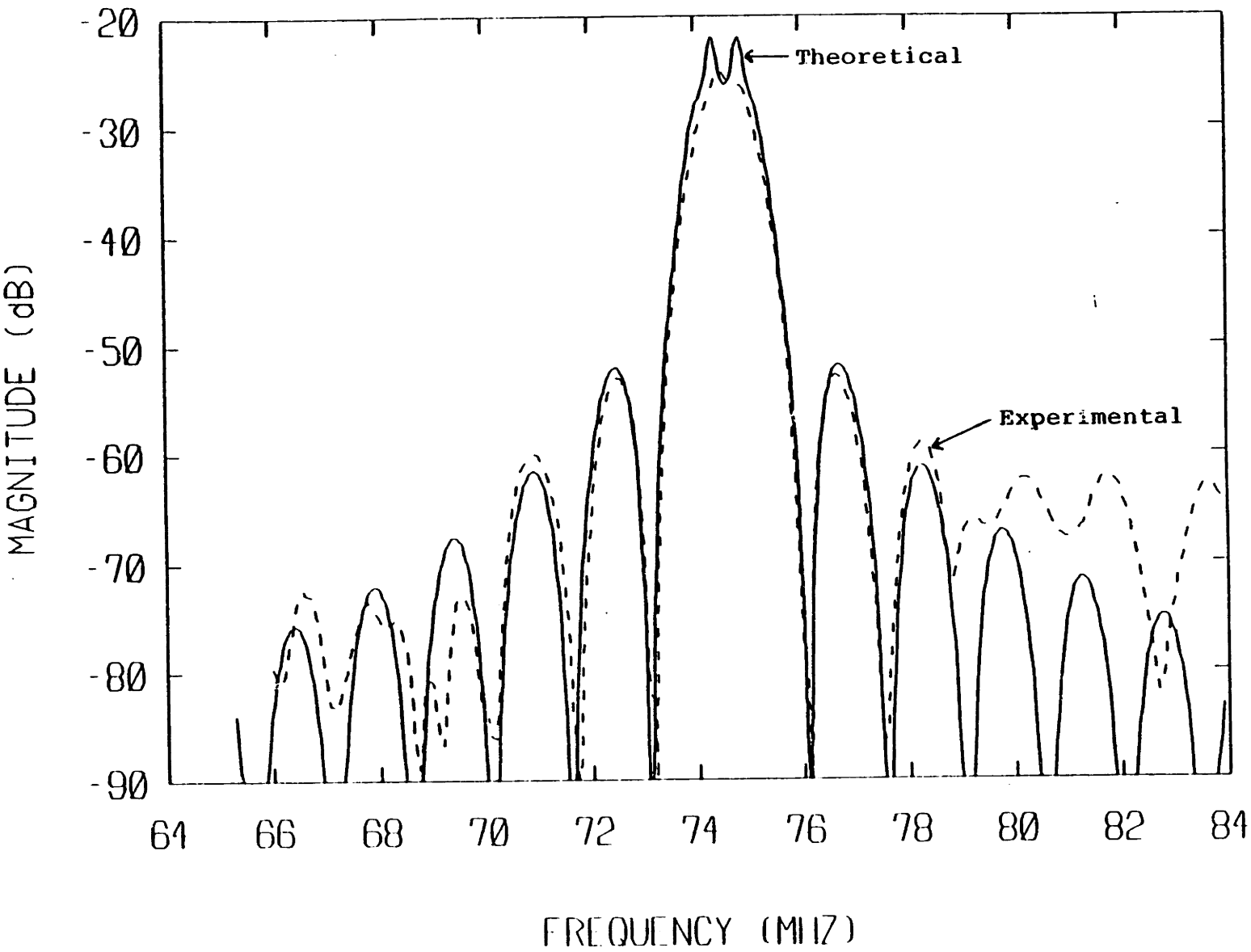

Figure 5.2a Insertion Loss S_{21}^{E} for an Unmatched SPUDT—Nominal Parameters
This data was taken in a 50 Ω system. Generally accepted parameters were used in addition to the measured reflection coefficient/gold-strip of $7.05x10^{-3}$. The parameters used are reported in Table 5.1

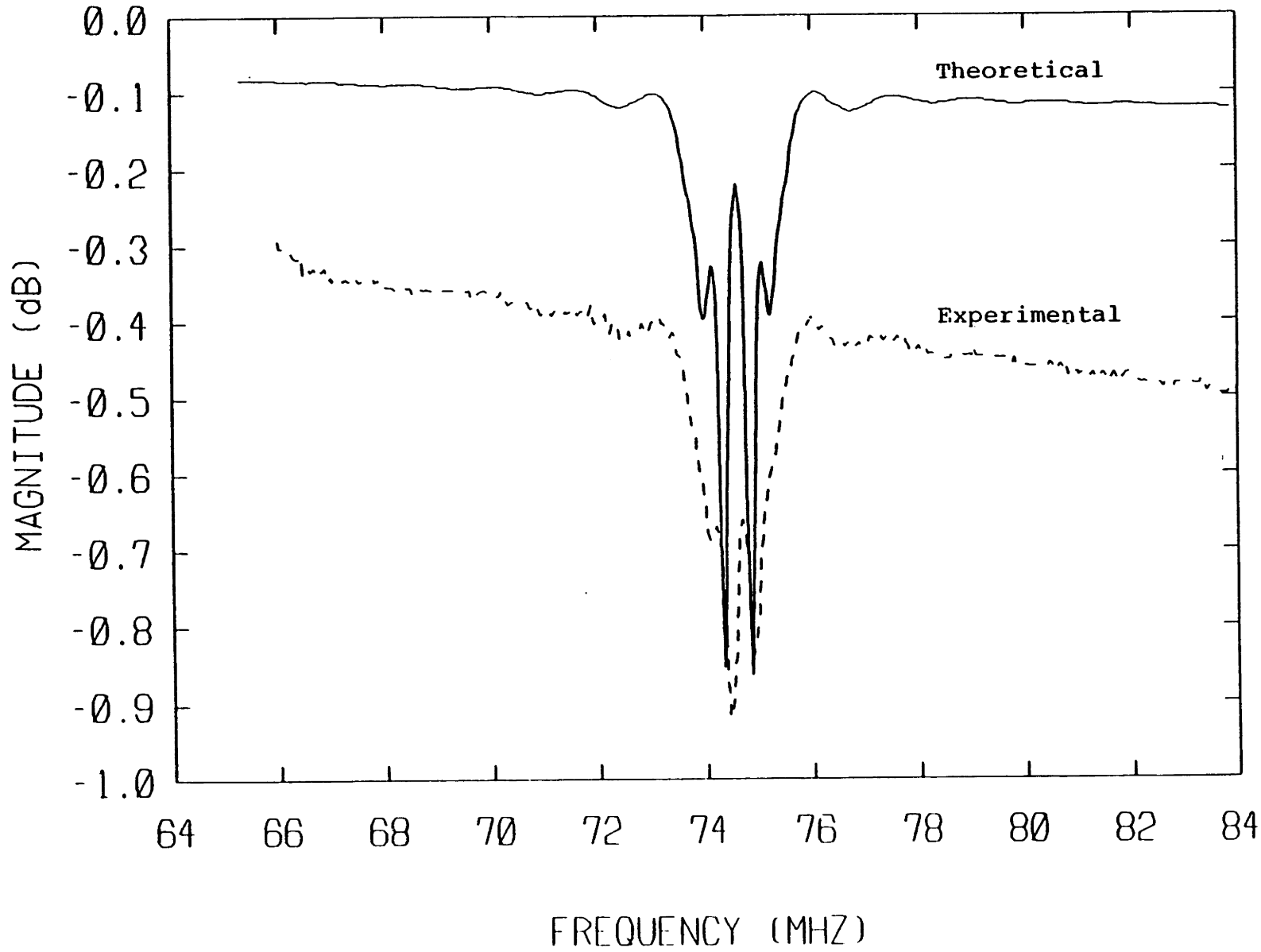

Figure 5.2b Return Loss S_{11}^{E} for an Unmatched SPUDT—Nominal Parameters
This data was taken in a 50 Ω system. Generally accepted parameters were used in addition to the measured reflection coefficient/gold-strip of $7.06x10^{-3}$. The parameters used are reported in Table 5.1

Reflection Coefficient per Gold Strip	$.45\, r_o$	$j3.20 \times 10^{-3}$
Sheet Resistivity	$4.1\ \rho_{so}$	$.66\Omega$/square
Velocity in the Spacer	$1.004\ V_o$	3.153×10^5cm/sec.

Table 5.2 Adjustments to the Nominal Parameters of Table 3.1 Used in the Theoretical Plots of Figs. (5.3, 5.4, 5.5, 5.6)

strips of the two transducers, the velocity is slightly higher in the spacer region since there are no reflectors. This velocity difference affects the relative phasing of the triple transit signal, and thereby the ripple asymmetry.

In order to check these ideas, new curves were generated (Figs. 5.3a–5.3d) with values for some of the parameters modified to better fit the experimental data. Sheet resistivity was increased by a factor of 4.1 from the nominal value recorded in Table 5.1. This was the amount necessary to make the theoretical return loss equal the observed return loss in the rejection band. It should be noted that increased propagation loss could not account for the higher loss in the rejection band since very little acoustic energy is generated, and thus even less can be dissipated. The reflection coefficient for each gold strip was scaled by a factor of .45 to make the height of the passband ripples more closely approximate what was observed. Finally the velocity in the spacer region was increased by .4% to match the asymmetry in the passband ripples*. These modifications to the nominal parameter values are summarized in Table 5.2.

As can be seen from Figs. (5.3a–5.3d), the agreement between theory and experiment for S_{11}^F is now excellent over the entire frequency range. In the case of S_{21}^F, the

* A change in the relative phase between κ and α can also cause asymmetry in the passband ripples. In our case, the difference in metalization ratio between the gold strips ($\eta = .38$) and the aluminum strips ($\eta = .33$) can cause such a phase shift. If the center of transduction, i.e. the point at which α is real, is assumed to be at the midpoint of the gap between fingers of opposite polarity, then this difference in metalization ratio causes the phase of κ to shift by 2.25° at this point. This results in an asymmetry of less than .1 dB in S_{21}^P, and thus is clearly insignificant compared to the effect of the spacer velocity shift.

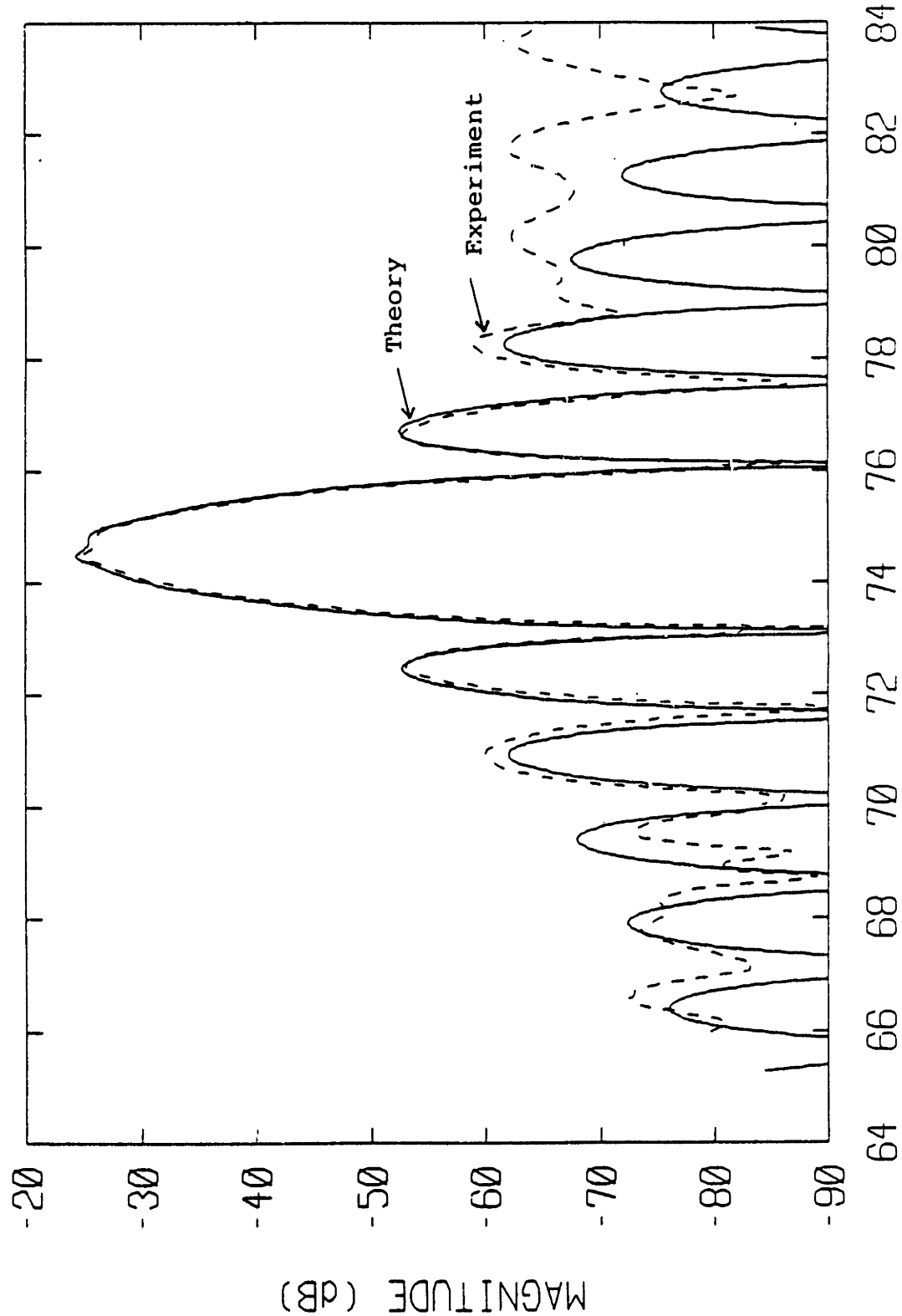

Figure 5.3a Insertion Loss S_{21}^F for an Unmatched SPUDT—Adjusted Parameters
This data was taken in a 50 Ω system. The parameters of Table 5.1 were used except for the modifications summarized in Table 5.2.

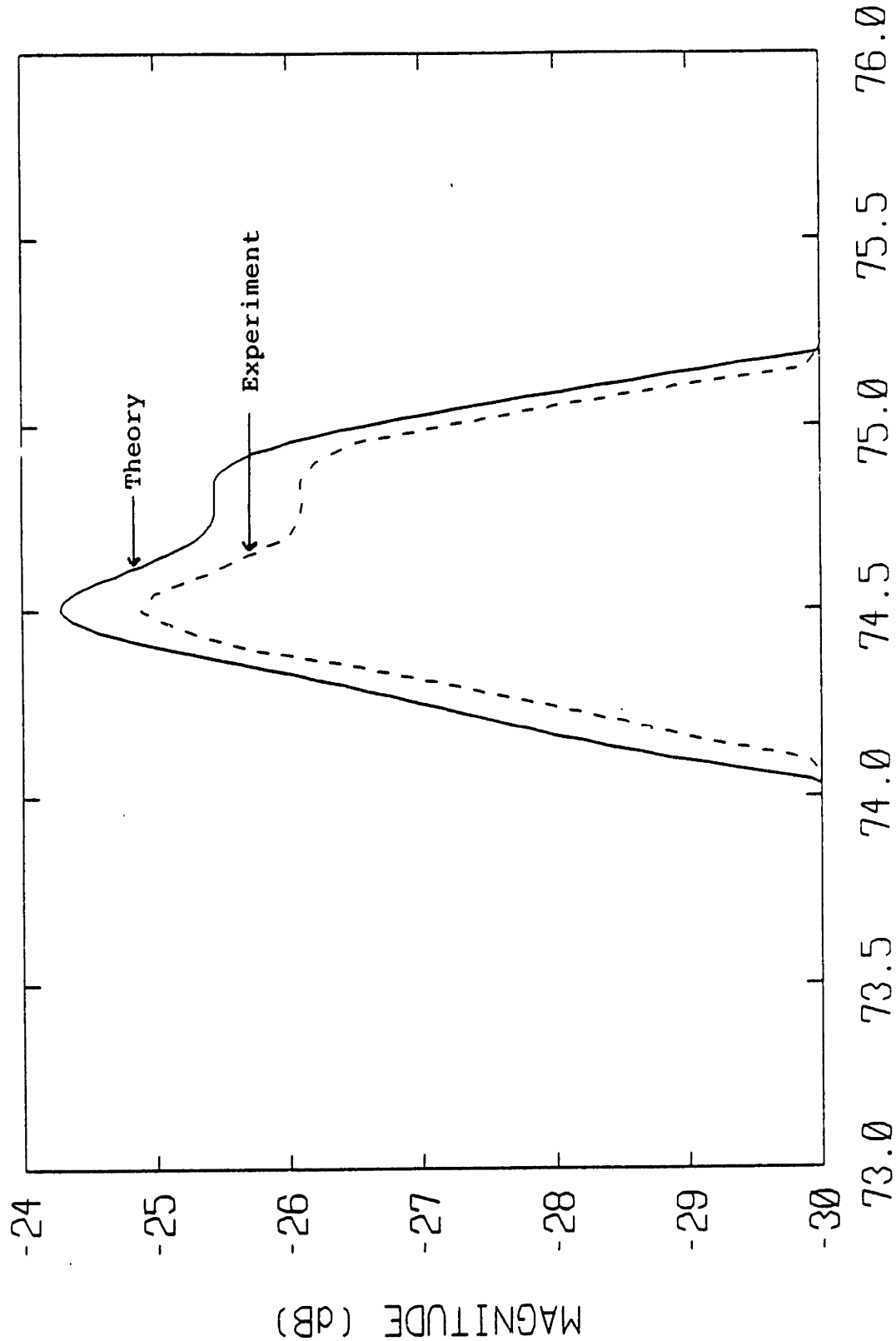

Figure 5.3b Insertion Loss S_{21}^F for an Unmatched SPUDT—Adjusted Parameters
This data was taken in a 50 Ω system. The parameters of Table 5.1 were used except for the modifications summarized in Table 5.2.

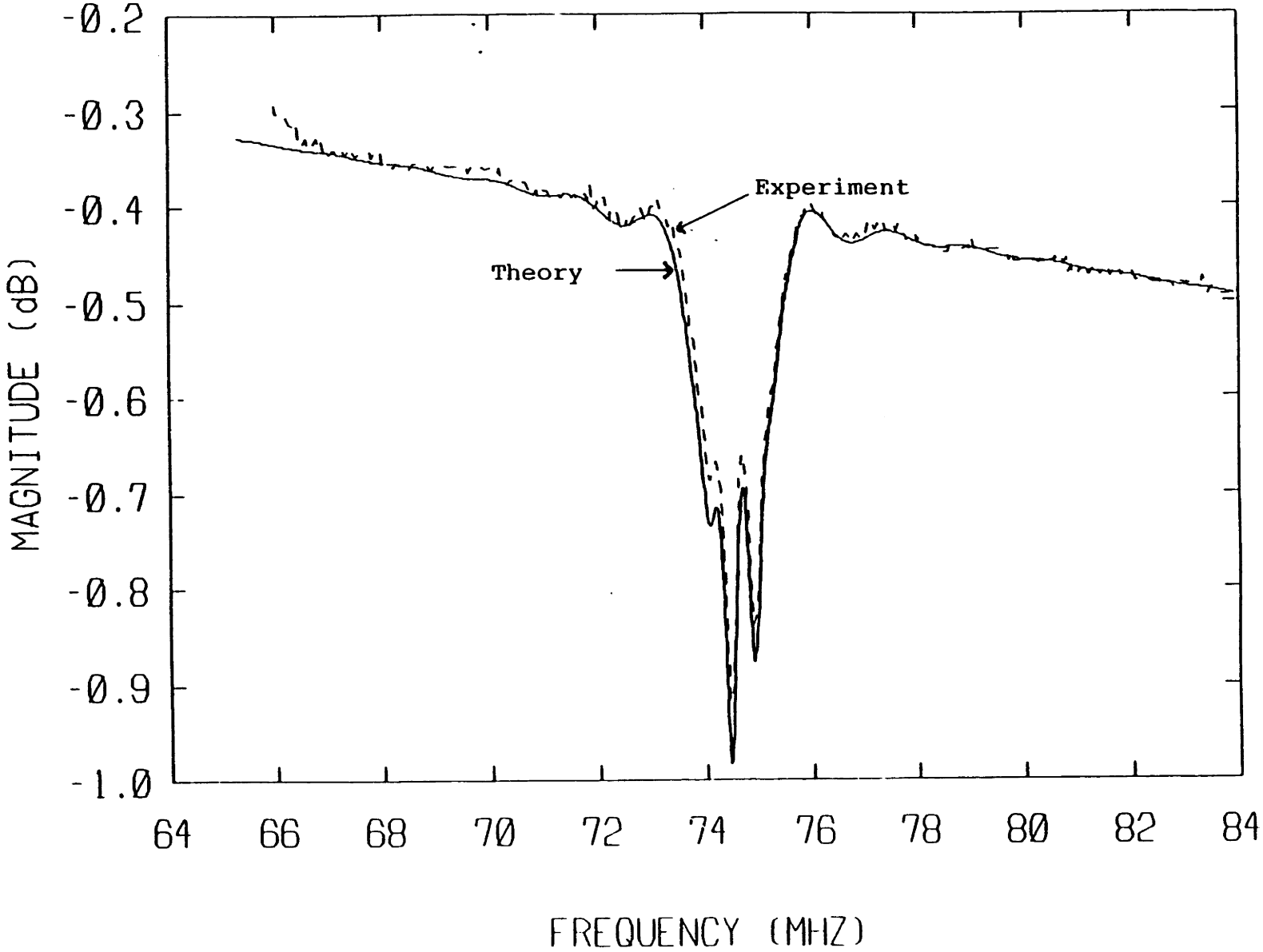

Figure 5.3c Return Loss S_{11}^F for an Unmatched SPUDT—Adjusted Parameters
This data was taken in a 50 Ω system. The parameters of Table 5.1 were used except for the modifications summarized in Table 5.2.

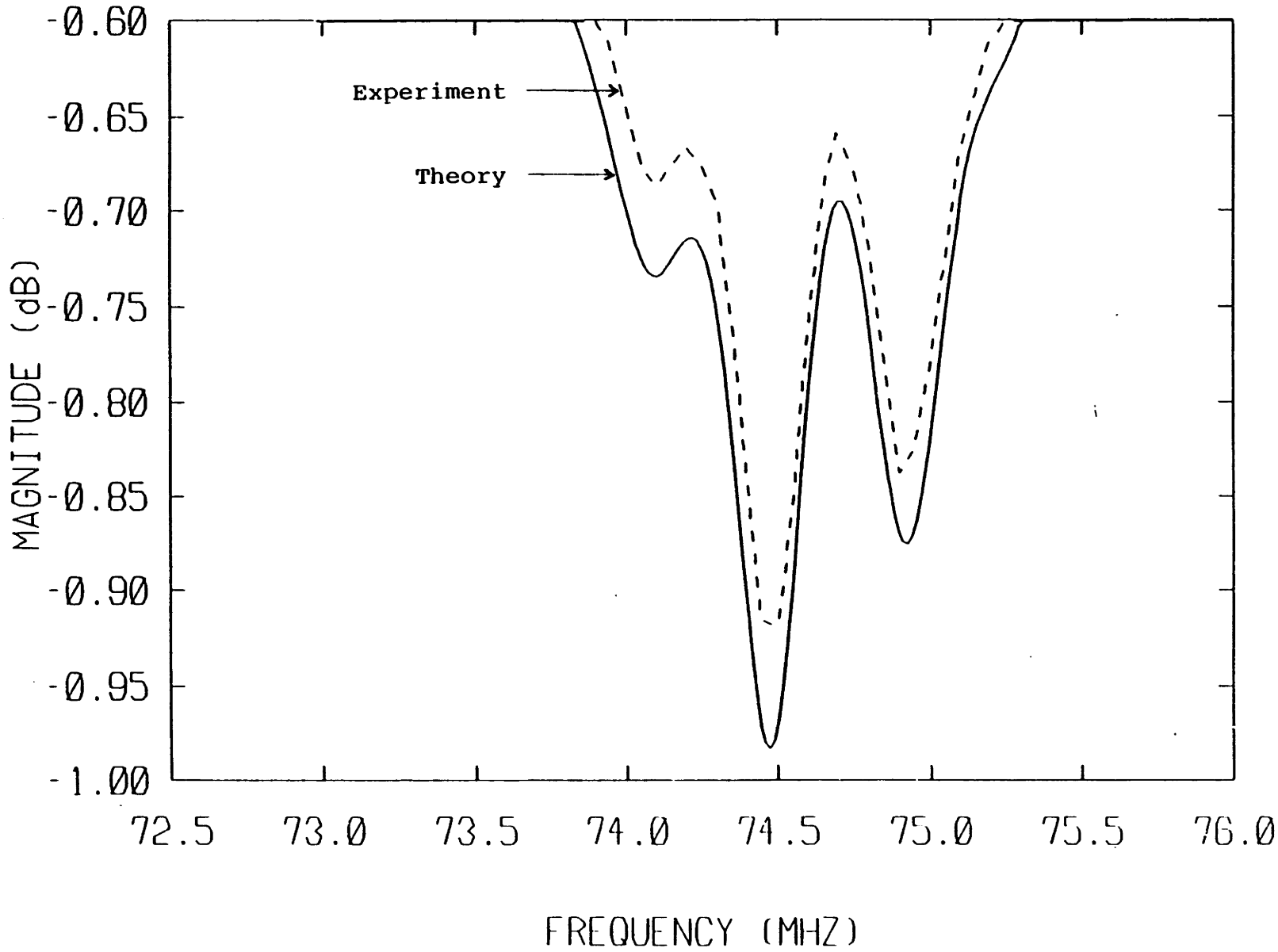

Figure 5.3d Return Loss S_{11}^F for an Unmatched SPUDT—Adjusted Parameters
This data was taken in a 50 Ω system. The parameters of Table 5.1 were used except for the modifications summarized in Table 5.2.

agreement is quite good in the passband* and the highest sidelobes. The lower level sidelobes (below -60 dB) on the high frequency side are corrupted by bulk modes which were not included in the model. Low level sidelobes were also affected by direct electromagnetic coupling between the transducers.

The corresponding theoretical and experimental impulse responses obtained by a digital Fourier transform of the frequency data of Fig. 5.3 after down shifting to DC is displayed in Fig. 5.4. The high triple transit signal at 3 μsec delay caused by the reflections from the gold fingers is responsible for the passband ripple of Fig. 5.3b. The electromagnetic coupling is present in the experimental impulse response in the spike near 0 time. The discrepancy between theory and experiment for large time is probably due to bulk modes.

It is disturbing that the mechanical reflection coefficient, κ, had to be reduced to obtain good agreement between theory and experiment, especially since κ was determined experimentally. Since the test structure was fabricated on a different slice, it is conceivable that the processing wasn't done exactly the same way on the two slices. Before it can be concluded that something is wrong with the theory, the experiments should be repeated with both the test structure and the device on the same wafer.

The sheet resistivity, ρ_s, was obtained by measuring the DC resistance of a section of the bus bar. Since the measurement was taken a long time after the device was fabricated, care had to be taken to scratch through the oxide layer with the probes to obtain good electrical contact to the aluminum. The sheet resistivity was measured to be .2 Ω /square. It thus seems that resistive loss is not being modeled properly since ρ_s had to be increased to .66 Ω /square** to obtain good agreement. One possible explanation is that in the loss calculation the current was assumed to be distributed uniformly throughout the cross

* Agreement in the passband could have been made even better by slightly increasing the propagation loss γ, but the author thought it would be best to adjust the minimum number of parameters necessary to obtain good agreement.

**It is conceivable that the resistivity at 74.6 MHz is higher than at DC. At extremely high frequencies skin depth can be a problem, but here it is not, since the skin depth is 9.8 μ while the aluminum film is only .2 μ thick.

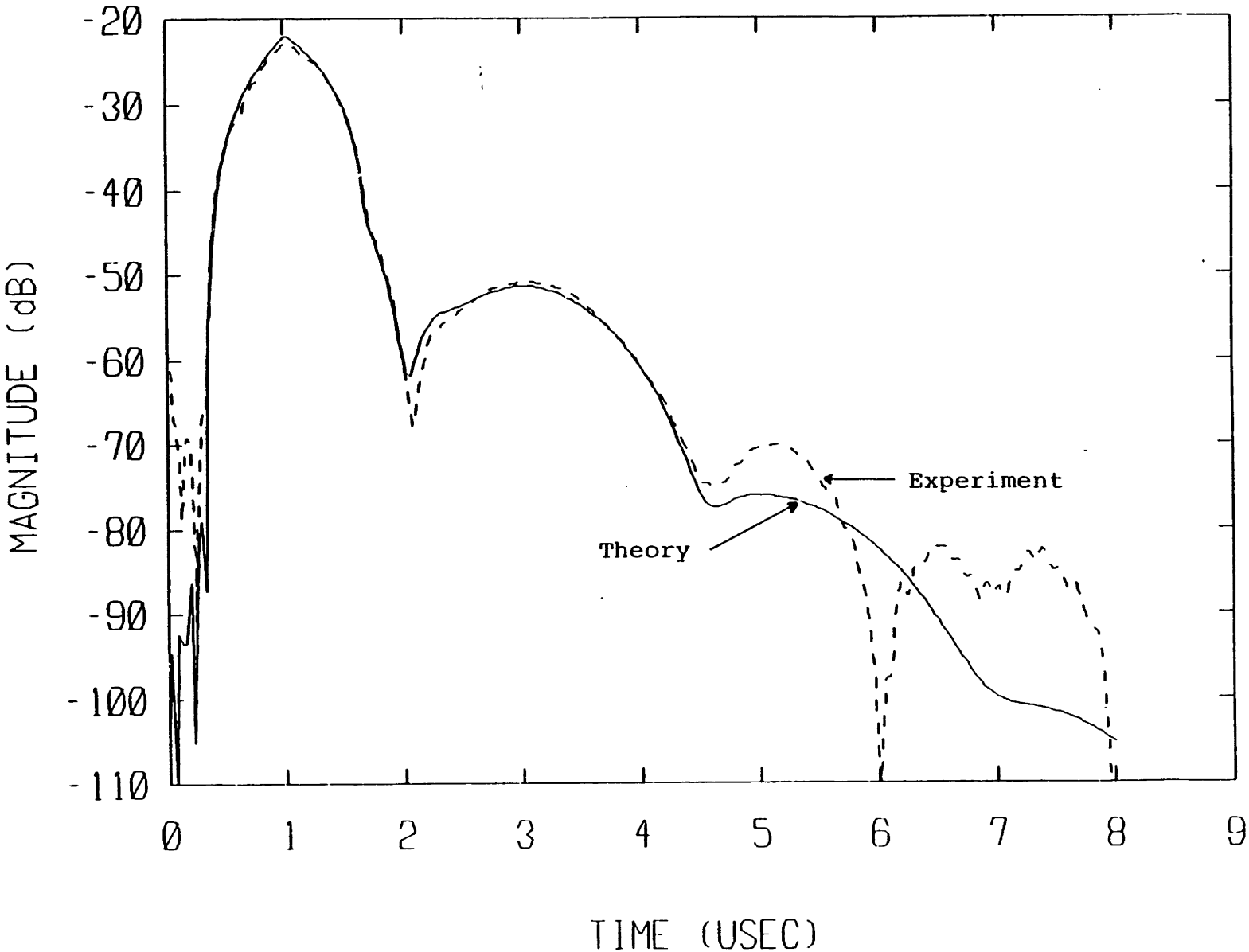

Figure 5.4 Insertion Loss S_{21}^E Time Response for an Unmatched SPUDT—Adjusted Parameters

These results are the digital Fourier transform of the results of Fig. 5.3. This data was taken in a 50 Ω system. The parameters of Table 5.1 were used except for the modifications summarized in Table 5.2.

section of a finger. Actually, the current is higher at the gap edges where the E-field is largest, as is the charge distribution plotted in Fig. 3.10. This will increase the equivalent resistance of a finger. For the SPUDT, this effect will be enhanced since the ion beam etching of the gold (discussed in Sec. 5.1) will thin the aluminum at the edges along with reducing the metalization ratio.

Further experimental and theoretical work is required to accurately determine why the reflection coefficient and sheet resistivity values had to be adjusted. Nevertheless, it is clear from the agreement between the experimental and theoretical results with modified parameters, that coupling of modes is capable of modeling transducers with internal reflection, and that resistive loss is responsible for the higher insertion loss and return loss.

Experiments were also conducted under conditions of a partial electrical match in order to check the concept behind the SPUDT. Air core inductors were placed in parallel with both transducers to cancel the capacitive admittance at the center frequency, and 3:1 trifilar [91,106] transformers were used to raise the impedance level to 450 Ω. This resulted in a minimum insertion loss of 11.3 dB (Fig. 5.5)*. The two trifilar transformers operated back-to-back accounted for 1.2 dB of loss, meaning that the filter itself exhibited a minimum insertion loss of 10.1 dB, which is 15 dB better than in the unmatched case. The discrepancy between the experimental and theoretical frequency responses is somewhat larger in the matched case probably due to increased spurious electromagnetic coupling arising from the matching circuit coils. This is exhibited in the impulse responses of Fig. 5.6 by the increased response at 0 time. Nevertheless, agreement is still quite good close to the center frequency, except for the slight increase in insertion loss.

* A perfect electrical match could be obtained and would result in lower insertion loss. It would be undesirable since then the reflection coefficient of the gold grating would not be large enough to cancel the reflection due to piezoelectric regeneration, and the triple transit signal would increase.

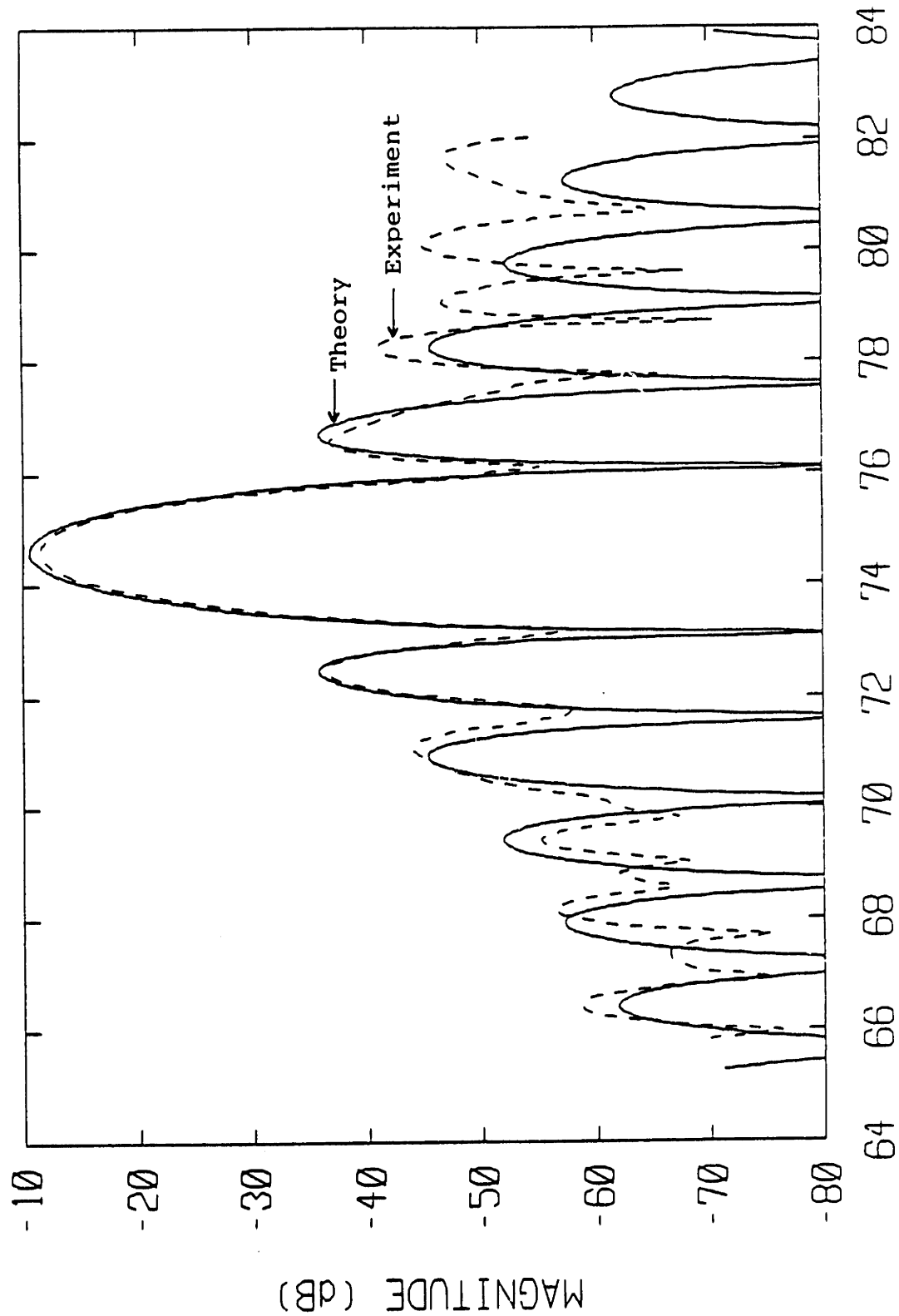

Figure 5.5 Insertion Loss S_{21}^F for Partially Matched SPUDT—Adjusted Parameters
This data was taken at a 450 Ω impedance level. The parameters of Table 5.1 were used except for the modifications summarized in Table 5.2.

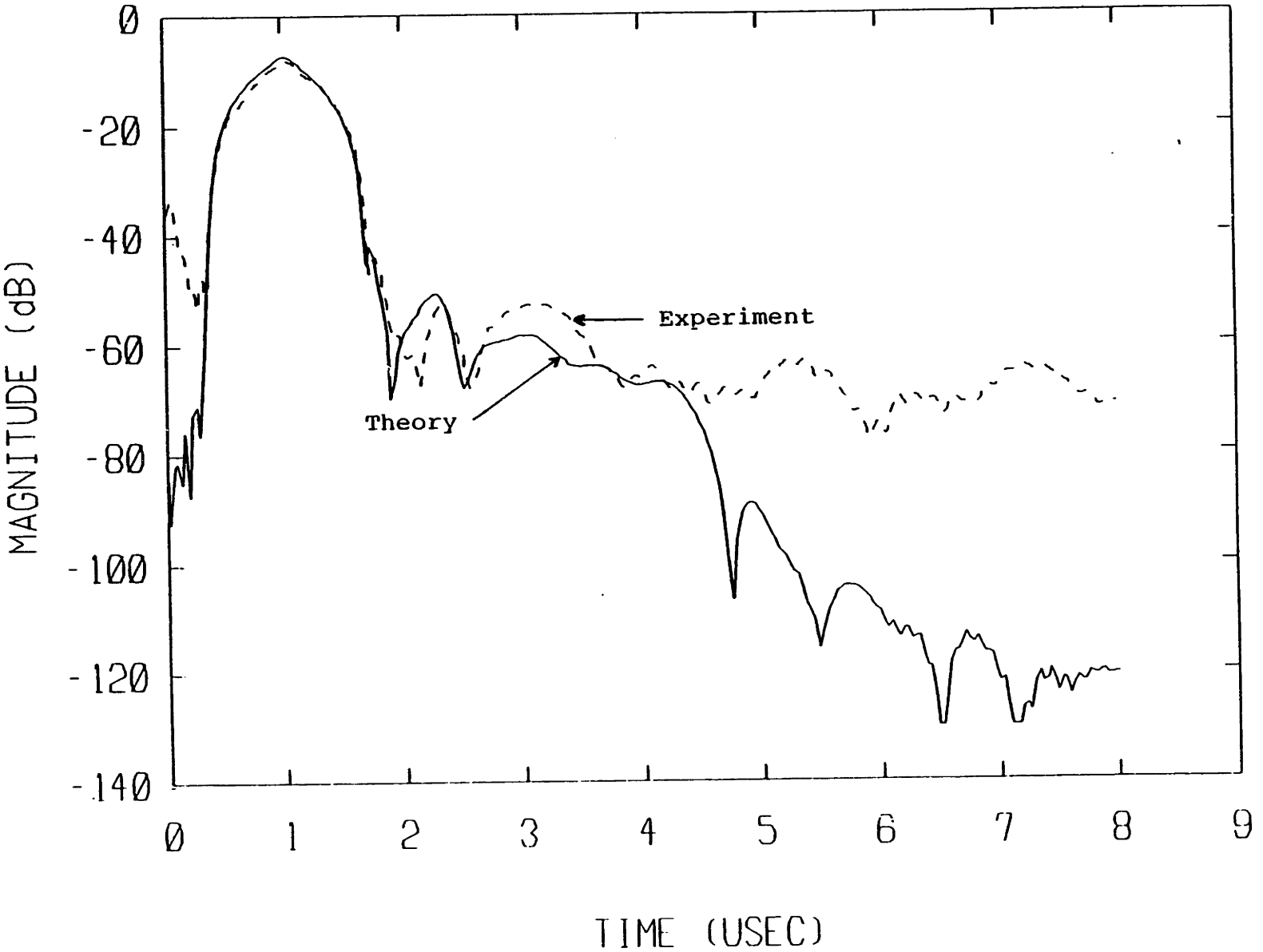

Figure 5.6 Insertion Loss S_{21}^E Time Response for a Partially Matched SPUDT—Adjusted Parameters

These results are the digital Fourier transform of the results of Fig. 5.5. This data was taken at a 450 Ω impedance level. The parameters of Table 5.1 were used except for the modifications summarized in Table 5.2.

	Unmatched	Matched
Insertion Loss	24.8 dB	10.1 dB
Triple Transit Level	-28.2 dB	-44.6 dB

Table 5.3 Performance of the SPUDT

The most obvious change from the unmatched case is the elimination of the passband ripple caused by the triple transit signal. The tremendous reduction in the triple transit signal, to – 44.6 dB below the main acoustic response, can be seen in the impulse responses presented in Fig. 5.6*. The fact that triple transit fell along with a reduction in insertion loss, which is precisely the opposite of what would happen with a standard bidirectional transducer, confirms the concept behind the SPUDT. Using Eq. (4.8), we compute that a lossless bidirectional IDT with the same 10.1 dB insertion loss as the SPUDT would have only 28.5 dB of triple transit suppression. Thus the SPUDT's triple transit suppression is 16.1 dB better. The results for the unmatched and partially matched cases are summarized in Table 5.3.

5.3 Conclusion

The experimental uniform single phase unidirectional transducer (SPUDT) did indeed work as expected. As the device was better matched, insertion loss fell along with a reduction in the triple transit level, unlike a standard bi-directional (BIDT) IDT. Indeed, the triple transit level of the SPUDT, which achieved 10.1 dB insertion loss, was 16.1 dB better than a BIDT matched for the same insertion loss. The coupled mode equations

* This reduction in the theoretical response is also responsible for an apparent increase in the bulk mode response in the matched case. Actually the bulk mode level is about 60 dB below that of the main acoustic signal in both cases.

were successful at modeling the SPUDT which critically depends on the interplay between distributed reflection and transduction.

There were two problems. One was that the reflection coefficient measured on a test structure had to be reduced by about a factor of two in order to obtain good agreement between theory and experiment. Since the test structure was fabricated on a different slice, it is possible that a difference in reflector thickness can account for this. The second problem was that the nominal aluminum sheet resistance had to be multiplied by about a factor of 4 in order to obtain good agreement. This may be due in part to inadequate modeling of the cross sectional current distribution of a finger, and to fabrication difficulties.

PART II

PHASE-ONLY

WEIGHTING

CHAPTER 6

PHASE-ONLY WEIGHTING

In this chapter, the design of SAW filters of uniform acoustic aperture is discussed. The design is based on the simplest analysis technique, Hartmann's impulse model [41], although a modification to the technique is discussed which can correct for higher order effects. The time or space domain weighting necessary to achieve good frequency responses is ultimately done solely by varying the spacing between sources of uniform strength. This result is obtained in three steps. First a low dynamic range amplitude and phase modulated (AM-PM) waveform is designed using a quasi-Newton optimization procedure. Then the design is nonuniformly sampled, and finally an improved version of Hartmann's [42] withdrawal weighting technique is used to reduce the dynamic range to unity. In addition, new structures are discussed which increase the accuracy of the withdrawal weighted approximation to the AM-PM prototype. This increases the bandwidth over which the filters' rejection band performance is good, and also reduces passband ripple.

6.1 Introduction

Much work has been done on periodically sampled finite impulse response filter synthesis in the digital signal processing field. The key result of this work is the Parks-McClellan [85,80] application of the Remez exchange algorithm [12] to this problem which yields linear phase filters that are optimal in the minimax sense. This technique is not

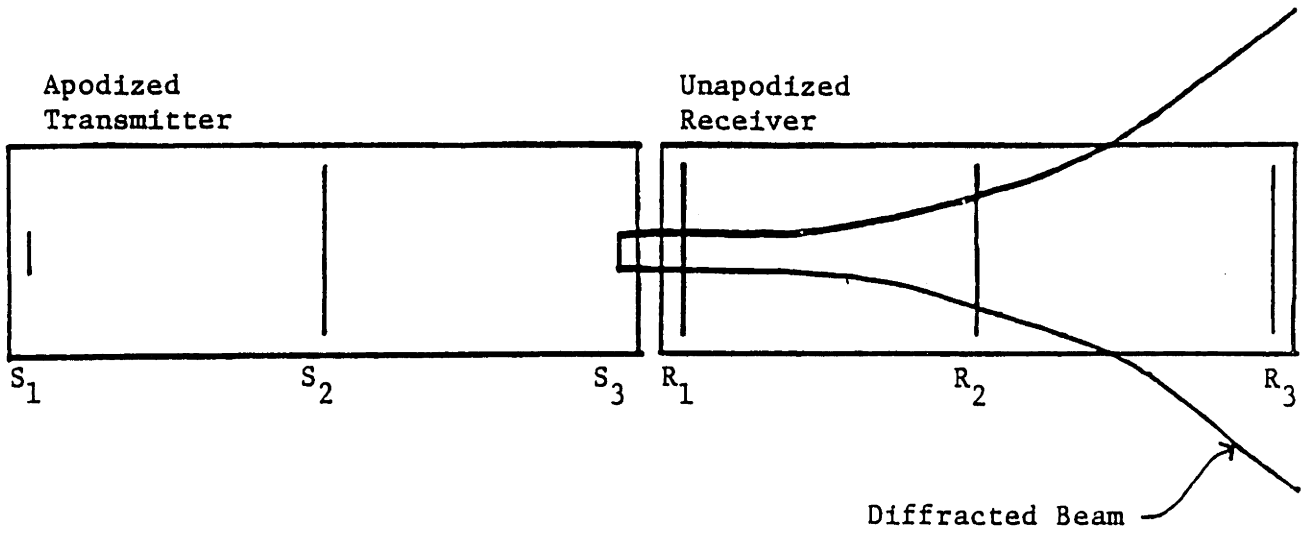

Figure 6.1 Fundamental Problem of Diffraction Compensation
Receiving aperture R1 could be in the Fresnel zone of source S3 while R3 could be in the Fraunhofer zone. Sources S1, S2 and receiving apertures R1, R3 can not be adjusted so that all 4 transfer ratios are correct simultaneously.

directly applicable to the design of moderate bandwidth, low shape factor SAW filters with low sidelobes and small passband ripple. The problem is that for high performance filters, the Remez algorithm yields weights with a large dynamic range. The response of a SAW filter of reasonable maximum aperture apodized with these weights will be degraded by diffraction [56,104,82] and transverse electrostatic end effects [107], preventing these weights from being achieved in practice.

For small overlaps, the fringing fields at the finger ends are significant and must be included to obtain the proper weighting. In principle, once the effect is computed, compensation should be relatively easy. In practice, however, fabrication inaccuracies may make this difficult. Diffraction compensation is much more difficult although some progress has been made [64,102]. The problem is illustrated in Fig. 6.1. Assume the first interdigital transducer (IDT), IDT1 is apodized and IDT2 is not, so that the full filter transfer function is approximately proportional to the product of the transfer functions of the individual transducers. In a sharp cut-off filter, S1 and S3 will be small aperture

sources since roughly speaking, they will be in the sidelobes of a $\sin(x)/x$ pattern. If the receiving transducer were very short, then the source strengths S1, S2 and S3 could simply be adjusted so they would be received in proper proportion at the location of the receiving transducer. However, when both the transmitting and receiving transducers are long, compensation is very difficult.

For example, receiving aperture R1 will be in the near Fresnel region of the diffraction pattern of source S3, thus the beam will spread very little, and there is no need to adjust the source aperture. On the other hand, receiving aperture R3 could very easily be in the Fraunhofer region of the diffraction pattern of source S3, and thus due to a large spreading of the beam, would pick up a reduced source strength. R3 could be increased to properly compensate for reception from S3 but then it would be much too small for reception from source S1 which would be even further into the Fraunhofer region.

In order to permit the ultimate in diffraction suppression, our goal is to design a filter in which the source weighting is achieved solely by adjusting the locations of sources, and not their strengths. Apodization could then be reserved for diffraction suppression. If arbitrary spacing of the sources is permitted, then linear phase will not result for each of the electroacoustic transfer functions. The total transfer function, $T(\beta)$, (copying Eq. 3.85), ignoring circuit factors, diffraction and reflections is

$$T(\beta) = -\frac{\omega W G_a}{4}|\sigma_o(\beta)|^2 \left[\sum_i S_i^1 \left(\frac{\beta_o}{\beta_i}\right)^q e^{j\beta x_i}\right] \left[\sum_k S_k^2 \left(\frac{\beta_o}{\beta_k}\right)^q e^{-j\beta y_k}\right] \qquad (6.1)$$

where the sources are located at x_i and the receivers at y_k, S_i^1 and S_i^2 are the strengths of the transmitting and receiving sources, β_i is the synchronous wavenumber, and q is a small* parameter which adjusts for source strength variations due to slight aperiodic spacing.

* q is .081 for 50% metalized gaps (See Sec. 3.9.1 and Fig. 3.16)

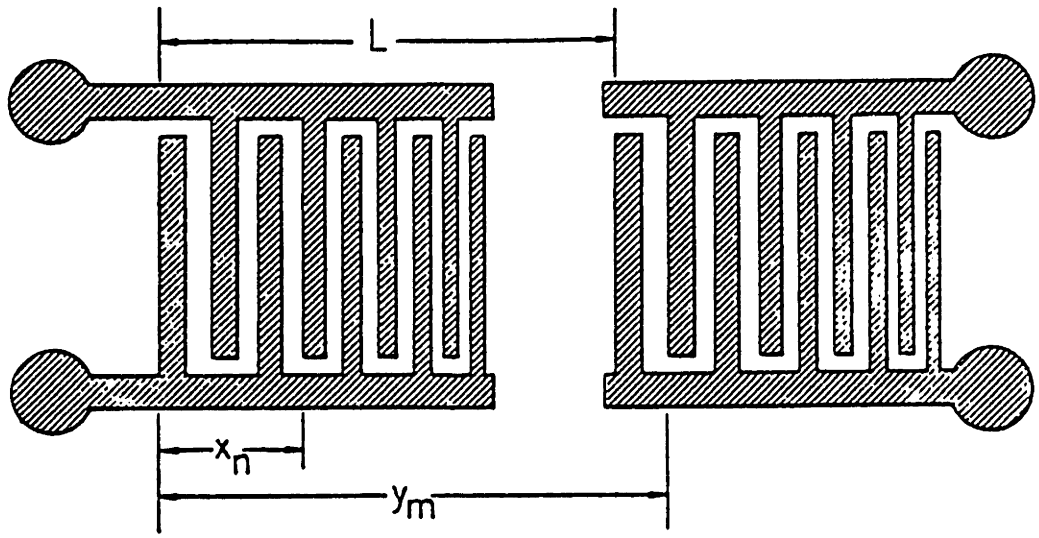

Figure 6.2 Nondispersive Filter Constructed from Two Nonuniformly Spaced Transducers The receiving and transmitting transducers form a matched pair. Note that $y_m = L + x_m$ (After [105])

We note that if the locations of the sources of the second IDT, y_k, are simply shifted by a constant distance, L, (See Fig. 6.2) from those of the input transducer, x_j, and if $S_j^1 = S_j^2$ for all j, then the transfer function will possess linear phase for arbitrarily spaced sources.

$$T(\beta) = -\frac{\omega W G_s}{4} |\sigma_o(\beta)|^2 e^{-j\beta L} \left| \sum_i S_i^1 \left(\frac{\beta_0}{\beta_i}\right)^q e^{j\beta x_i} \right|^2 \tag{6.2}$$

In this case the receiving transducer is matched to the transmitting one so that any dispersion is canceled. To make the formula more familiar to the signal processing community, in the remainder of this chapter βx_j will be replaced by $2\pi f x_j / v = 2\pi f t_j$, the linear phase term will be dropped and the element factor, $e(f)$, will be identified with

$$e(f) = -\frac{2\pi f W G_s}{4} \left| \sigma_o \left(\frac{2\pi f}{v}\right) \right|^2 \tag{6.3}$$

$$T(f) = e(f) \left| \sum_i S_i \left(\frac{f_o}{f_i}\right)^q e^{j2\pi f t_i} \right|^2 \tag{6.4}$$

For simplicity we will now ignore the element factor and we will assume that q is zero, in addition to neglecting diffraction, and all circuit loading and internal reflection effects. We will also ignore insertion loss and allow for an arbitrary gain factor, g. Later we will examine how these higher order effects can be handled. With these assumptions, the achievable frequency response is

$$M_A(f) = g\left|\sum_i S_i e^{j2\pi f t_i}\right|^2 \tag{6.5}$$

The desired frequency response to be approximated, $M_D(f)$, would typically be a sharp cut-off band pass filter (see Fig. 6.3). The desired response is unity in the passband and zero in the rejection band, with the response unspecified in the transition regions. The transition regions must be of finite width in order to obtain a finite length impulse response. Any achievable frequency response permitted by Eq. (6.5) will of course have some finite maximum error δ_1, in the passband and δ_2 in the rejection band. The problem at hand is then to select the times for the impulses t_j, and their sign S_j, to best approximate $M_D(f)$ with $M_A(f)$. Typically, a weighted minimax approximation would be desired, and then the error to be minimized is

$$E_f = \max_{f\in\left\{\begin{matrix}\text{rejection band}\\ \text{or passband}\end{matrix}\right\}} W(f)\,|M_D(f) - M_A(f)| \tag{6.6}$$

where $W(f)$ is a positive weighting function to permit the error to be of varying size in different frequency ranges.

The solution of the problem is very difficult for three reasons:

1) High performance filters, i.e. filters with low shape factors, low passband ripple and low sidelobes, can easily require hundreds of source samples (see Sec. 6.5.3). This is a

large scale time consuming problem to solve directly with an optimization algorithm, since the number of function evaluations required with a quasi-Newton optimization procedure using numerical differentiation is $O(N^2)$ (see Sec. 6.3.2), where N is the number of variables.

2) The S_j are discrete variables, with permissible values -1, 0, 1, and thus no derivatives can be defined which are necessary for continuous optimization procedures. Integer optimization techniques must be invoked which are very time consuming due to their combinatorial nature. Also these procedures are not as highly developed as their continuous counterparts [29] .

3) The times at which the sources occur enter into the desired function nonlinearly. Thus the Remez exchange algorithm [12] can not be used directly. Furthermore, even if Eq. (6.5) were linearized about t_{jo} , the resulting expression would not be in the form of a linear superposition of functions needed for the Remez algorithm due to presence of the magnitude squared.

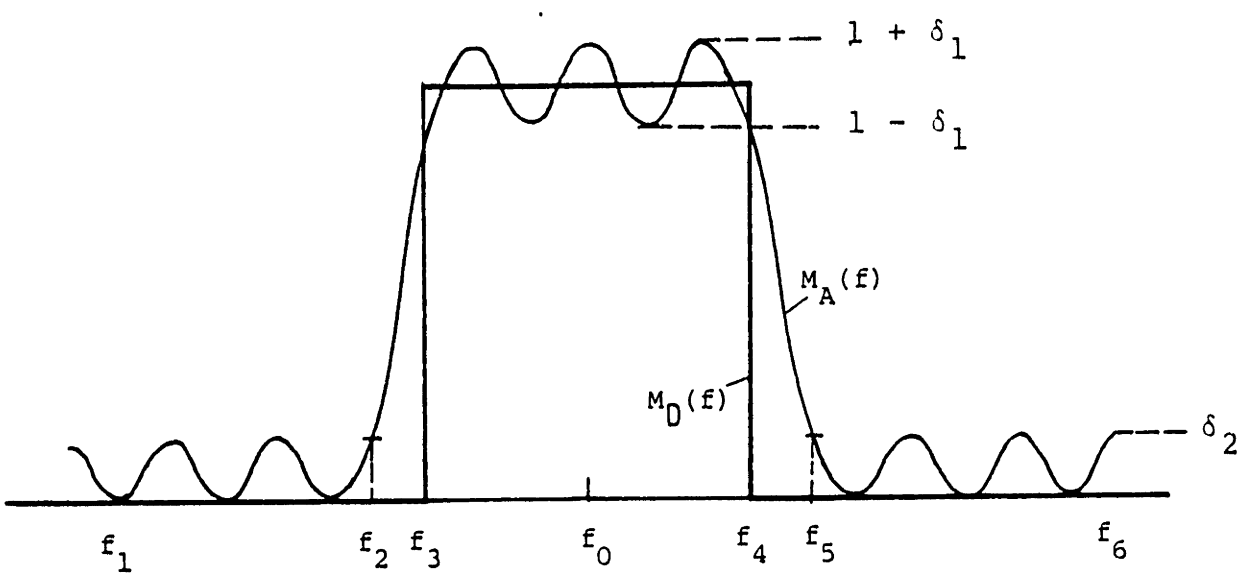

Figure 6.3 Sharp Cut-Off Bandpass Filter
Shape Factor = $(f_5 - f_2)/(f_4 - f_3)$
Achievable Frequency Response= $M_A(f)$
Desired Frequency Response= $M_D(f)$

The Remez algorithm is very efficient and can be used to find the solution to minimax approximation problems with hundreds of parameters. In our case, it seems that only general optimization procedures can be used which can not accommodate such a large number of parameters. Thus it is not really practical to directly minimize the error of Eq. (6.6)

Our approach, based on the necessity to tremendously reduce the number of parameters, is to split the problem into three parts. The basic outline is similar to that used by Hartmann [42]. First we design an amplitude and phase modulated (AM-PM) waveform, whose magnitude squared Fourier transform approximates the desired frequency response. In designing this waveform we try to keep the time envelope as flat as possible to facilitate the final step. Hartmann uses an iterative time-frequency approach to accomplish this, while others [30,75] have based their waveform design on the stationary phase approximation. In this thesis, a quasi-Newton [29] optimization procedure is used with multiple criteria. We shall see that this enables us to achieve substantially better frequency responses with the same size structure.

The second step is to sample this continuous AM-PM waveform. The standard technique of sampling at phase increments of π radians is used. Finally we use an improved version of Hartmann's [42] withdrawal weighting procedure to approximate the amplitude and phase modulated (AM-PM) signal with a uniform amplitude PM signal. The flatter the initial envelope produced by step-I, the better this approximation will be. Our withdrawal weighting technique is an extension of the standard one. Multiple envelopes are used, in addition to optimization over the quantization step, to broaden the bandwidth over which the withdrawal weighted frequency response closely approximates that of the AM-PM prototype. An improved structure which allows successive source weights to be of

the same sign also contributes to the broadening of the bandwidth over which withdrawal weighting is useful. Furthermore, it allows passband ripple to be reduced.

6.2 Optimal Design of Low Dynamic Range Amplitude and Phase Modulated Waveforms

At first we will ignore element factors, circuit loading effects, diffraction and all other second order effects. Then since the two transducers form a matched pair, the filter's frequency response is the squared magnitude of the Fourier transform of the impulse response of each transducer. The phase of the frequency response of each transducer cancels in the full filter transfer function.

We expect that the phase in the frequency domain will affect the impulse response. Certain phases may yield a lower dynamic range time response than others. For example, zero phase when associated with an ideal *brick wall* bandpass function yields a $\sin(x)/x$ time response which has a very large dynamic range. A quadratic phase which linearly chirps across the passband frequency range has a constant time envelope, but yet yields a *brick wall* frequency response in the limit of a very slow chirp rate, i.e. large time-bandwidth product [30] and long impulse response. Here we strive to achieve a design which lies between these two extremes.

Another degree of freedom is the shape of the transition band between the rejection band and passband. This algorithm selects the phase response and transition band shape in such a way so as to minimize the deviation between the desired and achieved frequency responses in the passband and rejection band. It simultaneously tries to obtain a relatively low dynamic range time envelope.

The parameterization for the optimization procedure is displayed in Fig. 6.4. First the frequency ranges for the reject, transition and pass bands are defined. Unity is typically

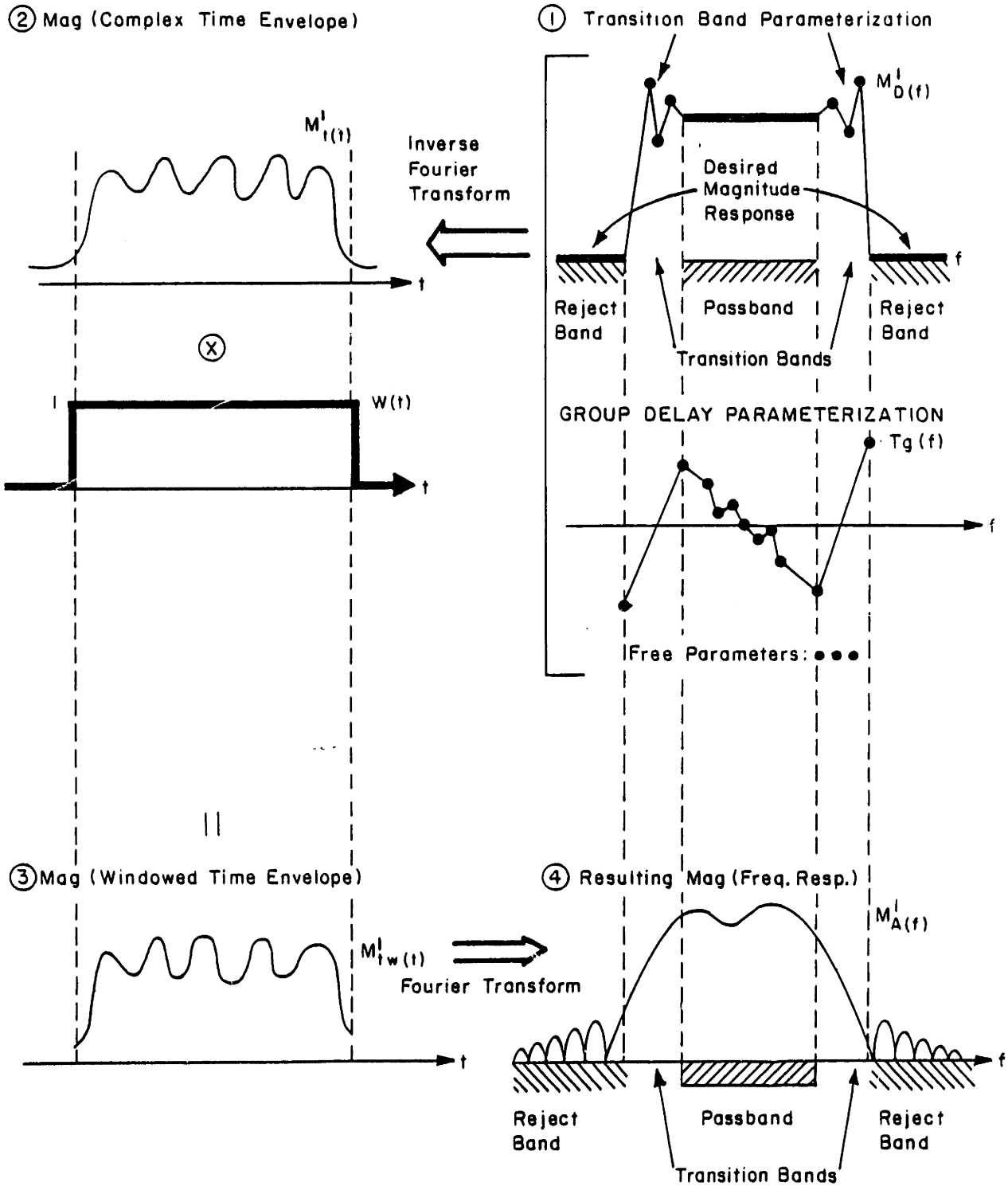

Figure 6.4 Parameterization and Signal Definition

1) The desired single transducer magnitude response is associated with the phase and transition band responses determined by the specified parameters. 2,3) This desired frequency response, $H^{1}_{D}(f)$, is inverse Fourier transformed to the time domain and windowed. The dynamic range of the time envelope is evaluated. 4) Finally the achieved frequency response is determined by Fourier transforming this truncated time response and computing the magnitude squared. The difference between the desired and achieved two-transducer frequency responses is examined to determine the frequency error.

selected for the desired passband frequency response although any shape is realizable. The desired rejection band response is zero, and the transition band shape is left unspecified. We parameterize the single transducer group delay by a few sample values. Linear interpolation is used to evaluate the group delay between sample points. Since the phase function is proportional to the integral of the group delay, the phase consists of segments of quadratic phase with both continuous function value and first derivative at the break points. The single transducer transition band response is parameterized in a similar manner, by samples of the magnitude response along with linear interpolation.

Once the desired full filter magnitude response, $M_D(f)$, is specified, and parameter values are determined, the entire initial single transducer frequency response is known. In the passband and rejection band, the square root of the desired full filter magnitude response is the desired magnitude response of each transducer, $M_D^1(f)$. In the transition band the parameterization directly specifies the desired single transducer magnitude response. The phase determined by the group delay parameterization is then associated with $M_D^1(f)$ to determine the full complex desired frequency response of each transducer, $H_D^1(f)$. As shown in Fig. 6.4, $H_D^1(f)$ is inverse Fourier transformed to the time domain, and then windowed to obtain the time envelope magnitude $M_{tw}^1(t)$. A time response error, E_t, is defined which measures the deviation of the envelope magnitude from its average value:

$$E_t = \left[\frac{1}{N_t} \sum_{i=1}^{N_t} e_{ti}^{2p_t} \right]^{1/Q_t} \tag{6.7}$$

where $e_{ti} = M_{tw}^1(t_i) - aV_t$, and aV_t is average time envelope magnitude.

The error of Eq. (6.7) is called an L_{2p_t} error definition. In the limit as p_t approaches infinity, E_t is dominated more and more by its largest term, and the error definition approaches the minimax one. Q_t does not affect the location of the minimum, but aids

in normalizing the error and affects the efficiency of the procedure. This procedure of optimizing in the minimax sense with a sequence of continuously differentiable L_{2p_f} errors was first proposed by Polya [84,88,28] . It has only been proven rigorously in the case of a linear superposition of functions, but its connection with the minimax error definition is so intuitive that it seems reasonable to try it in this nonlinear optimization problem.

Next we Fourier transform the windowed time response back to the frequency domain and find the magnitude squared to obtain the achieved frequency response, $M_A(f) = (M_A^1(f))^2$. The weighted deviation between the achieved response $M_A(f)$, and the desired response, $M_D(f)$, outside of the transition band is the frequency response error:

$$E_f = \left[\frac{1}{N_f} \sum_{i=1}^{N_f} (w_i e_{fi})^{2p_f} \right]^{1/Q_f} \tag{6.8}$$

where

$$e_{fi} = \begin{cases} M_A(f_i) - M_D(f_i) & \text{Passband} \\ \dfrac{M_A(f_i)}{\text{Average-passband-value}} & \text{Reject-band} \end{cases}$$

Note that the rejection band error is defined relative to the average passband level. This prevents the optimization procedure from attempting to improve the rejection level by reducing the overall gain. Again a minimax approximation is obtained in the limit as p_f approaches infinity. The error weights, w_i , allow reduced passband ripple to be traded for increased sidelobe rejection.

Another way of obtaining a minimax approximation for a continuously differentiable error definition is via a sequence of weighted L_2 optimizations. A procedure of this type is the Lawson [59,89] algorithm and is based on the intuitive idea of increasing the weight where the error is too large, and conversely reducing the weight where the error is smaller

than it needs to be. This is an alternative function of the weights w_i in the frequency error definition.

The total error to be minimized is

$$E = W_{tf} E_t + E_f \tag{6.9}$$

where W_{tf} is a parameter used to trade reduced frequency response error for increased time response dynamic range. As W_{tf} becomes smaller, the frequency response of the amplitude and phase modulated (AM-PM) waveform will improve, but the withdrawal weighted uniform aperture approximation will not be as accurate.

6.2.1 Baseband Fourier Analysis

In order to reduce the amount of computation required, all the Fourier transforms indicated in Fig. 6.4 are done baseband. This enables us to select a sampling interval for the transforms that is appropriate for the slowly varying time envelope rather than for the rapidly varying carrier frequency. We define the baseband desired frequency response, $H_{db}(f)$, as the upper half of the frequency response down shifted to DC (see Fig. 6.5).

$$\begin{aligned} H_{db}(f) &= H_d(f + f_0)U_{-1}(f + f_0) \\ U_{-1}(f) &= \text{Unit step function} \end{aligned} \tag{6.10}$$

The final frequency response is clearly

$$H_d(f) = H_{db}(f - f_0) + H^*_{db}(f + f_0) \tag{6.11}$$

since the initial impulse response is real. Using some symmetry properties of the Fourier transform [78], we express the full impulse response in terms of the desired baseband impulse response, $h_{db}(t)$

$$\begin{aligned} h(t) &= h_{db}(t)e^{j2\pi f_0 t} + h_{db}^*(t)e^{-j2\pi f_0 t} \\ &= 2Re\left[h_{db}(t)e^{j2\pi f_0 t}\right] \\ &= 2|h_{db}(t)|\cos[2\pi f_0 t + arg(h_{db}(t))] \end{aligned} \tag{6.12}$$

The time windowing is actually done on $h_{db}(t)$ yielding $h_{wb}(t)$ whose Fourier transform is $H_{wb}(f)$. The time envelope used to measure the deviation from flatness, E_t, is precisely $h_{wb}(t)$. The final achieved bandpass frequency response with the current parameter set is then

$$H_a(f) = H_{wb}(f - f_0) + H_{wb}^*(f + f_0) \tag{6.13}$$

It should be noted that this baseband procedure is mathematically equivalent to working with the full modulated time signal and frequency response. It therefore works equally well for low and high fractional bandwidth signals and for signals with little or much phase modulation.

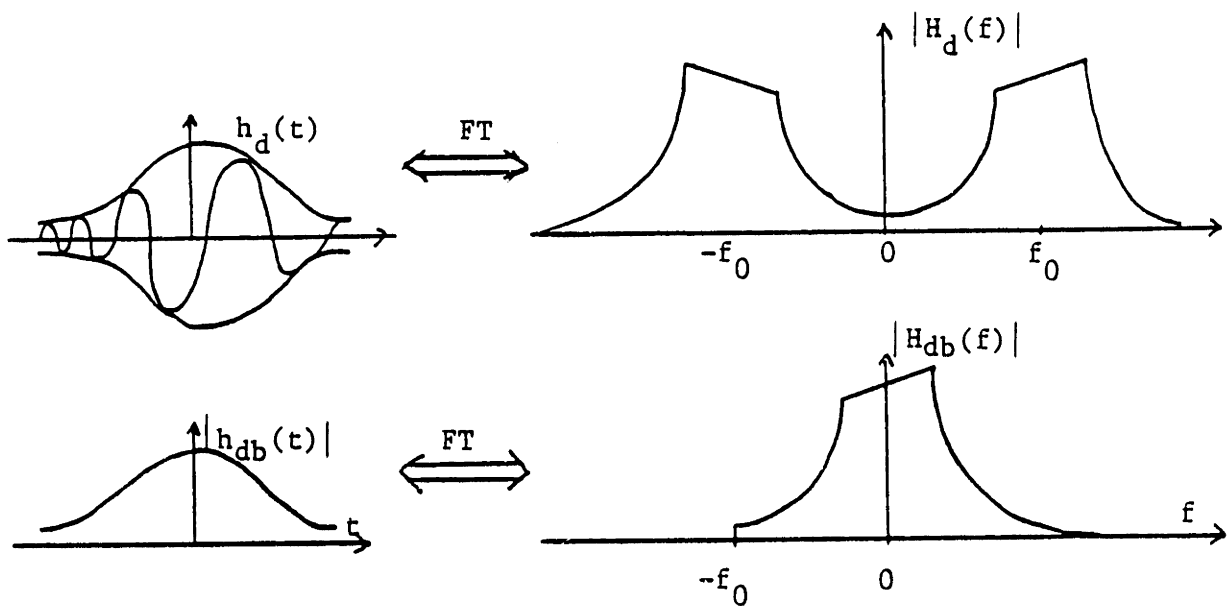

Figure 6.5 Baseband Representation of Bandpass Signals
a) The real modulated waveform and its Fourier transform.
b) The baseband complex impulse response and its Fourier transform.

6.3 The Optimization Algorithm

A full description of optimization procedures is quite lengthy and can be found in references [29,6,33,74] . Here we summarize some key results and provide some information as to how these techniques apply in this particular case.

6.3.1 The Newton Procedure

It is generally accepted that for smooth functions, when analytical formulas are available for the gradients and second derivatives, that the Newton method is best. It is an iterative technique which sequentially improves the estimate of the optimum, $\bar{x}_k$. In a Newton method, at the current point $\bar{x}_k$, a Taylor series expansion to second order in all N variables is computed. Thus the function value, $f(\bar{x}_k)$, gradient vector $\bar{g}(\bar{x}_k)$, and the hessian matrix of second derivatives $\overline{\overline{G}}(\bar{x}_k)$ must be evaluated at this point. Letting $\bar{s}$ be a small vector deviation from the current point, the Taylor series expansion is

$$f(\bar{x}_k + \bar{s}) = f(\bar{x}_k) + \bar{g}^T(\bar{x}_k)\bar{s} + \bar{s}^T\overline{\overline{G}}(\bar{x}_k)\bar{s} \tag{6.14}$$

where

$$g_i(\bar{x}_k) = \frac{\partial f}{\partial x_i}$$

and

$$G_{ij}(\bar{x}_k) = \frac{\partial^2 f}{\partial x_i \partial x_j}$$

The stationary point of this second order approximation to the surface is the point at

which the total gradient is zero. It is selected as the next estimate of the optimum.

$$\begin{aligned} \bar{x}_{k+1} &= \bar{x}_k + \bar{s}_k \\ s_k &= -\bar{\bar{G}}^{-1} g_k \end{aligned} \tag{6.15}$$

This procedure is repeated until convergence is achieved.

Since most smooth functions are approximately quadratic near their minima, this procedure converges very rapidly. In fact, near the answer x^+, the deviation between the exact minimum and the current best point falls quadratically.

$$|\bar{x}_{k+1} - \bar{x}^+| = a|\bar{x}_k - \bar{x}^+|^2 \tag{6.16}$$

Frequently a line search is done in the direction $\bar{s}_k$ instead of selecting $\bar{s}_k$ as the step to the next estimate of the optimal point. This is especially important far from the optimum where the quadratic approximation to the surface is poor, and where stepping by $\bar{s}_k$ can even cause the function to increase. In this case

$$\bar{x}_{k+1} = \bar{x}_k + \alpha_k \bar{s}_k = x_k + \bar{\delta}_k \tag{6.17}$$

where α_k should approach unity near the solution. Modifications must also be made to handle the special case in which $\bar{\bar{G}}$ is indefinite, in order to prevent termination at a saddle point. A reasonable modification in this case is to search in the direction of maximum negative curvature.

6.3.2 The Quasi-Newton Algorithm

In our case, the Newton algorithm is not really applicable since the function to be minimized, E of Eq. (6.9), depends on its parameters in a particularly complicated manner, involving two Fourier transforms as illustrated in Fig. 6.4. Thus, analytically obtaining the gradient vector and hessian matrix would be very difficult. Furthermore, it would also be quite time consuming to evaluate the resulting expressions since they would involve Fourier transforms. The gradient and hessian could both be evaluated by numerical differentiation, but this would also be quite costly since the hessian which must be evaluated on each iteration requires $(N^2 + N)/2$ functional evaluations in addition to the N required to find the gradient.

A more appropriate technique is the quasi-Newton algorithm. It is similar to the Newton procedure except that the hessian matrix is not recomputed on each iteration. Instead, an estimate of the hessian, $\overline{\overline{B}}_k$, is iteratively improved based only on first derivative information. The hessian update is done so that the curvature of the function along the current search direction is incorporated in the new hessian estimate. Mathematically, we require the updated hessian to account for the exact difference in gradients between the current and next points when the gradient is expanded in a Taylor series to first order.

$$\bar{g}(\bar{x}_k + \bar{\delta}_k) = \bar{g}(\bar{x}_k) + \overline{\overline{B}}_{k+1}\bar{\delta}_k \tag{6.18}$$

or

$$\bar{g}_{k+1} - \bar{g}_k = \bar{\gamma}_k = \overline{\overline{B}}_{k+1}\bar{\delta}_k \tag{6.19}$$

Matrices obeying Eq. (6.18) are said to satisfy the quasi-Newton condition.

Since a hessian matrix is symmetric, we would also like the estimated hessian to be symmetric. Since the only new information obtained on each iteration is the function value

and the gradient, totaling $N+1$ scalar values, it is unreasonable to try to independently modify all $N(N+1)/2$ elements of the hessian matrix. A particularly simple update for a matrix would be one in which its columns were comprised of a linear superposition of just a few vectors. A symmetric rank 2* update of the form

$$\overline{\overline{B}}_{k+1} = \overline{\overline{B}}_k + a\bar{u}\,\bar{u}^T + b\bar{v}\,\bar{v}^T \tag{6.20}$$

satisfies this requirement. Vectors $\bar{u}$, $\bar{v}$ and scalars a, b are chosen such that the updated matrix, $\overline{\overline{B}}_{k+1}$, satisfies the quasi-Newton condition.

$$\bar{\gamma}_k = \overline{\overline{B}}_{k+1}\bar{\delta}_k = \overline{\overline{B}}_k\bar{\delta}_k + a\bar{u}\,\bar{u}^T\bar{\delta}_k + b\bar{v}v^T\bar{\delta}_k \tag{6.21}$$

A simple solution is $u = \gamma_k$ to yield γ_k on the left side, and $v = \overline{\overline{B}}_k\bar{\delta}_k$, to enable us to cancel the $\overline{\overline{B}}_k\bar{\delta}_k$ term which is already present. On plugging this assumed form in Eq. (6.21) we evaluate a and b to obtain

$$\overline{\overline{B}}_{k+1} = \overline{\overline{B}}_k + \frac{\bar{\gamma}_k\bar{\gamma}_k^T}{\bar{\gamma}_k^T\bar{\delta}_k} - \frac{\overline{\overline{B}}_k\bar{\delta}_k\bar{\delta}_k^T\overline{\overline{B}}}{\bar{\delta}_k^T\overline{\overline{B}}_k\bar{\delta}_k} \tag{6.22}$$

This is called the BFGS update after its inventors Broyden [10], Fletcher [27], Goldfarb [34] and Shano [94], who independently derived this formula. This solution is not unique. There is a single parameter set of symmetric rank-2 updating formulas, the Broyden family, but many authors [29,6,33] state that based on numerical experiments on a wide variety of problems that the BFGS formula is generally accepted to be the best.

*An even simpler rank one update is not used since the positive definiteness of the updated hessians can not be guaranteed [29]. This is necessary for convergence of a quasi-Newton procedure as will be discussed in Sec. 6.3.2.1.

6.3.2.1 General Properties

It is worthwhile summarizing some key theoretical features which indicate why the quasi-Newton procedure works so well. In order to make consistent progress toward the minimum, it is necessary that the search direction always be one in which the function decreases. Thus the projection of the search direction, $\bar{s}$, on the gradient, $\bar{g}$, must always be negative. Using $\overline{\overline{B}}_k$ in place of $\overline{\overline{G}}_k$ in Eq. (6.15) we obtain

$$\bar{s}_k^T \overline{\overline{B}}_k \bar{s} > 0 \tag{6.23}$$

This is the definition of positive definiteness for a matrix. It has been shown [27] for general functions, that if the initial hessian estimate is positive definite, so will all subsequent $\overline{\overline{B}}_k$'s, provided that all the line searches are sufficiently accurate. All that is required is that the directional derivative in the old search direction at the new point be greater than the derivative in this direction at the previous point.

$$\bar{s}_k^T \bar{g}_{k+1} > \bar{s}_k^T \bar{g}_k \tag{6.24}$$

This should never be a problem since $s_k^T g_k$ is always negative, and $s_k^T g_{k+1}$ is zero for an exact line search. The line search can simply be continued until $s_k^T g_{k+1}$ is close enough to zero to satisfy Eq. (6.24).

Another important property is the rapid convergence of the algorithm near the optimal point x^+. Convergence is superlinear, meaning

$$\lim_{k \to \infty} \frac{|\bar{x}_{k+1} - \bar{x}^+|}{|\bar{x}_k - \bar{x}^+|} = 0 \tag{6.25}$$

If the function is a convex quadratic function of N variables, the algorithm converges to the exact answer in at most N iterations, provided that exact line searches are used. Furthermore, the final hessian after updating is the exact hessian.

It should be noted that these convergence properties are not as good as those of the Newton algorithm which achieves quadratic convergence in general, and finite termination in one step on a quadratic surface. Nevertheless, these convergence properties are quite good, and make the algorithm suitable for our application in which analytical formulas for the hessian matrix are not available.

6.3.2.2 The Line Search and Convergence

The line search algorithm used within the quasi-Newton procedure is based on a quadratic approximation to the function along the search direction.

$$h(\alpha) = f(\mathbf{x}_k + \alpha \mathbf{s}_k) \tag{6.26}$$

Both the function value and its slope are available at $\alpha = 0$ since that was the best previous estimate of the minimum. Usually the function value is evaluated next at $\alpha = 1$, which is the minimum of the quadratic approximation to the surface in N-space. Based on these two function values and one slope, a parabola is fitted to $g(\alpha)$. The function is typically evaluated next at the minimum of this parabola.

One could discard the point at which $g(\alpha)$ is largest, and use the remaining three points to define a new parabola whose minimum would yield the next point. This procedure could be repeated until convergence was achieved. Instead a similar but more reliable procedure was used in which a triplet, $\alpha_1 < \alpha_2 < \alpha_3$, is selected such that

$f(\alpha_2) < min(f(\alpha_1), f(\alpha_3))$. In this way a local minimum is sure to exist for $\alpha_1 < \alpha < \alpha_3$, and on subsequent iterations this interval, which must contain the minimum, shrinks. Also, interpolation is used in preference to extrapolation.

Special cases in which the parabola is concave down and thus has a minimum at $\pm\infty$ are handled by biasing the search toward $\alpha = 0$, where the slope is negative, and by limiting the maximum step which can be taken. Safeguards of this type are used throughout the algorithm to prevent wild steps from being taken, which would otherwise occur whenever the quadratic approximation to the surface was inaccurate. Safeguards are also used to prevent iterates and function values from becoming too close to one another. This is important since the computation of the minimum of the parabolic approximation, α^+ , involves differences between function values or α's .

$$\alpha^+ = \frac{1}{2}\frac{(\alpha_2 - \alpha_3^2)h_1 + (\alpha_3^2 - \alpha_1^2)h_2 + (\alpha_1^2 - \alpha_2^2)h_3}{(\alpha_2 - \alpha_3)h_1 + (\alpha_3 - \alpha_1)h_2 + (\alpha_1 - \alpha_2)h_3} \tag{6.27}$$

$$= \frac{1}{2}\frac{(h_3 - h_2)\alpha_1^2 + (h_1 - h_3)\alpha_2^2 + (h_2 - h_1)\alpha_3^2}{(h_3 - h_2)\alpha_1 + (h_1 - h_3)\alpha_2 + (h_2 - h_1)\alpha_3} \tag{6.28}$$

Due to the finite precision of any computer, many of the digits in these subtractions can cancel, resulting in a very inaccurate parabolic approximation. The end result of ignoring this issue is a large step away from the answer after almost achieving convergence.

In general, a one dimensional optimization procedure is terminated when the slope approaches zero and when successive iterates and function values both change very little. Here, since the line search is part of a multi-dimensional optimization procedure, more specific criteria for termination exist. We define the following three conditions:

$$h_k - h_{k+1} \geq -\rho h_k' \alpha \qquad 0 < \rho < 1 \tag{6.29}$$

$$|h'_{k+1}| \leq \sigma |h'_k| \qquad 0 \leq \sigma < 1 \tag{6.30}$$

$$\theta_k \leq \frac{\pi}{2} - \mu \qquad \mu > 0 \tag{6.31}$$

where

$$\cos(\theta_k) = \frac{-\bar{g}_k^T \bar{s}_k}{|\bar{g}_k||\bar{s}_k|} \tag{6.32}$$

Condition (6.29) requires that the function value be reduced by a certain fraction of that which would be produced by a linear approximation to the function at $\alpha = 0$. Condition (6.30) requires that the directional derivative along the line search direction be reduced to a fraction of what it was at the start of the line search. If $\sigma = 0$, then an exact line search is being required. The angle between the search direction and the direction of steepest descent is θ_k. Condition (6.31) requires that these directions never approach orthogonality. Fletcher [29] proves that if conditions (6.29, 6.30, 6.31) all hold, and if the function is uniformly continuous, that either the function has no minimum and $f_k \mapsto -\infty$, or $g_k = 0$ for some finite k, or that g_k approaches 0 in the limit as k approa infinity. Thus if a finite minimum exists, the algorithm can not converge to a nonstationary point. Therefore if conditions (6.29, 6.30) are used to define the termination of the line search, a quasi-Newton optimization procedure will be convergent as long as condition (6.31) holds. This condition is not naturally obeyed by the BFGS updates or any other rank-2 update, but it can be imposed.

Condition (6.30) was used as the main line search termination criterion, with the derivatives h'_k being computed via finite differences, using the function values already determined in the current triplet. The σ value used ranged from .01 to .001 meaning, that the line search was required to be quite accurate. This was done for good reliability. The parameter ρ was fixed at 10^{-4} so that if Eq. (6.30) was satisfied so would Eq. (6.29) almost all the time.

The function being minimized, Eq. (6.9) was rather rapidly varying, especially with the large p_t and p_f needed to obtain reasonable minimax type approximations. In addition, the conditioning number of the hessian, the ratio of the maximum to minimum eigenvalue, varied quite dramatically. This meant that as the algorithm progressed, the function became more sensitive to certain combinations of variables and quite insensitive to others. This made accurate estimation of the location of the minimum increasingly difficult. Furthermore, numerical errors became much more significant in solving for the Newton search direction.

This problem was solved by rescaling the independent variable whenever the condition number of the approximate hessian became large. The rescaling was based only on the diagonal hessian values computed with finite differences. The variables x_i were rescaled to $\hat{x}_i = Ax_i$ so that all diagonal elements of the new hessian were 1.

$$\hat{x}_i = \frac{1}{\sqrt{G_{ii}}} x_i \tag{6.33}$$

A full eigensystem analysis could have been done to transform the hessian to the identity matrix, but the above much less computationally intensive procedure, was sufficient to control the condition number.

In the actual implementation used, condition (6.31) was not explicitly imposed. Note however, that search directions almost orthogonal to the gradient can only occur if the ellipsoids of constant function value are highly elongated, which corresponds to an ill-conditioned hessian. Thus, since the condition number of the hessian is being controlled by dynamic rescaling, this potential problem is eliminated.

6.3.2.3 Numerical Differentiation

In this application, obtaining analytical formulas for the derivatives of the objective function, Eq. (6.9), is quite difficult. Therefore, finite-difference approximations to the gradient were used. The simplest approximation is the forward difference formula which is presented below for a function of one variable.

$$D_f(\Delta) = \frac{h(\alpha+\Delta)-h(\alpha)}{\Delta} = h'(\alpha)+\frac{\Delta}{2}h''(\alpha)+\cdots \tag{6.34}$$

The Taylor series truncation error is made arbitrarily small by shrinking the interval over which the differencing is being done. This yields very bad results in practice on a physical finite precision computer, since $h(\alpha+\Delta)$ will be very ciose to $h(\alpha)$. Thus most of the significant digits in the difference will be lost due to cancellation error.

Let us assume that at the current location, the absolute numerical error in functional evaluation is bounded by ϵ_A. Then the cancellation error in the forward finite difference approximation is bounded by

$$E_{cf} = \frac{2\epsilon_A}{\Delta} \tag{6.35}$$

since in the worst case the errors will add. An estimate of the total error is then

$$E_{tf}(\Delta) = \frac{\Delta}{2}h''(\alpha)+\frac{2\epsilon_A}{\Delta} \tag{6.36}$$

and is minimized by choosing

$$\Delta_f = 2\sqrt{\frac{\epsilon_A}{h''(\alpha)}} \tag{6.37}$$

This differencing procedure was used in the optimization algorithm with the second derivative estimates generally obtained from the diagonal entries of the updated hessian matrix. If fewer than N iterations are completed so that the hessian estimate is not complete, then the curvature along the line search direction closest to the current search direction is used. This is reasonable as long as the condition number of the hessian is not large.

If the estimated gradient is small or if the estimated relative error in the gradient, E_{tf}, is large, then the central difference formula is used, whose truncation error is $O(\Delta^2)$, but which requires twice the number of function evaluations.

$$D_c(\Delta) = \frac{h(\alpha+\Delta)-h(\alpha-\Delta)}{2\Delta} = h'(\alpha)+\frac{\Delta^2}{12}h'''(\alpha)+\cdots \tag{6.38}$$

Using the same procedure as above, the optimal differencing interval, Δ_c, is now substantially larger.

$$\Delta_c = \sqrt[3]{\frac{3\epsilon_A}{h'''(\alpha)}} \tag{6.39}$$

Instead of estimating the third derivative which would have required four additional function evaluations, the function was assumed to be sufficiently smoothly varying for $h''(\alpha)$ to be roughly the same order of magnitude as the third derivative. If a transformation of the independent variable of the form $\hat{\alpha} = a\alpha$ is performed, then $h''(\alpha)$ scales by $1/a^2$ while $h'''(\alpha)$ scales by $1/a^3$. The correct scaling relationship is preserved in the following formula

$$\Delta_c = \sqrt[3]{\frac{3\epsilon_A}{h''(\alpha)}}\max(1,\alpha^{\frac{1}{3}}) \tag{6.40}$$

Note that if α is small, Δ_c is not multiplied by $\alpha^{\frac{1}{3}}$. This prevents the differencing interval from becoming arbitrarily small, yielding a large cancellation error.

Much of what is stated above about the difficulties of numerical differentiation is quite obvious, but nevertheless it is crucial to the successful implementation of the waveform synthesis procedure. Accuracy in the gradients is important since they not only affect the search direction on the current iteration, but on all future iterations via Eq. (6.22) in updating the hessian matrix.

6.3.2.4 Typical Performance

Termination of the routine is based on simultaneously achieving a low gradient, and having $|x_{k+1} - x_k|$ and $|f_{k+1} - f_k|$ both become small. The condition number of the quasi-Newton hessian was examined at termination to check for numerical difficulties. In order to check whether a local minimum was achieved, a random search was done to check for lower function values, and for directions of negative curvature. In addition, a finite difference approximation to the entire hessian was computed at termination and checked for negative eigenvalues to ascertain whether termination occurred at a saddle point.

This quasi-Newton procedure was used for filter design by minimizing the error of Eq. (6.9) using from 4 to 32 parameters. With N parameters, convergence was typically achieved in $2N$ to $3N$ iterations of the optimization procedure if a L_2 error definition was used, and if the starting point was reasonably close to the answer. If a bad initial starting point was used, $5N$ iterations were sometimes necessary.

Minimax type designs were attempted with reasonably large values for p_t and p_f such as 300 and 100 respectively. In this case, convergence was often difficult to achieve

even after $23N$ iterations and many diagonal renormalizations, with all computations done in double precision to 17 decimal digit accuracy. Nevertheless, the error was almost always substantially reduced and good answers were obtained. The source of the problem was the hessian matrices condition numbers being driven to values as high as one million without diagonal scaling. Using diagonal renormalization, they fell to around 30000. It is possible that a full eigensystem analysis and diagonalization would solve this problem if the eigenvalues and eigenvectors could be computed accurately enough. Instead, most computations were done with p_t and p_f at least 10 times smaller. Then this problem did not occur and convergence once again occurred in $2.5N$ to $5N$ iterations.

6.4 Nonuniform Sampling

The second basic step in our algorithm for constant time-amplitude filter synthesis is sampling the waveforms. If $H_c(f)$ is the frequency response of the continuous waveform, then

$$H_s(f) = f_s \sum_{k=-\infty}^{\infty} H_c(f - nf_s) \tag{6.41}$$

is the frequency response [76] resulting from sampling the continuous impulse response with unit area impulses spaced in time by $1/f_s$. If the continuous waveform was of bandwidth Δf centered at f_o, then according to Eq. (6.41), the waveform would have to be sampled at least at $f_s = 2(f_o + \Delta f/2)$ to avoid aliasing of the upper replica of the response into the fundamental. Depicted in Fig. 6.6 is the case of sampling exactly at the above minimum sampling frequency, the Nyquist frequency. Note that there is another passband just above the desired one caused by aliasing. This destroys the rejection

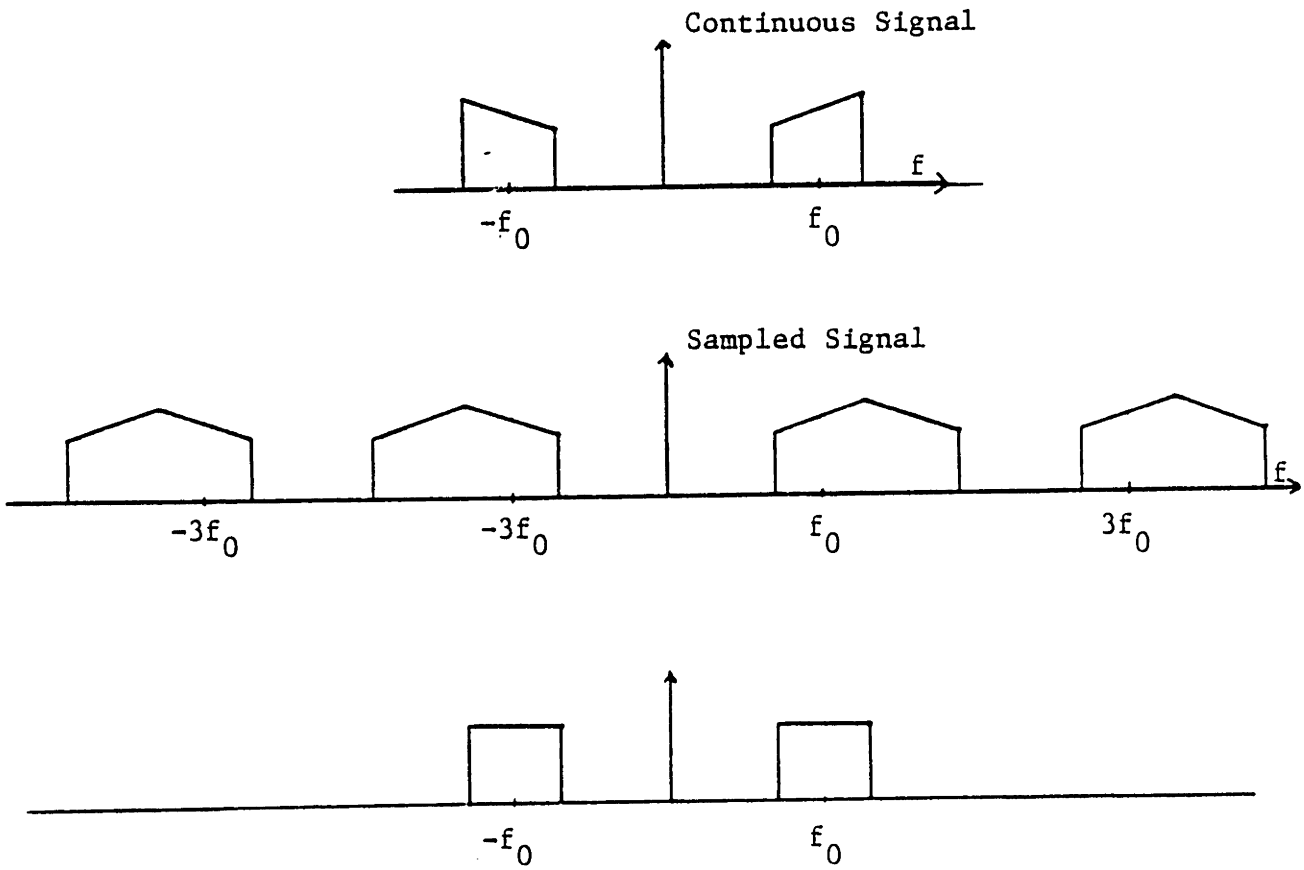

Figure 6.6 Uniform Sampling at the Nyquist Frequency
Note the aliased passband just above the desired passband.

performance on the high frequency side. In order to push this aliased passband up to $2f_0$ or $3f_o$, the sampling frequency would have to be increased to $3f_o$ or $4f_o$ respectively.

These high sampling rates are only necessary if the frequency responses have no particular symmetry. If the desired frequency response is conjugate symmetric about f_o, then the sampling frequency can be reduced to $2f_o$ and the next highest passband is at $3f_o$. Fig. 6.7 shows how we take advantage of aliasing to achieve this result with half the sampling rate. In this case, the samples are taken at the peaks and valleys of the real modulated time signal.

In our case, the frequency responses can not be conjugate symmetric about the center frequency since that would imply that the baseband impulse response is real, which by Eq. (6.12) precludes any phase modulation. This means that four samples per period would

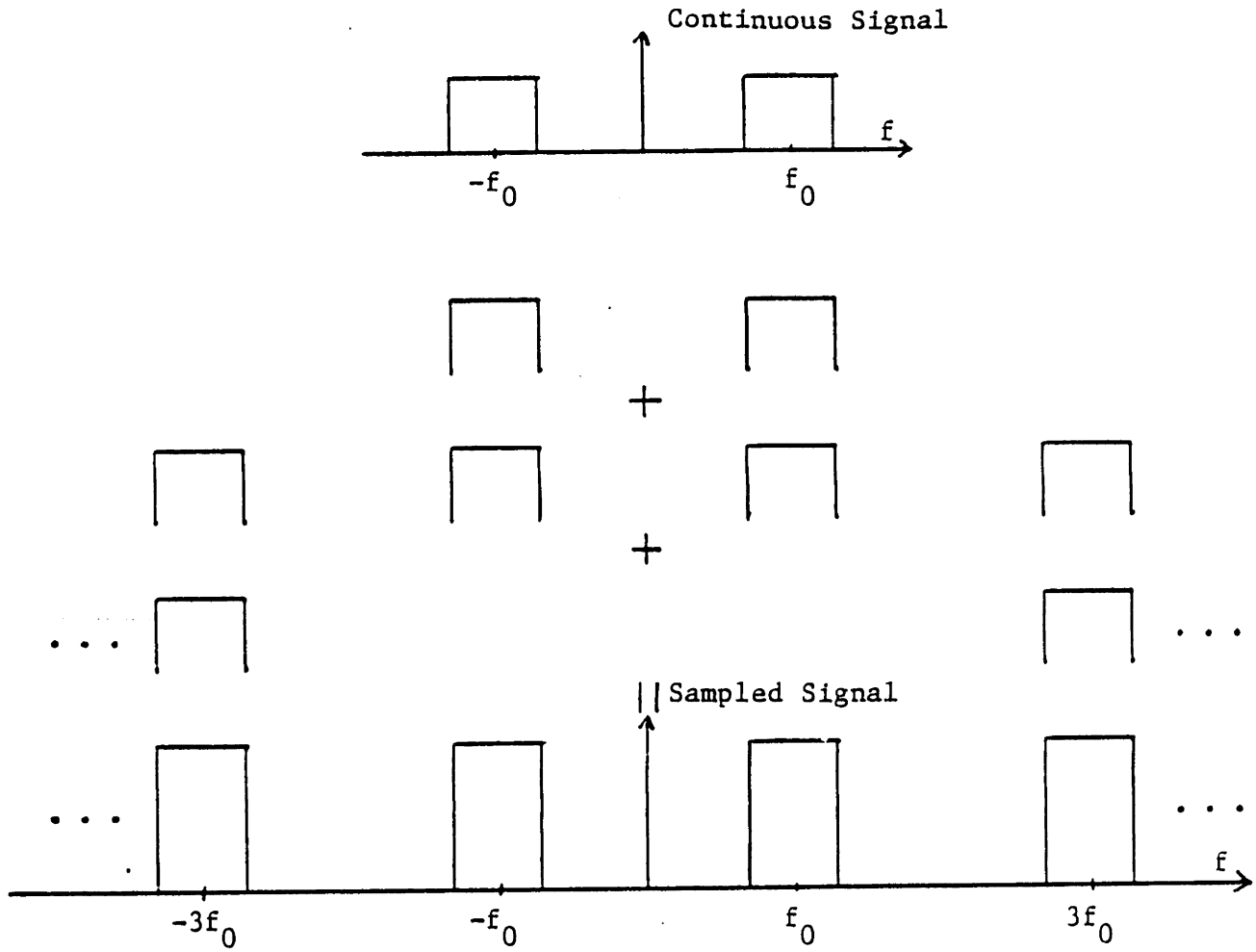

Figure 6.7 Uniform Sampling for Conjugate Symmetric Bandpass Signals
The frequency response is assumed to be conjugate symmetric about the center frequency. Real symmetric responses are sketched for simplicity. Note how the aliased responses add exactly on top of the unaliased responses.

be required to obtain a reasonable rejection region on the high frequency side. Some of the samples would be near the peaks and valleys, yet others would be near zero crossings where the signal is changing rapidly. This is undesirable since a large dynamic range would be required in the sample weights which is precisely what we wanted to avoid by obtaining a low dynamic range complex time envelope. Furthermore, placement of samples where the waveform is rapidly varying would seem to increase the sensitivity of the final device to errors in the positioning of these samples.

For the above reasons, it was decided to use an alternative procedure in which samples are placed near the extrema of the signal. In the case of a phase modulated waveform, the sampling interval will no longer be uniform. Atzeni and Masotti [3] developed a theory for nonuniform sampling of this type. They place the samples at points where the phase is an integral multiple of π.

Let us express the AM-PM waveform to be sampled in the baseband form of Eq. (6.12).

$$f(t) = a(t)\cos(\phi(t)) = a(t)\cos(2\pi f_0 t + \theta(t)) \tag{6.42}$$

where a(t) is twice the magnitude of the complex baseband envelope, and $\theta(t)$ is its phase. The baseband response, $f_b(t)$, is then

$$f_b(t) = \frac{a(t)}{2} e^{j\theta(t)} \tag{6.43}$$

Let us first work with

$$g(t) = \cos(\phi(t)) \tag{6.44}$$

which is just the phase modulation. We regard $\tilde{g}(\phi(t)) = g(t)$ to be a function of ϕ and then sample it with impulses separated by π radians in ϕ space.

$$\tilde{g}_s(\phi) = \sum_{n=-\infty}^{\infty} \cos(n\pi)\delta(\phi - n\pi) = \sum_{n=-\infty}^{\infty} (-1)^n \delta(\phi - n\pi) \tag{6.45}$$

Since $\tilde{g}_s(\phi)$ is a periodic function in ϕ with period 2π, it can be represented as a Fourier series

$$\tilde{g}_s(\phi) = \frac{2}{\pi} \sum_{m=1,3,5,\ldots}^{\infty} \cos(m\phi) \tag{6.46}$$

Now we re-express $g_s(\phi)$ as a function of t

$$\tilde{g}_s(\phi(t)) = \sum_{n=-\infty}^{\infty} (-1)^n \delta(\phi(t) - n\pi) = \sum_{n=-\infty}^{\infty} (-1)^n \frac{\delta(t - t_n)}{\phi'(t_n)} \tag{6.47}$$

where

$$\phi(t_n) = 2\pi f_0 t_n + \theta(t_n) = n\pi \tag{6.48}$$

Note that here it is assumed that $\phi(t_n) = n\pi$ has a maximum of one solution. If there are more solutions, then one impulse must be added for each additional solution. The fact that $\delta(\phi(t) - n\pi)$ has area $1/\phi'(t_n)$ when expressed explicitly as a function of t is easily demonstrated by direct integration with a change of variables.

$$\begin{aligned} \int_{-\infty}^{\infty} \delta[\phi(t) - n\pi]\, dt &= \int_{-\infty}^{\infty} \delta(x) \frac{d\phi^{-1}}{dx}(x + n\pi) dx \\ &= \int_{-\infty}^{\infty} \delta(x) \frac{dx}{\phi'(t)} = \frac{1}{\phi'(t_n)} \end{aligned} \tag{6.49}$$

where

$$x = \phi(t) - n\pi$$

and

$$x = 0 \quad at \quad \phi(t_n) = n\pi$$

Combining Eqs. (6.46, 6.47) we obtain

$$g_s(t) = \tilde{g}_s(\phi(t)) = \sum_{n=-\infty}^{\infty} \frac{(-1)^n \delta(t - t_n)}{\phi'(t_n)} = \frac{2}{\pi} \sum_{m=1,3,5,\ldots}^{\infty} \cos(m\phi(t)) \tag{6.50}$$

Upon multiplication by $\frac{\pi}{2}a(t)$ we obtain the final result

$$\frac{\pi}{2}\sum_{n=-\infty}^{\infty}(-1)^n\frac{a(t_n)\delta(t-t_n)}{2\pi f_0+\theta'(t_n)} = a(t)\sum_{m=1,3,5,\ldots}^{\infty}\cos(m2\pi f_0 t+m\theta(t)) \tag{6.51}$$

We note that the first term on the right side of Eq. (6.51) is precisely $f(t)$, while the others are concentrated near the odd harmonics just as in the uniformly sampled case with $f_s=4f_o$ in general, or with $f_s=2f_o$ in the conjugate symmetric case.

In our case, the complex time envelope, $f_b(t)$, is not really a continuous function. It is computed with fast Fourier transforms (FFT's) and is thus known on a coarse uniformly spaced grid. The points at which the phase is an integral multiple of π, t_n, generally do not lie on this grid. Thus interpolation is necessary to evaluate the complex envelope at arbitrary time. Bandlimited interpolation is used which corresponds to passing the sampled version of $f_b(t)$ through a lowpass filter. The interpolated result, $f_{bi}(t)$, is then [76]

$$f_{bi}(t) = \sum_{n=-\infty}^{\infty}f_b(nTs)\,\mathrm{sinc}\left(\frac{\pi}{T_s}(t-nT_s)\right) \tag{6.52}$$

where T_s is the spacing between time samples.

The nonlinear equation for the sampling times, t_n, is then

$$\arg[f_{bi}(t_n)] = n\pi \tag{6.53}$$

This equation was solved numerically using the line search minimization routine of the quasi-Newton optimization procedure. The function to be minimized is

$$e(t) = [\arg(f_{bi}(t_n))-n\pi]^2 \tag{6.54}$$

The only values of n needed are 0 and 1, since a branch cut for the angle determination is placed at $-\pi/2$. Initial guesses are obtained using linear interpolation on the phase between sampling times.

The most important practical difference between uniform and nonuniform sampling is that the sample values in the nonuniformly sampled case are not the sample values of the envelope; they must be divided by the local instantaneous frequency. This is intuitive, since otherwise the weight would be higher in regions of higher instantaneous frequency due to the higher concentration of samples.

6.5 Low Dynamic Range Design Examples

The basic algorithm described in the previous four sections was used to fully design four amplitude and phase modulated (AM-PM) waveforms with low dynamic range. These will be referenced as prototypes I through IV. In all cases, each transducer's impulse response was 251.5 wavelengths long with a 7.1% fractional bandwidth. They were *brick wall* filters whose shape factors* ranged from 1.15 to 1.18. The Fourier transforms were done with 1024 point FFT's and a time sampling corresponding to one sample every $2\frac{1}{3}$ wavelengths at the center frequency. This means that the unaliased frequency range extends from $.786f_o$ to $1.214f_o$ which was certainly sufficient, since all the frequency responses were well into the rejection band outside this region. The design of the first AM-PM prototype will be used to illustrate every step of the algorithm, and then the new results obtained with the three other waveforms will be summarized.

*Here shape factor is defined as the ratio of the bandwidth at the rejection level to that at the level of the passband minimum. (see Fig. 6.3)

In order to halve the number of parameters required, the first filter was designed assuming a symmetrical phase response. An antisymmetrical phase response would also halve the number of parameters but would not be suitable. The problem is that when combined with the desired symmetrical ideal bandpass magnitude response, $H_{db}(f)$ would be conjugate symmetric, yielding a real baseband impulse response, and would not possess any phase modulation according to Eq. (6.12). In addition, the same parameters were associated with both transition bands. Twenty parameters were used in total, of which 17 were allocated to the phase function and 3 to the transition bands. This is indeed a substantial reduction, since if we had parameterized by the time samples and their signs as in the initial problem statement, we would need 503 continuous variables in addition to 503 discrete ones. Since computation time is $O(N^2)$, even if we ignore the combinatorial problem in 503 discrete variables, this represents a savings of almost 3 orders of magnitude.

The desired response at the first step of the algorithm is zero in the rejection band and unity in the passband as depicted in Fig. 6.4. The initial parameterization of the transition band was such that the desired single transducer response varied linearly from 0 to 1. The breakpoints for the group delay response were selected to lie on a line, and correspond in the time domain to a quadratic phase, i.e. to a linear chirp over the passband of the filter response. In Fig. 6.8a is displayed the final desired magnitude squared frequency response selected by the optimization procedure. The parameters only affect the transition band response which is seen to oscillate wildly. If the achieved transition band magnitude response actually behaved in this manner, it would be undesirable. We will soon see that truncation in the time domain smooths out the achieved transition band response. The only purpose of the rapidly varying transition band response is to prevent the time envelope from falling off too rapidly near the end of the desired time window, thereby reducing the dynamic range.

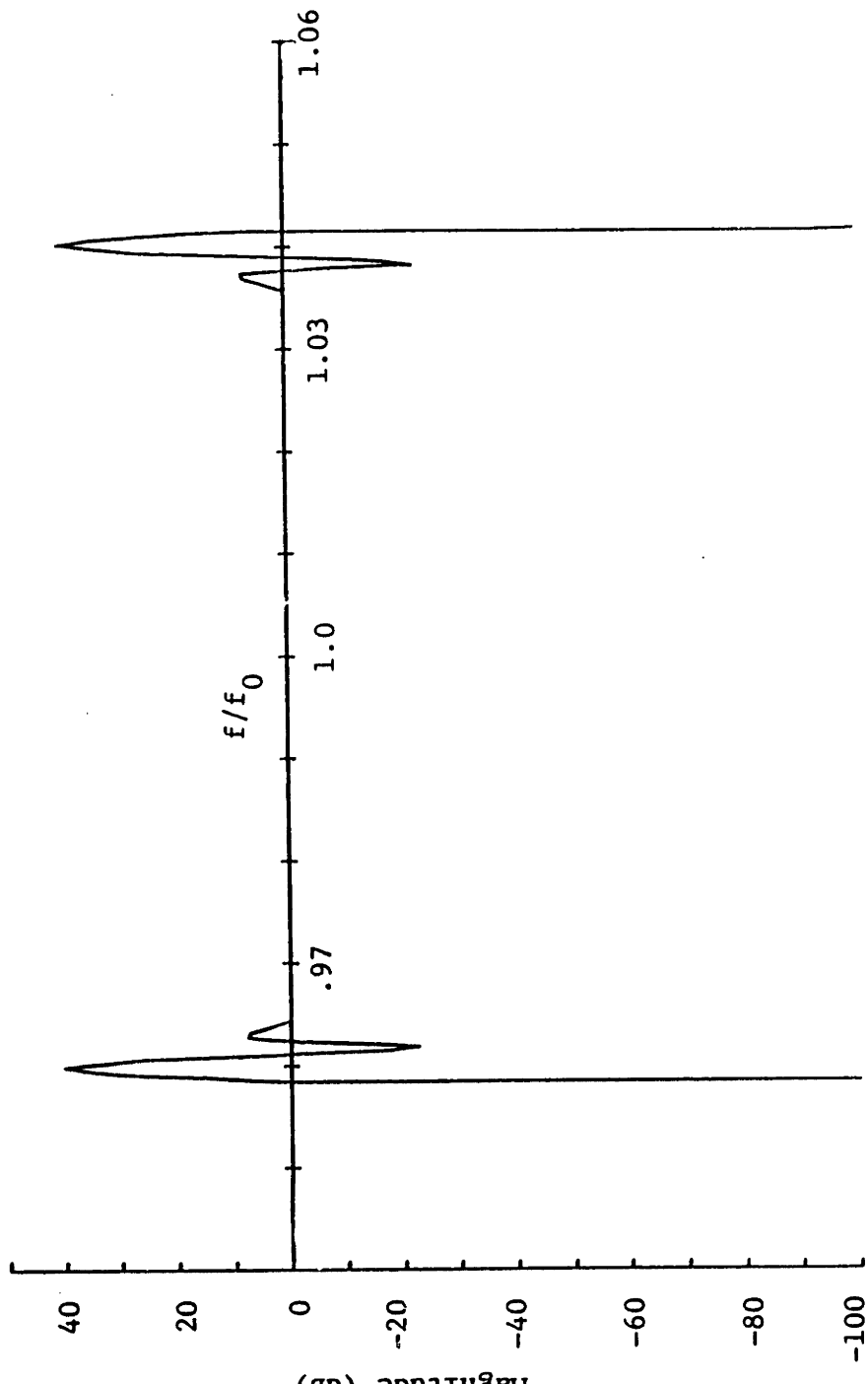

Figure 6.8a Final Desired Frequency Response: Prototype-I
Desired magnitude-squared response

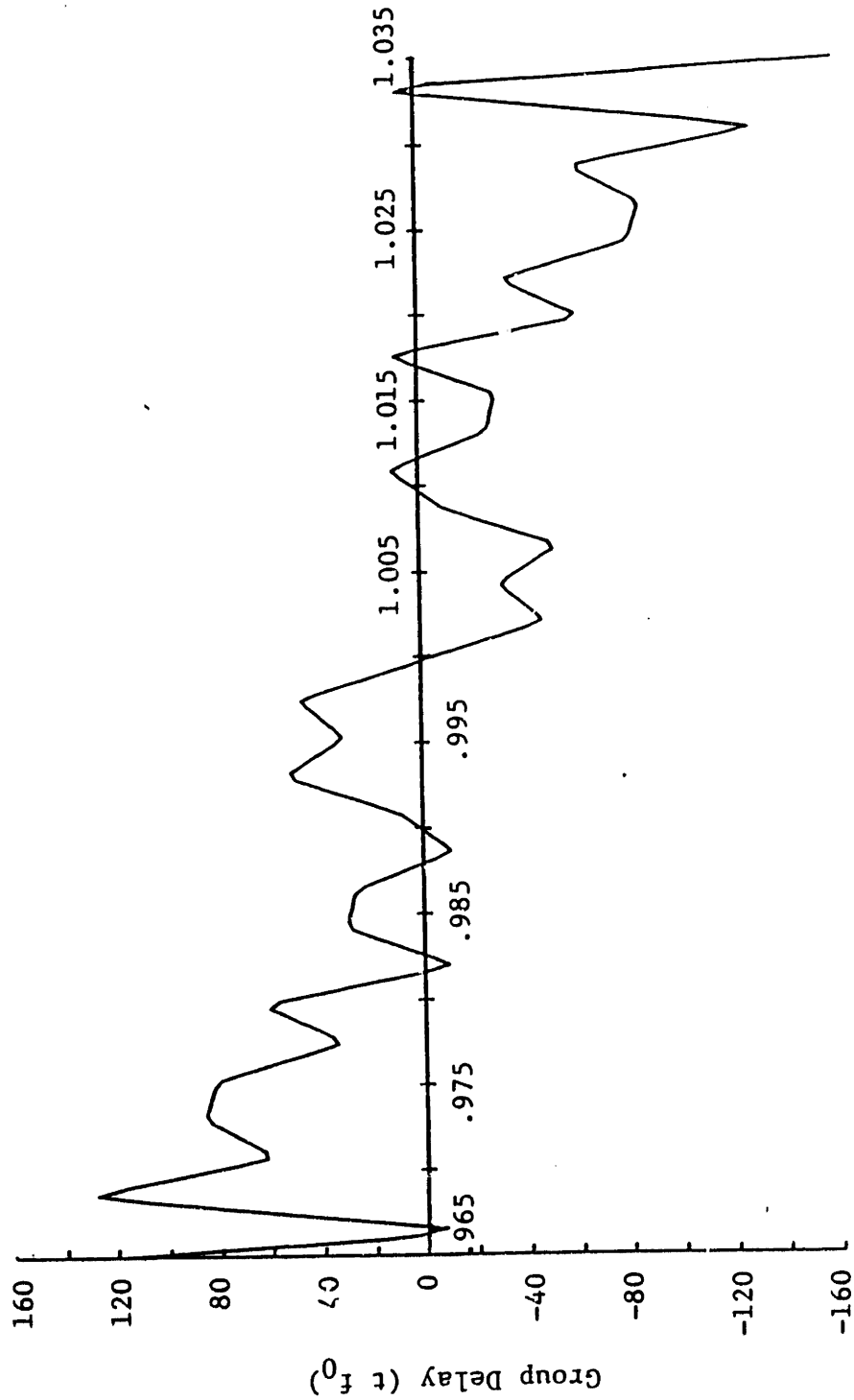

Figure 6.8b Final Desired Frequency Response: Prototype-I
Desired single transducer group delay response

The desired group delay response is displayed in Fig. 6.8b. Its general trend is linear as would be expected for a linear chirp, but it too oscillates quite a bit. Note that many frequencies have the same group delay. Using the stationary phase approximation to compute the inverse Fourier transform, only frequencies with group delay t_{go} contribute to the time response at time t_{go}. Thus there no longer is a one to one relationship between time and frequency as there is in the invertible group delay functions typically used in SAW devices for radar applications.

The time response after windowing to 251.5 periods at the fundamental, is displayed in Fig. 6.9a. We note that the time envelope is not as flat as we desired nor is it equiripple*. This is a result of having used $p_t = 30$ to obtain a L_{60} error definition for the time error in Eq. (6.7). A larger value for p_t could have been used to obtain a flat time envelope in the minimax sense, but this would have made the numerical optimization more difficult as discussed in Sec. 6.3.2.4. Nevertheless, the ratio of the maximum to minimum envelope value is only 5.8 (See Table 6.1 in Sec. 6.5.2.). This is orders of magnitude better than that which would be achieved via a straightforward inverse Fourier transform of the desired frequency response with zero phase, or via the Parks-McClellan [85] algorithm (See Table 6.2 in Sec. 6.5.3.). The associated instantaneous frequency response is displayed in Fig. 6.9b. As with the desired group delay, it is not monotonic. At relative frequencies ranging from .95 to 1.05, there are several times that are synchronous simultaneously.

Finally this windowed time response is Fourier transformed to obtain the achieved frequency response and is displayed in Figs. (6.10–6.12). The desired sharp cutoff characteristic was obtained with -51.8 dB sidelobes and .2 dB peak to peak passband ripple (See Table 6.1 in Sec. 6.5.2.). As with the time response, a minimax frequency

*It is not clear whether the optimal minimax solution is equiripple. The minimax solution has only been proven to be equiripple for a linear superposition of basis functions satisfying the Haar condition [12,88]. The Haar condition requires linear independence for any set of N vectors, $[\phi_i(x_1), \phi_i(x_2), \ldots, \phi_i(x_N)], i = 1, N$ for N distinct points, x_i, in the interval over which the approximation is being done, where $[\phi_1, \phi_2, \ldots, \phi_N]$ is the set of basis functions for the approximation.

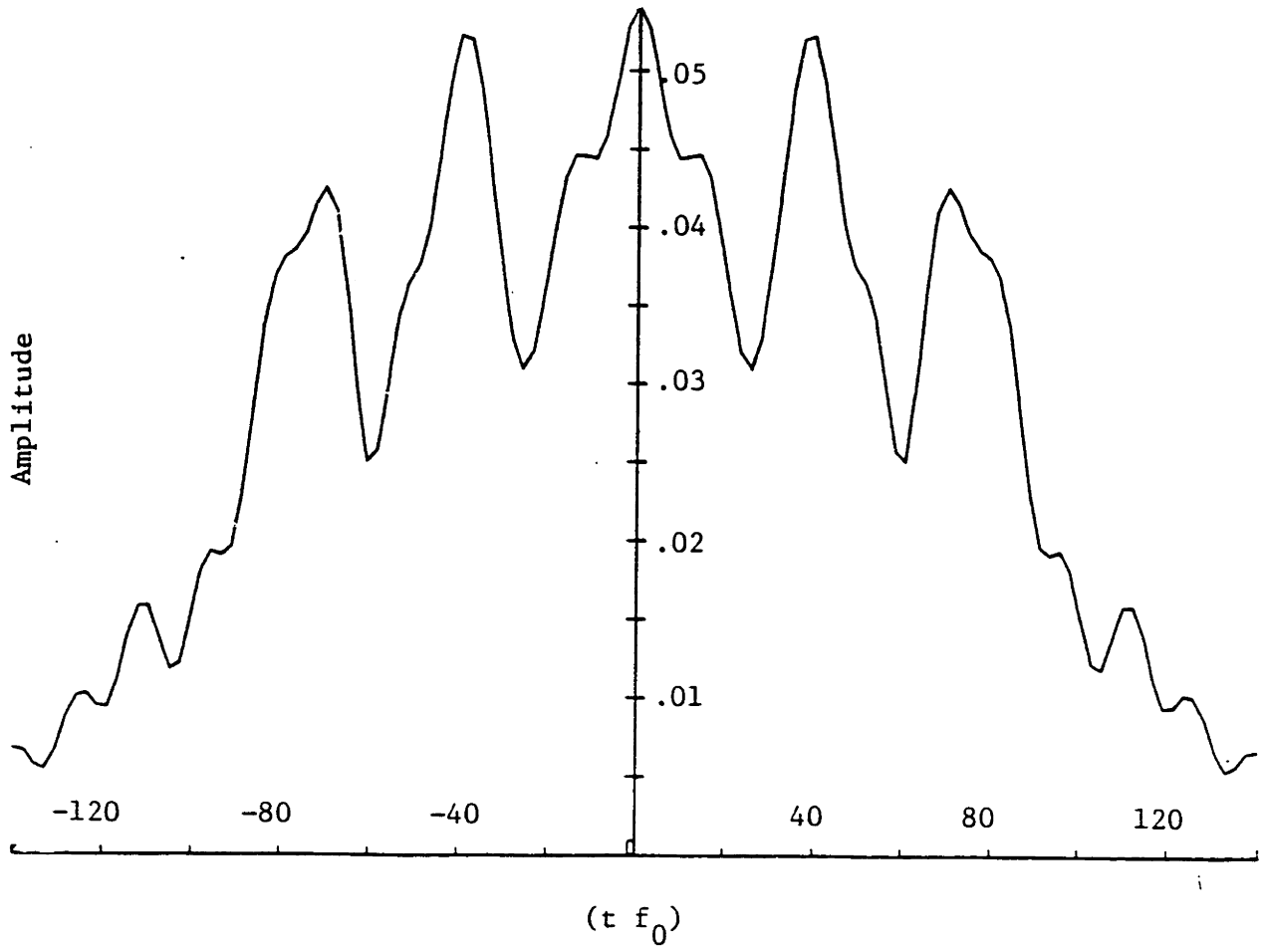

Figure 6.9a Final Single Transducer Time Domain Response: Prototype-I
Magnitude of the baseband time envelope

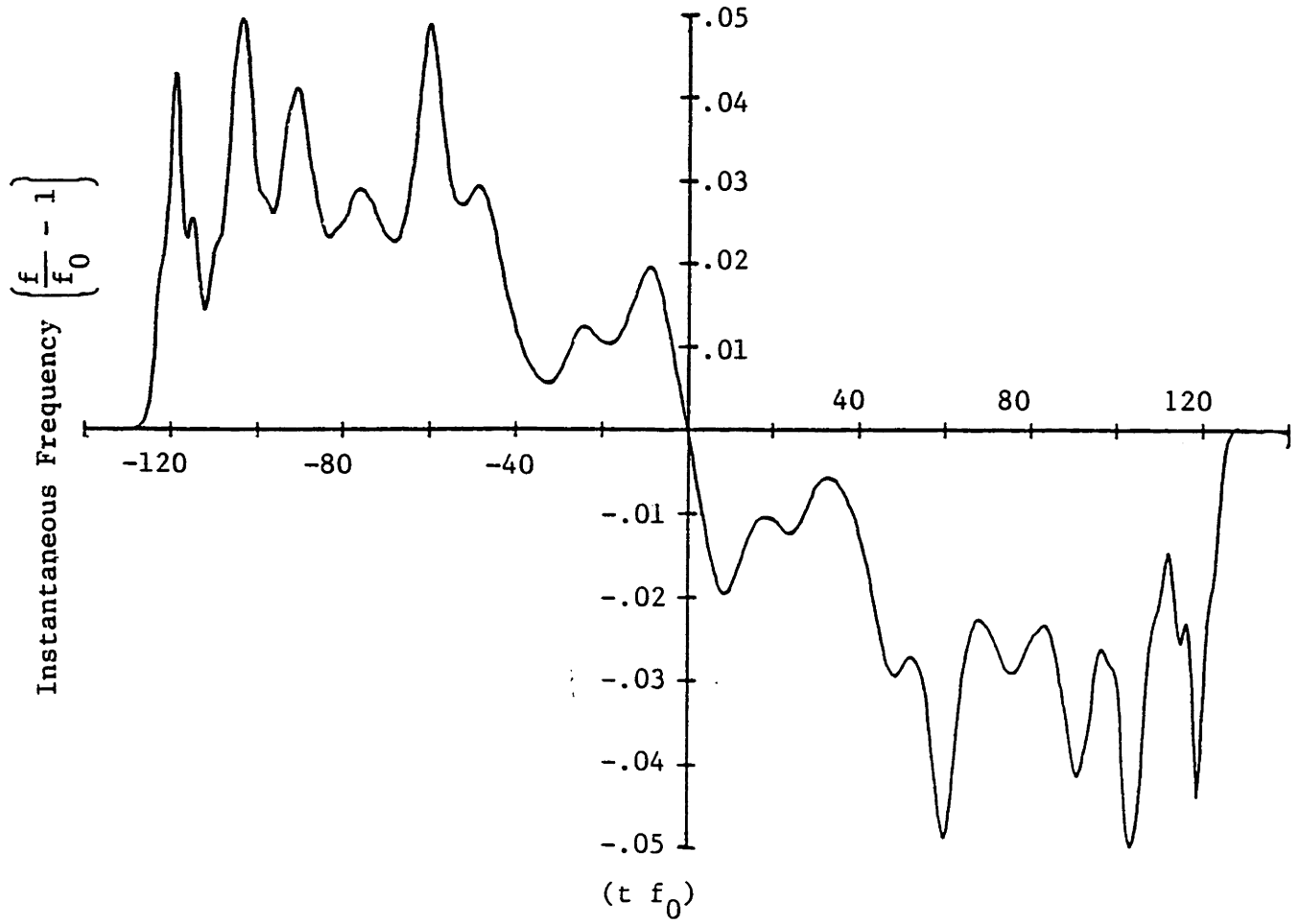

Figure 6.9b Final Single Transducer Time Domain Response: Prototype-I
Instantaneous frequency

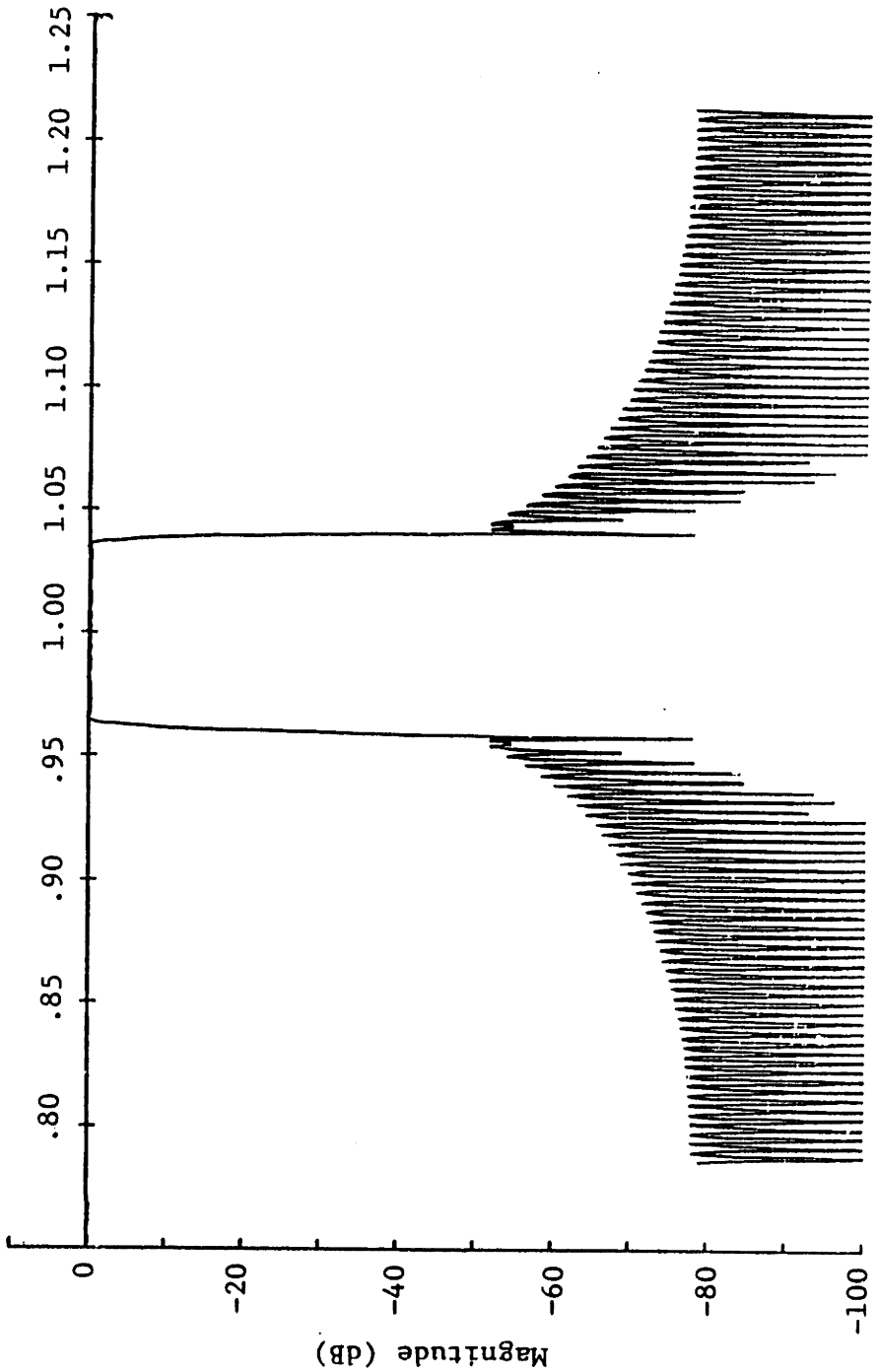

Figure 6.10a Final Achieved Frequency Response: Prototype-I
Magnitude-squared response over a 50% fractional bandwidth.

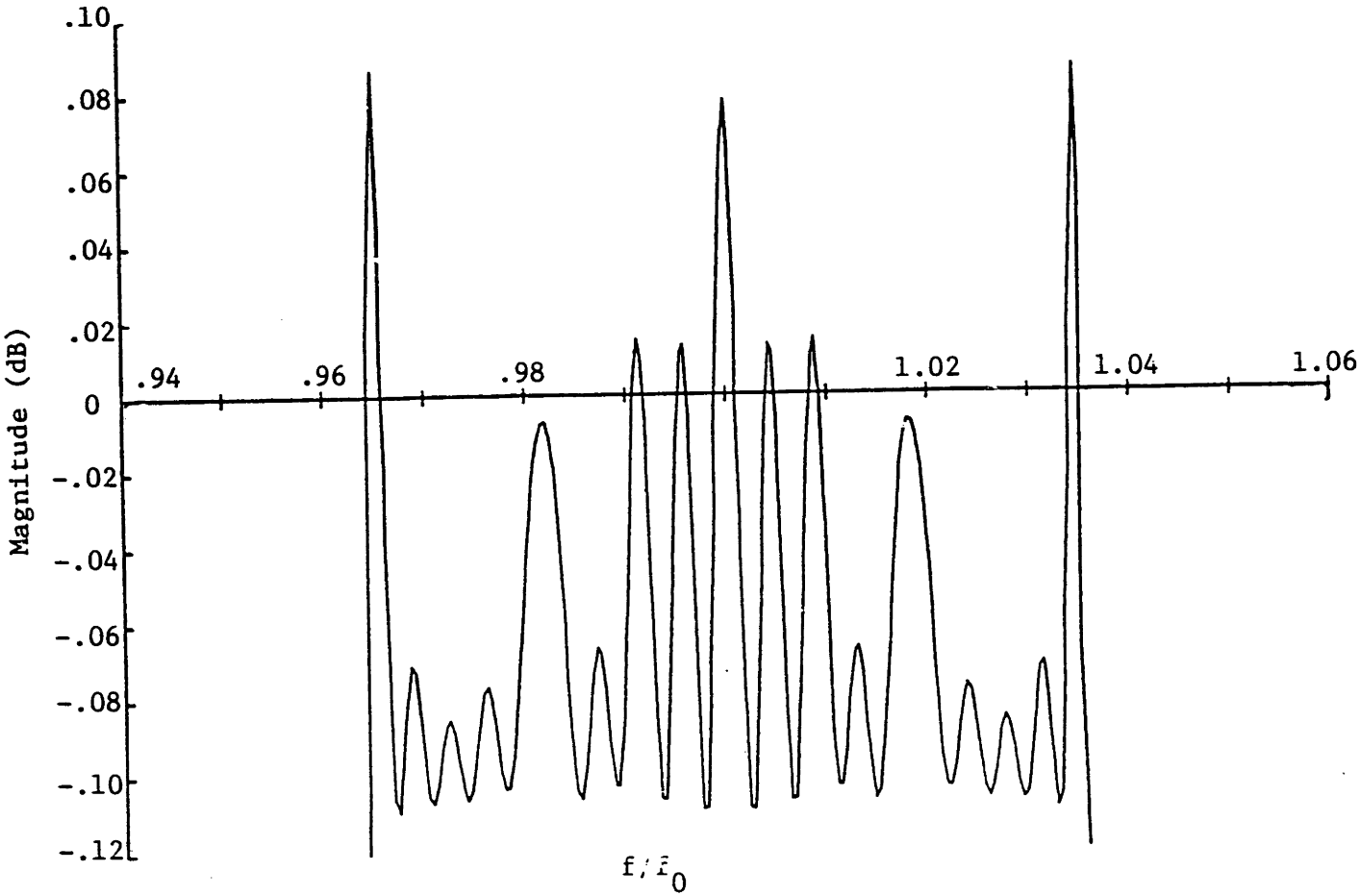

Figure 6.10b Final Achieved Frequency Response: Prototype-I
Magnitude-squared response over the passband.

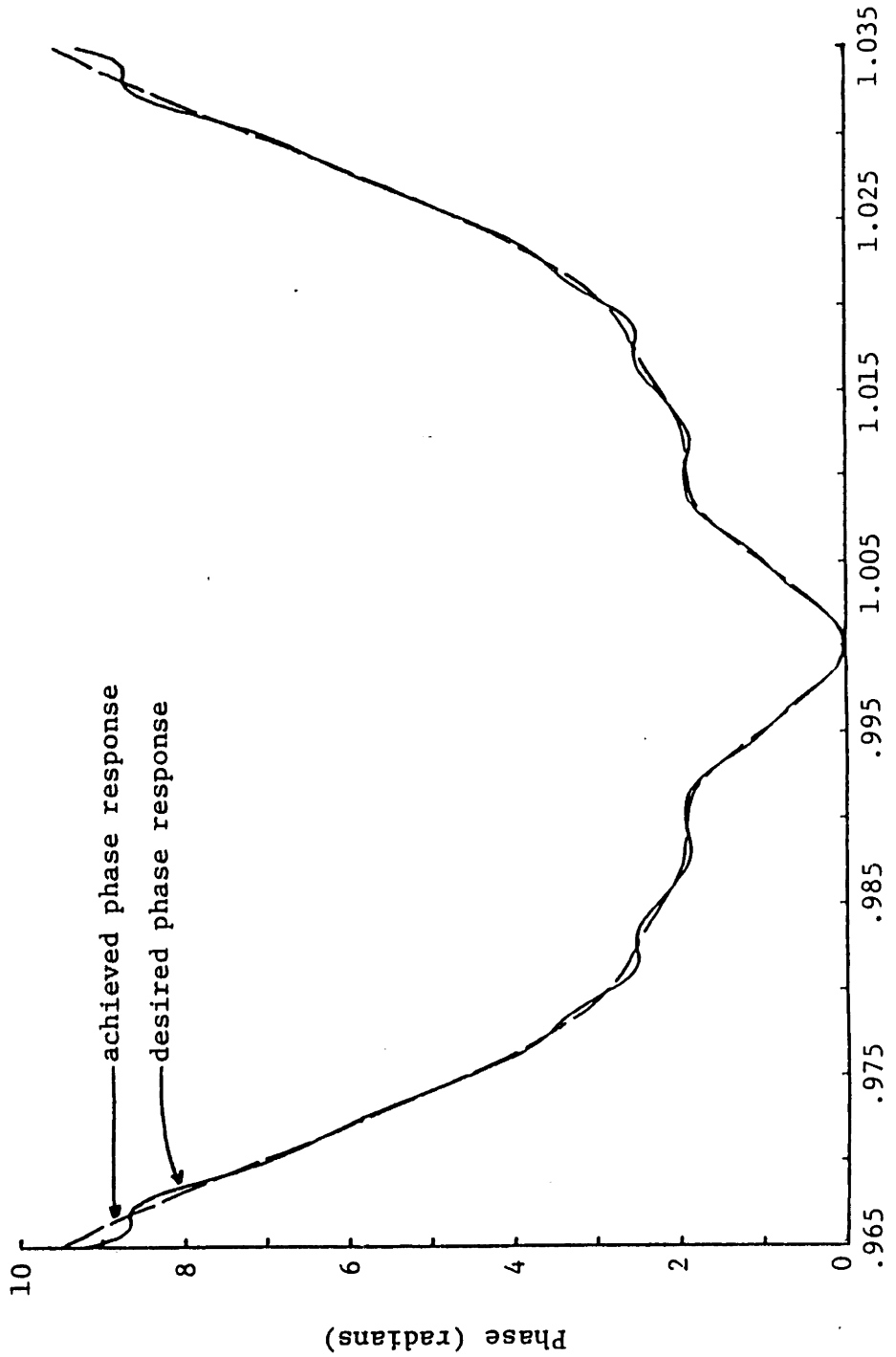

Figure 6.11 Final Desired and Achieved Single Transducer Phase Responses: Prototype-I

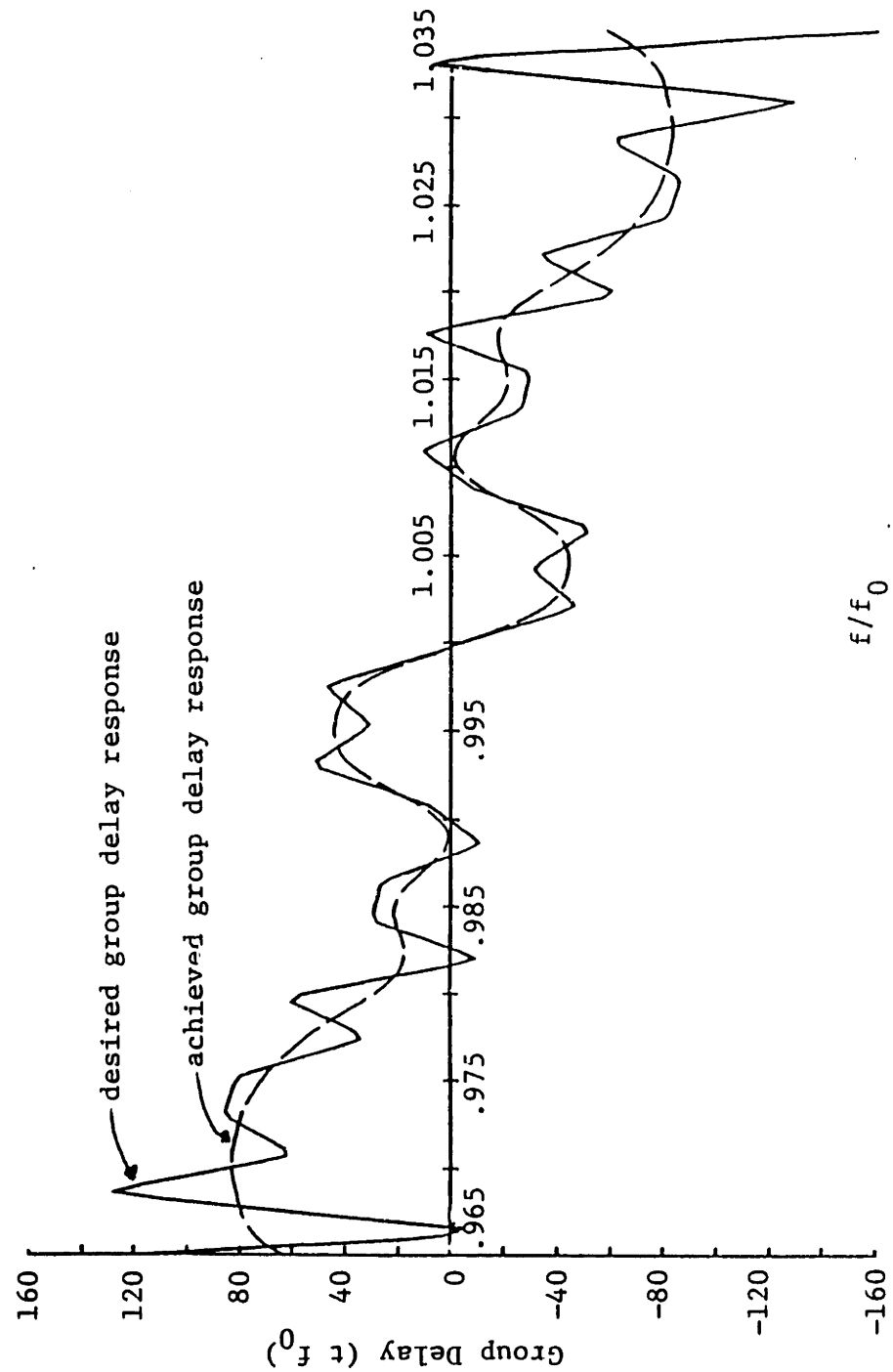

Figure 6.12 Final Desired and Achieved Single Transducer Group Delay Responses: Prototype-I

response was probably not obtained, since p_f (Eq. (6.8)) was only 10, meaning that a L_{20} error definition was used. Fig. 6.12 demonstrates that the initially specified group delay response at step-I of the error definition in Fig. 6.4 was not achieved, but that a smoothed approximation resulted. This smoothing was caused by windowing in the time domain. The phase responses displayed in Fig. 6.11 agree much more closely since the integration required to go from a group delay response to a phase response is also a smoothing operation.

The waveform was then nonuniformly sampled using the procedure outlined in Eqs. (6.42–6.54) over the region in which the uniformly sampled envelope was non-zero. The right-most third of this waveform is displayed in Fig. 6.13. The spacing is chirped so slowly that it is difficult to observe the non-periodicity. This indicates that our assumption embodied in Eq. (3.85) of a single element factor whose amplitude is slightly scaled to account for the slight aperiodicity was a reasonable one. The frequency response of the nonuniformly spaced samples is plotted along with the response of the uniformly spaced samples in Figs. (6.14a, 6.14b). These responses agree reasonably well in the rejection region, but there is a huge degradation in the passband. The nonuniform sampling increased the passband ripple by about a factor of three.

In order to improve the approximation of the uniformly spaced samples by the nonuniformly spaced ones, Eq. (6.52) was used to extrapolate the nonuniformly spaced samples beyond the end of the uniformly sampled prototype. Extrapolation was done until the sample values stopped decreasing in magnitude. The total number of samples increased from from 503 to 514 with 6 points added to the left and 5 added to the right. As shown in Fig. 6.15, the sample values decrease smoothly to zero instead of being truncated abruptly. This of course increases the dynamic range of the impulse response,

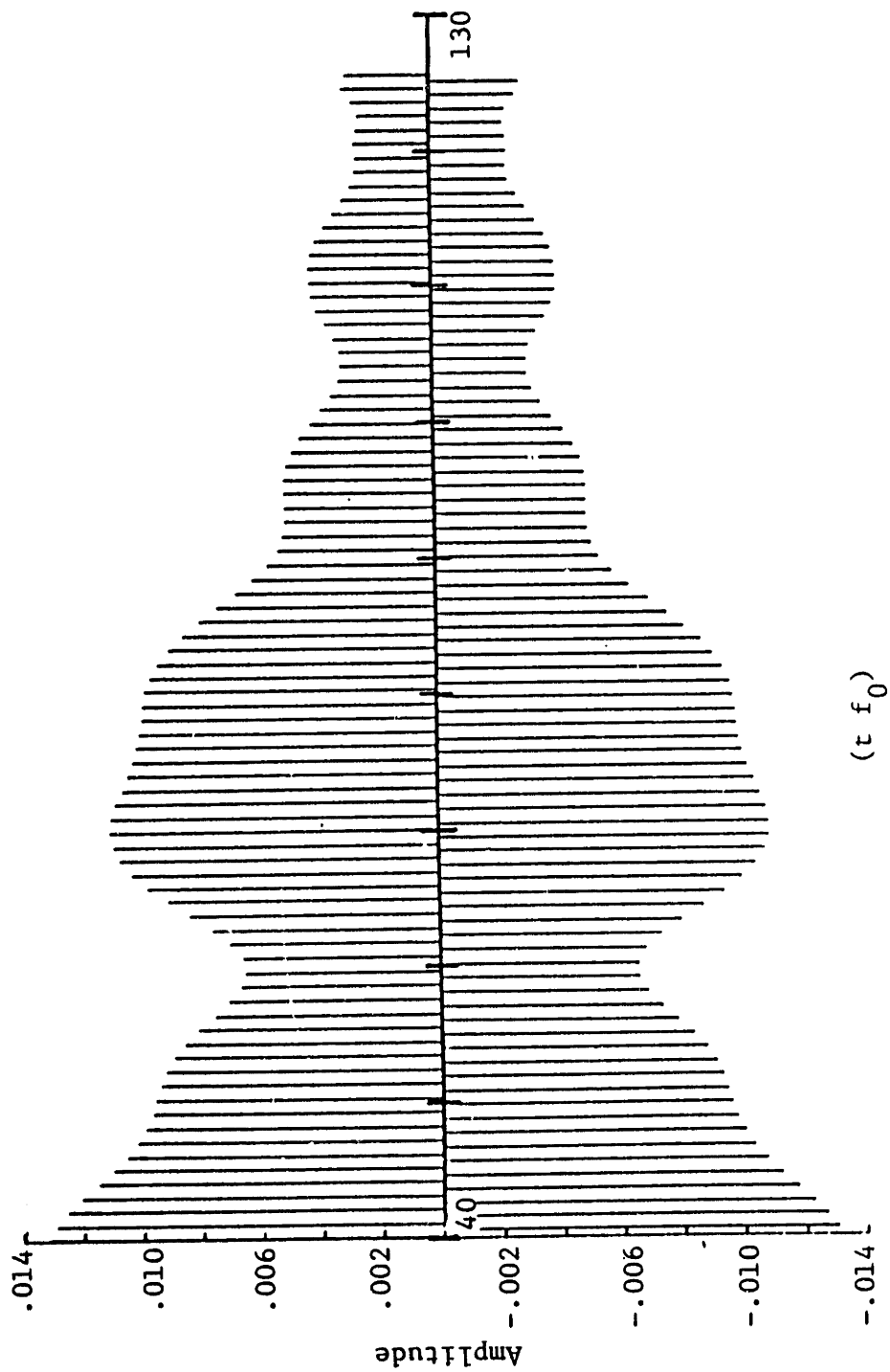

Figure 6.13 Right-Most Third of Prototype-I After Nonuniform Sampling with No Extrapolation

Note that the samples go to zero abruptly

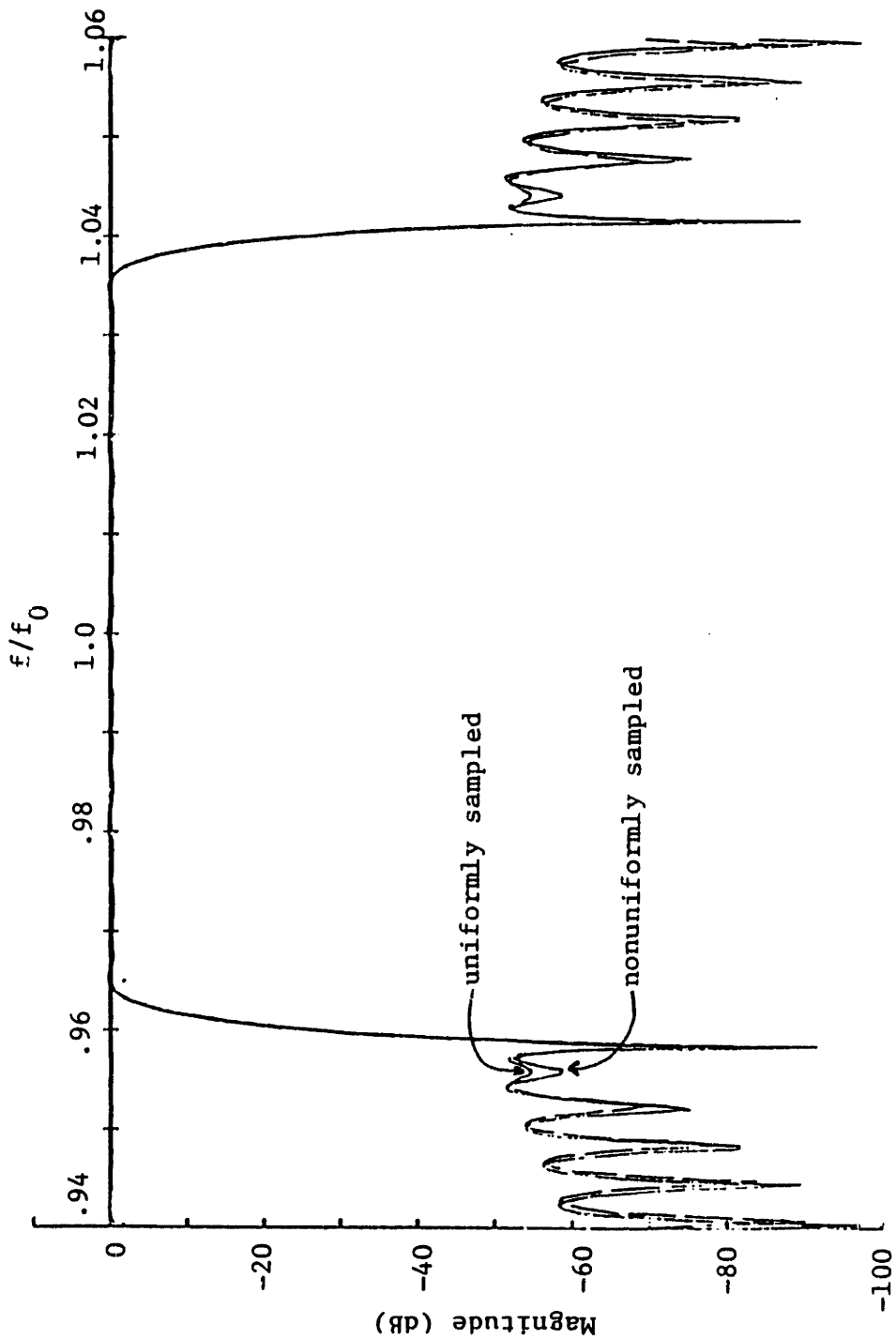

Figure 6.14a Frequency Response of Prototype-I After Nonuniform Sampling with No Extrapolation

Passband and rejection band responses.

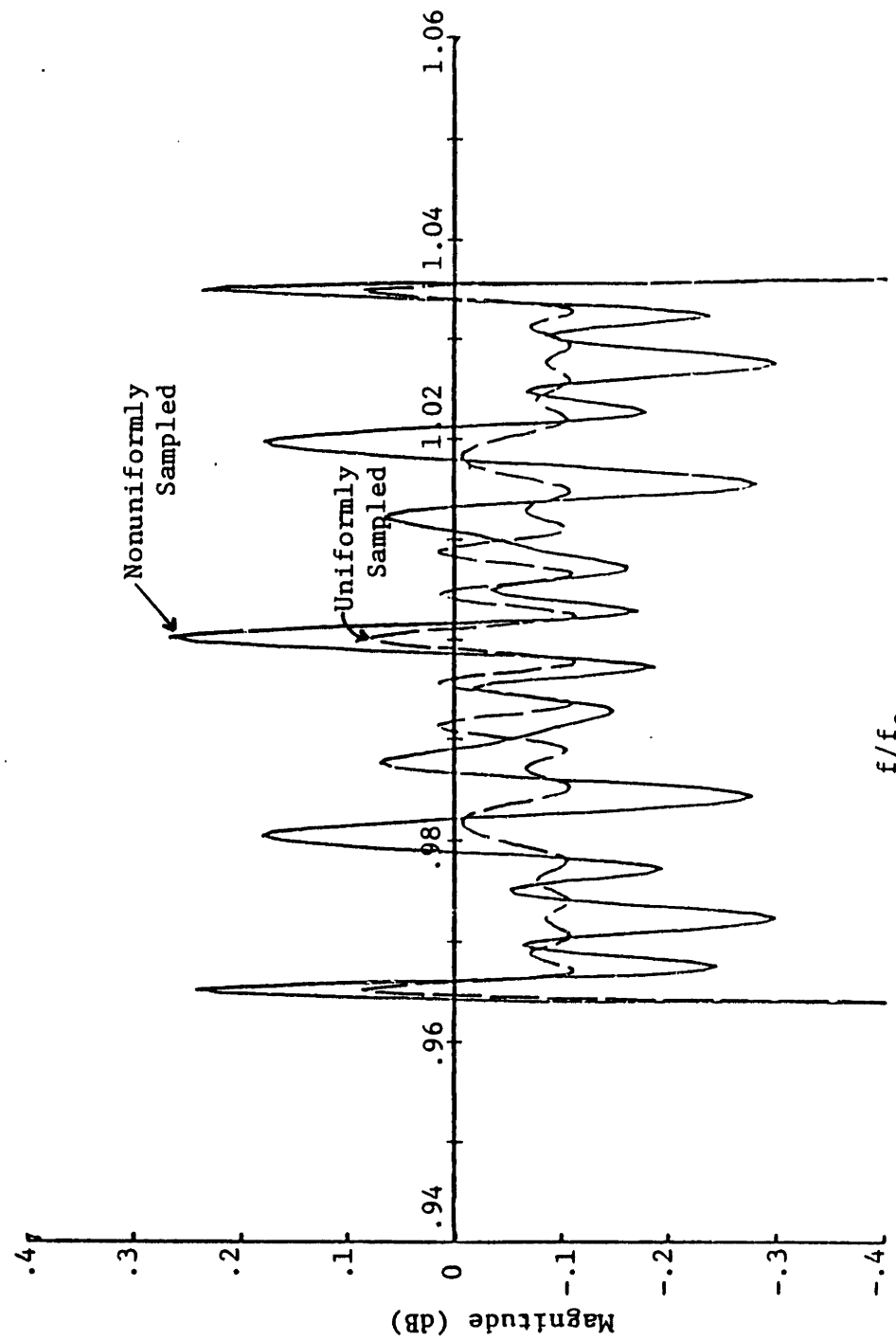

Figure 6.14b Frequency Response of Prototype-I After Nonuniform Sampling with No Extrapolation
Passband response.

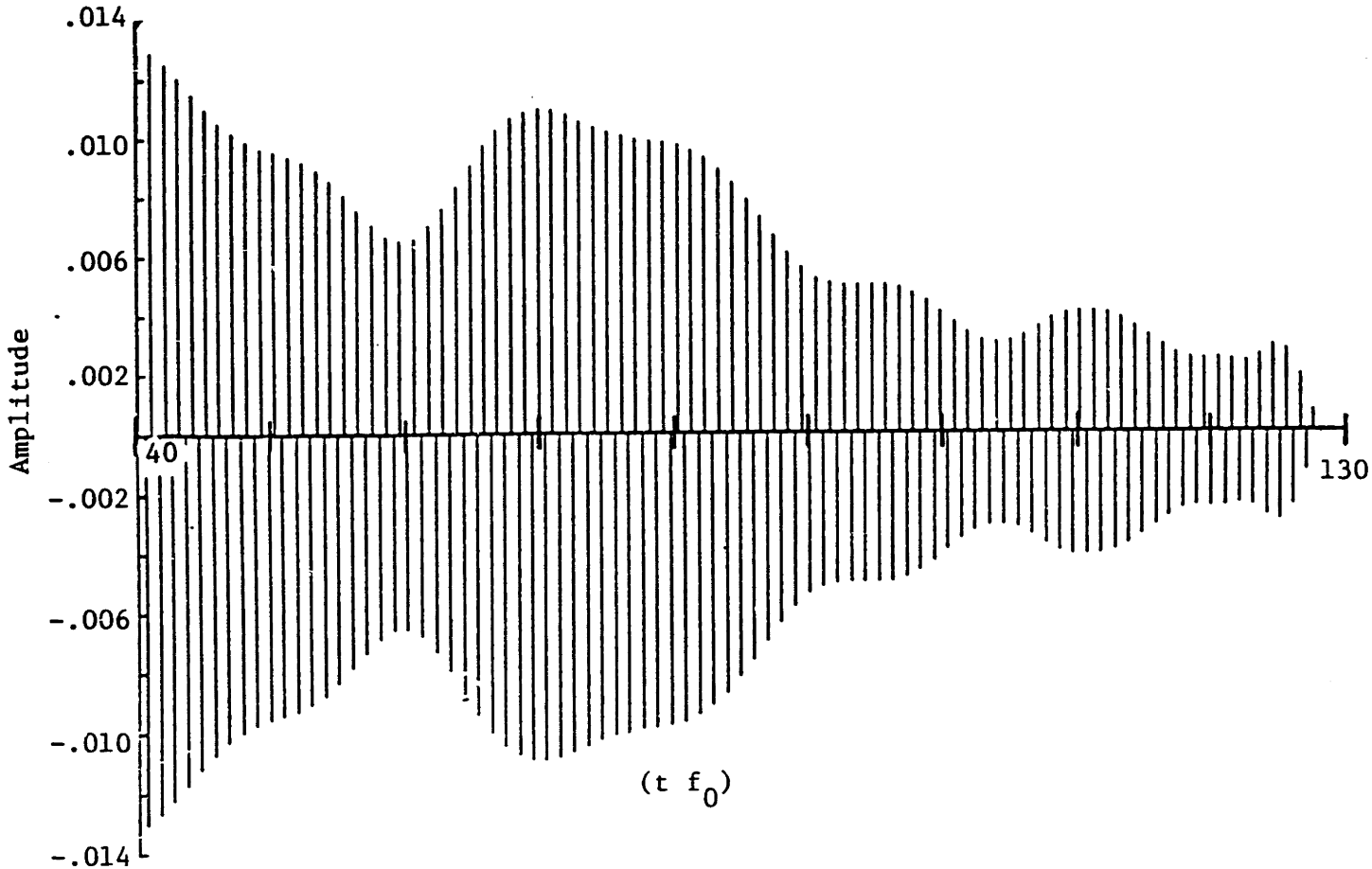

Figure 6.15 Right-Most Third of Prototype-I After Nonuniform Sampling with Extrapolation

Bandlimited extrapolation was used to increase the length from 503 to 514 samples. Note that the samples go to zero smoothly

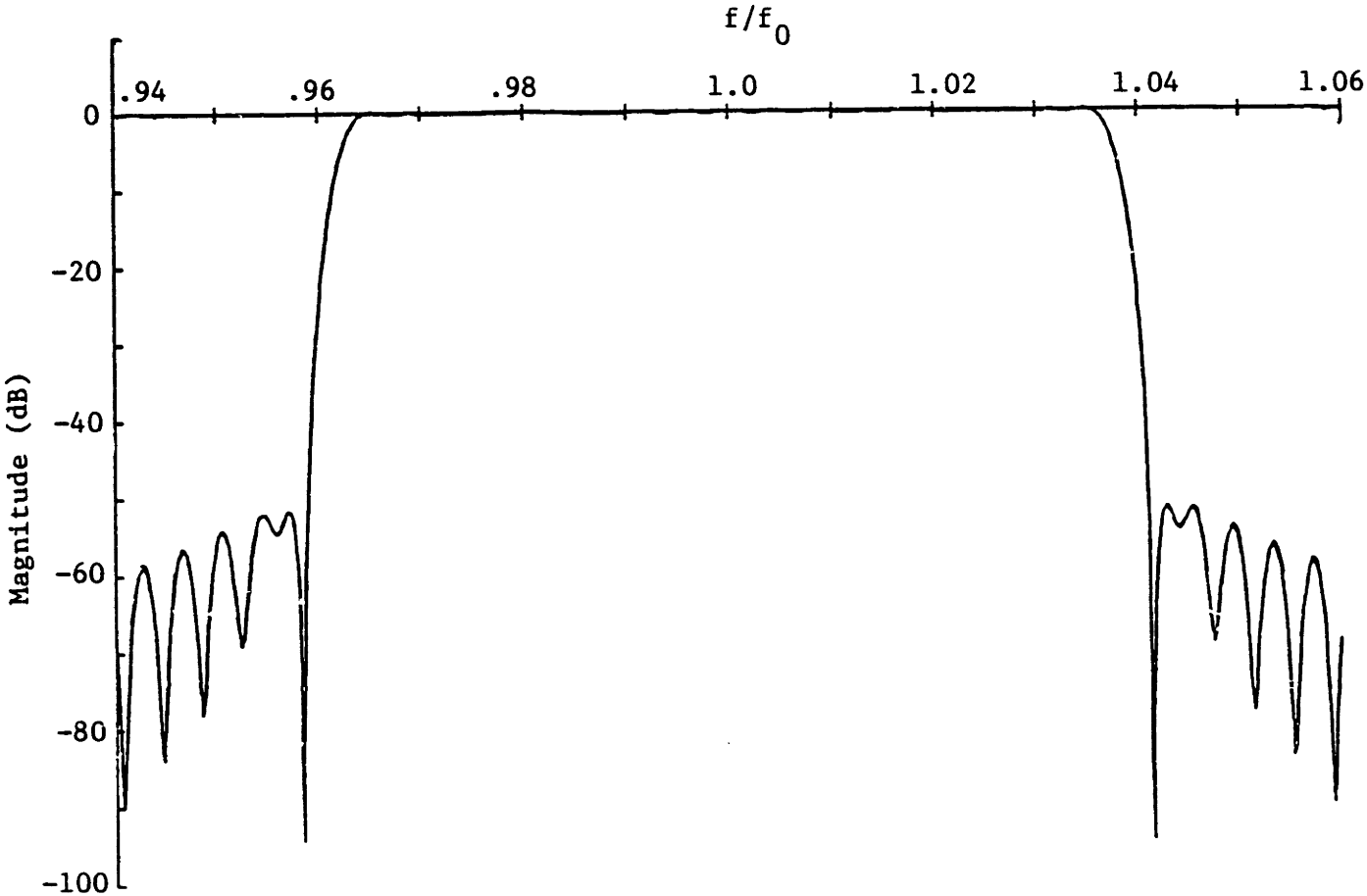

Figure 6.16a Frequency Response of Prototype-I After Nonuniform Sampling with Extrapolation

The time function was extrapolated by 11 points from 503 to 514. Note that on this scale, the uniformly and nonuniformly sampled frequency responses are indistinguishable.

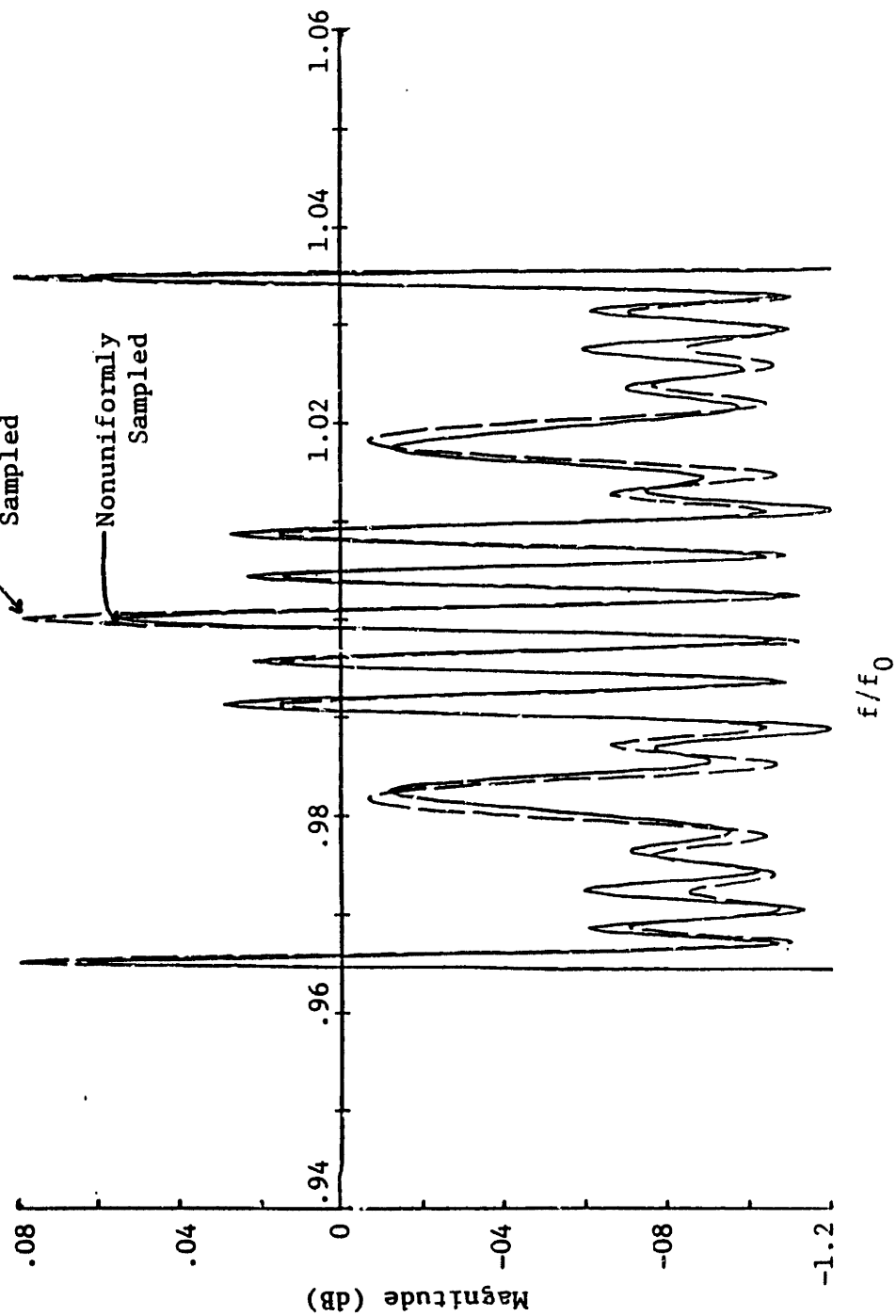

Figure 6.16b Frequency Response of Prototype-1 After Nonuniform Sampling with Extrapolation

The time function was extrapolated by 11 points from 503 to 514.

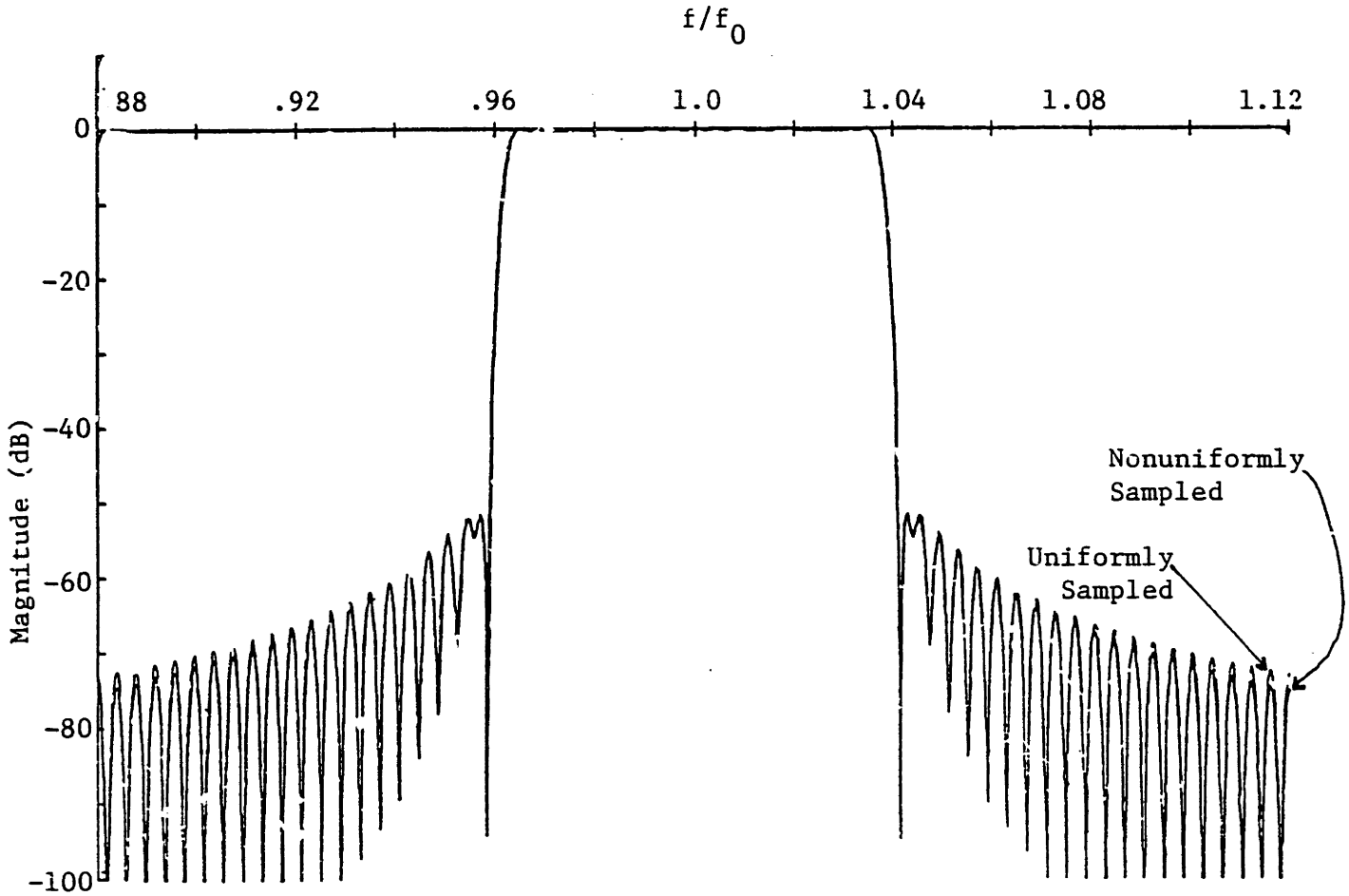

Figure 6.16c Frequency Response of Prototype-I After Nonuniform Sampling with Extrapolation

The time function was extrapolated by 11 points from 503 to 514.

but since there are only a few small samples, we anticipate that withdrawal weighting to be discussed in Sec 6.6 will be able to handle the situation. The frequency response of this waveform is displayed in Figs. (6.16a–6.16c). The agreement in the frequency responses between the nonuniformly and uniformly sampled waveforms is now very good in the passband, only differing by a few hundredths of a dB. In the rejection band, the nonuniformly sampled waveform has lower sidelobes. This is due to the smooth fall-off of the extrapolated samples.

6.5.1 Compensation for Second Order Effects

In the design of the first prototype waveform, we used the impulse model. This is the simplest model for the calculation of a SAW filter's frequency response. In theory, the same design algorithm could be used with a more accurate model to properly handle second order effects such as circuit factors, element factors, acoustic reflections and diffraction. In practice though, this can not be done unless extremely fast algorithms are developed for the evaluation of these effects. In order to not slow down the procedure significantly, the second order effects would have to be computable as rapidly as FFT's.

An alternative is to place the compensation for second order effects outside the optimized design loop. One possibility would be to compute the distortion caused by the second order effects to an optimized design which ignored these effects. The distortion can be modeled either as a multiplicative or as an additive effect, whichever is more accurate for the effect under study. If the distortion is small, then it is reasonable to assume that the perturbation in sample locations and amplitudes necessary to correct for this effect will also be small. Thus the distortion caused by the corrected function can be regarded as being the same as for the initial function. Using this technique, the second order effects

need only be computed once, and this same correction can be applied to all subsequent computed frequency responses within the optimization loop. Once an answer is obtained the exact response can be recomputed. If the second order effects have not been corrected to sufficient accuracy, this procedure can be repeated.

A different procedure was used which is based on the same premise of small second order effects requiring only small corrections. As an example, we correct for the element factor, $e(f)$, which according to Eq. (6.4) is a multiplicative distortion. We start with a prototype response which is optimized ignoring the element factor. The optimized desired magnitude response for each transducer is then divided by the square root of this element factor. This predistorted magnitude response is associated with the optimized single transducer phase response, inverse Fourier transformed to the time domain, windowed, and retransformed to the frequency domain. Finally this frequency response is multiplied by the element factor to obtain the achieved frequency response. It should be noted that this correction procedure is not iterative. It basically consists of one pass around the loop of Fig. 6.4 which defines the error to be minimized by the optimization procedure. Any desired magnitude response can be designed by this procedure. The key questions are how much does the dynamic range of the time function increase, and how much does the achieved frequency response degrade from the optimized uncompensated prototype. If the effect for which we want to compensate is small, we expect that only small changes to the optimal group delay and transition band shapes will be necessary.

An advantage of this procedure over the first, is that corrections to the phase response can also be achieved. We initially assumed that both transducers were to have opposite dispersion so that using the approximations implicit in Eq. (6.4), the final filter response would possess linear phase. Including circuit loading effects, acoustic reflections and

diffraction, this is not the case. If the computed full filter frequency response has an uncanceled phase, $e^{j\theta(f)}$ and we would like our filter to be nondispersive, then we simply use the above procedure twice. The first time the prototype response would be divided by $e^{j\theta(f)/2}$ and the second time by $e^{-j\theta(f)/2}$. Thus the lowest order phase response would be $e^{-j\theta(f)}$, which to first order would cancel the undesired perturbation.

The magnitude only element factor correction procedure was applied to prototype-I. The final achieved frequency response before multiplication by the element factor is displayed in Fig. 6.17. This indicates that we are trying to compensate for a passband tilt of about .7 dB caused by the deviation of the elemental sources from pure impulses. The achieved frequency response after multiplication by the element factor is presented in Fig. 6.18 along with the response of prototype-I. We note that the two responses are nearly identical in the passband; they differ by about .01 dB. Plots which compare the rejection band performance of prototypes I and II over a wider frequency band are not presented since they are indistinguishable. Fig. 6.19 confirms that only slight changes in the amplitude of the time function was required to compensate for the element factor. The difference in the instantaneous frequency responses was so small as not to be discernible on a plot. Thus, the viability of this optimization procedure to the design of filters corrupted by second order effects has been demonstrated.

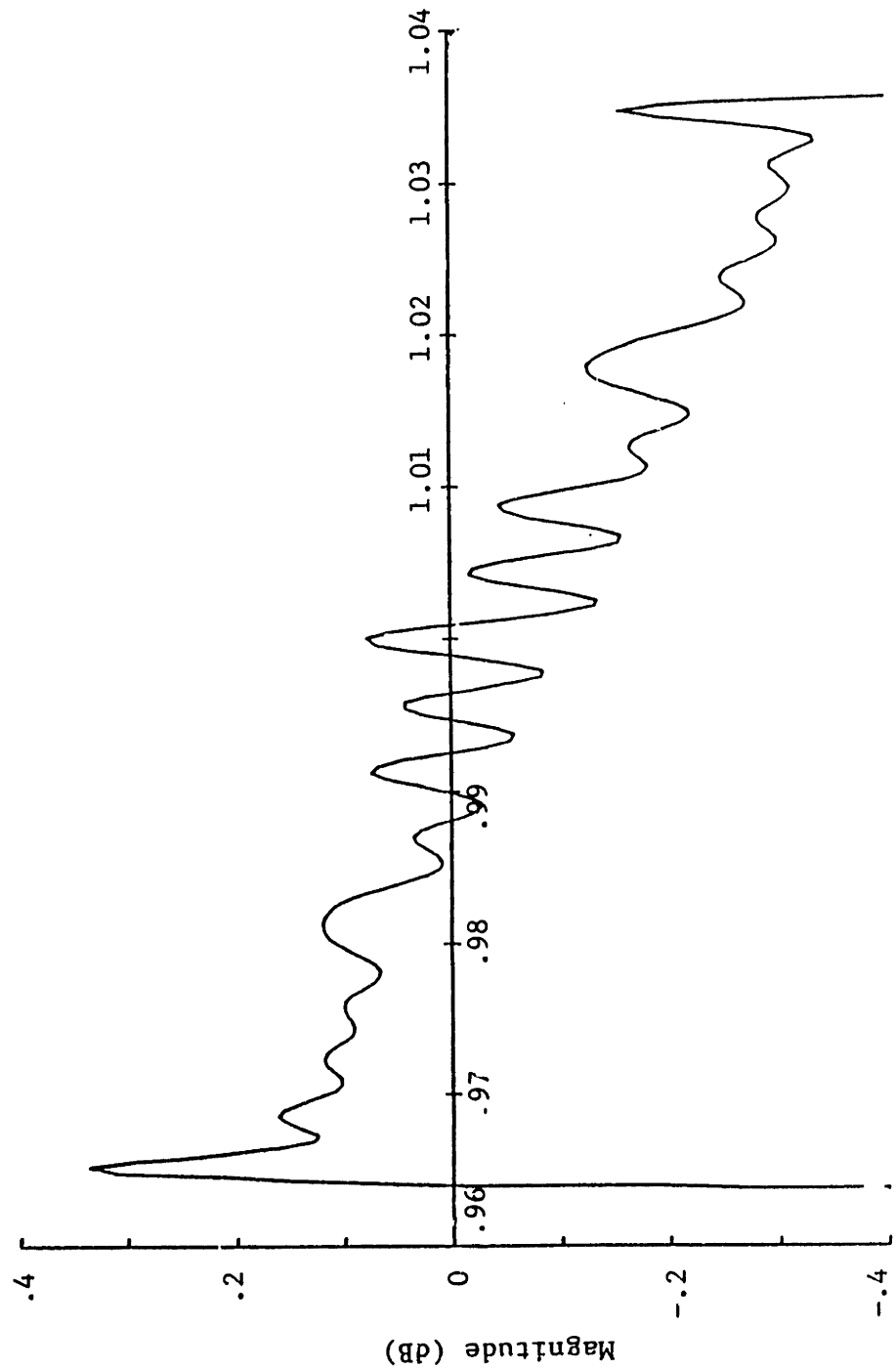

Figure 6.17 Achieved Frequency Response Before Multiplication by the Element Factor: Prototype-II

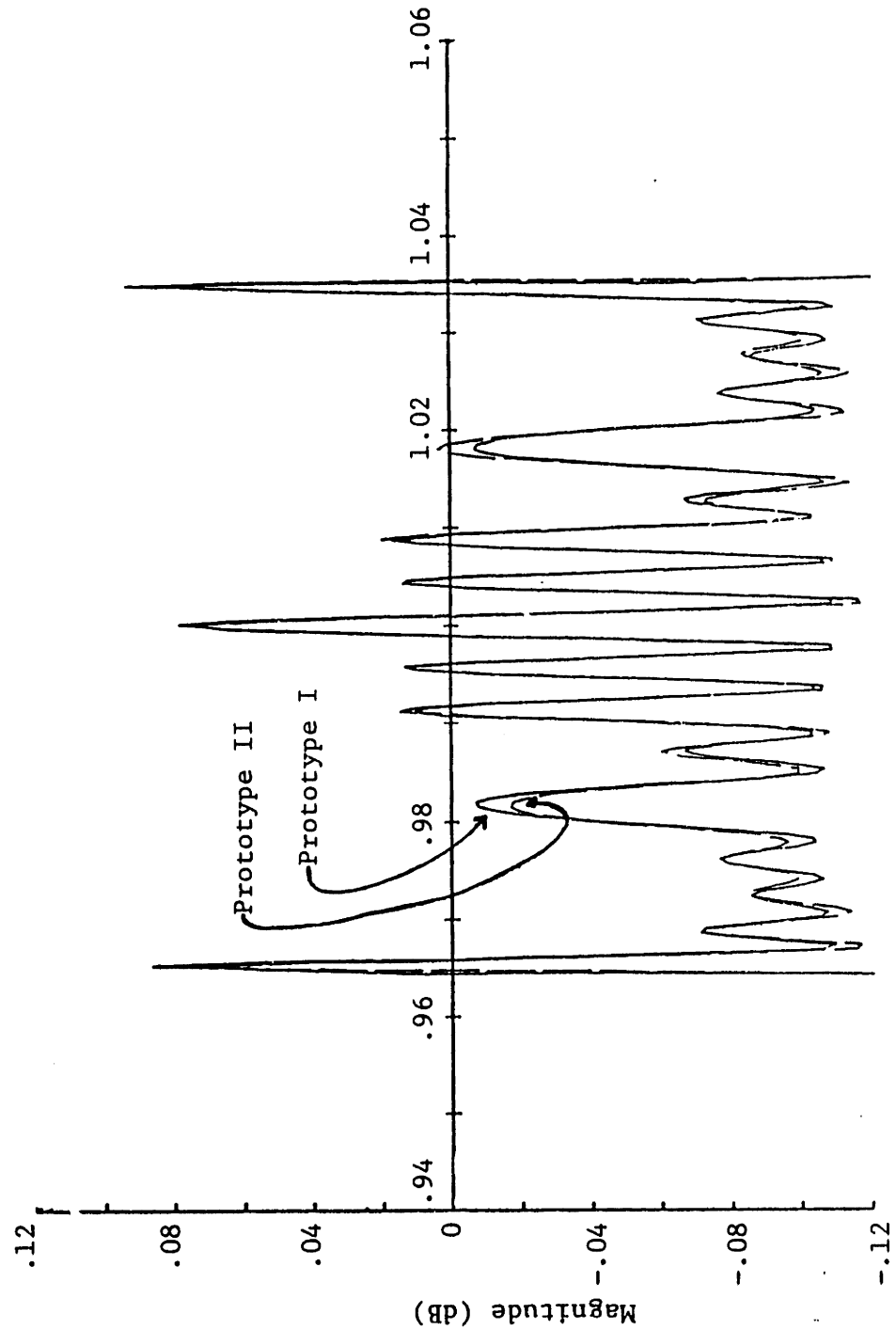

Figure 6.18 Compensated Prototype-II and Uncompensated Prototype-I Frequency Responses

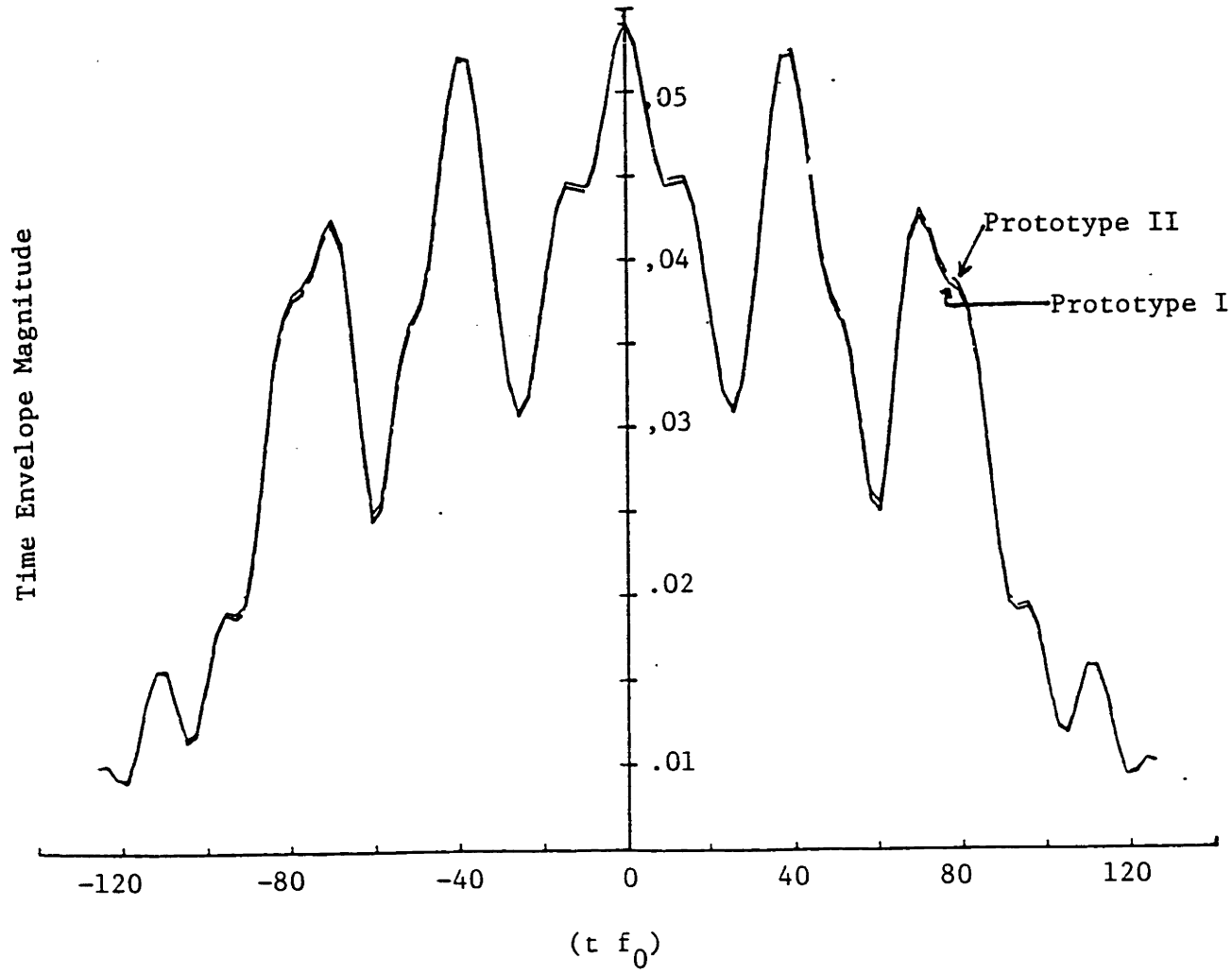

Figure 6.19 Final Single Transducer Time Domain Responses: Prototypes I and II
Magnitude of the baseband time envelopes

6.5.2 Minimax Approximation with a Sequence of Weighted L_2 Minimizations

Both prototypes I and II were designed assuming the group delay to be antisymmetrical. In these cases, minimax type designs were attempted with moderately large values for p_t and p_f in the L_{2p_t} and L_{2p_f} error definitions for the time and frequency errors respectively. In the design of prototype-IV we remove the symmetry condition on the group delay. In addition we use the L_2 error definitions for both time and frequency and attempt to obtain a minimax frequency response using a Lawson [89,59] type design.

The basic idea of the Lawson procedure is to perform a sequence of weighted L_2 error minimizations to obtain an L_∞ approximation. The weighting function is increased wherever the error is too large and decreased where it is too small. The end result is that the weighting function is non-zero only at the points of maximum error in the minimax approximation. The rationale behind this is that L_2 error approximations are much easier to compute than L_∞ ones. Lawson proved convergence if the approximation consists of a linear superposition of functions satisfying the Haar* condition, and if the approximation is being done on a discrete set instead of a continuum. This convergence proof depended on a particular sequence of weighting functions. Lawson could initialize his procedure with any positive weighting function. Then if e_i^k and w_i^k are the error and weighting function respectively on the k^{th} iteration at the i^{th} point of the finite set over which the approximation is being done,

$$w_i^{k+1} = \frac{w_i^k |e_i^k|}{\sum_i w_i^k |e_i^k|} \tag{6.55}$$

* The Haar condition requires linear independence for any set of N vectors, $[\phi_i(x_1), \phi_i(x_2), \ldots, \phi_i(x_N)], i = 1, N$ for N distinct points, x_i, in the interval over which the approximation is being done, where $[\phi_1, \phi_2, \ldots, \phi_N]$ is the set of basis functions for the approximation.

If at an early stage in the algorithm w_i is *accidentally* zero because the error e_i happens to be zero, then the weighting function must be perturbed away from zero at that point and then the algorithm can proceed. The denominator in Eq. (6.55) serves to maintain the area under the weighting function at one. According to Eq. (6.55) the ratio of the weight at two points is modified by the ratio of the errors at these points

$$\frac{w_i^{k+1}}{w_j^{k+1}} = \left(\frac{w_i^k}{w_j^k}\right)\frac{|e_i^k|}{|e_j^k|} \tag{6.56}$$

Thus as we expected, the weight is increased where the error is large and decreased where it is small.

In our case, the Lawson algorithm does not really apply since our approximation is not being done with a linear superposition of functions satisfying the Haar condition. Furthermore Lawson's algorithm was found to converge extremely slowly. For example, a test case with $N = 4$ parameters and $M = 50$ points at which the error is to be measured, required about 250 L_2 optimizations. Rice and Usow [89] present an acceleration scheme which reduces this dramatically to about 14. When N was increased to 10 and M was increased to 100, 40 L_2 optimizations were required using the acceleration scheme. Our problem is substantially larger with $N = 35$ and $M = 1024$, and would require even more optimizations, making this approach impractical. Thus, it was decided to use the basic idea behind the Lawson algorithm, but not the same procedure.

In contrast with the Lawson procedure, smooth weighting functions were used which were characterized by a few sample values. Linear interpolation was used between these break points. Using an L_2 error criterion, the main problem is a broadening of the transition region, both into the rejection band and the passband. Thus at first, most of the effort was focussed on adjusting the break point values at the rejection band and passband

edges. At first these break points were adjusted inversely proportional to the desired error reduction. For example, if the error of the passband edge were e_1, while if the peak error near the center frequency were e_2, then the weights at positions 1 and 2 would be adjusted so that

$$\frac{w_1^{k+1}}{w_2^{k+1}} = \frac{|e_1^k|}{|e_2^k|}\frac{w_1^k}{w_2^k} \tag{6.57}$$

After the L_2 optimization was performed using this new weighting function, the new errors e_1^{k+1} and e_2^{k+1} are typically found to be closer, but not equal. It is assumed that therefore a larger correction in the weighting function should have been made. Assuming linearity, the weights should have been corrected by an additional factor of e_1^{k+1}/e_2^{k+1} yielding the formula

$$\frac{w_1^{k+1}}{w_2^{k+1}} = \frac{|e_1^k|}{|e_2^k|}\frac{w_1^k}{w_2^k}\frac{e_1^{k+1}}{e_2^{k+1}} \tag{6.58}$$

Unfortunately e_1^{k+1} is not known until w_1^{k+1} is found after the optimization is done. Thus, this correction factor is used to find the next value of the weighting function

$$\frac{w_1^{k+2}}{w_2^{k+2}} = \frac{|e_1^{k+1}|}{|e_2^{k+1}|}\frac{w_1^{k+1}}{w_2^{k+1}}\frac{|e_1^{k+1}|}{|e_2^{k+1}|} \tag{6.59}$$

This version of the update was also suggested by Lawson as a possible acceleration procedure but without the above intuitive explanation. Unfortunately, Eq. (6.59) often leads to an overcorrection and would thus lead to divergence if used all the time. A continuum of updates ranging from that of Eq. (6.57) to Eq. (6.59) can be defined with a

parameter p ranging from 1 to 2

$$\frac{w_1^{k+2}}{w_2^{k+2}} = \frac{w_1^{k+1}}{w_2^{k+1}}\left(\frac{e_1^{k+1}}{e_2^{k+1}}\right)^p \tag{6.60}$$

Depending on whether the previous result was overcorrected or undercorrected, a value of p was selected for the next modification to the weighting function breakpoint values.

In the rejection band, the weighting function was constant on the first iteration. This served to set the tradeoff between the passband ripple level and the sidelobe level. On subsequent iterations, the weighting function was non-zero only near the band edge in order to sharpen the transition region. It was a triangular function, running from the first null to the rejection band edge. The band edge rejection level was controlled in a manner similar to that used for the passband, except that weights w_1 and w_2 in Eqs. (6.57–6.60) were the total area under the weighting function in the rejection band and passband respectively.

This procedure was used to design a prototype AM-PM waveform with no symmetry imposed on the phase function. In this case, the element factor compensating function was inside the optimization loop. The starting point was a linear group delay similar to that of prototype-I, but with a randomized sign sequence applied to the group delay break point values in order to break the symmetry. The optimization was done over $N = 35$ parameters, all of which were used to characterize the phase. The desired transition band shape was not adjusted; it was assumed to be linear. In order to conserve computer time, the L_2 optimizations were sometimes terminated before convergence to high accuracy. The initial weighting function was increased in the rejection band in order to trade degraded passband performance for improved rejection band performance. After 5 L_2 optimizations, each consisting of $1.5N$ to $2.7N$ quasi-Newton iterations, prototype-IV resulted which is displayed in Figs. (6.20a–6.21). Note that the weighting function had

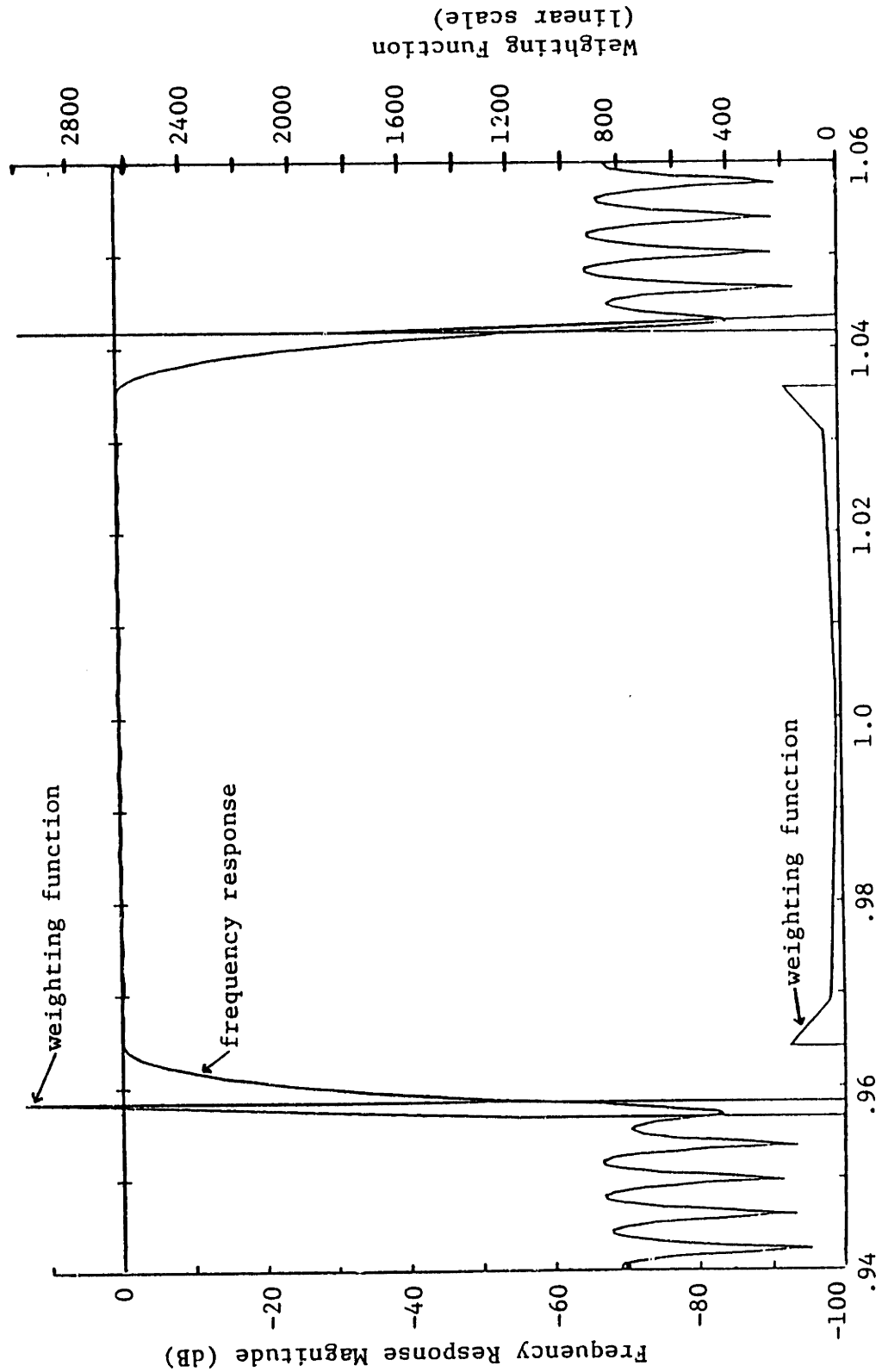

Figure 6.20a Achieved Frequency Response and Weighting Function: Prototype-IV
Passband and Rejection Band

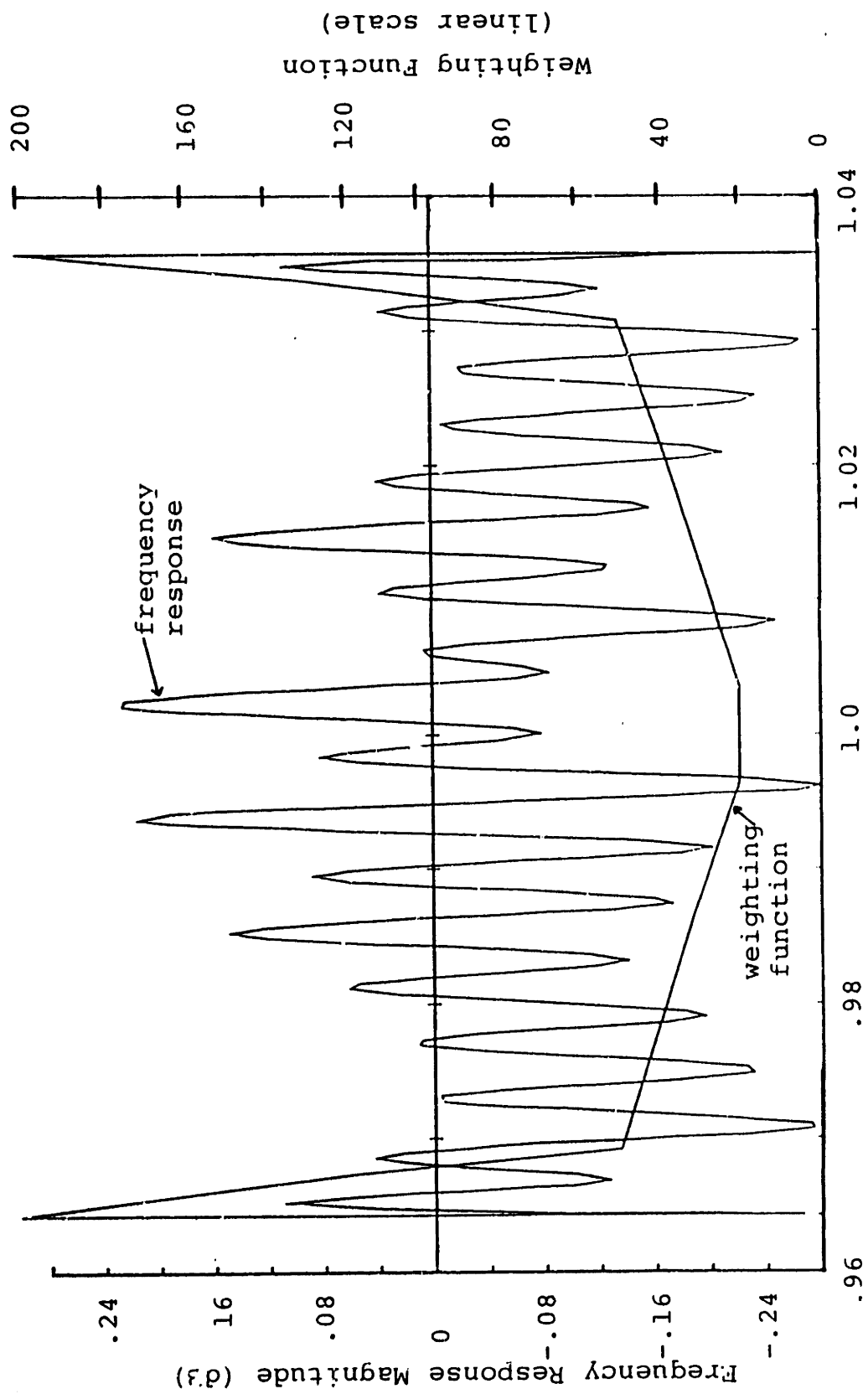

Figure 6.20b Achieved Frequency Response and Weighting Function: Prototype-IV
Passband

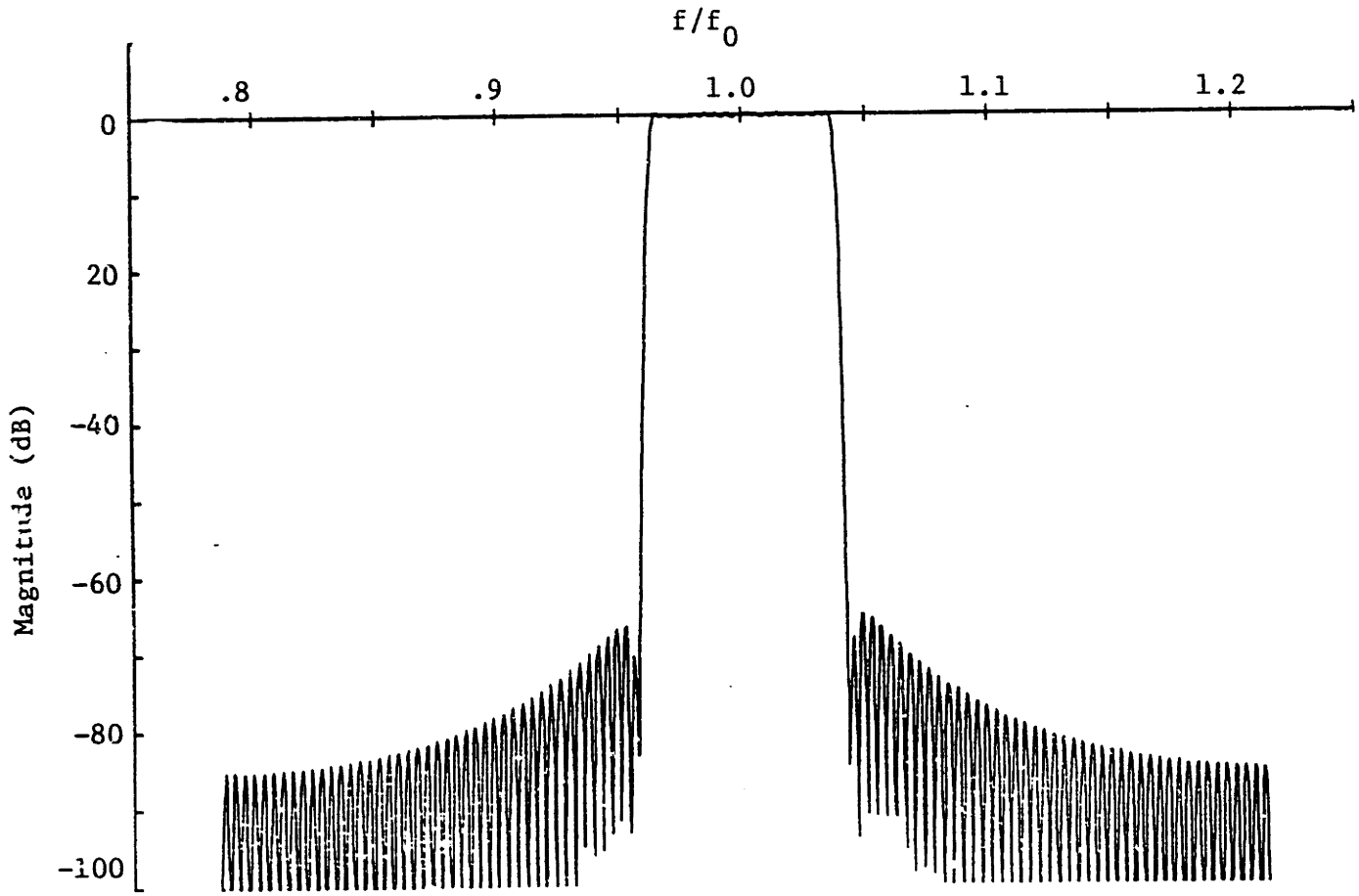

Figure 6.21 Achieved Frequency Response: Prototype-IV
Wideband Response

Prototype	# of group-delay prms.	# of transition band prms.	group-delay anti-symmetry	Compensation for the element factor	P_t Eqs. 6.7, 6.8	P_f Eqs. 6.7, 6.8	Dynamic† range	Peak* reject band level	Peak-* peak pass-band ripple	Shape-* factor ††	Fractional* band-width
I	17	3	yes	no	30	10	5.78	-51.8 -51.5	.20 .19	1.156 1.154	.0712 .0712
II	17	3	yes	yes	30	10	5.87	-51.6 -51.5	.21 .20	1.155 1.154	.0712 .0712
III	33	0	yes	yes	1	1	12.17	-66.8 -66.8	.40 .40	1.176 1.176	.0712 .0712
IV	35	0	no	yes	1	1	6.60	-65.2 -65.7	.51 .50	1.177 1.176	.0714 .0714

Table 6.1 Summary of Results: Low Dynamic Range AM-PM Waveforms
Each Amplitude and Phase Modulated (AM-PM) waveform is 252 wavelengths long, while the nonuniformly sampled waveforms after bandlimited extrapolation are 256.5 wavelengths long. * The upper value applies to the uniformly sampled result of the optimization procedure, while the lower value applies to the result after nonuniform sampling. † The dynamic range is the ratio of the maximum to the minimum baseband time envelope magnitude. †† See Fig. 6.3 for the definition of shape factor.

to be very large at both the rejection band and passband edges in order to achieve the desired sharp cut-off. The remaining plots characterizing this design are presented in Figs. (6.22a–6.23).

From the results presented in Table 6.1, we note that in going from prototype I to IV, we have successfully traded passband performance for sidelobe rejection. Sidelobe rejection increased by about 15 dB at a cost of a .3 dB increase in peak to peak passband ripple. Unfortunately, the shape factor degraded from 1.156 to 1.177. This is not an indication that something is wrong with using a sequence of L_2 optimizations. The problem occurred because the discrete uniformly spaced points of the FFT at which the frequency response was computed, did not coincide with the reject band and passband edges. The solution would be to add additional points to the frequency error definition

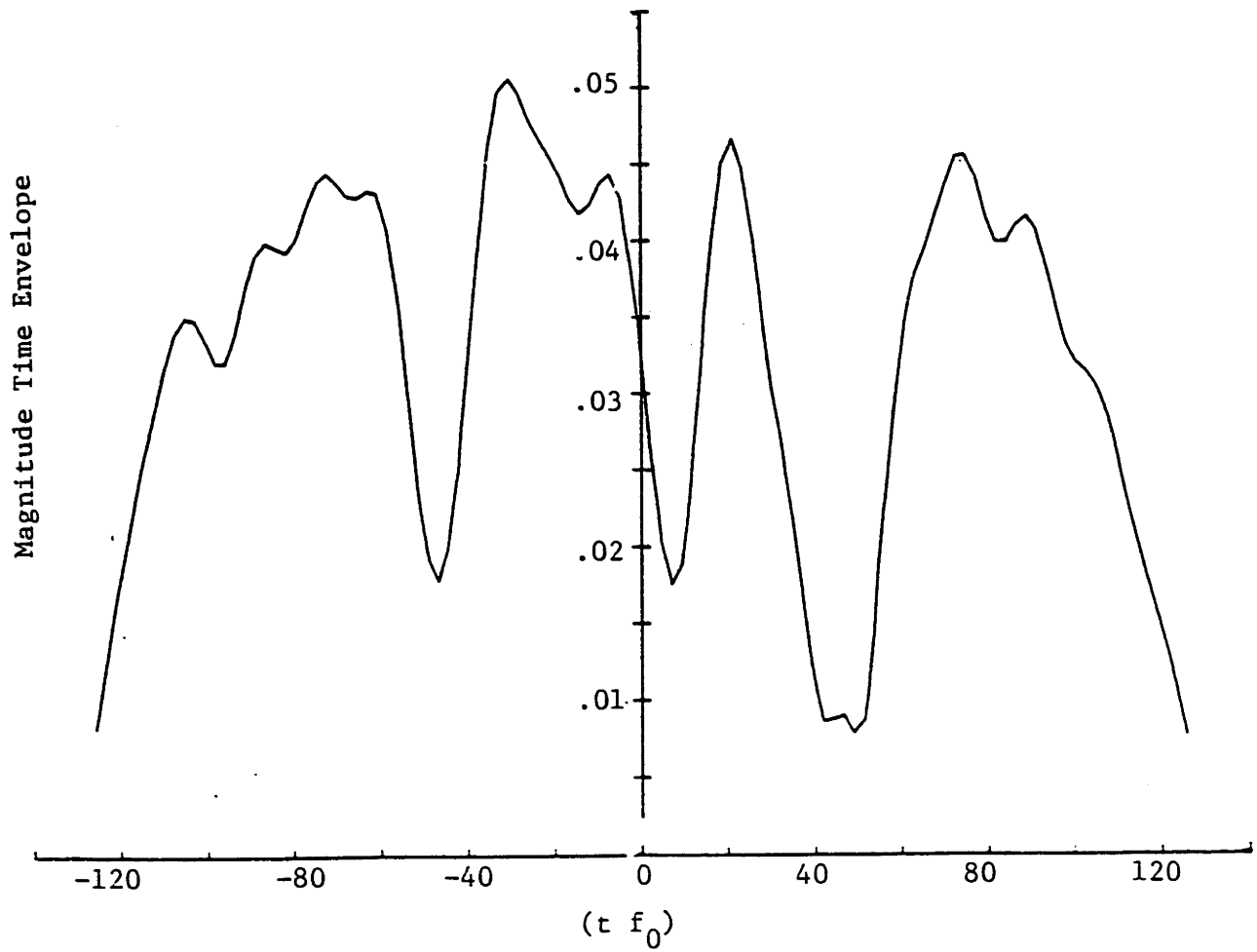

Figure 6.22a Final Single Transducer Time Domain Response: Prototype-IV
Magnitude of the baseband time envelope

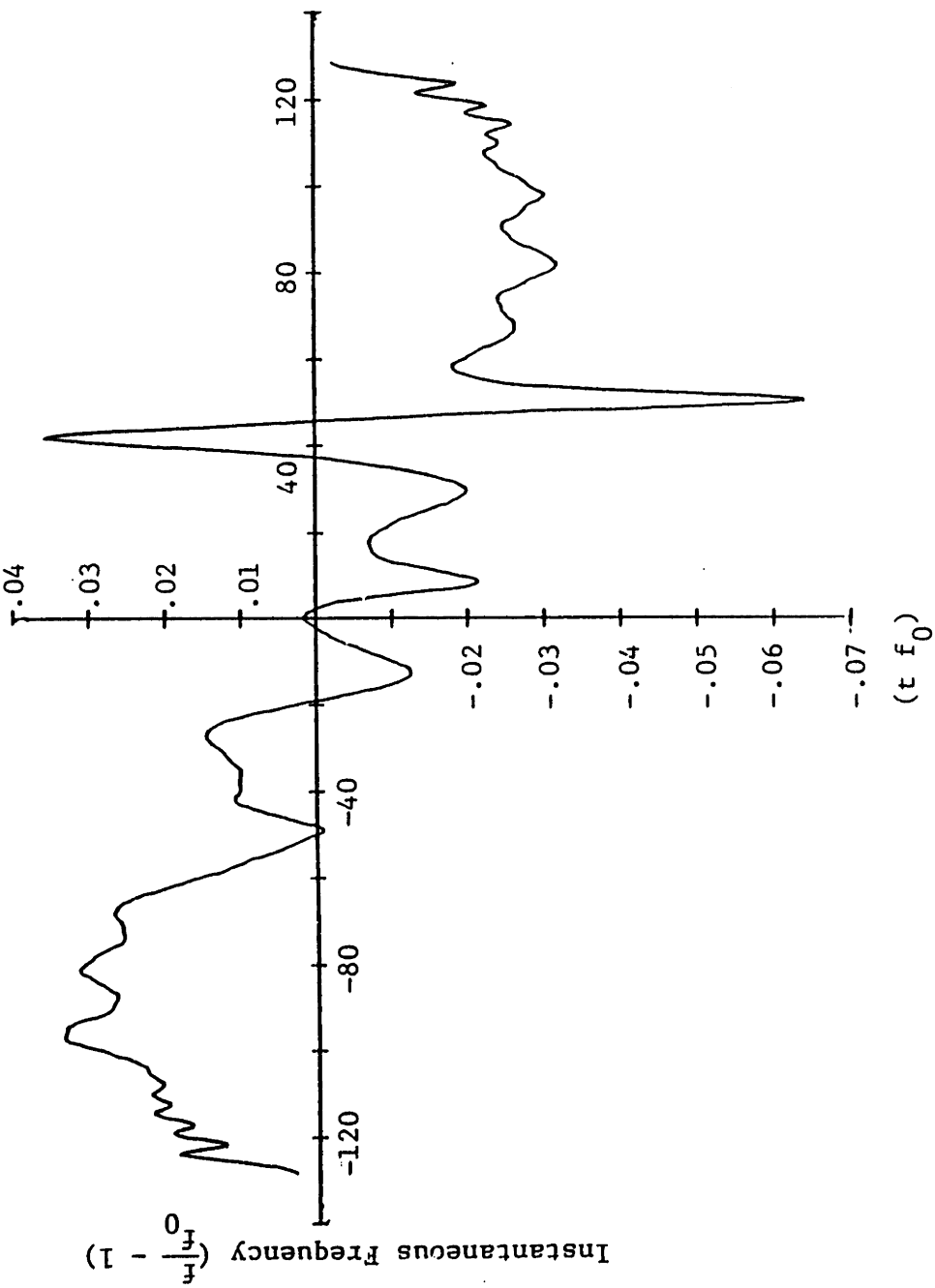

Figure 6.22b Final Single Transducer Time Domain Response: Prototype-IV
Instantaneous frequency

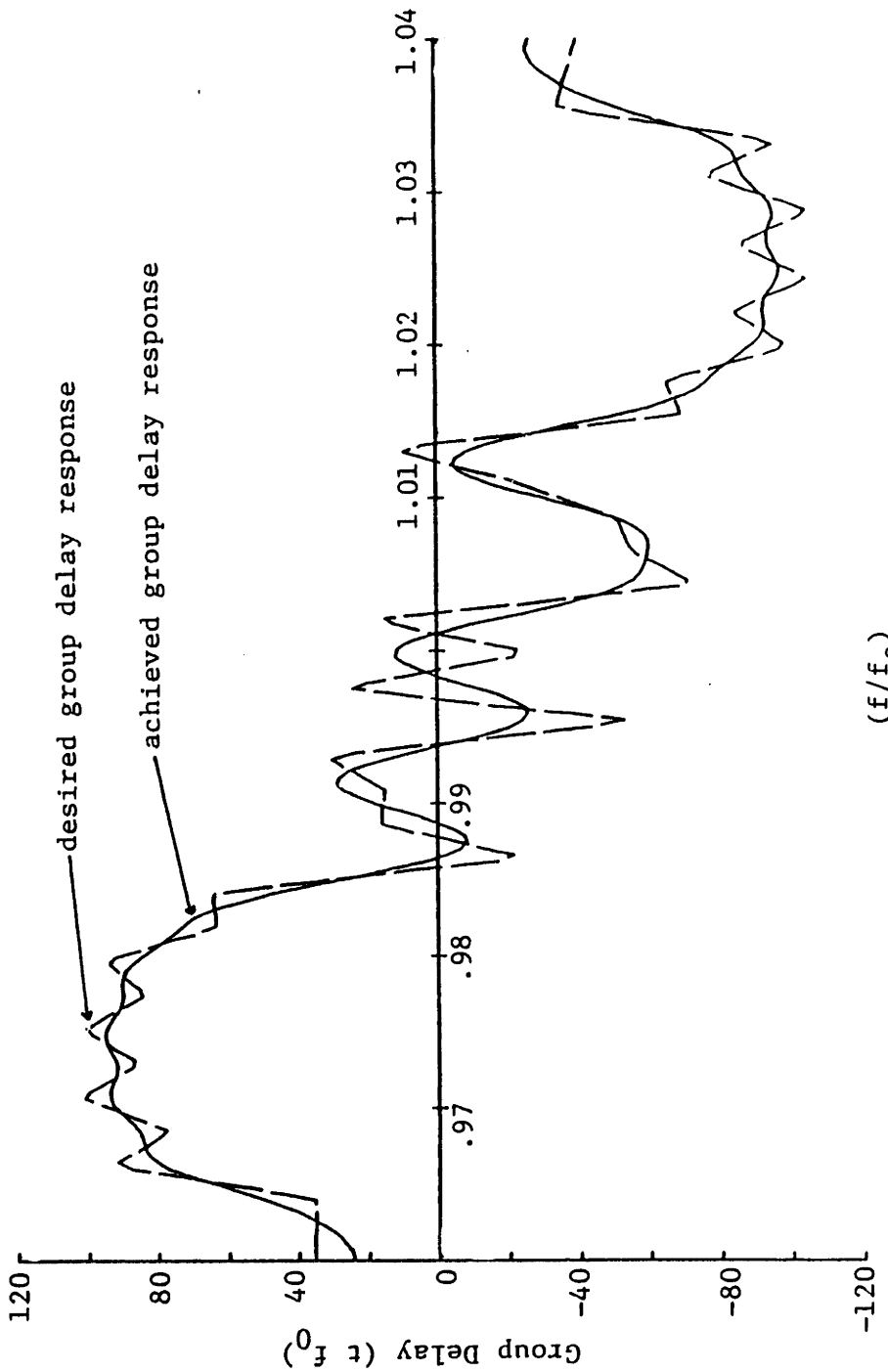

Figure 6.23 Final Desired and Achieved Single Transducer Group Delay Responses: Prototype-IV

which are exactly at these band edge frequencies. These values could be obtained by interpolation from the closest FFT sample values.

The final waveform, prototype-III, was designed in much the same way as prototype-IV, using a sequence of weighted L_2 optimizations with varying weights. This time an antisymmetric group delay was used. The starting point was prototype-IV, except that the group delay for negative time was flipped in sign and used for positive time. This cut the number of parameters by a factor of two. In order to keep roughly the same number of parameters, new group delay break points were introduced at the midpoint between existing break points. Linear interpolation was used to obtain the initial group delay values at these extra points.

Plots detailing the performance of prototype-III are presented in Figs. (6.24a–6.26). From Table 6.1 we see that the final frequency response resulting from prototypes III and IV are roughly equivalent as to passband ripple and rejection level. Prototype-IV however achieves this level of performance with half the dynamic range required by prototype-III. This seems to indicate that it is advantageous to allow the group delay shape to be completely general, i.e. not to force antisymmetry on the group delay. This demonstration is not a conclusive proof, however, since it is also possible that there exists a deeper local minimum of the error for prototype-III which would make the performance of prototypes III and IV comparable.

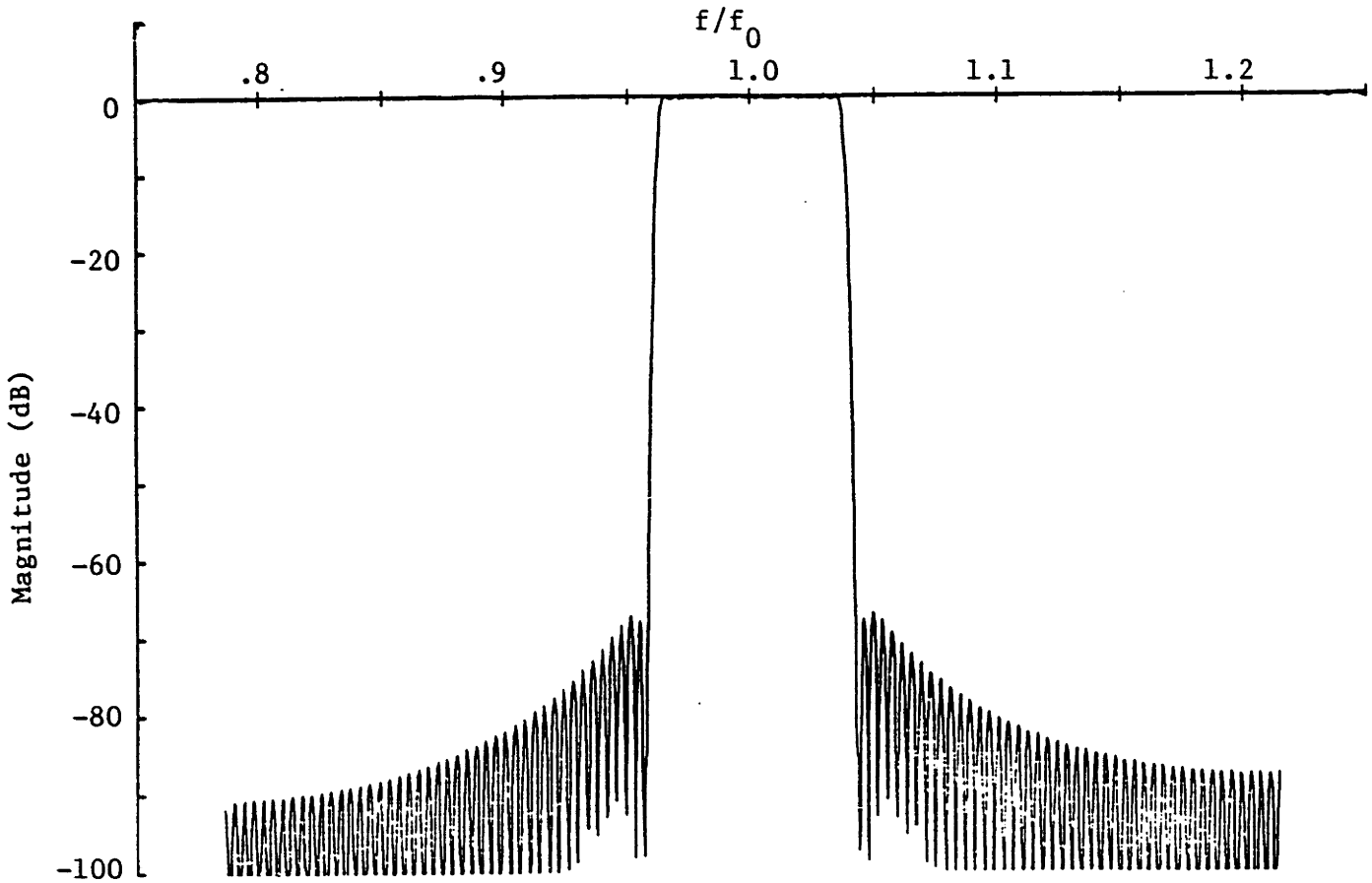

Figure 6.24a Achieved Frequency Response: Prototype-III
Wideband Response

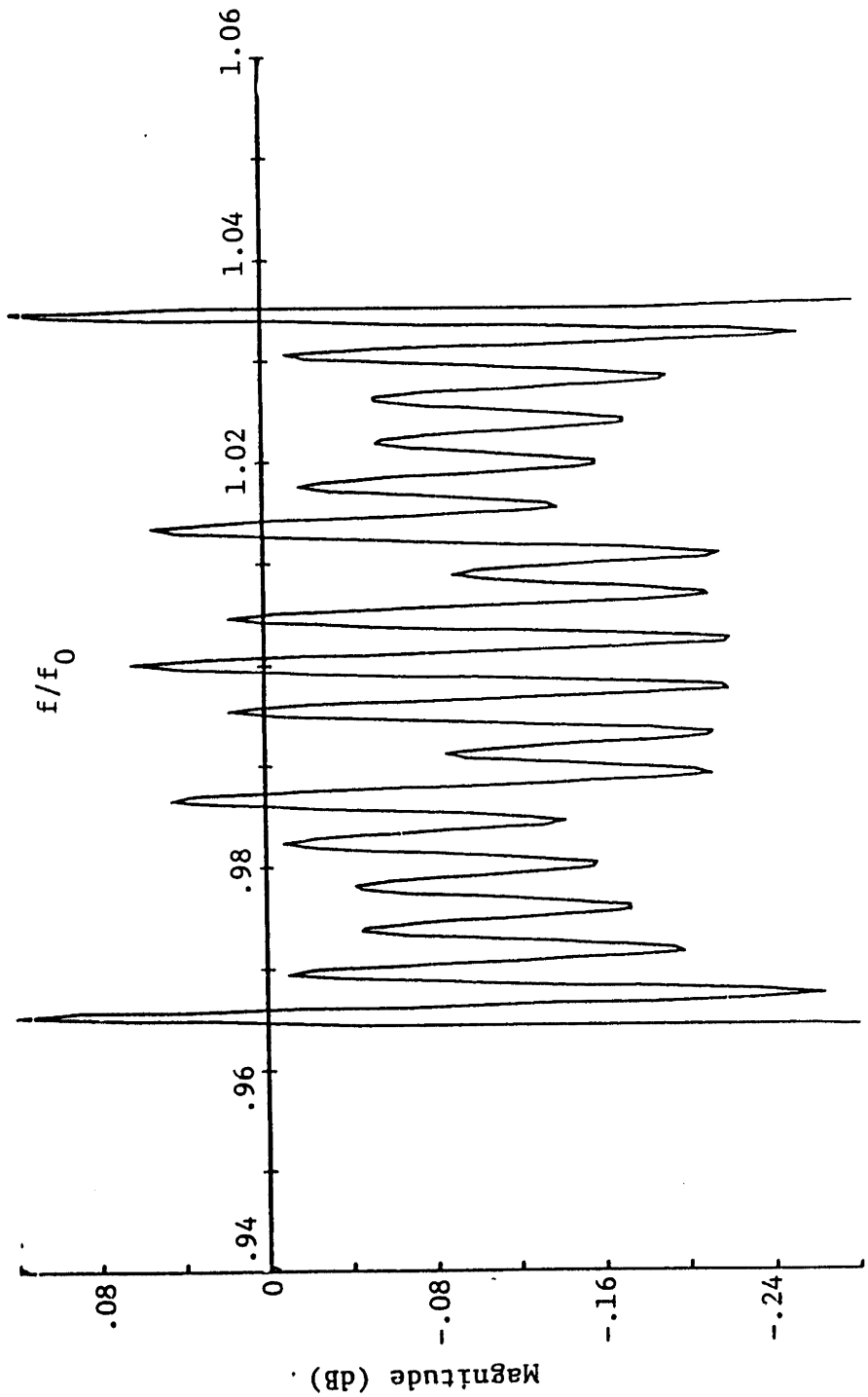

Figure 6.24b Achieved Frequency Response: Prototype-III
Passband Response

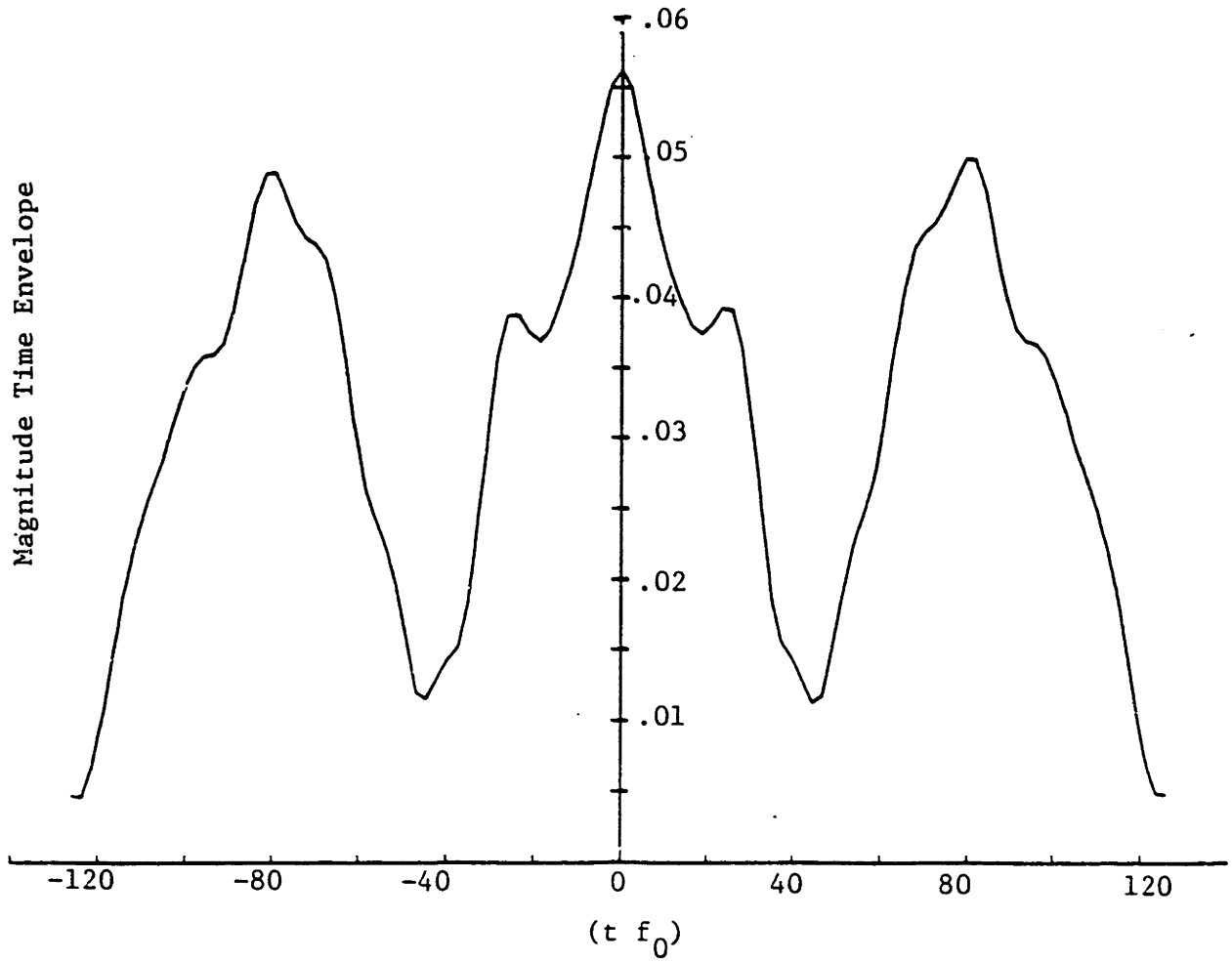

Figure 6.25a Final Single Transducer Time Domain Response: Prototype-III
Magnitude of the baseband time envelope

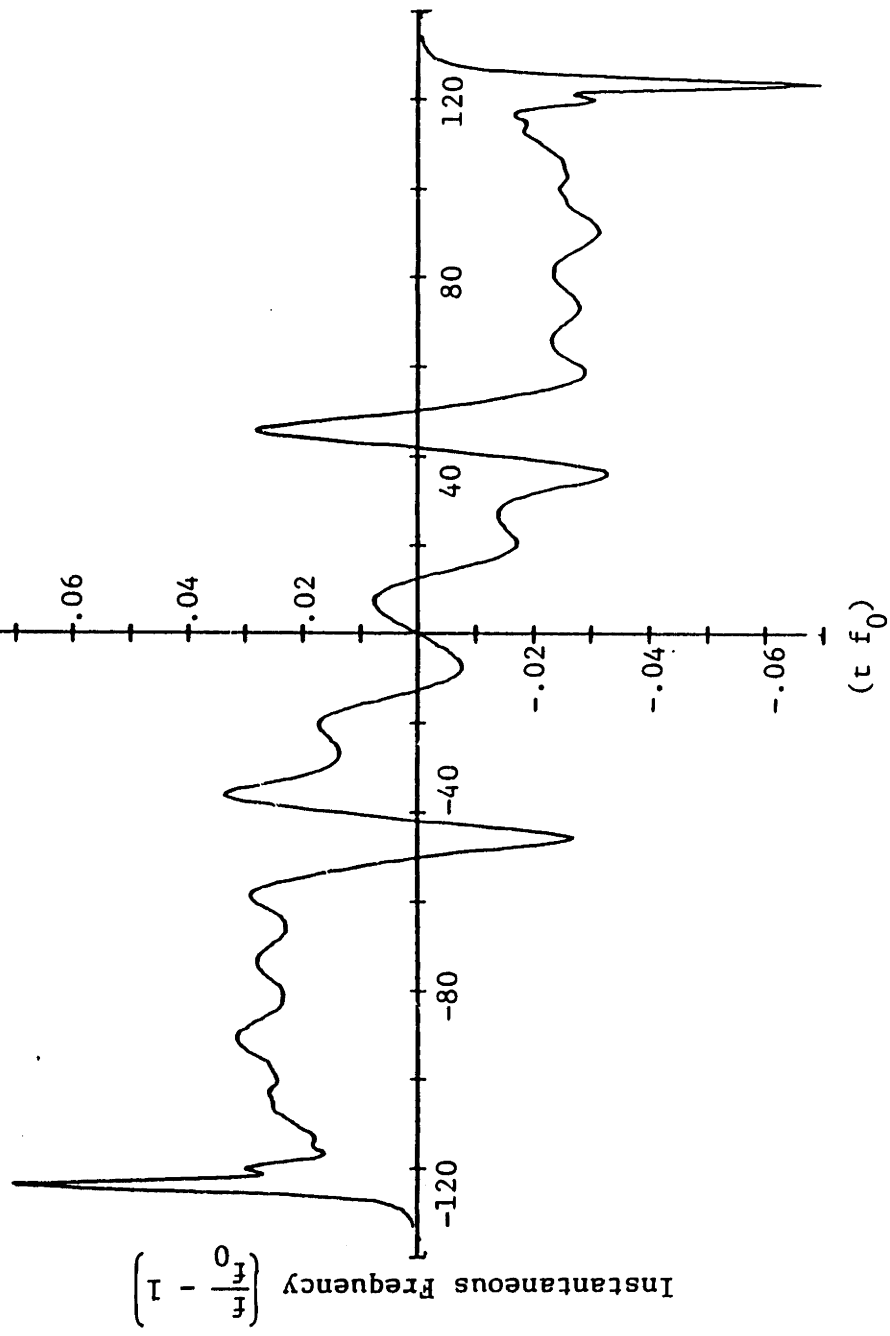

Figure 6.25b Final Single Transducer Time Domain Response: Prototype-III
Instantaneous frequency

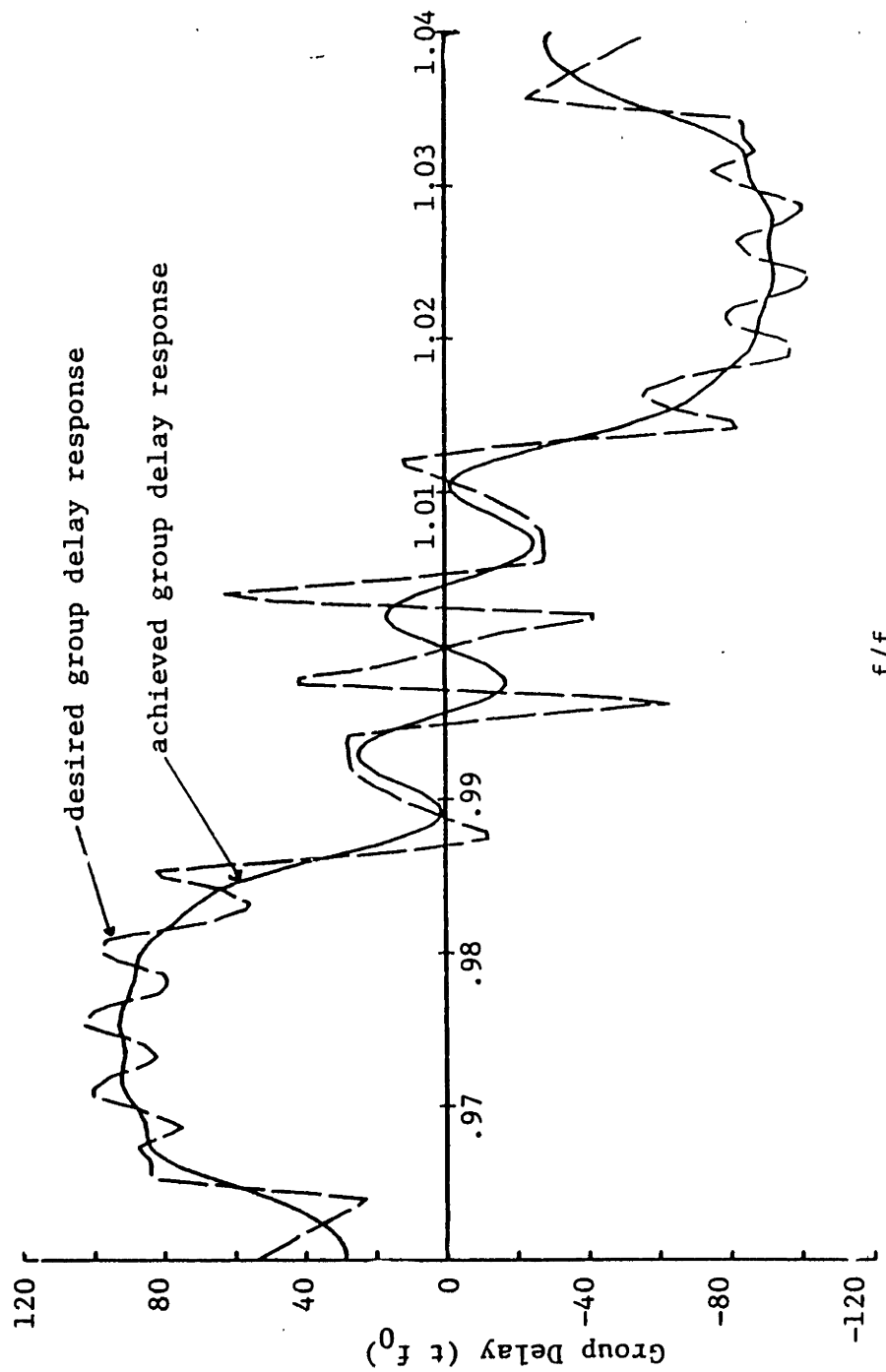

Figure 6.26 Final Desired and Achieved Single Transducer Group Delay Responses: Prototype-III

6.5.3 Summary of Results: Low Dynamic Range Synthesis

Although the prototype filters were designed using an optimization procedure, no claim can be made as to the global optimality of the resultant filters. All that can be guaranteed is convergence to a local minimum of the error function. There probably are many local minima, only one of which is the global optimum. Another problem is that the parameterization used is not general enough to include all possible nonuniformly spaced low dynamic range waveforms. It should be noted however, that arbitrary spacing should not really be allowed. If the spacing is highly irregular, the assumption of a relatively constant element factor breaks down, and the the achieved frequency response would be quite different from that described by Eq. (6.4).

Nevertheless, it is important to gain some feel as to how good these pseudo-optimal designs are. In Table (6.2) we compare the results obtained with the prototype-I amplitude and phase modulated design, with some optimal amplitude modulated uniformly sampled designs produced by the Parks-McClellan [85] Remez [12] (PMR) algorithm. The comparison is made between filters with the same passband ripple, rejection level, fractional bandwidth, and shape factor. We note that if two identical transducers are used in both cases, that the PMR design must be 16% longer to achieve the same performance. If the full response is placed in a single transducer, however, the PMR design is 19% shorter than prototype-I. Note that the dynamic range required by the AM-PM waveform is only 6.03, while it is 283 and 654 for the optimal PMR designs. The PMR designs would therefore be much more affected by diffraction and electrostatic end effects if they were implemented with apodization, than would the AM-PM designs. We have thus demonstrated that this procedure can yield waveforms similar in performance to those produced by the optimal Parks-algorithm, but with much lower dynamic range.

	Length of Full Device	Peak Sidelobe Level (dB)	Peak-Peak Passband Ripple (dB)	Shape† Factor	Dynamic* Range of Time Weighting Required
Nonuniformly Sampled Prototype-I (2 identical IDTs)	513	-51.5	.19	1.154	6.03
Parks-McClellan Algorithm (2 identical IDTs)	595	-51.6	.18	1.154	283
Parks-McClellan Algorithm (all filtering in 1-Transducer)	417.5	-51.5	.18	1.154	654

Table 6.2 Comparison of Prototype-I Low Dynamic Range Design with the Optimal Parks-McClellan Amplitude Modulated Designs

* Here dynamic range is defined as the ratio of the maximum sample value to the average of the minimum 10%. This prevents the measure of the dynamic range from being unduly affected by a few very small samples.

† See Fig. 6.3 for the definition of shape factor.

6.6 Withdrawal Weighting

Withdrawal weighting [42] is the final step in our algorithm for high performance filter synthesis without apodization. We take the nonuniformly sampled prototype amplitude and phase modulated (AM-PM) waveform with a relatively flat time envelope, and approximate it with a sequence of constant amplitude samples and zero weight ones. The technique is based on the fact that in a narrow band sense, source weights can be moved by half a wavelength at the center frequency, and flipped in sign, without affecting the response very much. Thus we would approximate the sequence of source strengths $\frac{1}{2}$, $-\frac{1}{2}$, $\frac{1}{2}$, $-\frac{1}{2}$, with the withdrawal weighted sequence 1, 0, 1, 0. The end result is that in regions in which the envelope amplitude is large, most of the samples are retained, while in regions with much smaller envelope amplitude, most of the samples are set to zero. This is depicted in Fig. 6.27.

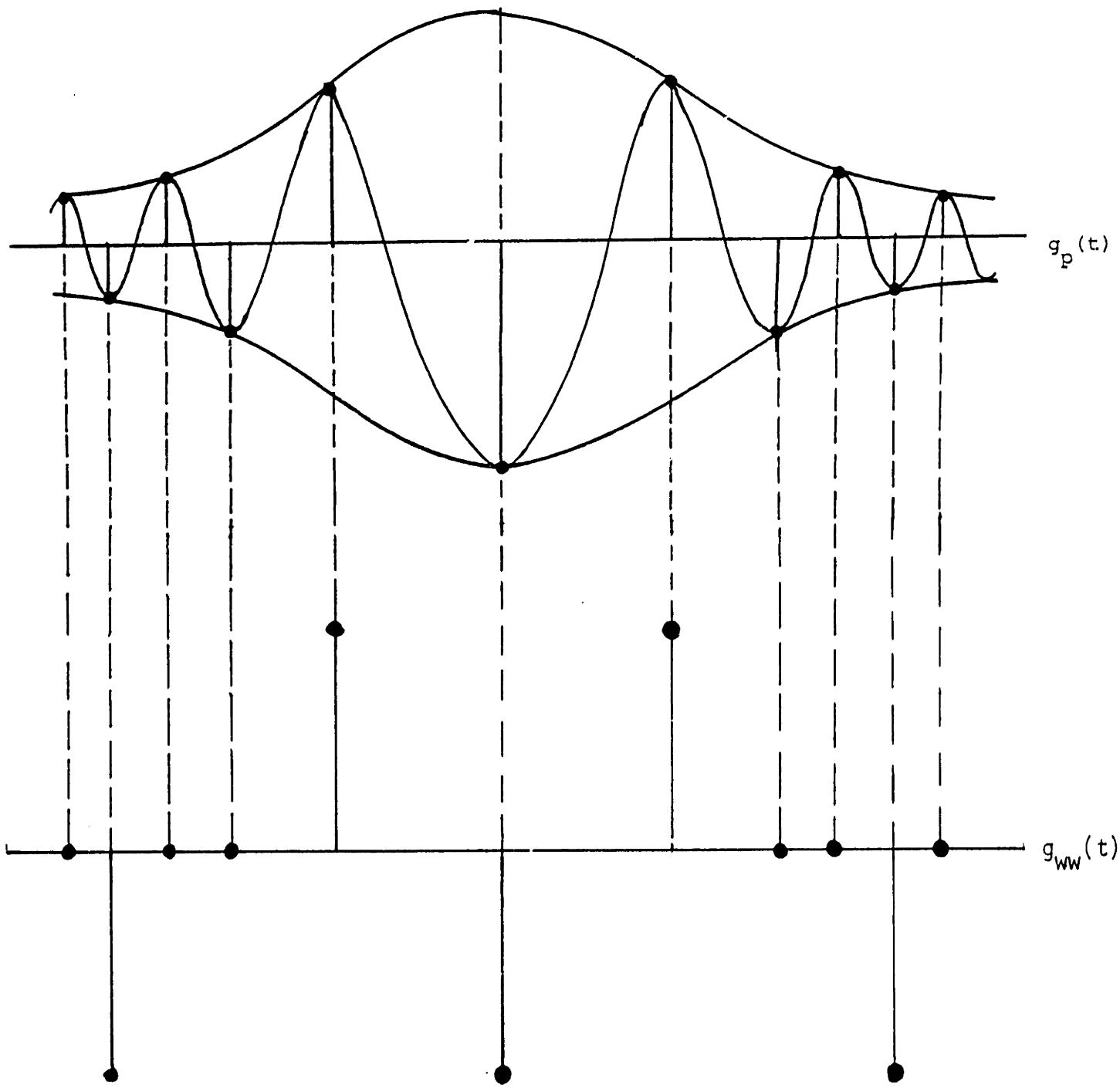

Figure 6.27 Intuitive Concept of Withdrawal Weighting
$g_p(t)$ is a sampled prototype amplitude and phase modulated waveform. $g_{ww}(t)$ is the withdrawal weighted approximation. Note that where the envelope of $g_p(t)$ is large, most of the samples are retained in $g_{ww}(t)$, while the converse is true where the envelope is small.

6.6.1 Physical Structures

Before the withdrawal weighting can be done, a structure must be selected so we know what constraints must be satisfied. In Figs. 6.28, 6.29 two possible structures are displayed. Both are split finger designs making it reasonable to have ignored reflections in the synthesis procedure. Structure-I is the standard one in which every finger is connected to one of two bus bars of opposite polarity. It is a topological necessity with this structure that nonzero gap weights alternate in sign. This is a rather strong restriction. With structure-I, we would not be able to use the sequence 1, 0, 1, 0 to represent in a withdrawal weighted sense the frequently needed sequence of half strength samples $\frac{1}{2}$, $-\frac{1}{2}$, $\frac{1}{2}$, $-\frac{1}{2}$. Following the restrictions of structure-I, this would have to be implemented as $-1, 1, 0, 0, -1, 1, 0, 0$ which is clearly a worse approximation. Here the averaging must be done over four samples, instead of only over two, to see that half weight samples are being approximated.

One of the newly invented structures (IIa) is sketched in Fig. 6.29. Here two grounded fingers are introduced between successive gaps of the same polarity. This yields half weight gaps of the same sign separated by half a wavelength at the points labeled *a* and *b* in Fig. 6.29. Thus, transduction at these points will cancel over a broad bandwidth about

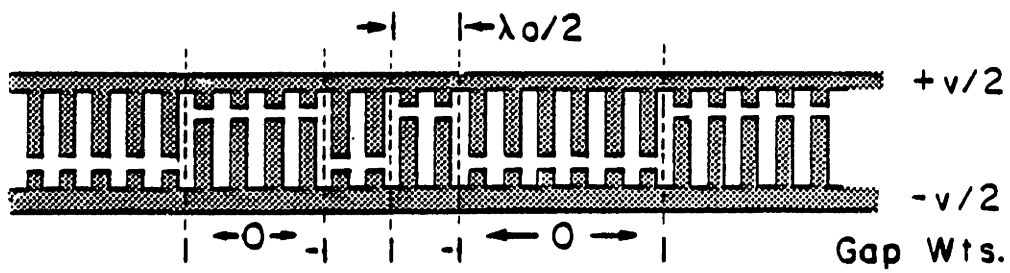

Figure 6.28 Structure-I: The Standard Structure for Withdrawal Weighting
Note that although 3 weights are allowed (– 1, 0, 1), the non-zero gap weights must alternate in sign.

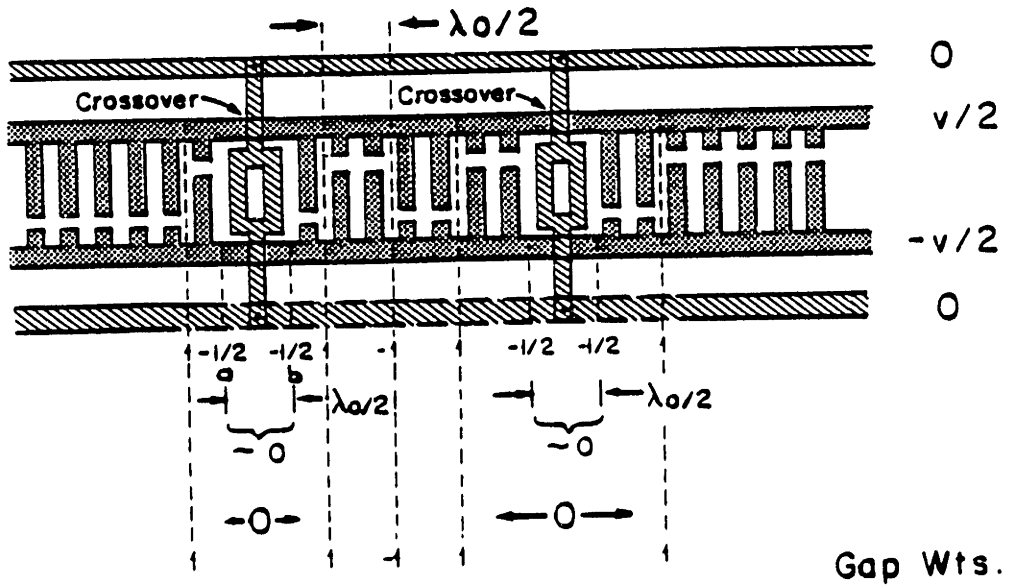

Figure 6.29 Structure-IIa: A New Structure for Withdrawal Weighting
Note: Two levels of metalization are required as well as crossovers. Three weights are allowed (− 1, 0, 1) in any sequence. The only restriction being that gaps of the same polarity must be separated by at least one wavelength.

the center frequency, allowing sequences with successive gaps of the same sign (such as 1, 0, 1, 0) to be implemented. The only remaining restriction is that there must be at least one full wavelength between gaps of the same sign. This is not really a significant problem, since if the spacing between gaps of the same sign were only half a wavelength, transduction would cancel over a broad frequency range.

The major problem with structure-IIa lies in the added processing required to fabricate the necessary crossovers. It is important to recognize though, that far fewer crossovers are required than in a three-phase unidirectional transducer [38] . The additional capacitance from the crossovers may very well be insignificant compared to the interelectrode capacitance, especially on high permittivity substrates like $LiNbO_3$. If this were the case, ordinary high capacitance crossovers would be sufficient; there would be no need for the complicated air-gap crossovers [90] .

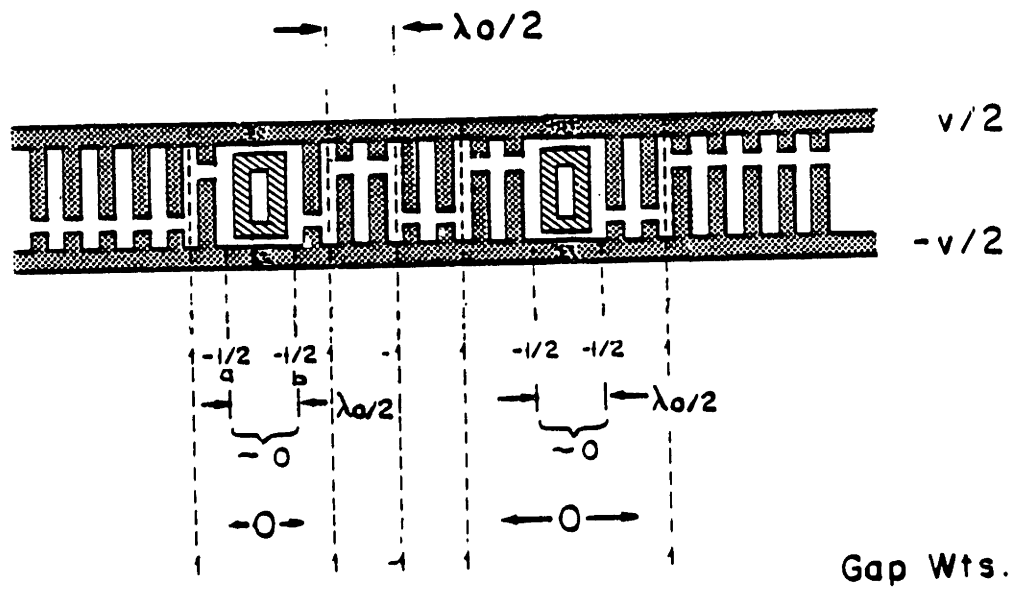

Figure 6.30 Structure-IIb: A New Structure for Withdrawal Weighting
Note: Only a single level of Metalization is required. Three weights are allowed (– 1, 0, 1) in any sequence. The only restriction being that gaps of the same polarity must be separated by at least one wavelength.

On weakly piezoelectric substrates, such as quartz and Gallium Arsenide, no crossovers may be needed. Then the structure reduces to that of Fig. 6.30 and can be fabricated with only one level of metalization just like the standard SAW devices. If the crossovers are open circuited, the shorted spacers will float to ground potential, and therefore on transduction, the structure behaves very much like structure-IIa. The floating spacer will in general reflect at the center frequency, and it will in addition cause a velocity shift [2] . If the velocity shift is accurately known, the positions of the fingers can be adjusted to compensate for this effect. In addition, it may be possible to eliminate the reflection problem by a proper choice of the metalization thickness and ratio to cancel the reflection of mechanical origin with the piezoelectrically generated one [11,51] .

6.6.2 Multiple Envelopes, Look-Ahead and Quantization Step Optimization

The standard withdrawal weighting [42] technique of spreading source weights over a number of wavelengths is implemented in two steps. First we integrate the envelope of the prototype waveform to obtain its cumulative distribution. Then the samples of the withdrawal weighted waveform are quantized at three discrete levels, $-WWQNT$, 0, $WWQNT$, in such a way so as to minimize the difference between the cumulative distributions of the withdrawal weighted and prototype envelopes (see Fig. 6.31). Here $WWQNT$ is used to denote the withdrawal weighting quantization step size.

It is clear from the above discussion that withdrawal weighting is a narrow band approximation. It is best at the center frequency and deteriorates as one deviates from f_0. Using a procedure similar to that used by Doyle [21a] in his work on antenna arrays, we can show how this comes about. Let us define $g_p(t)$, $G_p(f)$ to be a Fourier transform pair for the nonuniformly sampled prototype phase and amplitude modulated waveform, and let $g_{ww}(t)$ and $G_{ww}(f)$ be the corresponding quantities for the withdrawal weighted waveform. The definition of an envelope must be modified to properly handle the withdrawal weighting of phase modulated signals. The appropriate definition is the waveform demodulated by $exp(-j2\pi f_i t)$, where f_i will typically be some frequency in the filter's passband, although this need not be the case. We also define cumulative distributions for these baseband time functions:*

$$g^i_{cp}(t) = \int_{-\infty}^{t} d\tau\, g_p(\tau) e^{-j2\pi f_i \tau} \tag{6.61}$$

$$g^i_{cww}(t) = \int_{-\infty}^{t} d\tau\, g_{ww}(\tau) e^{-j2\pi f_i \tau} \tag{6.62}$$

* Note that these definitions reduce to the standard ones in the case of a uniformly sampled non-chirped waveform with two samples/period since the envelopes are real, and the complex exponentials are $(-1)^n$ at the sampling times

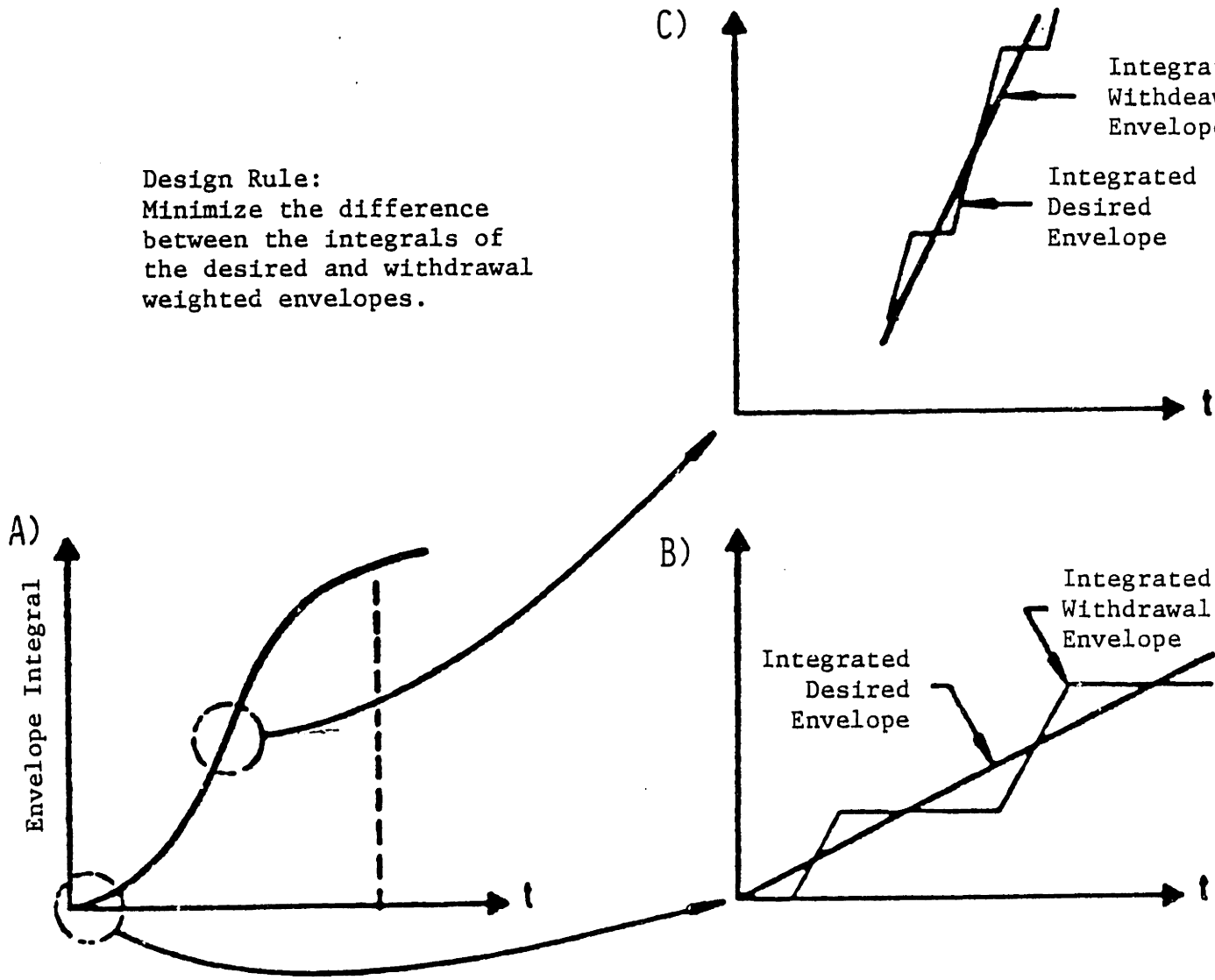

Figure 6.31 The Standard Withdrawal Weighting Procedure
A) Integral of the desired source envelope function. B,C) Approximation of this integrated envelope by withdrawal weighting. (After [42])

Let us also define $d_{ct}(t)$ and $D_f(f)$ as the error between the cumulative distributions of the time envelopes and the error between the prototype and withdrawal weighted frequency responses respectively:

$$d_{ct}(t) = g_{cp}(t) - g_{cww}(t) \tag{6.63}$$

$$D_f(f) = G_p(f) - G_{ww}(f) \tag{6.64}$$

For simplicity, let all the time functions be zero for positive time. Upon integrating by parts and applying Parseval's theorem, we obtain

$$\int_{-\infty}^{\infty} df \frac{|D_f(f) - D_f(f_i)|^2}{(f - f_i)} = (2\pi)^2 \int_{-\infty}^{0} dt \, |d_{ct}(t)|^2 \tag{6.65}$$

The withdrawal weights can always be scaled by an appropriate constant to make $D_f(f)$ zero at any one frequency:

$$\int_{-\infty}^{\infty} df \frac{|G_p(f) - G_{ww}(f)|^2}{(f - f_i)^2} = (2\pi)^2 \int_{-\infty}^{0} dt \, |g_{cp}(t) - g_{cww}(t)|^2 \tag{6.66}$$

Withdrawal weighting corresponds to minimizing the right hand side of Eq. (6.66). Thus, via withdrawal weighting, we obtain a weighted minimum square error approximation to the desired frequency response, using a weighting function which is sharply peaked near the demodulation frequency, f_i, used to define the envelope.

Since the prototype source weights are small near the ends of the waveform, all withdrawal weighting was done from the midpoint of the signal, first to the right and then to the left. Thus 2 new prototype cumulative distributions (CDF) are defined:

$$g_{cpr}(t) = \int_{t_{mid} - \frac{\tau_{ovrlp}}{2}}^{t} d\tau \, g_p(\tau) e^{-j2\pi f_i \tau} \qquad t > t_{mid} - \frac{\tau_{ovrlp}}{2} \tag{6.67}$$

$$g_{cpl}(t) = \int_{t}^{t_{mid} + \frac{\tau_{ovrlp}}{2}} d\tau \, g_p(\tau) e^{-j2\pi f_i \tau} \qquad t < t_{mid} + \frac{\tau_{ovrlp}}{2} \tag{6.68}$$

where τ_{ovrlp}, the overlap between the right and left prototype envelopes, is used to reduce the chance of discontinuities appearing where these two envelopes are joined. Right and left withdrawal envelopes $g_{cwwr}(t)$ and $g_{cwwl}(t)$ are defined in a similar manner. The sample locations of the withdrawal weights are the same as those in the prototype waveform.

The simplest procedure for choosing the withdrawal weights would be to find the error $E_{wwr}(t_n)$ between the cumulative distribution of the withdrawal weights and that of the continuous weights for the current sample,

$$E_{wwr}(t_n) = g_{cpr}(t_n) - g_{cwwr}(t_n) \tag{6.69}$$

for each of the possible withdrawal weights, and then to choose the one which minimizes this error. The possible quantized withdrawal weights are $-WWQNT$, 0, $WWQNT$,* subject to the constraints imposed by physical structures I and II. The weight assigned to each source, $WWQNT$, is related to the fraction of non-zero withdrawal weights. This fraction is roughly equal, or at least proportional to the ratio of the average prototype weight to $WWQNT$. In order to achieve the best results, the frequency response error should be minimized with respect to $WWQNT$.

Further improvement can be achieved by using look-ahead, ($lkhd$), in the withdrawal weighting procedure. If look-ahead is used over n_{lkhd} points, then at each time step all realizable withdrawal sequences of length n_{lkhd} from the current point are examined. The total error over these n_{lkhd} points, E_{wwtot}, is computed for each of these possible sequences where

$$E_{wwtot}(n, n_{lkhd}) = \sum_{k=n}^{n+n_{lkhd}-1} E_{wwr}(t_k) \tag{6.70}$$

Finally, the withdrawal weight corresponding to the minimum total error over n_{lkhd} points is selected.

In order to broaden the bandwidth over which a good approximation to $G_p(f)$ can be obtained, and to more evenly spread out the approximation error in frequency, we

*In the actual implementation, these weights were multiplied by $(f_o/f_i)^q$ when computing the cumulative distribution at at f_i, thereby accounting for the effect of the instantaneous frequency on the source strength (See Eq. (6.4).

can compute cumulative envelope distributions at many frequencies both in the passband and in the rejection band, and do the withdrawal weighting so as to control the errors in all these cumulative distributions simultaneously. It is important to note that when we do this, Eq. (6.65) applies, since it is impossible in general to select one gain factor to zero $D_f(f_i)$ at several frequencies at once. Thus by this procedure, in the vicinity of each demodulation frequency f_i, we strive to keep the frequency error as small as it is exactly at f_i.

The relationship between frequency response errors and cumulative distribution (CDF) errors is theoretically represented by Eqs. (6.65, 6.66) in terms of weighted mean-square errors. Practically however, we would prefer an error definition based on the maximum deviation of an achieved frequency response from a desired frequency response. In Fig. 6.32, we present a plot of the peak frequency response error, E_{peakf}, and the maximum of 17 mean-square CDF errors, E_{cdfmx}, versus the quantization step used in the withdrawal weighting. If the E_{cdfmx} curve is smoothed, we see that the broad major minimum of the two curves occur in roughly the same place, for $WWQNT$ between 1.7 and 1.9. There is poor agreement, however, in the fine structure, local maxima of E_{cdfmx} do not generally occur at minima of E_{peakf}. Thus although E_{cdfmx} is easier to compute than E_{peakf}, it seems that for optimum performance, E_{peakf} should be minimized with respect to $WWQNT$, and not E_{cdfmx}.

6.6.3 Design Examples

In Figs. (6.33a–6.33f), we present cumulative distributions (CDF's) of the prototype and withdrawal weighted waveforms done at several passband and rejection band frequencies. No look-ahead was used, $n_{lkhd} = 1$, but the withdrawal weighting was done at 17 passband

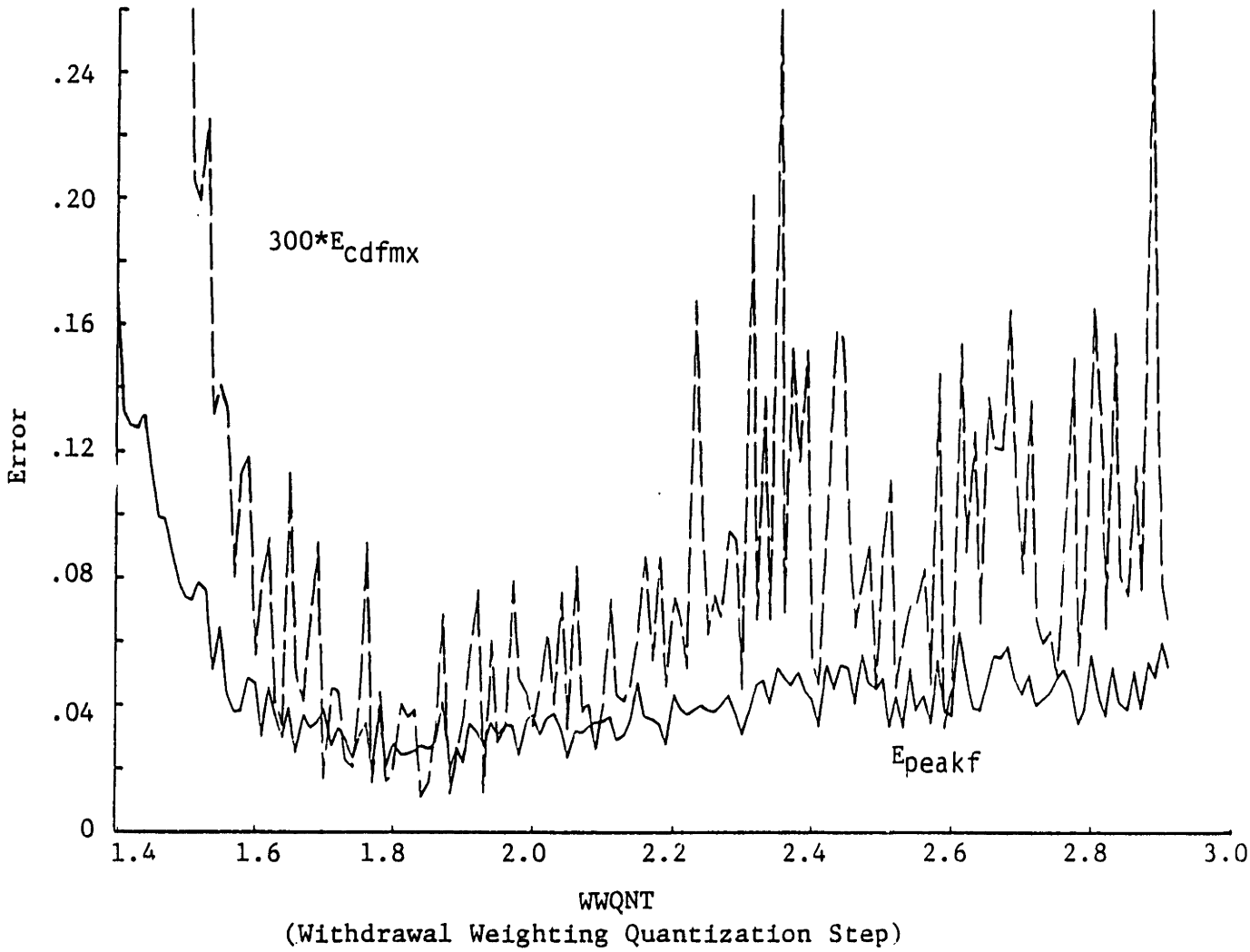

Figure 6.32 Peak Frequency Response Error (E_{peakf}) and the Maximum Mean Square CDF Error (E_{cdfmx}) Versus the Withdrawal Weighting Quantization Step ($WWQNT$)

E_{peakf} =max(passband error, 4.9 × rejection band error over a 25% fractional bandwidth)
E_{cdfmx} = maximum deviation between the cumulative distributions of the prototype and withdrawal weighted envelopes over all the demodulation frequencies Note: This data is for waveform 1.11.8 of Table 6.5 in Sec. 6.6.3.

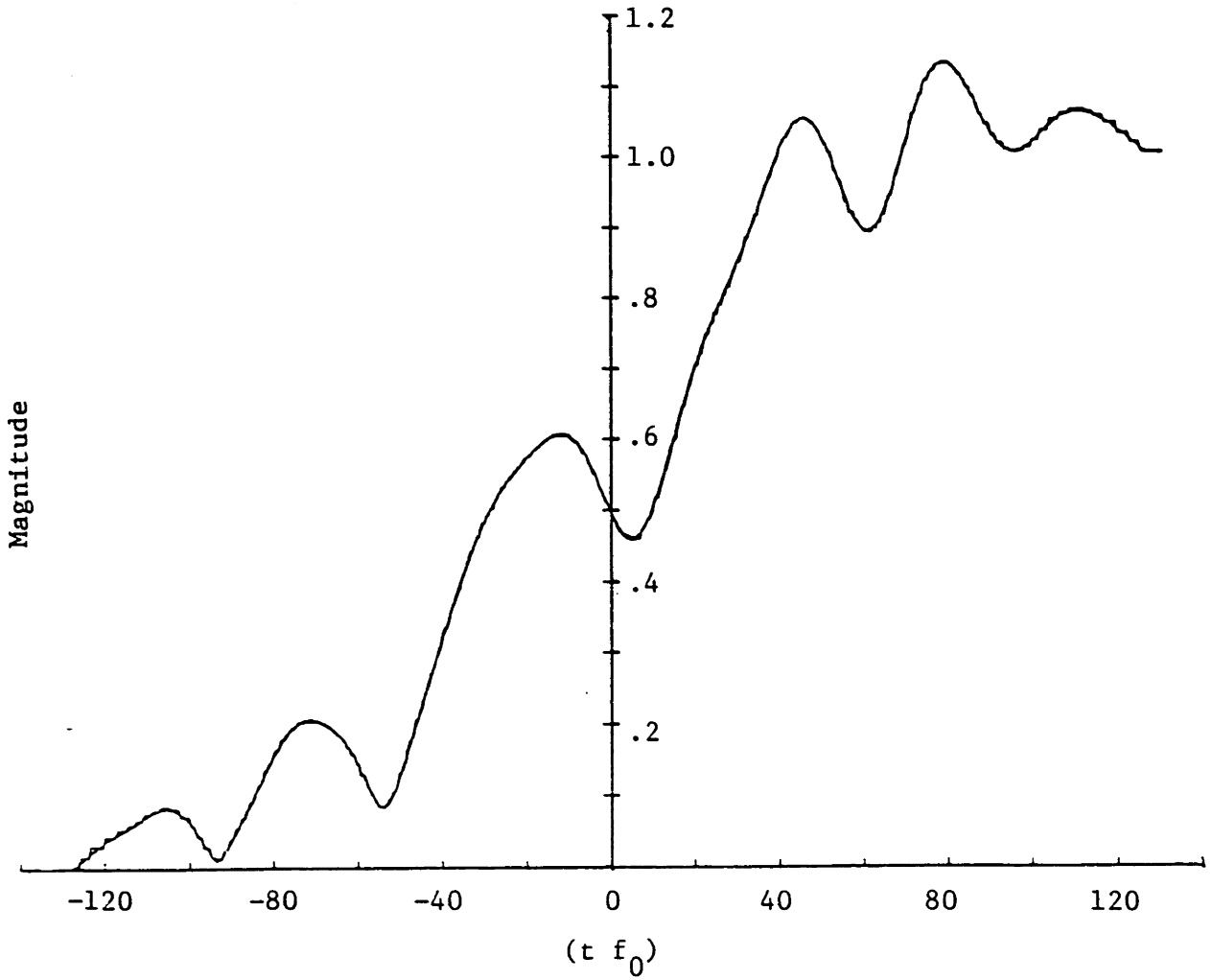

Figure 6.33a The Prototype and Withdrawal Weighted Cumulative Distribution Functions: $f_i = 1.0$
(f_i is at the center frequency.) The smooth and jagged curves are the prototype and withdrawal weighted CDF's respectively. Waveform I.II.5 of Table 6.5

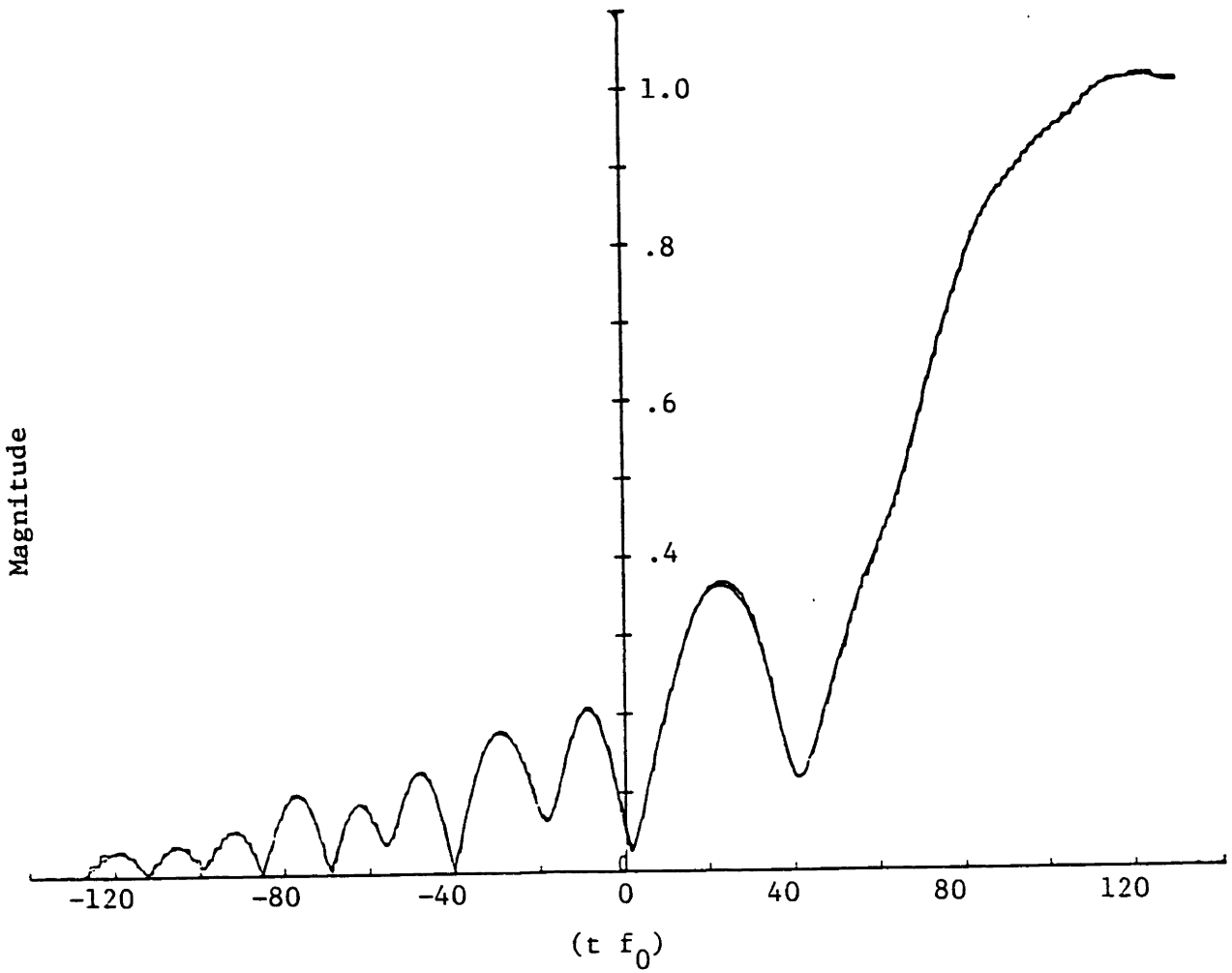

Figure 6.33b The Prototype and Withdrawal Weighted Cumulative Distribution Functions: $f_i = .9650$

(f_i is at the peak of the leftmost passband ripple.) The smooth and jagged curves are the prototype and withdrawal weighted CDF's respectively. Waveform I.II.5 of Table 6.5

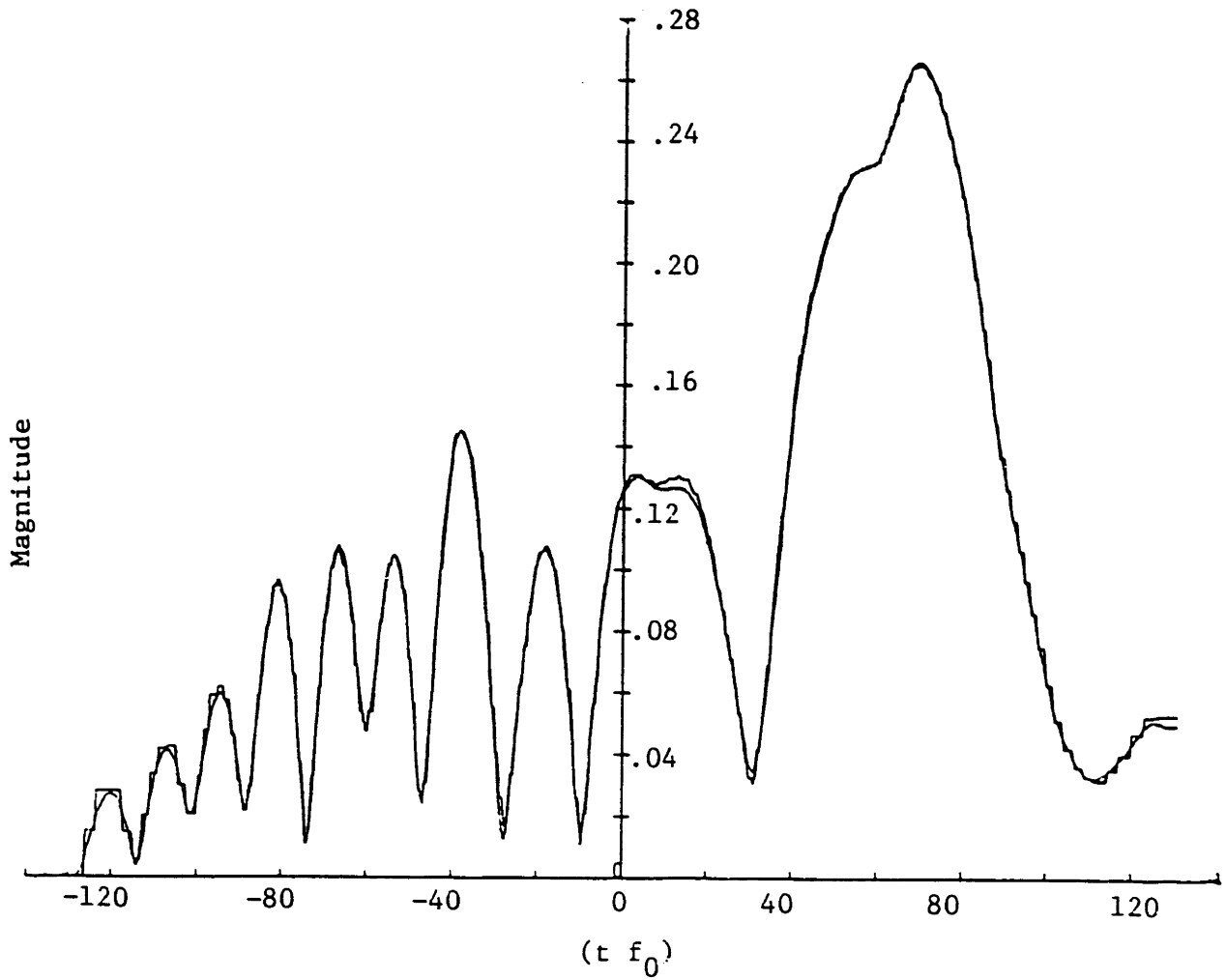

Figure 6.33c The Prototype and Withdrawal Weighted Cumulative Distribution Functions: $f_i = .9548$

(f_i is at the peak of the innermost sidelobe.) The smooth and jagged curves are the prototype and withdrawal weighted CDF's respectively. Waveform 1.11.5 of Table 6.5

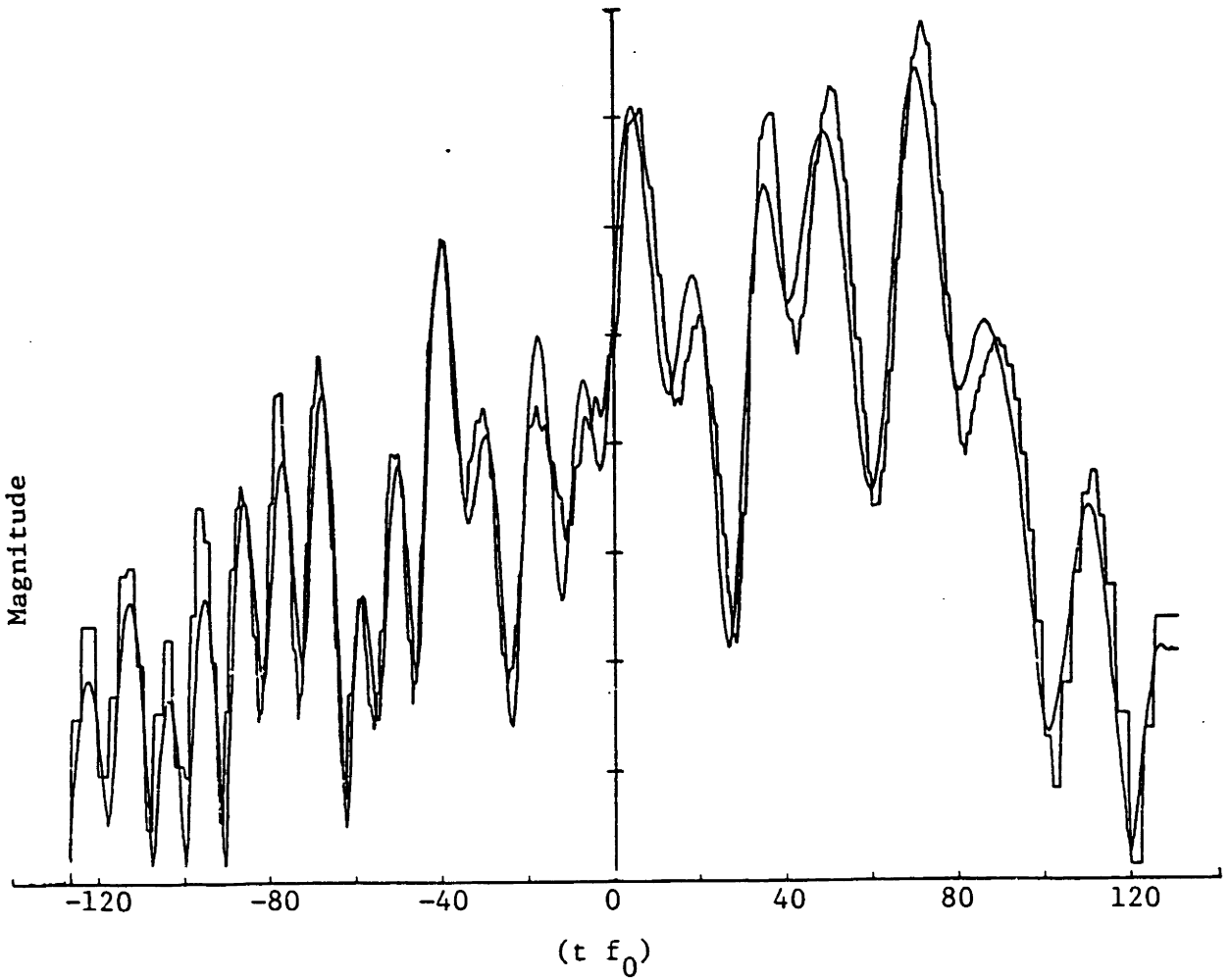

Figure 6.33d The Prototype and Withdrawal Weighted Cumulative Distribution Functions: $f_i = .9194$

(f_i is at the peak of the 10^{th} sidelobe counting left.) The smooth and jagged curves are the prototype and withdrawal weighted CDF's respectively. Waveform I.II.5 of Table 6.5

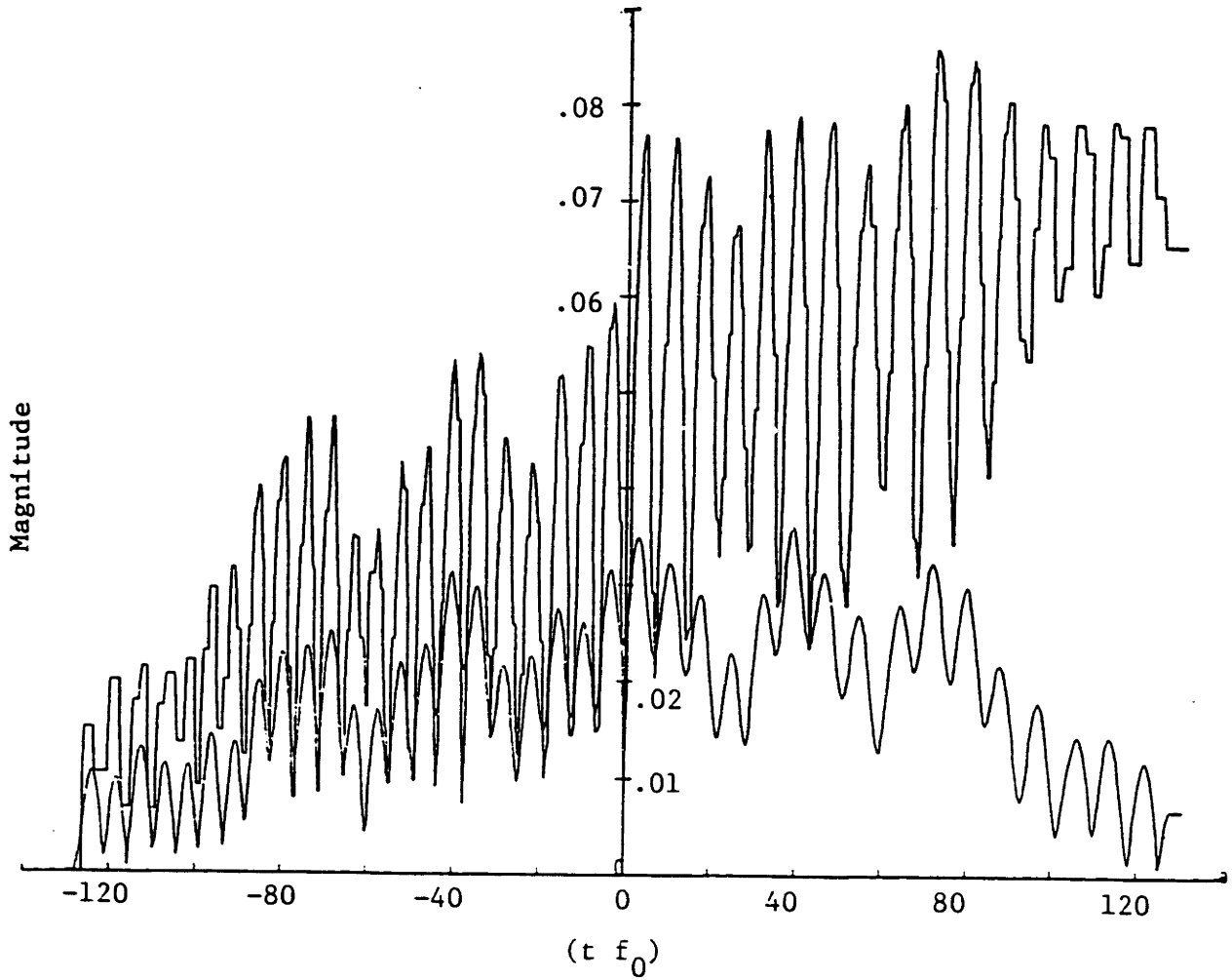

Figure 6.33e The Prototype and Withdrawal Weighted Cumulative Distribution Functions: $f_i = .8496$

(f_i is at the peak of the 23^{rd} sidelobe counting left.) The smooth and jagged curves are the prototype and withdrawal weighted CDF's respectively. Waveform I.II.5 of Table 6.5

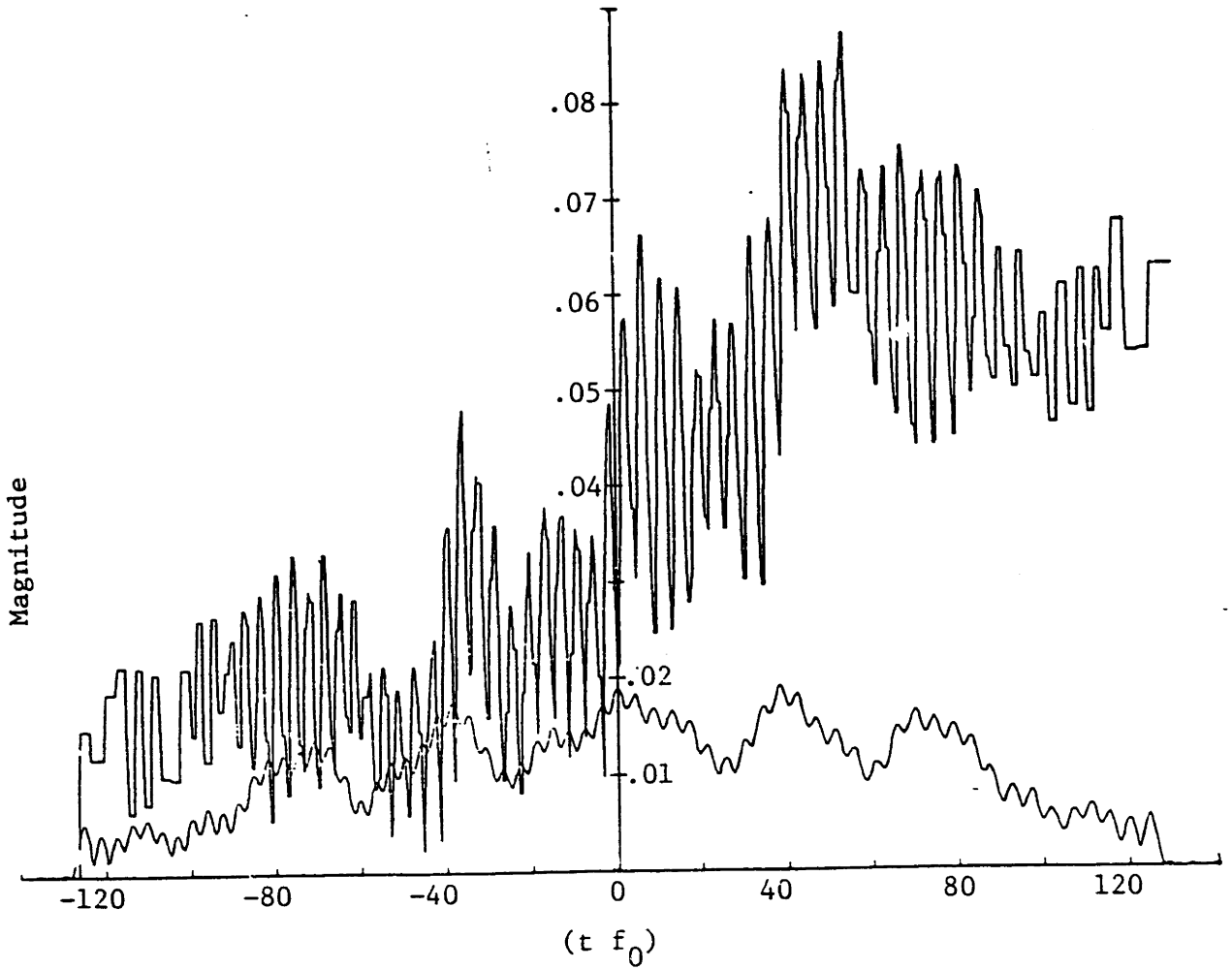

Figure 6.33f The Prototype and Withdrawal Weighted Cumulative Distribution Functions: f_i =.7514

(f_i is at the peak of the 38^{th} sidelobe counting left.) The smooth and jagged curves are the prototype and withdrawal weighted CDF's respectively. Waveform I.II.5 of Table 6.5

frequencies. The frequency responses of the corresponding prototype and withdrawal weighted waveforms are displayed Figs. 6.34 and 6.35 respectively. We note from Fig. 6.33a that at the center frequency, the withdrawal weighted cumulative distribution function (CDF) is an excellent staircase approximation to the prototype CDF, with each step being very small compared to the features of interest. Near the transition band, both within the passband (Fig. 6.33b) and in the rejection band (Fig. 6.33c), the agreement is also very good. Even at the tenth sidelobe peak, agreement is quite reasonable (Fig. 6.33d), although the peak CDF value has dropped substantially since we are far from synchronism. At the peak of the twenty-third sidelobe, there is little resemblance between the two CDF's although the peaks and valleys agree, and by the time the thirty-eighth sidelobe peak is reached (Fig. 6.33f), there is no resemblance in the CDF's at all. Nevertheless, the frequency response is still quite good, better than 44.5 dB rejection over a 55% fractional bandwidth.

In the frequency regimes in which the prototype and withdrawal CDF's agree reasonably well, this agreement is a sufficient explanation for the good frequency response. Outside this region, it must be the lack of synchronism which accounts for the low excitation. Thus, it is pointless to define CDF's for frequencies in this second region. For completeness, we present in Fig. 6.36 a plot of the frequency response error over a broad 200% fractional bandwidth. We note that beyond the above mentioned 55% fractional bandwidth, the sidelobe level increases substantially. In this region, absence of synchronism is not sufficient to yield a good rejection level; the abruptness of the withdrawal weighted approximation must be responsible for these high sidelobe levels far from the center frequency.

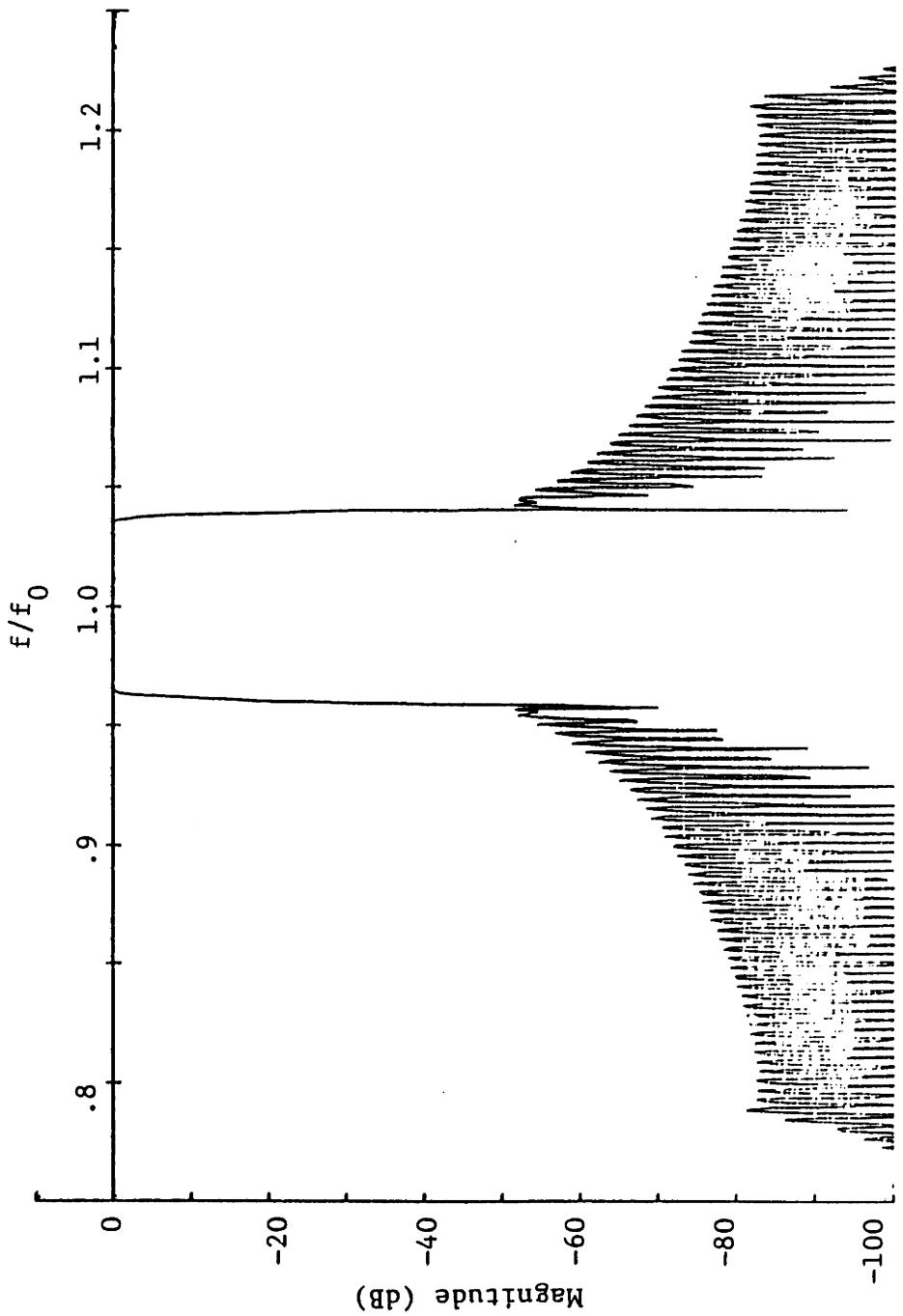

Figure 6.34 Frequency Response of Prototype-I
(See Table 6.1 of Sec. 6.5.2 for more information.)

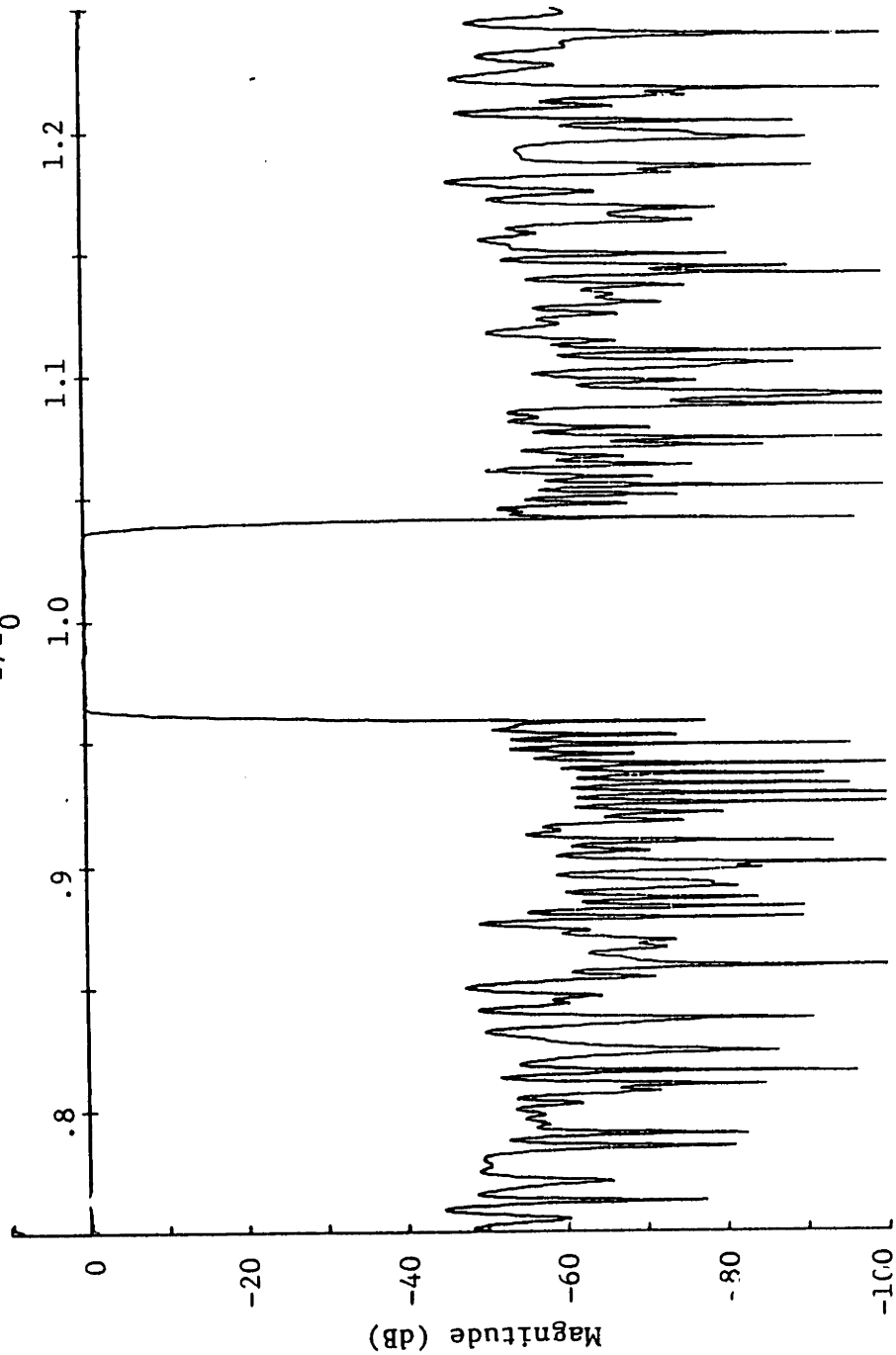

Figure 6.35 Frequency Response of Withdrawal Weighted Waveform 1.11.5
Prototype-1, Structure-II, 17 passband CDF's. $n_{WHd} = 1$ (See Table 6.5 for more information.)

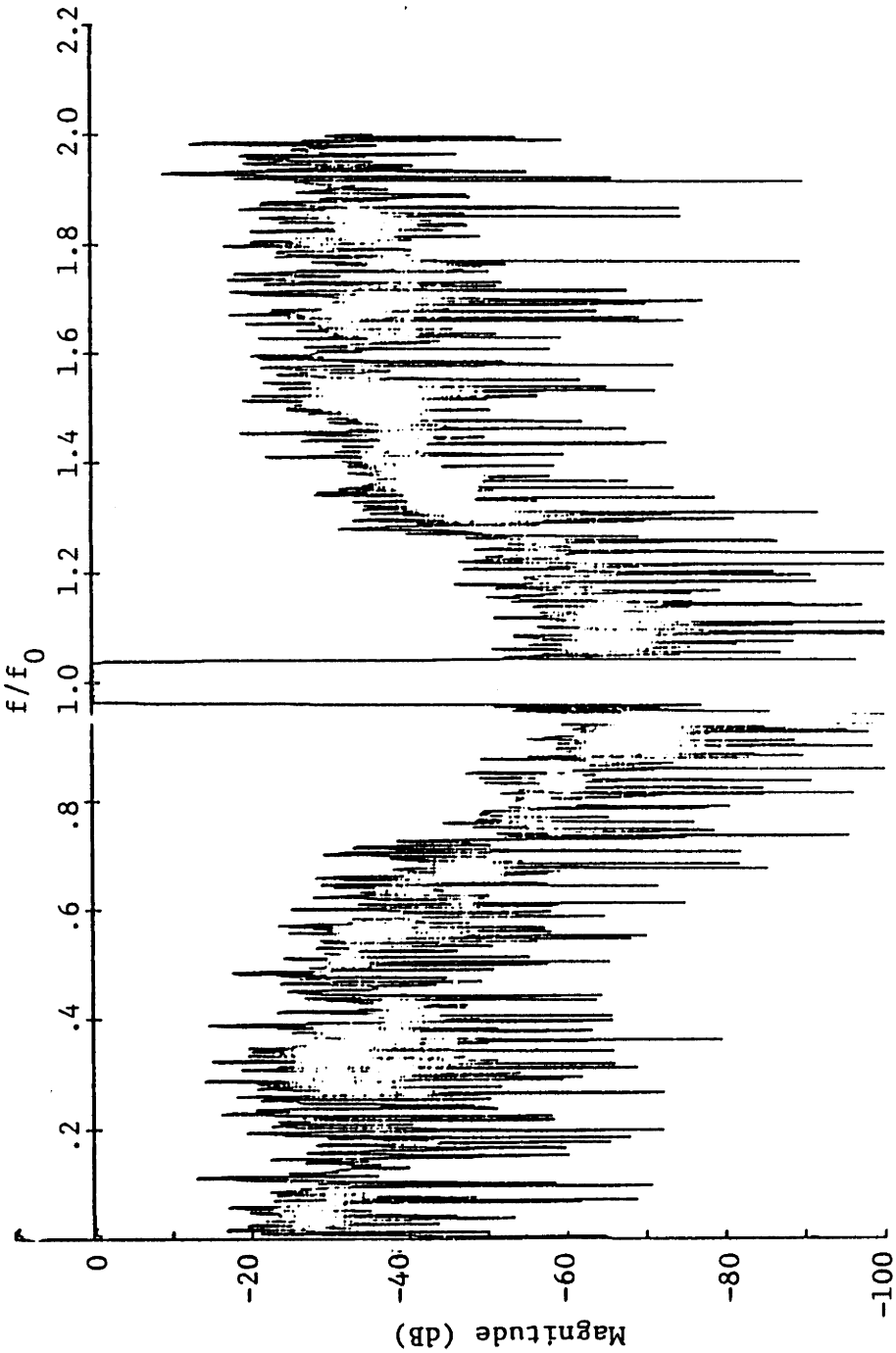

Figure 6.36 Frequency Response of Withdrawal Weighted Waveform I.II.5 over a Wide Bandwidth

Prototype-I, Structure-II, 17 passband CDFs, $n_{ikhd} = 1$ (See Table 6.5 for more information.)

Waveform	Length in Wavelengths	Shape* Factor	Peak Sidelobe (dB)	Peak-Peak Passband Ripple (dB)	Dynamic† Range
I	256.5	1.1544	-51.5	.185	6.027
II	256.5	1.1761	-66.8	.385	8.373

Table 6.3 Parameters of Amplitude and Phase Modulated Nonuniformly-Sampled Prototype Waveforms, I and III

Note: Prototype waveform-III is not symmetric. It was predistorted by the frequency response of the elemental gap source with a 50% metalization ratio. * Ratio of bandwidth at the rejection level to the bandwidth at the passband ripple level. An ideal *brick wall* bandpass filter has a shape factor of 1. (See Fig. 6.3) † (maximum sample value)/(average of the smallest 10%)

If it is desired to further increase the bandwidth over which the sidelobes are controlled, then either more levels are required in the withdrawal weighting necessitating a different structure, or a flatter prototype waveform is needed. Since the prototype waveform is nearly optimal, this can only be done at the expense of a reduced rejection level, increased passband ripple, or more dispersion can be used which will increase the length of the device.

Withdrawal weighting was done both on prototype waveforms I and III. Prototype waveform-III was predistorted to compensate for the element factor, while prototype waveform-I was not. The characteristics of these amplitude and phase modulated waveforms (AM-PM) after nonuniform sampling are summarized in Table 6.3.

The withdrawal weighting was done many times with varying amounts of look-ahead and cumulative distribution function (CDF) demodulation frequencies. In all cases, the results were optimized with respect to $WWQNT$, the quantized constant weight assigned to each source. The results are presented in Tables 6.4–6.7. Additional sample Frequency Responses are presented in Figs. 6.37–6.39.

Waveform Identifier	# of CDF Demodulation Frequencies	Amount of look-ahead (n_{lkhd})	Peak-to-Peak Passband Ripple (dB)	Peak Sidelobe over a 25% Fractional Bandwidth (dB)
I.I.1	1	2	.67	-43.2
I.I.2	1	8	.62	-44.0
I.I.3	17	2	.58	-45.8
I.I.4	17	4	.72	-45.2
I.I.5	21*	2	.86	-47.5

Table 6.4 Withdrawal Weighting Data of Prototype-I using Structure-I
All the CDF demodulation frequencies are in the passband except for the last waveform. * 4 of the 21 demodulation frequencies are in the rejection band. They are at the peak of the 2 innermost sidelobes at the right and left of the center frequency.

Waveform Identifier	# of CDF Demodulation Frequencies	Amount of Look-ahead (n_{lkhd})	Peak-Peak Passboard Ripple (dB)	Peak Sidelobe over a 25% fractional bandwidth (db)
I.II.1	1	1	.33	-48.2
I.II.2	3	1	.67	-50.6
I.II.3	3	2	.43	-48.7
I.II.4	3	4	.35	-50.1
I.II.5	17	1	.37	-51.0
I.II.6	17	2	.46	-48.5
I.II.7	17	2	.52	-49.8
I.II.8	17	4	.33	-50.7

Table 6.5 Withdrawal Weighting Data of Prototype-I Using Structure-II
Note: All the CDF demodulation frequencies are in the passband

These data demonstrate that in general more demodulation frequencies and more look-ahead improve performance, although this is not always the case. By comparing the results presented in Tables 6.6 and 6.7 for one demodulation frequency, and no look-ahead ($n_{lkhd} = 1$), we note that with Structure-I, the performance is especially poor if there is no look-ahead. When n_{lkhd} was increased to 2, the passband ripple was cut from 5.7 dB to 1.3 dB, and simultaneously the peak sidelobe level improved from – 39.6 dB to – 50.2 dB.

Waveform Identifier	# of CDF Demodulation Frequencies	Amount of Look-ahead (n_{lkhd})	Peak-peak Passboard (dB)	Peak Sidelobe over a 25% fractional bandwidth
III.I.1	1	1	5.7	-39.6
III.I.2	1	2	1.3	-50.2
III.I.3	1	2	.91	-38.4
III.I.4	1	6	.84	-49.3
III.I.5	1	8	1.06	-47.8
III.I.6	1	8	.75	-42.7
III.I.7	3	6	1.56	-45.2
III.I.8	3	6	1.07	-34.5
III.I.9	17	2	1.01	-48.4
III.I.10	17	2	.76	-37.1
III.I.11	17	6	.82	-46.9

Table 6.6 Withdrawal Weighting Data for Prototype-III Using Structure-I
Note: All the demodulation frequencies are in the passband.

Waveform Identifier	# of CDF Demodulation Frequencies	Amount of look-ahead (n_{lkhd}) (dB)	Peak-Peak Passboard Ripple (dB)	Peak Sidelobe over a 25% Fractional Bandwidth
III.II.1	1	1	.60	-53.1
III.II.2	17	1	.55	-54.2
III.II.3	1	6	.56	-53.4
III.II.4	3	6	.52	-54.4
III.II.5	9	4	.56	-55.3
III.II.6	9	4	.68	-60.1
III.II.7	9	4	.62	-57.0
III.II.8	17	4	.57	-57.9

Table 6.7 Withdrawal Weighting Data for Prototype-II Using Structure-II
Note: All the demodulation frequencies are in the passband.

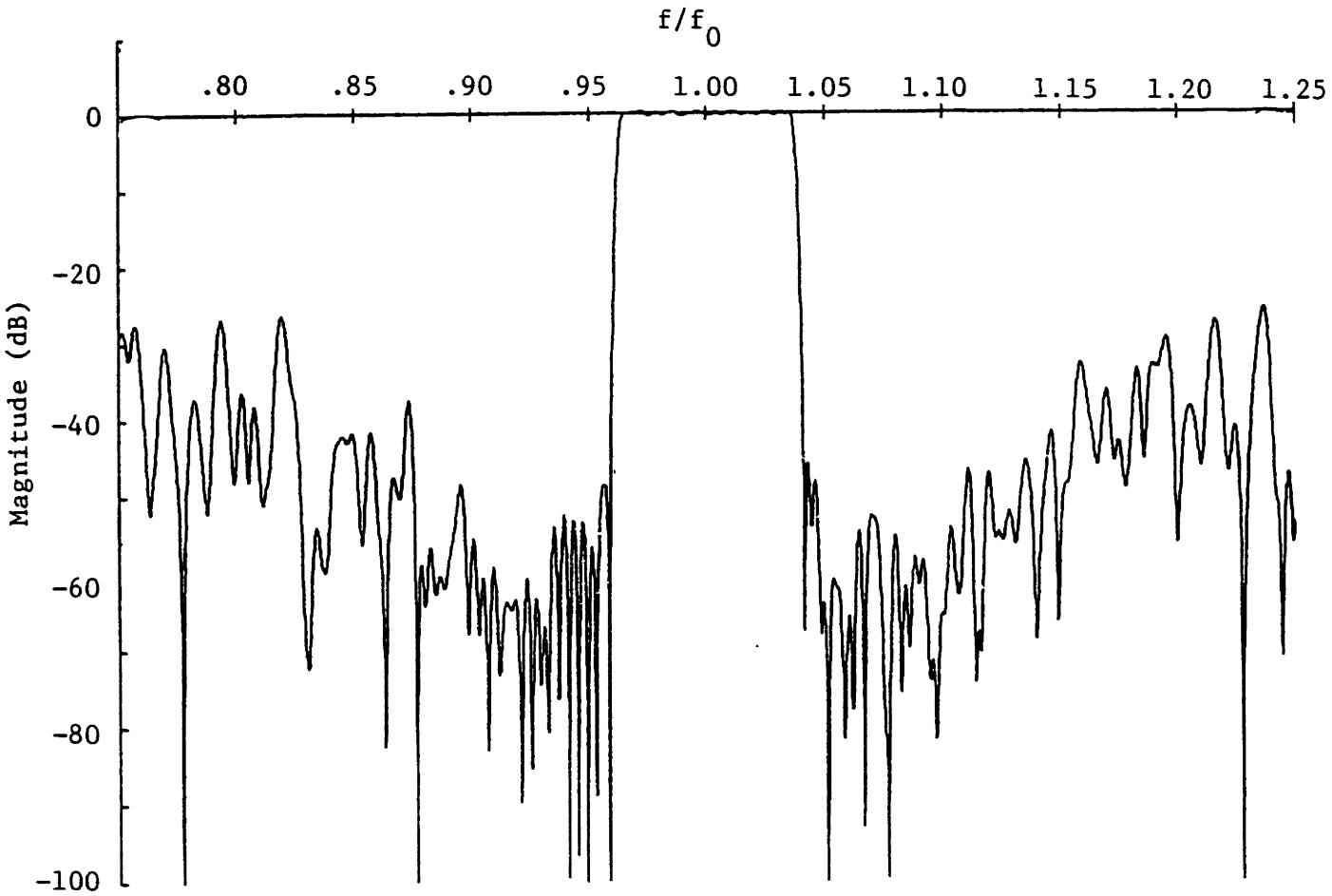

Figure 6.37 Frequency Response of Withdrawal Weighted Waveform I.I.3
Prototype-I, Structure-II, 17 passband CDF's, $n_{ikhd} = 2$ (See Table 6.4 for more information.)

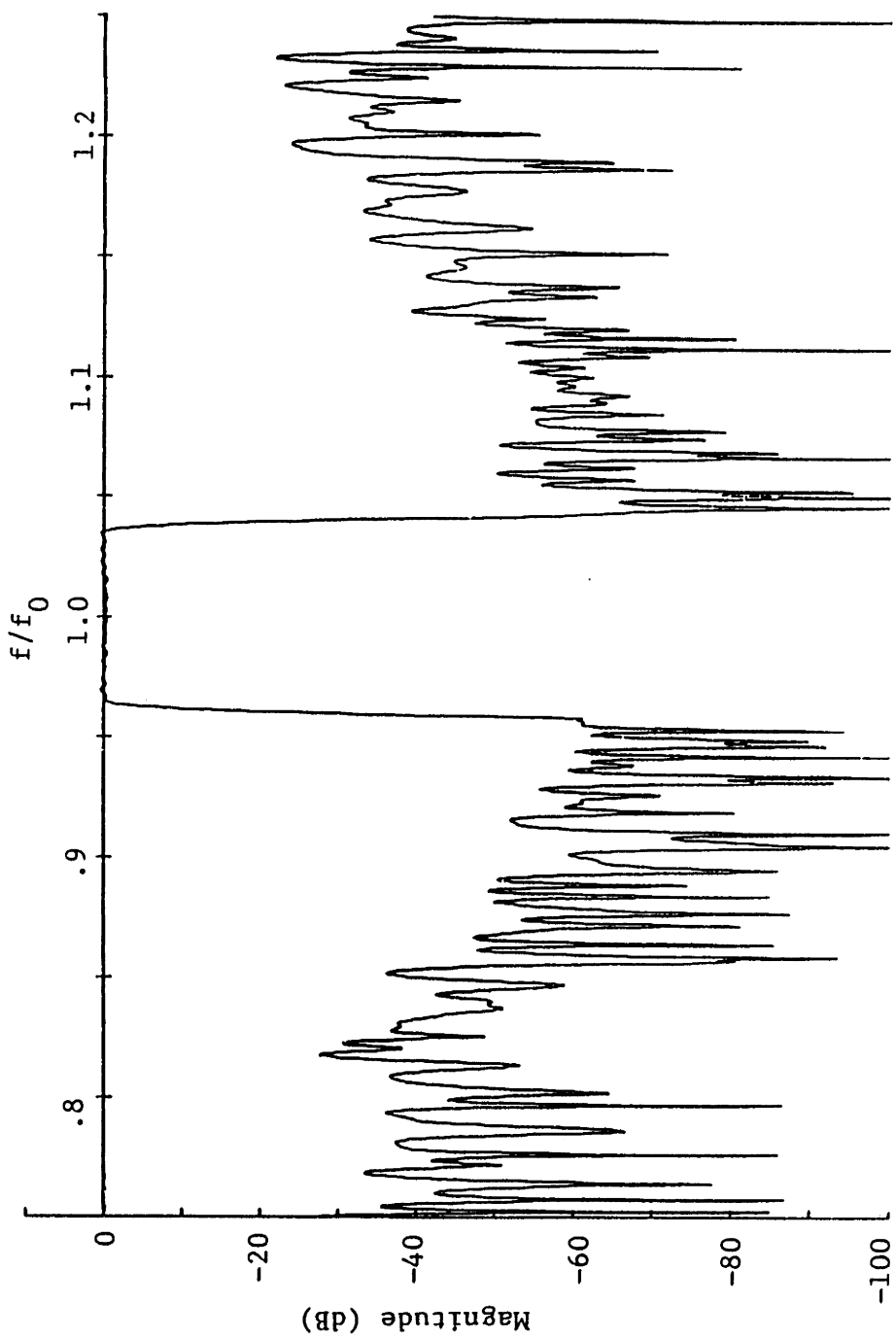

Figure 6.38 Frequency Response of Withdrawal Weighted Waveform III.I.4
Prototype-III, Structure-I, 1 passband CDF, $n_{lkhd} = 6$ (See Table 6.6 for more information.)

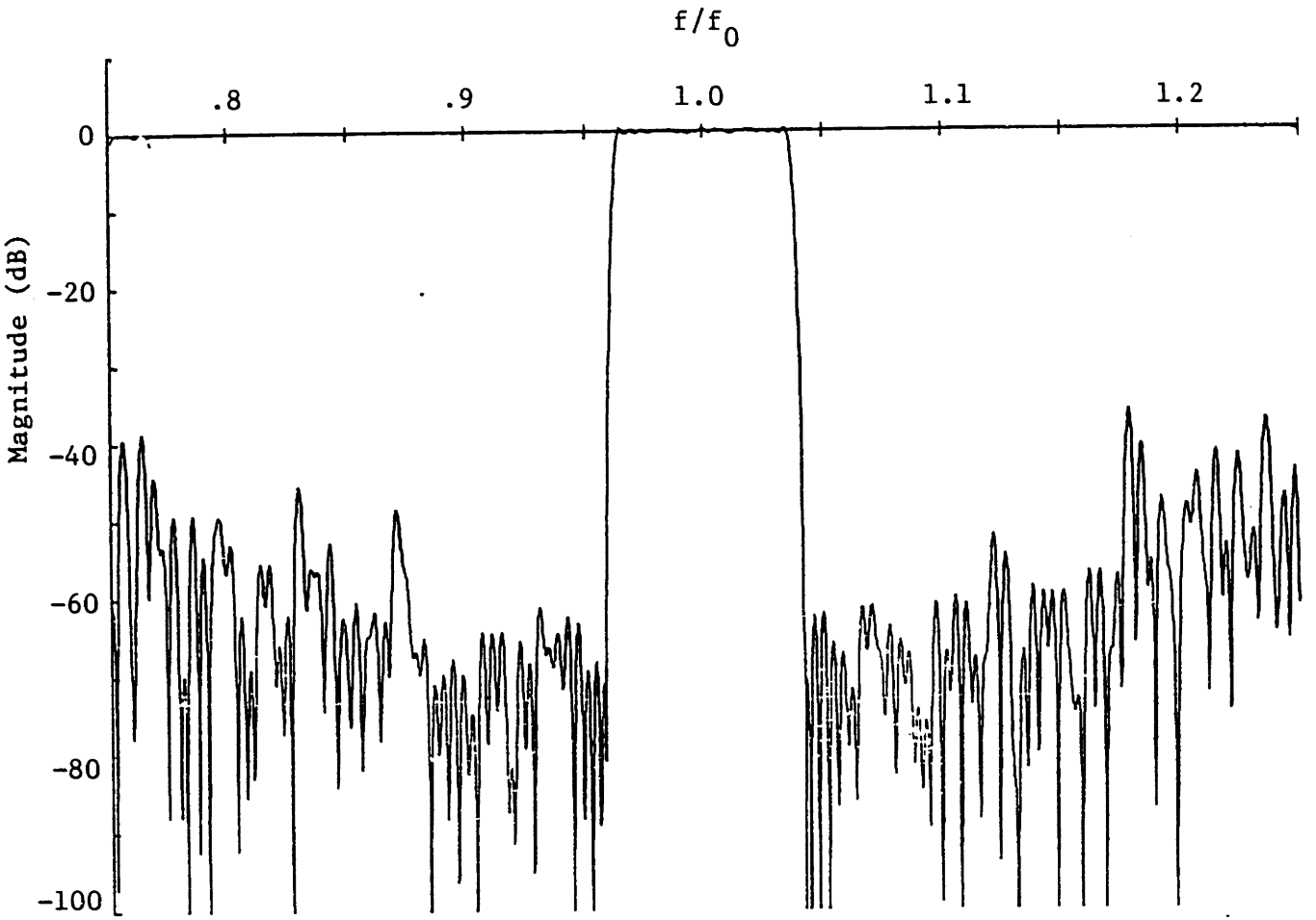

Figure 6.39 Frequency Response of Withdrawal Weighted Waveform III.II.6
Prototype-III, Structure-II, 9 passband CDF's, $n_{lkhd} = 4$ (See Table 6.7 for more information.)

Let us study waveforms I.II.1 and I.II.8 in more detail. From Table 6.5, we note a gain of only an additional 2.5 dB in sidelobe rejection at a cost of 16 additional CDF frequencies and an increase of 3 in the look-ahead interval. In Fig. 6.40 is a plot of the peak error against the quantization step used in withdrawal weighting ($WWQNT$), for these two waveforms. The curve corresponding to waveform-I.II.8, the one with more look-ahead and CDF frequencies is almost always significantly below that of I.II.8; only at isolated points are they comparable. Thus with a lot of look-ahead and many CDF frequencies, good results are always achieved, while with little look-ahead and few CDF frequencies, optimization with respect to $WWQNT$ is crucial.

The final withdrawal weighted waveforms for prototype-I are presented in Figs. (6.41–6.42). Each vertical bar represents an excited gap of the interdigitated electrode structure of a SAW device. Up and down pointing bars represent gaps of opposite polarity. All the non-zero weights are the same amplitude as we set out to do. In Fig. 6.41 structure-I is assumed, so the weights alternate in sign. In the case of Fig. 6.42 this restriction is relaxed, and structure-II would be used in the physical implementation. Comparing both these withdrawal weighted sequences with the prototype waveform of Fig. 6.9a, we see that in regions where the envelope is large, for example in the middle, there is a high concentration of weights. Similarly, at the ends where the prototype envelope rolls off, the density of samples is much lower as we expect.

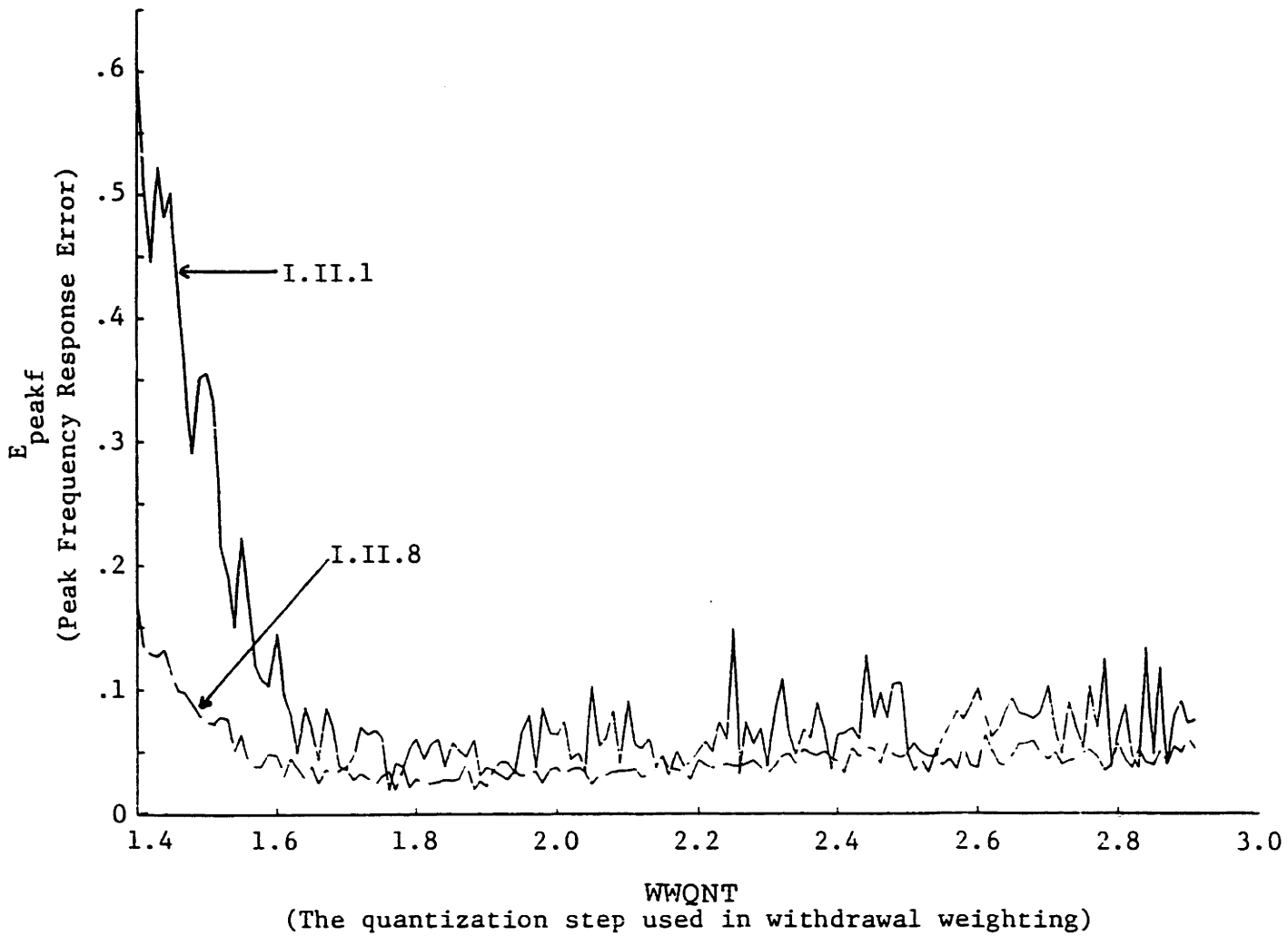

Figure 6.40 Comparative Performance of Two Withdrawal Weighted Designs Versus *WWQNT*

waveform I.II.8 1: passband CDF, $n_{lkhd} = 1$ waveform I.II.8 17: passband CDF's $n_{lkhd} = 4$

E_{peakf} = max(passband error, 4.9 × rejection band error over a 25% fractional bandwidth)

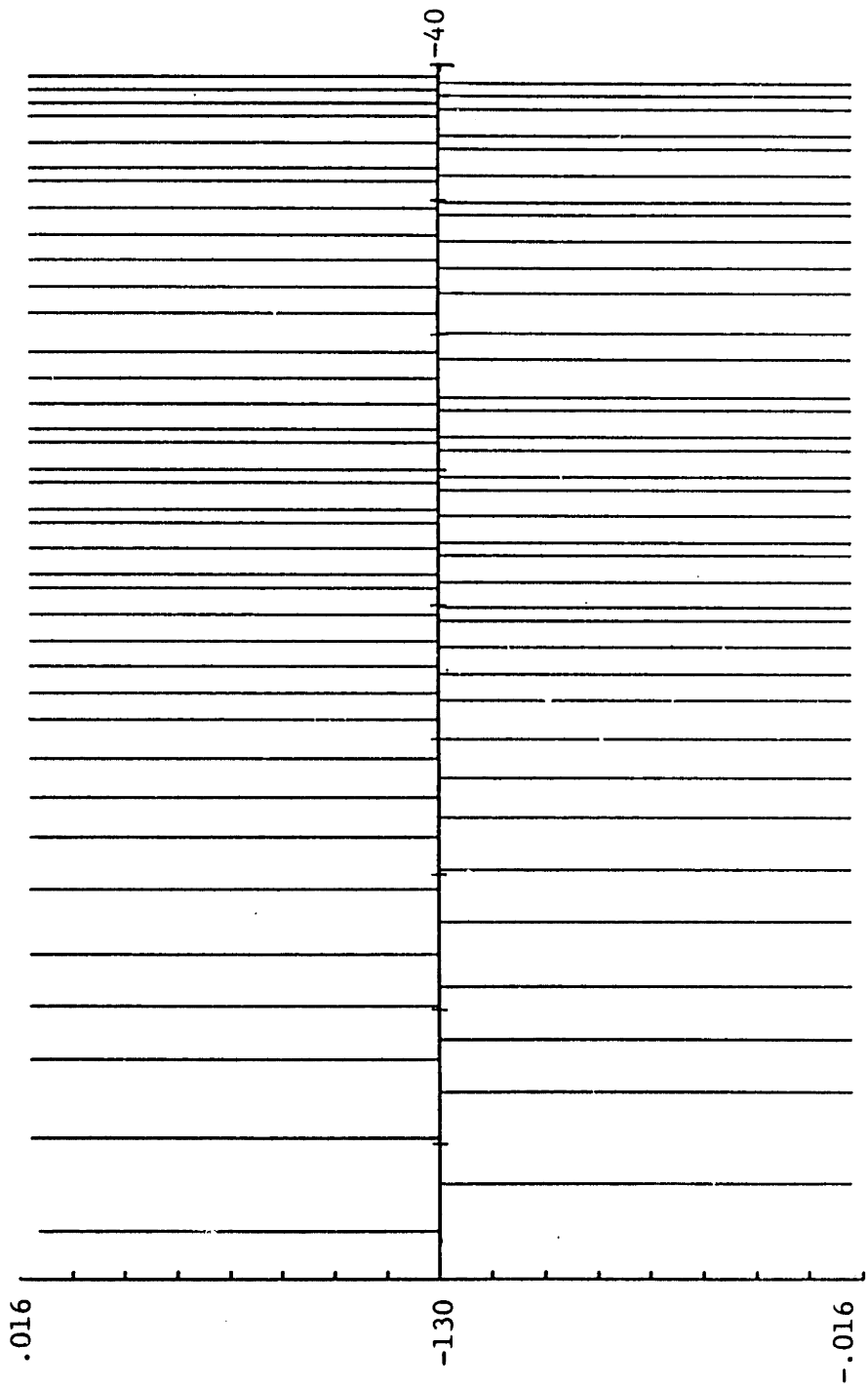

Figure 6.41a Withdrawal Weighted Waveform I.I.3: (Leftmost Section)
Adjacent weights alternate in sign permitting structure-1 to be used in the physical implementation.

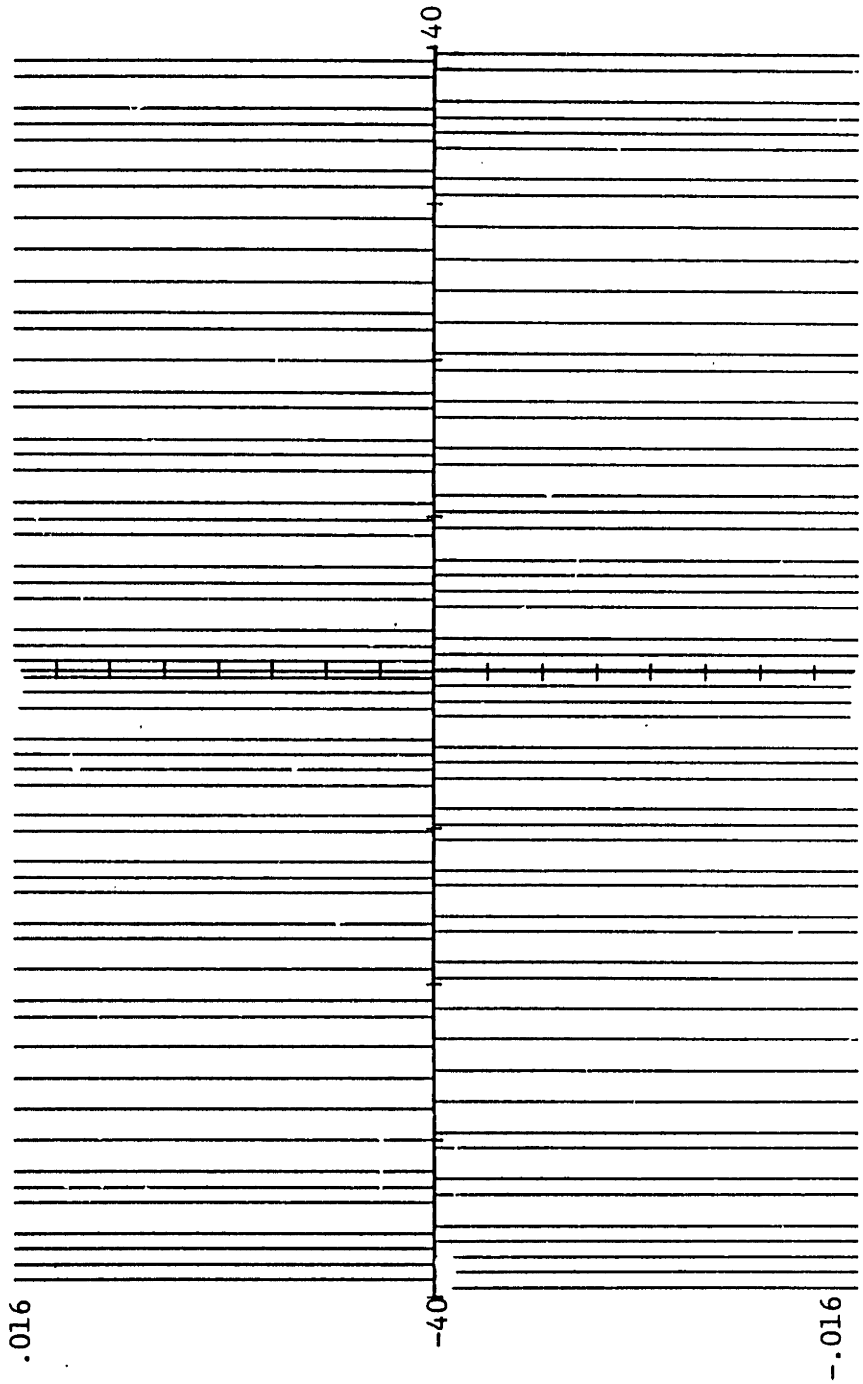

Figure 6.41b Withdrawal Weighted Waveform I.I.3: (Center Section)
Adjacent weights alternate in sign permitting structure-I to be used in the physical implementation.

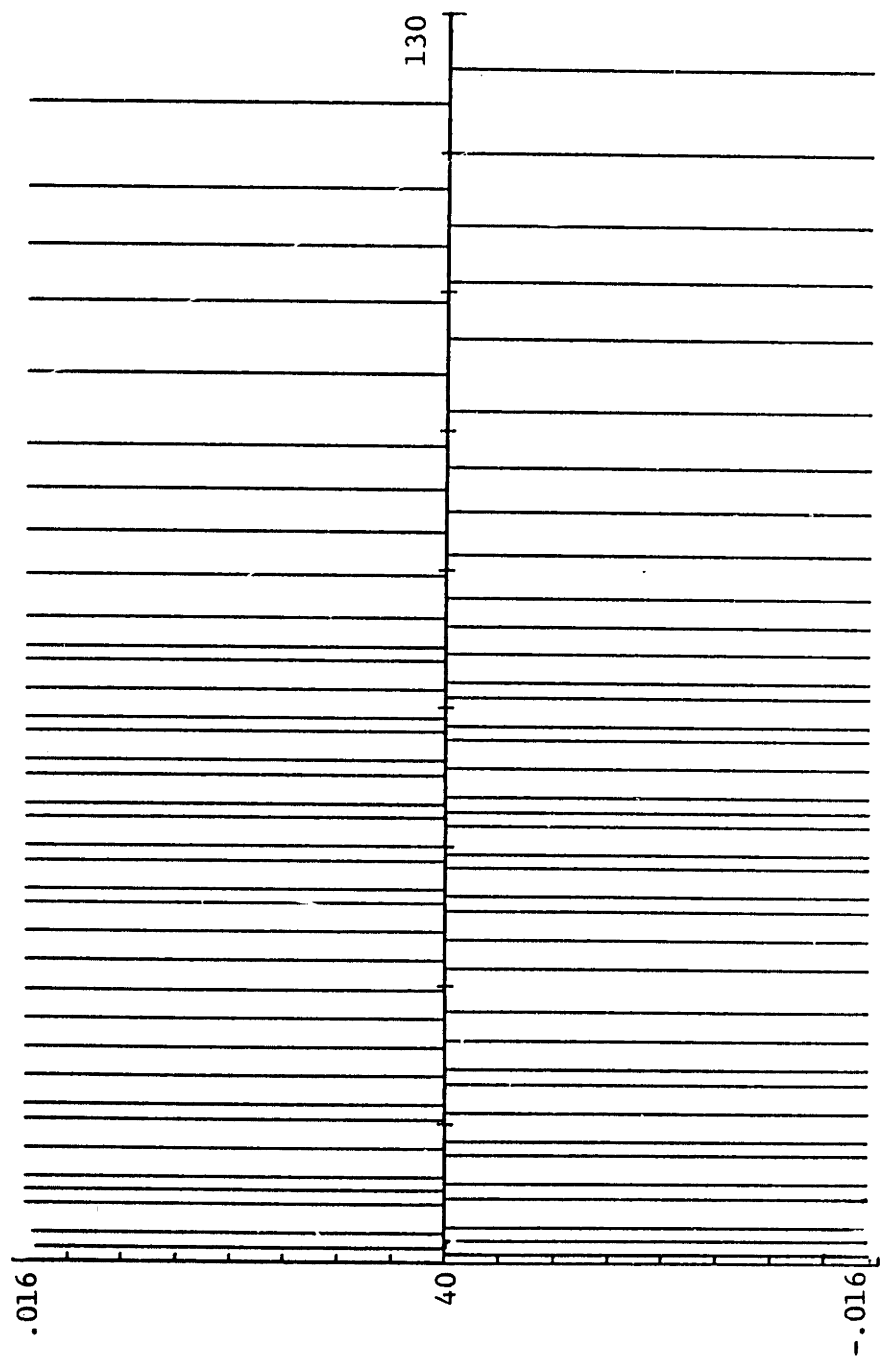

Figure 6.41c Withdrawal Weighted Waveform I.I.3: (Rightmost Section)
Adjacent weights alternate in sign permitting structure-I to be used in the physical implementation.

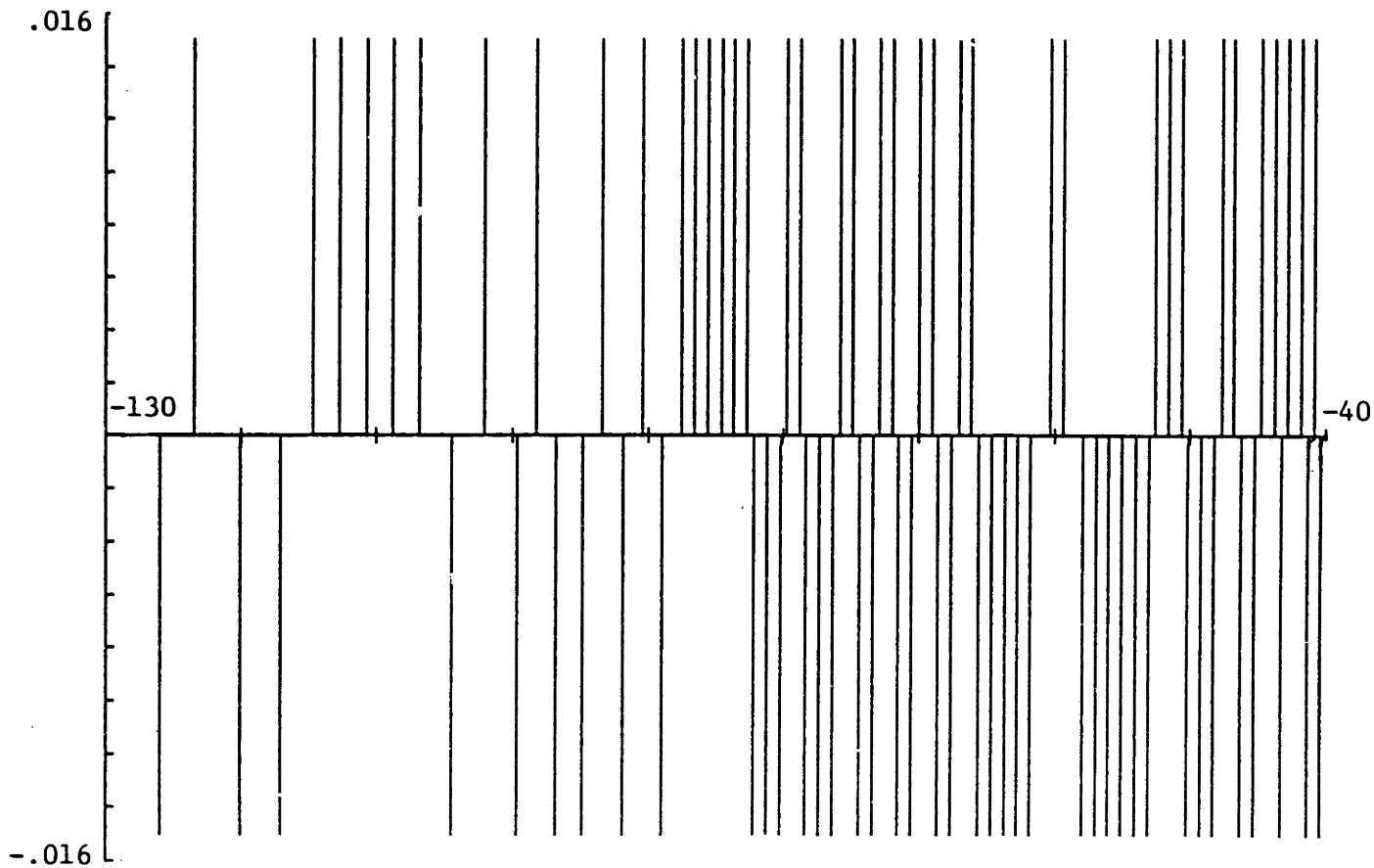

Figure 6.42a Withdrawal Weighted Waveform I.II.5: (Leftmost Section)
Adjacent weights do not necessarily alternate in sign, thereby necessitating the use of structure-II in the physical implementation.

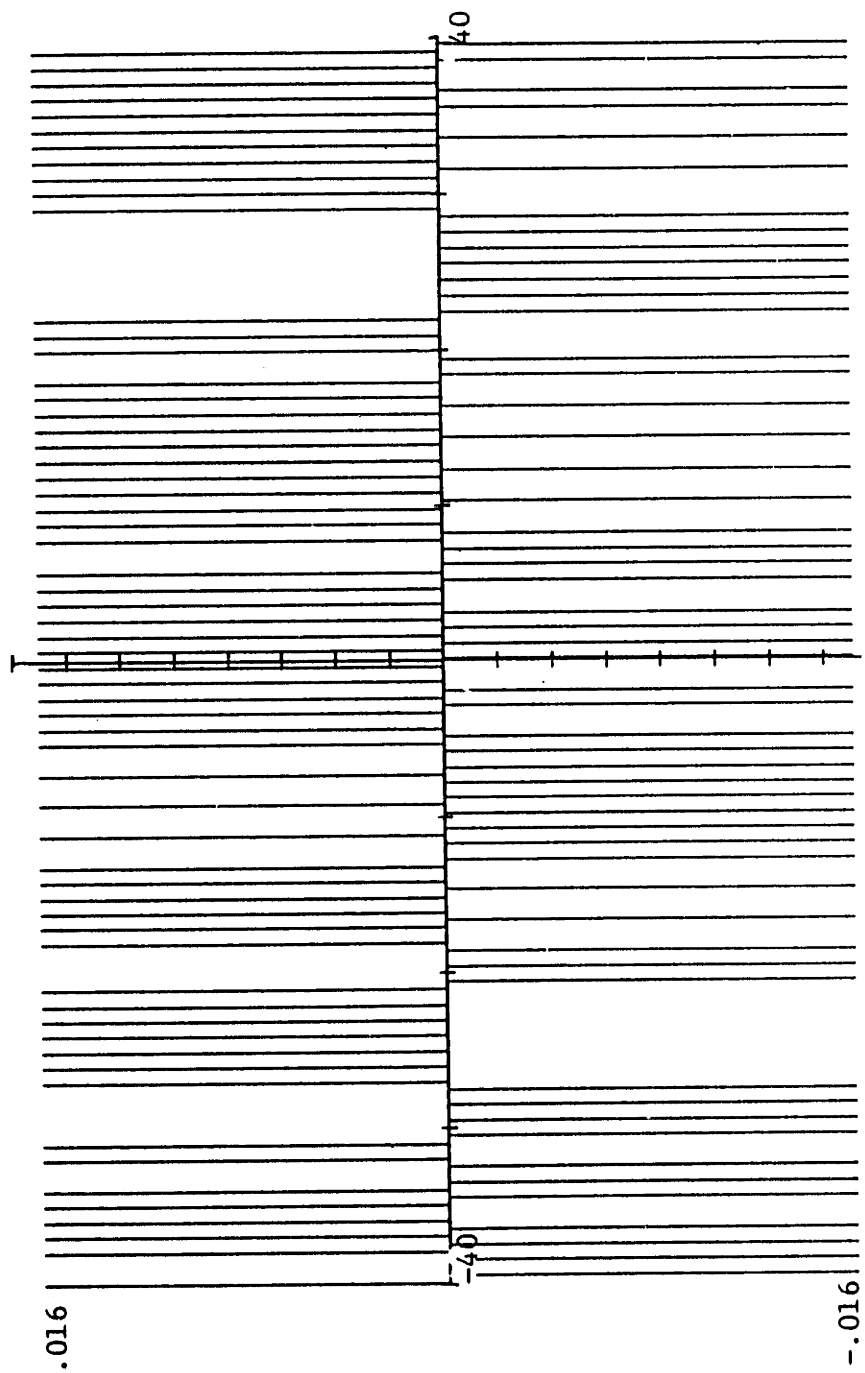

Figure 6.42b Withdrawal Weighted Waveform I.II.5: (Center Section)
Adjacent weights do not necessarily alternate in sign, thereby necessitating the use of structure-II in the physical implementation.

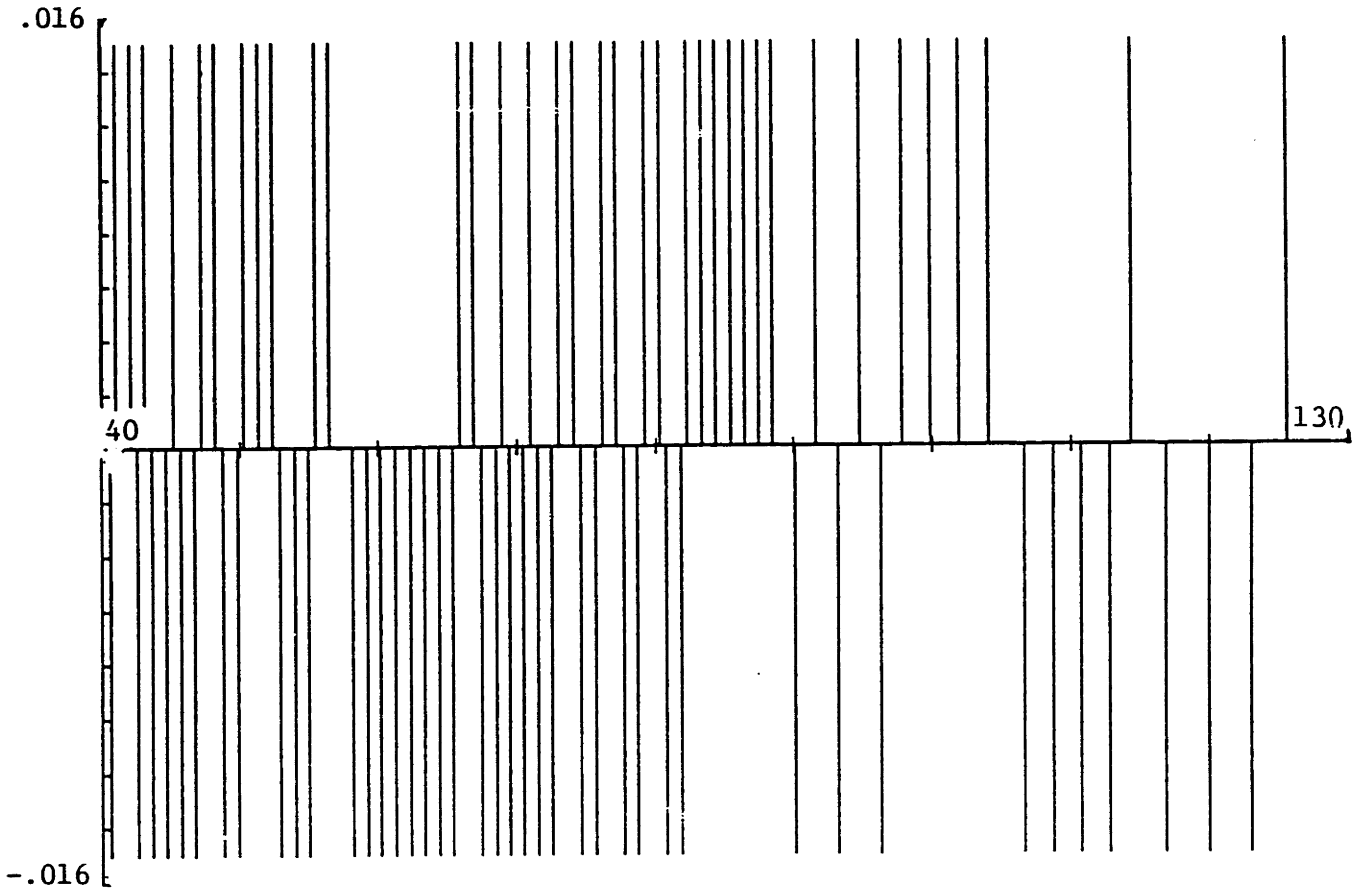

Figure 6.42c Withdrawal Weighted Waveform 1.11.5: (Rightmost Section)
Adjacent weights do not necessarily alternate in sign, thereby necessitating the use of structure-II in the physical implementation.

6.6.4 Summary of Results: Withdrawal Weighting

All the withdrawal weighted results are presented in graphical form in Fig. 6.43. It is clear that structure-II permits substantially better results than structure-I, as it should, due to the added freedom of not requiring strict sign alternation of the source weights. In general, sidelobe levels and passband ripple are substantially lower in the case of structure-II. An added bonus of structure-II is that the bandwidth over which the withdrawal weighting is accurate, is substantially broader. For example, in the case of prototype-I, we see from Figs. 6.35 and 6.37 that the bandwidth over which the sidelobes remain below – 40 dB is 60% broader for structure-II.

Although prototype-III is substantially better than prototype-I, once the withdrawal weighting is done, a substantial portion of this advantage is lost. The difficulty of withdrawal weighting prototype-III and the higher performance, both result from the higher dynamic range of prototype-III, 12.2 versus 5.8 for prototype-I (See Table 6.1 of Sec. 6.5.2.). Another fact apparent from Fig. 6.43 is that the spread of values for prototype-III, structure-I is much broader than the others. This indicates that the high dynamic range of prototype-III is really too large for the forced sign alternation of the sources imposed by structure-I.

In Table 6.8, we summarize some of the key results obtained with waveform-I and compare our results with what has been previously achieved. Standardizing on 252 wavelengths for each transducer, we see that a uniform amplitude phase weighted design based on the stationary phase approximation [30,75] has a rather large 5.3 dB peak to peak passband ripple. If a shape factor of 1.15 is required, it is only able to achieve 9.4 dB of rejection at the band edge since the response falls off very slowly outside the synchronous region. In order to achieve a reasonable rejection level of 51 dB, with a

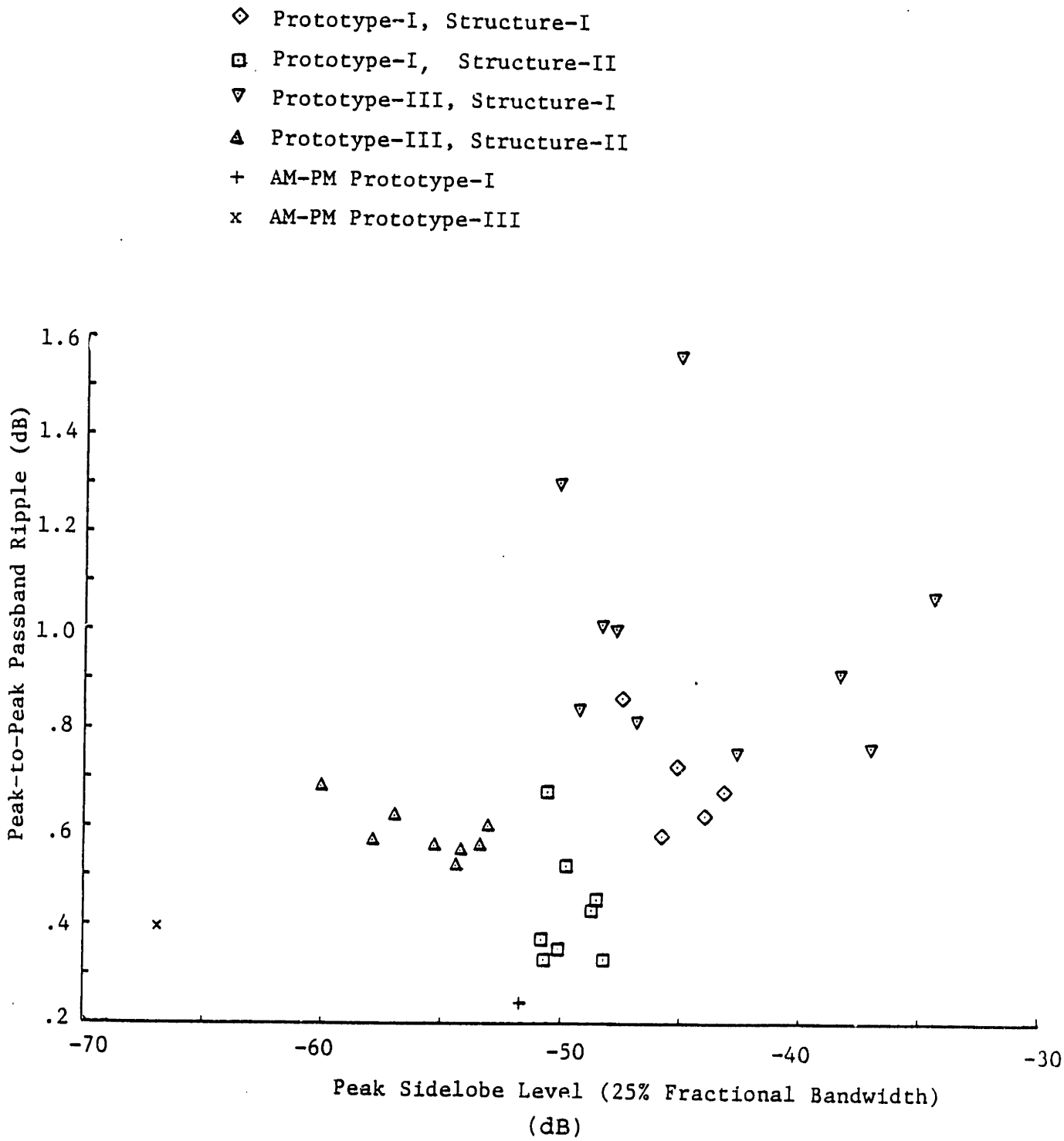

Figure 6.43 Performance Comparison of the Withdrawal Weighted Designs

shape factor of 1.15, the linearly chirped waveform must be 100 times longer than any of the other waveforms in the table. Hartmann's technique [42] represents a very significant improvement. Using the same length restriction of 252 wavelengths, the rejection level was improved by about 20 dB and the passband ripple was cut by a factor of three. The withdrawal weighted version of prototype-I using structure-II improved the rejection level by another 20 dB and cut the passband ripple by more than a factor of 4.5.

It is important to note that chirped designs need not be excessively long. In fact, the nonlinearly chirped design with a noninvertible instantaneous frequency discussed here, is shorter than the Parks-McClellan [85] design of similar performance. The main penalty we pay is a reduction in the bandwidth over which the sidelobes remain controlled. This seems to be a reasonable tradeoff since we gain from a reduction of two orders of magnitude in the required weighting dynamic range at a cost of increased far out sidelobes which can be reduced by the matching circuit. Due to the reduction in diffraction and transverse electrostatic end effects arising from the uniform aperture, high performance filters of much narrower maximum aperture should be realizable.

	Length of Each Transducer	Peak Inner Sidelobe (dB)	Peak-Peak Passband Ripple (dB)	Fractional Bandwidth of Controlled Sidelobes (-40 dB)	Dynamic Range* of Time Weighting Required
Structure-I Waveform I.I.5	252	-47.5	.86	34%	1
Structure-II Waveform I.II.5	252	-51.0	.37	55%	1
Hartmann's Iterative Procedure [42]	252	-28.4	1.7	--	1
Linear Chirp (Stationary Phase)	252	- 9.4	5.3	300%	1
Linear Chirp (Stationary Phase)	29330	-50.8	5.0	300%	1
AM-PM Prototype-I	252	-51.8	.20	300%	5.8
Parks-McClellan [85] (2 Identical IDTs)	270	-51.0	.37	300%	239

Table 6.8 Comparison of Final Results (Prototype-I) with Previous Work
All the above filters have a 7.1% fractional bandwidth, and a shape factor of approx. 1.15. *Dynamic range is defined as the ratio of the maximum to minimum source weight except in the case of the Parks-McClellan design. In this case, we use the ratio of the maximum weight to the average of the minimum 10%. This prevents a few very small weights from dominating the measure of the dynamic range.

REFERENCES

[1] Andersen Laboratories (1980), "Handbook of Acoustic Signal Processing, Vol. I, second edition," Bloomfield, Conn.

[2] Acki, T. and K. A. Ingebrigtsen (1977), "Acoustic Surface Waves in Split Strip Periodic Metal Gratings on a Piezoelectric Surface," *IEEE Trans. on Sonics and Ultrasonics*, SU-24, 179–193.

[3] Atzeni, C. and L. Masotti (1970), "A New Sampling Procedure for the Synthesis of Linear Transversal Filters," *IEEE Trans. on Aerospace and Electronic Systems*, AES-7, 662–670.

[4] Auld, B. A. (1973), *Acoustic Fields and Waves in Solids, Vol. II*, Wiley, New York.

[5] Bagdasaryan, A. S., A. M. Kmita and Yu. M. Shchukin (1981), "Two Channel Surface-Acoustic-Wave Filters with Capacitive Electrode Weighting," *Sov. Phys. Tech. Phys.*, 26, 1285–1286.

[6] Bertsekas, D. P. (1982), "Notes on Nonlinear Programming and Discrete-Time Optimal Control," *MIT Laboratory for Information and Decision Systems Report*, LIDS-R-919.

[7] Blotekjaer, K., K. A Ingebrigtsen and H. Skeie (1973), "A Method for Analyzing Waves in Structures Consisting of Metal Strips on Dispersive Media," *IEEE Trans. on Electron Devices*, ED-20, 1133–1138.

[8] Bristol, T. W. (1972), "Synthesis of Periodic Unapodized Surface Wave Transducers," *Proc. IEEE 1972 Ultrasonics Symp.*, 377–380.

[9] Broyden, C. G. (1965), "A Class of Methods for Solving Non-Linear Simultaneous Equations," *Math. Comp.*, 19, 577–593.

[10] Broyden, C. G. (1970), "The Convergence of a class of Double Rank Minimization Algorithms," Parts I and II, *J. Inst. Maths. Applns.*, 6, 76–90 and 222–231.

[11] Chen, D. P. and H. A. Haus (1985), "Analysis of Metal Strip SAW Gratings and Transducers," accepted for publication, *IEEE Trans. on Sonics and Ultrasonics*, January 1985.

[12] Cheney, E. W. (1966), *Introduction to Approximation Theory*, McGraw-Hill, New York.

[13] Collins, J. H., H. M. Gerard, T. M. Reeder and H. J. Shaw (1969), "Unidirectional Surface Wave Transducer," *Proc. IEEE*, **57**, 833–835.

[14] Dahlquist, G. and A. Bjorck (1974), *Numerical Methods*, Prentice Hall, Englewood Cliffs, NJ.

[15] Datta, S. and B. J. Hunsinger (1979), "First Order Reflection Coefficient of Surface Acoustic Waves from Thin-Strip Overlays," *J. Appl. Phys.*, **50**, 5661–5665.

[16] Datta, S., B. J. Hunsinger and D. C. Malocha (1979), "A Generalized Model for Periodic Transducers with Arbitrary Voltages," *IEEE Trans. on Sonics and Ultrasonics*, **SU-26**, 235–242.

[17] Datta, S. and B. J. Hunsinger (1980), "An Analytical Theory for the Scattering of Surface Acoustic Waves by a Single Electrode in a Periodic Array on a Piezoelectric Substrate," *J. Appl. Phys.*, **51**, 4817–4823.

[18] Datta, S. and B. J. Hunsinger (1980), "An Analysis of Energy Storage Effects on SAW Propagation in Periodic Arrays," *IEEE Trans. on Sonics and Ultrasonics*, **SU-27**, 333–341.

[19] Datta, S. and B. J. Hunsinger (1980), "Element Factor for Periodic Transducers," *IEEE Trans. on Sonics and Ultrasonics*, **SU-27**, 42–44.

[20] Davidon, W. C. (1959), "Variable Metric Method for Minimization," *AEC Research and Development Report*, **AN2-5990**.

[21] Deczky, A. G. (1974), "Equiripple and Minimax (Chebyshev) Approximations for Recursive Digital Filters," *IEEE Trans. on Acoustics, Speech and Signal Processing*, **ASSP-22**, 98–111.

[21a] Doyle, W. (1963), "On Approximating Linear Array Factors," Rand Corp. Research Memorandum **RM-3530-PR**.

[22] Dunnrowicz, C., F. Sandy and T. Parker (1976), "Reflection of Surface Waves from Periodic Discontinuities," *Proc. IEEE (1976) Ultrasonics Symposium*, 386–390.

[23] Engan, H. (1967) "Interdigital Electrode Transducers for the Excitation of Elastic Surface Waves in Piezoelectric Media," The Norwegian Institute of Technology, Trondheim, Norway, *Elab. Rept.* **TE-91**.

[24] Engan, H. (1969), "Excitation of Elastic Surface Waves by Spatial Harmonics of Interdigital Transducers," *IEEE Trans. on Electron Devices*, **ED-16**, 1014–1017.

[25] Engan, H. (1975), "Surface Acoustic Wave Multielectrode Transducers," *IEEE Trans. on Sonics and Ultrasonics*, **SU-22**, 395–401.

[26] Fletcher, R. and M. J. D. Powell (1963), "A Rapidly Convergent Descent Method for Minimization," *Computer Journal*, **6**, 163–168.

[27] Fletcher, R. (1970), "A New Approach to Variable Metric Algorithms," *Computer Journal*, **13**, 317–322.

[28] Fletcher, R., J. A. Grant and M. D. Hebder (1974), "Linear Minimax Approximation as the Limit of Best L_p -Approximation," *SIAM J. Numer. Anal.*, **11**, 123–136.

[29] Fletcher, R. (1981), *Practical Methods of Optimization* Vols. I and II, John Wiley and Sons, New York.

[30] Fowle, E. N. (1964), "The Design of FM Pulse Compression Signals," *IEEE Trans. on Information Theory*, **IT-10**, 61–67.

[31] Garber, E. M. and H. A. Haus (1983), "Synthesis of High Performance SAW Filters with Nonuniformly Spaced Fingers," *Proc. of the IEEE 1983 Ultrasonics Symposium*, 27–32.

[32] Gerard, H. M. (1978),"Principles of Surface Wave Filter Design," in *Topics in Applied Physics*, Vol. 24: Acoustic Surface Waves, edited by A. A. Oliner, Springer-Verlag, New York.

[33] Gill, P. E., W. Murray and M. H. Wright (1981), *Practical Optimization*, Academic Press, New York.

[34] Goldfarb, D. (1970), "A Family of Variable Metric Methods Derived by Variational Methods," *Maths. Comput.*, **24**, 23–26.

[35] Greebe, C. A. A. J., P. A. Van Dalen, T. J. B. Swanenburg and J. Walter (1971), "Electric Coupling Properties of Acoustic and Electric Surface Waves," *Physics Reports* (Section C of *Physics Letters*) **1**, 235–268.

[36] Guillemin, E. A. (1949), *The Mathematics of Circuit Analysis*, Wiley, New York.

[37] Hanma, K. and B. J. Hunsinger (1976), "A Triple Transit Suppression Technique," *Proc. IEEE 1976 Ultrasonic Symposium*, 328–331.

[38] Hartmann, C. S., W. S. Jones and H. Vollers (1972), "Wideband Unidirectional Interdigital Surface Wave Transducers," *IEEE Trans. on Sonics and Ultrasonics*, **SU-19**, 378–381.

[39] Hartmann, C. S. and B. G. Secrest (1972), "End Effects in Interdigital Surface Wave Transducers," *Proc. IEEE 1972 Ultrasonic Symposium*, 413–416.

[40] Hartmann, C. S., D. T. Bell, Jr. and R. C. Rosenfeld (1973), "Designing Acoustic Surface Wave Filters," *Texas Instruments Advanced Technology Laboratory Technical Report*, TR # **-08-73-12.**

[41] Hartmann, C. S., D. T. Bell, Jr. and R. C. Rosenfeld (1973), "Impulse Model Design of Acoustic Surface Wave Filters," *IEEE Trans. on Sonics and Ultrasonics*, **SU-20**, 80–93.

[42] Hartmann, C. S. (1973), "Weighting Interdigital Surface Wave Transducers by Selective Withdrawal of Electrodes," *Proc. IEEE 1973 Ultrasonics Symposium*, 423–426.

[43] Hartmann, C. S., R. J. Kansy, H. A. Haus and P. V. Wright (1981), "Theoretical Modeling of an Innovative Unidirectional Surface Acoustic Wave Transducer," *Final Report for NSF Grant DAR-8009600.*

[44] Hartmann, C. S., P. V. Wright, R. J. Kansy and E. M. Garber (1982), "An Analysis of SAW Interdigital Transducers with Internal Reflection and the Application to the Design of Single-Phase Unidirectional Transducers," *Proc. IEEE 1982 Ultrasonics Symposium*, 27–32.

[45] Haus, H. A. (1977), "Modes in SAW Grating Resonators," *J. Appl. Phys.*, **48**, 4955–4961.

[46] Haus, H. A. and R. V. Schmidt (1977), "Cascaded SAW Gratings as Passband filters," *Electronics Letters*, 13, 445–446.

[47] Haus, H. A. (1984), *Waves and Fields in Optoelectronics*, Prentice-Hall, Englewood Cliffs, NJ.

[48] Hildebrand, F. B. (1976), *Advanced Calculus for Applications* (Second Edition), Prentice-Hall, Englewood Cliffs, NJ.

[49] Hodjat, F. and S. A. Hovanessian (1978), "Nonuniformly Spaced Linear and Planar Array Antennas for Sidelobe Reduction," *IEEE Trans. on Antennas and Propagation*, **AP-26**, 198–204.

[50] Hunsinger, B. J. and R. J. Kansy (1975), "SAW Filter Sampling Techniques," *IEEE Trans. on Sonics and Ultrasonics*, **SU-22**, 270–273.

[51] Hunsinger, B. J. (1981), "Research to Provide a Theoretical Determination of Surface Acoustic Wave Velocity and Impedance Differences Between Metal Strips and Free Surface Regions of Metallic Gratings," *Rome Air Development Center Report* **RADC-TR-81-173.**

[52] Ingebrigsten, K. A. (1969), "Surface Waves in Piezoelectrics," *J. Applied Physics*, **40**, 2681–2686.

[53] Ingebrigtsen, K. A. (1973), "A Normal Mode Representation of Surface Wave Multistrip Couplers," *Proc. IEEE 1973 Ultrasonics Symposium*, 163–167.

[54] Islam, M. N., H. A. Haus and J. Melngailis (1984), "Bulk Radiation by Surface Acoustic Waves Propagating Under a Grating," *IEEE Trans. on Sonics and Ultrasonics*, **SU-31**, 123–135.

[55] Joshi, S. G. and R. M. White (1968), "Dispersion of Surface Elastic Wave Produced by a Conducting Grating on a Piezoelectric Crystal," *J. Appl. Phys.*, 39, 5819–5827.

[56] Kharusi, M. S. and G. W. Farnell (1972), "On Diffraction and Focusing in Anisotropic Crystals," *Proc. IEEE*, 60, 945–956.

[57] Kogelnik, H. (1976), "Filter Response of Nonuniform Almost-Periodic Structures," *Bell System Technical Journal*, 55, 109–126.

[58] Lakin, K. M. (1974), "Electrode Resistance Effects in Interdigital Transducers," *IEEE Trans. on Microwave Theory and Techniques*, MTT-22, 418–424.

[59] Lawson, C. L. (1969), "Contributions to the Theory of Linear Least Maximum Approximations, Ph.D. Thesis, UCLA, Los Angeles.

[60] Lewis, M. F. (1973), "Surface Acoustic-Wave Filters Employing Symmetric Phase-Weighted Transducers," *Electronics Lett.*, 9, 138–140.

[61] Lewis, B., P. M. Jordan, R. F. Milsom and D. P. Morgan (1978), "Charge and Field Superposition Methods for Analysis of Generalized SAW Interdigital Transducers," *Proc. IEEE 1978 Ultrasonics Symposium*, 709–714.

[62] Li, R. C. M. and J. Melngailis (1975), "The Influence of Stored Energy at Step Discontinuities on the Behavior of Surface-Wave Gratings," *IEEE Trans. on Sonic and Ultrasonics*, SU-22, 189–198.

[63] Louisell, W. (1960), *Coupled Mode and Parametric Electronics*, Wiley, New York.

[64] Mader, W. R., C. Ruppel and E. Ehrman-Falkenau (1982), "Universal Method for Compensation of SAW Diffraction and Other Second Order Effects," *Proc. IEEE 1982 Ultrasonics Symposium*, 23–28.

[65] Malocha, D. C. and B. J. Hunsinger (1977), "Capacitive Tap Weighted SAW Transducers," *IEEE Trans. on Sonics and Ultrasonics*, SU-24, 293–301.

[66] Marshall, F. G. and E. G. S. Paige (1971), "A Novel Acoustic-Surface-Wave Directional Coupler with Diverse Applications," *Electronics Lett.*, 7, 460–462.

[67] Marshall, F. G. and E. G. S. Paige, (1971), "Observed Properties of an Acoustic-Surface-Wave Multistrip Coupler," *Electronics Lett.*, 7, 463–464.

[68] Marshall, F. G. and E. G. S. Paige and A. J. Young (1971), "New Unidirectional Transducer and Broadband Reflector of Acoustic Surface-Waves," *Electronics Lett.*, 7, 638–640.

[69] Milsom, R. F., Reilly, N. H. C. and Redwood, M. (1977), "Analysis of Generation and Detection of Surface and Bulk Acoustic Waves by Interdigital Transducers," *IEEE Trans. on Sonics and Ultrasonics* SU-24, 147–166.

[70] Milsom, R. F., M. Redwood and N. H. C. Reilly (1977), "The Interdigital Transducer," in *Surface Wave Filters*, edited by H. Matthews, Chapt. 2, Wiley, New York.

[71] Mitchell, R. F. (1971), "Acoustic-Surface Wave Filters," *Phillips Tech. Rev.*, **32**, 179–189.

[72] Morgan, D. P., B. Lewis and J. G. Metcalfe (1979), "Fundamental Charge Distributions for Surface-Wave Interdigital Transducer Analysis," *Electronics Lett.*, **15**, 583–585.

[73] Morgan, D. P. (1980), "Quasistatic Analysis of Generalized SAW Transducers Using the Green's Function Method," *IEEE Trans. on Sonics and Ultrasonics*, **SU-27**, 111–123.

[74] Murray, W. (ed.) (1972), *Numerical Methods for Unconstrained Optimization*, Academic Press, New York.

[75] Nudd, G. R., M. Waldner and R. L. Zimmerman (1974), "Design of Unapodized Surface-Wave Transducers with Spectral Weighting," *IEEE Trans. on Microwave Theory and Techniques*, **MTT-22**, 25–32.

[76] Oppenheim, A. V. and R. W. Schafer (1975), *Digital Signal Processing*, Prentice-Hall, Englewood-Cliffs, NJ.

[77] Panasik, C. M. and B. J. Hunsinger (1981), "Scattering Matrix Analysis of Surface Acoustic-Wave Transducers Reflectors and Transducers," *IEEE Trans. on Sonics and Ultrasonics*, **SU-28**, 79–91.

[78] Papoulis, A. (1962), *The Fourier Integral and Its Applications*, McGraw-Hill, New York.

[80] Parks, T. W. and J. H. McClellan (1972), "Chebyshev Approximation for Nonrecursive Digital Filters with Linear Phase," *IEEE Trans. on Circuit Theory*, **CT-19**, 189–194.

[81] Peach, R. C. (1981), "A General Approach to the Electrostatic Problem of the SAW Interdigital Transducer," *IEEE Trans. on Sonics and Ultrasonics*, **SU-28**, 96–105.

[82] Peach, R. C. (1983), "General Diffraction Analysis for Surface Acoustic Wave Filters," *Proc. IEEE 1983 Ultrasonics Symposium*, 98–103.

[83] Penunuri, D. (1978), "A Numerical Technique for SAW Diffraction Simulation," *IEEE Trans. on Microwave Theory and Techniques*, **MTT-26**, 288–294.

[83a] Pierce, J. R. (1954) "Coupling of Modes of Propagation," *J. Appl. Phys.*, **25**, 179–183.

[84] Polya, G. (1913), "Sur Une Algorithme Toujours Convergent Pour Obtenir Les Polynomes de Meillure Approximation de Tchebycheff Pour Une Fonction Continue Quelconque," *Comptes Rendus.*, **157**, 840–843.

[85] Rabiner, L. R., J. H. McClellan and T. W. Parks (1975), "FIR Digital Filter Design Techniques Using Weighted Chebyshev Approximation," *Proc. IEEE*, **63**, 595–610.

[86] Rabiner, L. R. and B. Gold (1975), *Theory and Applications of Digital Signal Processing*, Prentice-Hall, Englewood-Cliffs, NJ.

[87] Redlich, R. W. (1973), "Iterative Least-Squares Synthesis of Nonuniformly Spaced Linear Arrays," *IEEE Trans. on Antennas and Propagation*, AP-21, 106–108.

[88] Rice, J. R. (1963), *The Approximation of Functions*, Addison-Wesley, Reading, MA.

[89] Rice, J. R. and K. H. Usow (1968), "The Lawson Algorithm and Extensions," *Math. Com.*, 22, 118–127.

[90] Rosenfeld, R. C., C. S. Hartmann and R. B. Brown (1974), "Low Loss Unidirectional Acoustic Surface Wave Filters," *Proc. of the 28th Ann. Symp. on Freq. Control, U.S. Army Electronics Command*, Fort Monmouth, NJ, 299–303.

[91] Ruthroff, C. L. (1959), "Some Broad-Band Transformers", *Proc. IRE*, 47, 1337–1342.

[92] Sato, H., T. Meguro, K. Yamanouchi and K. Shibayama (1978), "Piezoelectric Thin Film Unidirectional SAW Transducer and Filter," *Proc. IEEE*, 66, 102–104.

[93] Schulz, M. B. and J. H. Matsinger (1972), "Rayleigh-Wave Electromechanical Coupling Constants," *Applied Physics Lett.*, 20, 367–369.

[94] Shano, D. F. (1970), "Conditioning of quasi-Newton Methods for Function Minimization," *Maths. Comput.*, 24, 647–656.

[95] Shibayama, K., K. Yamanouchi, H. Sato and T. Meguro (1976), "Optimum Cut for Rotated Y-Cut $LiNbO_3$ Crystal Used as the Substrate of Acoustic-Surface-Wave Filters, Proc. *IEEE*, 64, 595–597.

[96] Shimizu Y. and T. Hata (1977), "Unidirectional Surface Acoustic Wave Transducers with a ZnO Film on Glass Substrate," *Electronics Lett.*, 13, 384.

[97] Skeie, H. (1970), "Electrical and Mechanical Loading of a Piezoelectric Surface Supporting Surface Waves," *J. Acoust. Soc. Amer.*, 48, 1098–1109.

[98] Slobodnik Jr., A. J. (1976), "Surface Acoustic Waves and SAW Materials," Proc. IEEE, 64, 581–595.

[99] Slobodnik Jr., A. J., K. R. Laker, T. L. Szabo, W. J. Kearns, and G. A. Roberts (1977), "Low Sidelobe SAW Filters Using Overlap and Withdrawal Weighted Transducers," *Proc. IEEE 1977 Ultrasonics Symposium*, 757–762.

[100] Smith, H. I., R. C. Williamson and W. T. Brogan (1972), "Ion Beam Etching of Reflective Array Filters," *Proc. IEEE 1972 Ultrasonics Symposium*, 198–201.

[101] Smith, W. R., H. M. Gerard, J. H. Collins, T. M. Reeder and H. J. Shaw (1969), "Design of Surface Wave Delay Lines with Interdigital Transducers". *IEEE Trans. Microwave Theory and Techniques*, MTT-17, 865–873.

[102] Streibl, I., B. Syrett, M. Suthers and D. Conn (1983), "SAW Diffraction Compensation on Y-Z Lithium Niobate," *Proc. IEEE 1983 Ultrasonics Symposium*, 62–65.

[103] Swenson, G. and Y. T. Lo, (1961), "The University of Illinois Radio Telescope," *IRE Trans. on Antennas and Propagation*, AP-9, 9–16.

[104] Szabo, T. L. and A. J. Slobodnik Jr. (1973), "The Effect of Diffraction on the Design of Acoustic Surface Wave Devices," *IEEE Trans. on Sonics and Ultrasonics*, SU-20, 240–251.

[105] Tancrell, R. H. and M. G. Holland (1971), "Acoustic Surface Wave Filters," *Proc. IEEE*, 59, 393–409.

[106] Tansal, S. and H. Sobol (1963), "Wide-Band Pulse Transformers for Matching Low Impedance Loads," *Rev. of Scientific Instruments*, 34, 1075–1081.

[107] Wagers, R. S. (1976), "Transverse Electrostatic End Effects in Interdigital Transducers," *Proc. IEEE 1976 Ultrasonics Symposium*, 536–539.

[108] Waldron, R. A. (1969), "Principles of Wideband Unidirectional Piezoelectric Transducers," MIT Lincoln Labs Technical Note **1969-54.**

[109] Weglein, R. D. and G. R. Nudd (1972), "Space-Harmonic Response of Surface Wave Transducers," *Proc. IEEE 1972 Ultrasonics Symposium*, 346–352.

[110] White, R. M. and F W. Voltmer (1965), "Direct Piezoelectric Coupling to Surface Elastic Waves," *Appl. Phys. Lett.*, 7, 314–316.

[111] Worley, J. C. (1973), "Bandpass Filters Using Non-Linear FM Surface-Wave Transducers," *IEEE Trans. on Microwave Theory and Techniques*, MTT-21, 302–303.

[112] Wright, P. V. and H. A. Haus (1980), "Theoretical Analysis of Second-Order Effects in Surface-Wave Gratings," *Proc. 34th Ann. Symp. on Freq. Control*, U.S. Army Electronics Command, Fort Monmouth, NJ, 262–268.

[113] Wright, P. V. and H. A. Haus (1980), "A Closed Form Analysis of Reflective-Array Gratings," *Proc. IEEE 1980 Ultrasonics Symposium*, 282–287.

[114] Wright, P. V. (1981), "A Coupling-of-Modes Analysis of SAW Grating Structures," Ph.D. Thesis, MIT, Cambridge, MA.

[115] Wright, P. V. and S. A. Wilkus (1983), "A Prototype Low-Loss Filter Employing Single-Phase Unidirectional Transducers," *Proc. IEEE 1983 Ultrasonics Symposium*, 72–76.

[116] Yamaguchi, M., K. Hashimoto and H. Kogo (1978), "Withdrawal of Interdigital Electrodes for Sidelobe Reduction of SAW Filters by Implicit Enumeration Algorithm for 0-1 Type Integer Optimization," *Trans. IECE Japan*, **E61**, 631–632.

[117] Yamaguchi, M., K. Hashimoto and H. Kogo (1979), "Suboptimization of Electrode-Withdrawal Weighted SAW Filters," *IEEE Trans. on Sonics and Ultrasonics*, **SU-26**, 53–59.

[118] Yamaguchi, M., K. Hashimoto and H. Kogo (1979), "A Simple Method of Reducing Sidelobes for Electrode-Withdrawal Weighted SAW Filters," *IEEE Trans. on Sonics and Ultrasonics*, **SU-26**, 334–339.

[119] Yamanouchi, K., F. M. Nyffeler and K. Shibayama (1975), "Low Insertion Loss Acoustic Surface Wave Filter Using Group-Type Unidirectional Interdigital Transducer," *Proc. IEEE 1975 Ultrasonics Symposium*, 317–321.

[120] Yariv, A. (1973), "Coupled Mode Theory of Guided Wave Optics," *IEEE J. Quant. Electronics*, **QE-9**, 919–933.